Acknowledgements

It is with deep gratitude and privilege that I am able to perform the research that I do. Medical isotopes, and the production of, were quite new to me when I began this journey. The initial reason why I applied to this research topic was actually for practical reasons. I saw that I could use techniques that I have learned in nanochemistry to this project and that my skillset might provide a unique perspective on the research that had been done up to that period. Medical isotopes were a new world to me and "In the beginning, when the world was new and nothing had a name…"[1] I was not alone. Throughout everything, I had the help of great mentors, technicians, family and friends, without whom this thesis would not exist. I grew to love and appreciate every component of my research, from the scientific and technical components, to the interpersonal and communicative aspects. As a team, I believe we have opened doors in this topic and shed light on important new ideas to extract and purify isotopes. It is here that I have the space to thank all of those whom have made this journey possible and successful. Although the acknowledgements maybe the smallest part of any thesis, may it represent the most meaningful and most sincere of all that is written.

To my mentors:

Thank you for giving me this opportunity and supporting me throughout my research. I met Dr. Sven Van den Berghe and Dr. Ann Leenaers one week before the application deadline in a skype interview. The first question asked was, "You don't have background in nuclear, so why are you applying?"... Somehow, I knew this is what I wanted to do and I felt that my mentors always trusted me despite being new to the field. I feel that we have grown together throughout this project and we will continue to grow even after.

Similarly, I met Prof. Dr. Thomas Pardoen the day that I had to defend my topic in front of a jury. Even early on, I felt that we worked well

[1] From One Hundred years of solitude by **Gabriel García Márquez**

together. Although we meet only every other month, I find our discussion insightful and meaningful. I feel that Thomas has always valued my opinion with respect and we discovered the world of medical isotopes together as researchers.

I would like to give a special thanks to Dr. Valery Host and Dr. Christophe Wylocke. Following an unsuccessful PhD researcher in this topic, I was worried that my own research would have started with doubt and disbelief. However, I have always had their support. Although they were always incredibly busy with the conversion from HEU to LEU, I feel that they somehow always managed to respond to me quickly and enthusiastically. Together, through meetings and lunch conversations, we have solved many problems, developed patents, and advanced our understanding of LEU fuel digestions.

To my family,

I am very privilege to have my family. My mother 順子 (Junko) and father Robert (Bob) have supported me and everything that I chose to do. My father joined the air force to support himself and my family which gave us a chance to travel the world. He showed me what life is like when you love your job and family. My mother took care of us everywhere we went. It is my mother who pushed me to pursue higher education. Born in a time and place shadowed by the battle of Okinawa, she put me into English school systems and always reminded me of how privileged I was to be able to have an education. She has always impressed upon me the importance of “reading the air” (空気を読む), the importance of understanding, and she shaped who I am today. She is a mountain; a place to look for guidance, strength, and clarity. If this is the only part of my thesis she can read, I want her to know that I am here because of her.

家族へ

わたしは、わたしの家族の一員であることを大変誇らしく思う。わたしの母・順子と、父・ロバートはわたしを、わたしが選んだこと全てを応援してくれた。ピアノ、野球、さまざまな国での留学、どんな場合であっても、わたしが疲れ切ったときは気遣ってくれるか、ただただ私の話に耳を傾けてくれた。２人はいつでもわたしのことを深く信頼してくれている。父は空軍に入隊し、家族を支え、世界中を旅する機会を家族に与えてくれた。彼は、仕事と家族を愛する人生がどのようなものかということを示してくれた。母は、わたしたちがどこにいても気に掛けてくれた。わたしに高等教育を究めることを勧めたのは彼女だ。母は、沖縄戦の傷がまだ残るころにかの地で生まれた。わたしを英語教育の課程に入れ、勉強ができるということがどんなに素晴らしいことなのかを、常々言い聞かせた。彼女から空気を読むことや理解することの大切さを教えこまれたことが、今日の私を形づくった。彼女は「山」だ。つまり、向かうべき方向、強さ、そして明快さを探すための場所だ。論文の中で、この文章が唯一彼女の理解できるパートであるならば、ここで伝えたい。わたしが今ここにいるのは彼女のお陰だということを。

A big thank you to my other family members, near and far, who have always been there for me. Nancy and David, who supported my education early on, have also taught me the importance of bringing family together and eating well. Dennis, Brian, Joe and Rika have raised me and continue to do so. Pat, Seal, Jet, Betty, Peter, Dicky, Ruth, Rachael, Mikey, Michelle, Grandma, and to the rest of my family who have brought me joy, I thank you.

To my friends,

It was my best friend Bob Blasdel who encouraged me to continue studying after having a burnout. We met in August 2006 at The Evergreen State College, and we continue to inspire each other to work

in sciences and enjoy life. As he was studying bacteriophages at KU Leuven, I found my own way there to study nanoscience and nanotechnology. Our friendship is an inseparable force and I cannot imagine life without him… and as my support needs support, I am happy that he has met Katja Reuter. She saves the day, every day.

On the first PhD day to defend our topic I met Daniele Salvato and we immediately became friends. Never have I met such a brilliant thinker who inspires me every day. Although we did not collaborate directly on each other's projects, I am confident to say that neither of us would be here without the other. Our friendship reminds me that, an important component of research and life is camaraderie.

Thanks to my family, Vitaly, Alena, Yuna, and Konstantin. I feel very honored to be a part of your family and it brings me more joy than you may know. No matter how far you guys are, you are always in my thoughts.

To my army of friends and support circle; Russ Kaehler, Aaron Neier, Larry, Alma, Ravi, Eric, Kate, Johnatan, Lennart, Lenny, Kenneth, Dieter… all of you.. I know I can count on you as much as you can count on me.

I would like to also give a special thanks to my high school English teacher Patricia (Patti) Wagner. Not only was she an inspiring teacher but she also guided me personally during a time in my life that I needed extra help. I hope every student has at least one such role model in their life.

Also, a big thanks to my piano teacher Bart Orye. Thank you for balancing my life in Mol and teaching me many new things on the piano. I hope we can continue learning music together.

Finally, to Sammy. You always make me smile and you have supported me while writing this thesis. I hope we will continue to learn from each other and grow together. Thank you for everything and all that you do. Also, a big thank you to Marina Verbrugghe and Dany for being so supportive!

Abstract

Every year, hospitals around the world diagnose and treat 48 million patients with medical isotopes [1]. Around 40 million of these procedures use the medical isotope technicium-99m, the daughter isotope of molybdenum-99, for diagnostic imaging. To this day, the majority of medical isotopes are produced by the fission of high-enriched uranium ($^{235}U > 20\%$) in the forms of UAlx (UAl_4, UAl_3, and UAl_2) targets, in a handful of test reactors around the world. After irradiation, the isotopes are extracted in a basic media (NaOH and $NaNO_3$) to be purified and sent to hospitals.

Under the Global Threat Reduction Initiative (GTRI) it is agreed to convert isotope production to low-enriched uranium (LEU, $^{235}U < 20\%$) sources to help keep fissile material out of the hands of rogue states and terrorists. However, in a direct LEU conversion, the yield of ^{99}Mo would be about 20% of the HEU target it replaces because of the reduced ^{235}U mass and increased neutron capture from the presence of ^{238}U, while leading to five times the volume of waste from the extraction process.

This thesis investigates in parallel, how to improve the current UAlx based medical isotope production method and the potential use of the high-density U_6Mn alloy to replace the fissile material in next generation targets. U_6Mn (U-density 16.8 g cm^{-3}) has the highest known U-density intermetallic, which is significantly higher than the currently used UAlx fuel (U-density 3 - 4.5 g cm^{-3}). High density materials would be ideal to increase the total amount of ^{235}U in a target. However, not much is known on how to extract isotopes after the irradiation process. The oxidation or “digestion” of these materials are studied in basic media, as a function of time and concentration of digestion reagents, to optimize the extraction of isotopes from these fuel types.

Part 1 of this thesis studies the digestion of UAlx materials. In UAlx materials, it is found through SEM and energy-dispersive X-ray (EDX) images, that oxidation of triple junctions and intergranular oxidation are key mechanisms in converting UAlx fuel, to UO_2 and $Na_2U_2O_7$ (yellow cake). An aluminum phase present at the grain boundaries is shown to highly enhance oxidation. Electron backscatter diffraction (EBSD) is used to further investigate oxidation at the grain boundaries, leading to the discovery of favorable and

unfavorable grain boundaries for oxidation in this material. Small grain sizes are shown to outperform large grain sizes, and particles sizes were shown to have little to no effect.

Part 2 of this thesis studies the digestion of U_6Mn. In contrast, U_6Mn fuel is resistant to corrosion or oxidation in the same medium and conditions, which would leave the produced isotopes bound to the fuel. The use of the oxidant potassium permanganate ($KMnO_4$) is shown to interact with U_6Mn particle surfaces to form $Na_2U_2O_7$. This demonstrates for the first time a successful process that makes this fuel feasible for isotope production. This method, if up-scaled to industry standards, could produce 3 to 5 times the amount of isotopes per target while producing the same or less waste.

By studying these two processes together, the results provided here can be compared to assess current and future isotope production methods. The grain boundary engineering of UAlx fuel can improve isotope extraction without adding any additional oxidants, while the use of an accelerant in high density fuels provides us with a new economically advantageous method for isotope extraction in next generation LEU targets.

Scientific Output

Papers

- Cea, Andrew Ken, et al. "Microstructure and calorimetric analysis of the UMn binary system." *Journal of Nuclear Materials* 514 (2019): 380-392.
- Simonet, V., Damay, F., Ferlay, S., Cea, A., Maxim, C., & Train, C. (2019). Magnetic Investigation of an Atypical Three-Dimensional Bimetallic Oxalate-Based Magnet. *Journal of Physical Chemistry C*, *124*(1), 952-957.

Patents – as first inventor

- Cea, Andrew Ken, et al. “A method for the digestion of a uranium basted material” European Patent Application No. EP20156652.8, filed February 11, 2020
- Cea, Andrew Ken, et al. “Nuclear fuel for isotope extraction” European Patent Application No. EP20182530.4, filed June 26, 2020

Conferences

Talks

- 2019 – SCK•CEN Day of the PhDs “Advancements in LEU based medical isotope production”
- 2018 – SCK•CEN Day of the PhDs “Calorimetric analysis of U-Mn alloys”
- 2018 March 11-15 – RRFM Munich “Microstructure and thermal analysis of U-Mn alloys”

Posters

- 2019 May 9 – 7th symposium on medial radioisotopes "Digestion of UAlx fuel for isotope production"
- 2018 Sept23-26 - Mo-99 topical meeting "Grain boundary design for digestion of UAl fuel".
- 2018 Oct. 23-24 – Technical Meeting on Global Capabilities for the Production and Manufacture of Non-High Enriched Uranium Mo99 Targets

Other Achievements

- 1st Place student competition – RRFM 2018 for "Microstructure and thermal analysis of U-Mn alloys"

List of abbreviations

Al-GB	Aluminum grain boundary
BSE	Backscattered electron
CSL	Coincident site lattice
DOE	Department of Energy
DSC	Differential scanning calorimetry
EBSD	Electron Backscatter diffraction
EDX	Energy-dispersive X-ray spectroscopy
EOB	End of bombardment
GB	Grain boundary
GBE	Grain boundary engineering
HEU	High enriched uranium
IAEA	International Atomic Energy Agency
LEU	Low enriched uranium
MRBC	Maximum random boundary connectivity
NC	Nanocrystalline
SCK•CEN	Studiecentrum voor Kernenergie Centre d'Étude de l'énergy Nucléaire
SE	Secondary electron
SEM	scanning electron microscope
SS	Solute segregated
TGA	Thermal gravimetric analysis
TJ	Triple junction
XRD	X-ray diffraction
UFC	Ultra fine grain

Chemicals and formulas

$KMnO_4$	Potassium permanganate
MnO_2	Manganese dioxide
$Na_2U_2O_7$	Sodium diuranate or "Yellow Cake"
$NaCO_3$	Sodium carbonate
$NaNO_3$	Sodium nitrate
NaOH	Sodium hydroxide
UO_2	Uranium dioxide

Table of contents

Chapter I 1

Introduction 1

1 Introduction 3

2 Radioisotopes used for medical purposes 6

2.1 History 6

2.2 Generation of ^{99}Mo and medical isotopes 6

2.3 Supply chain of medical isotopes 9

3 Targets for fission isotopes 10

3.1 Design 10

3.2 Irradiation 12

4 Extraction of ^{99}Mo 13

4.1 Acidic and basic digestion processes 14

4.2 ROMOL99 method 15

4.3 Modifying the ROMOL99 process – choosing the oxidant $KMnO_4$ 19

5 International efforts to convert HEU to LEU 23

5.1 Considerations for a successful LEU conversion 25

5.2 High U-density alloys 26

5.3 Additional requirements of high-density fuels 29

5.4 Processability of high-density compounds 31

6 Models of dissolution and digestion of solids 32

6.1 Introduction to digestion and dissolution mechanisms 32

6.2 Oxidation events in digestion 35

7 Research area, strategy, and philosophy 35

Part I 42

Digestion of UAlx fuel 42

Chapter 2 43
Extraction of medical isotopes from UAlx fuel 43
1 Introduction 48
1.1 Background 48
1.2 Digestion experiments 49
2 Experimental methods 50
2.1 Fabrication of fuel particles 50
2.2 Digestion of fuel particles 50
2.3 Sample preparation 51
2.4 Analysis technique – scanning electron microscopy 51
2.5 Particle classification, cross-sections and limitations 55
3 Results 56
3.1 Experiment 1: Digestion of annealed UAl_3, ROMOL-99 conditions 56
3.2 Experiment 2 Digestion of as-cast UAl_3 70
3.3 Experiment 3: Digestion of annealed UAl_3 in 8M NaOH 81
4 Discussion – towards optimized digestion of UAl_3 86
4.1 Oxidation behavior and junction classification in UAlx fuel . 86
4.2 Optimally designed grain boundaries for the controlled oxidation properties of UAlx Alloys 90
4.3 Strategies for the production of oxidation susceptible UAlx alloys and its successful digestion 91
4.4 Further discussion on selective oxidation 93
5 Conclusion 94
Chapter 3 99
Grain boundary engineering for enhanced extraction of medical isotopes 99
1 Introduction 102
2 Grain boundary engineering 103

3 Electron Backscatter Diffraction (EBSD) 104
3.1 Background 104
3.2 Coincident site lattice in cubic materials 106
4 Experimental Methods 107
4.1 EBSD specifications and sample preparations 107
4.2 Cleanup of low confidence index patterns in EBSD maps .. 109
4.3 Experimental outline 111
5 Results 113
5.1 Grain Boundary Analysis at 120 minutes of digestion 113
5.2 Analysis of an aluminum phase along the grain boundary. 116
5.3 Effects of grain size on oxidation rate 118
6 Discussion 124
7 Conclusions and outlook 126
Chapter 4 131
Digestion of mixed UAl_3-UAl_4 fuel and target analysis 131
1 Introduction 134
2 Materials and experimental procedure 135
2.1 Sample description and characterization 135
2.2 Experimental procedures 139
3 Experimental Results 139
3.1 Digestion of UAl_3-UAl_4 target: stage 1 - target breach 139
3.2 Digestion of UAl_3-UAl_4 target: stage 2- Advanced oxidation front 141
3.3 Digestion of UAl_3-UAl_4 target: stage 3 – Indiscernible digested fragments 142
3.4 Digestion of large single grain UAl_3 phases inside a target. 143
3.5 Digestion of UAl_3-UAl_4 fuel – as fabricated 144
3.6 Summary of results 147
4 Discussion 149

5 Conclusion 151
Part II 155
Qualification and digestion of U_6Mn fuel 155
Introduction 157
Good practices for the qualification of high density low enriched uranium for isotope production 158
Chemical qualification of new fuel for isotope production 158
Chapter 5 161
Microstructure and calorimetric analysis of the U-Mn binary system 161
1 Introduction 164
2 Phase equilibria and thermochemical information on U-Mn 166
3 Experimental Methods 168
3.1 Alloy synthesis and preparation 168
3.2 Microstructural characterization and composition analysis 171
3.3 Thermal Analysis 173
4 Results 173
4.1 Microstructure Characterization 173
4.2 XRD 178
4.3 Transformation temperature and U-Mn phase diagram 180
4.4 Effects on heating rates and temperature variations 184
4.5 Enthalpies of transformation 187
5 Discussion 189
6 Conclusion 192
Chapter 6 197
Digestion of U_6Mn and UAlx fuel with oxidative accelerants 197
1 Introduction 201

2 Results 203
2.1 Experiment 1: Digestion of U_6Mn in ROMOL-99 conditions 203
2.2 Experiment 2: digestion of U_6Mn with oxidants 208
2.3 Experiment 3: Digestion of UAlx + $KMnO_4$ 212
2.4 Experiment 4: Digestion by leaching - sodium carbonate 221
2.5 Experiment 5: Methods of advancing the digestion front 224
2.6 Chapter discussion 230
2.7 Conclusions 232
Chapter 7 237
Conclusions and future outlook 237
1 Conclusion 238
2 Perspectives and outlook 241
2.1 Comparison on the digestion of UAlx and U_6Mn 241
2.2 Bringing U_6Mn technology from lab scale to industry 244
2.3 Expanding grain boundary engineering 246

Chapter I

Introduction

Table of Contents

1 Introduction 3

2 Radioisotopes used for medical purposes 6

2.1 History 6

2.2 Generation of ^{99}Mo and medical isotopes 6

2.3 Supply chain of medical isotopes 9

3 Targets for fission isotopes 10

3.1 Design 10

3.2 Irradiation 12

4 Extraction of ^{99}Mo 13

4.1 Acidic and basic digestion processes 14

4.2 ROMOL99 method 15

4.3 Modifying the ROMOL99 process – choosing the oxidant $KMnO_4$ 19

5 International efforts to convert HEU to LEU 23

5.1 Considerations for a successful LEU conversion 25

5.2 High U-density alloys 26

5.3 Additional requirements of high-density fuels 29

5.4 Processability of high-density compounds 31

6 Models of dissolution and digestion of solids 32

6.1 Introduction to digestion and dissolution mechanisms 32

6.2 Oxidation events in digestion 35

7 Research area, strategy, and philosophy 35

1 Introduction

Society has found many peaceful ways to utilize the radiation emitted from radioisotopes. Isotopes made from the fission of ^{235}U can be found in the food and agriculture industry, insect control, smoke detectors, industrial tracers, carbon dating, medical diagnostics and therapy. It is the latter two that involves medical applications that this research seeks to advance. Medical isotopes directly affects the quality of our lives and it is important to continuously improve how we produce them.

Medical diagnostics is based on imaging the inside of the human body. However, this is a difficult task to perform. Unlike imaging the outside of the body, we cannot depend on visible light (380 to 740nm) and we cannot depend on conventional cameras that we use to take pictures of ourselves. Our ability to see within is blocked by a layer of skin cells and hair preventing visible light from escaping or entering our body. Our skin forms as a layer to protect our bodies from outside harm, while maintaining our body's homeostasis.

However, there are many reasons why people and doctors would like to image the inside of a body. It can be to "see" something static, like inspecting the conditions of bones or it can be used to visualize something dynamic, like where blood is flowing, clotted, or hemorrhaging. Radio isotopes can be used for these reasons as these isotopes emit gamma radiation which escapes the body and can be captured by a gamma camera. Cardiovascular disease, cancer, lung diseases, respiratory problems, and dementia are likely to require a specialist in nuclear medicine to image the condition for diagnostics. In approximately 90 percent of these cases, an imaging scan will be performed so that a doctor can determine the appropriate treatment.

An example of a brain scan that uses ^{99}Tc is presented is presented in Figure 1 [1]. Image A, is acquired from a ^{99m}Tc cerebral blood flow brain scan of a person with Alzheimer's disease. The arrows indicate areas of diminished blood flow due to the disease. Image B, is acquired from a cardiac perfusion SPECT study at stress and rest using a ^{99m}Tc radiotracer. Images on the top are taken during stress and the images on the bottom row are at periods of rest. Arrows on the images show areas of decreased profusion.

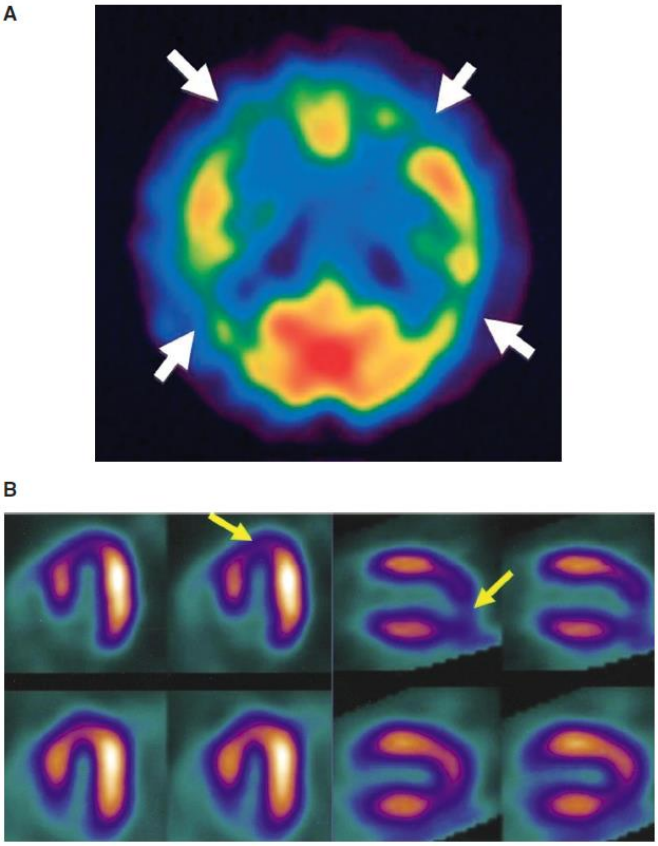

Figure 1) a)Image acquired from a Tc-99m cerebral blood flow brain scan of a person with Alzheimer's disease. The arrows indicate areas of diminished blood flow due to the disease; b)Images acquired from a cardiac perfusion SPECT study at stress and rest using a Tc-99M radiotracer. Images on the top row are taken during stress and the images taken at rest are shown on the bottom. Arrows indicate areas of decreased profusion [1].

Every year, hospitals around the world diagnose and treat 48 million patients with medical isotopes. Around 40 million of these procedures use the medical isotope technicium-99m, the daughter isotope of molybdenum-99, for diagnostic imaging, earning its nickname as the work horse of radiopharmacology. Its world market value is estimated to be about USD $550 million per year, with the world demand for this isotope around 20,000 Tbq[2] per year.

[2] One bacquerel is defined as the activity of a quantity of radioactive material in which one nucleus decays per second.

The use of isotopes in medicine has been around since the 40s, with mass production starting in the 60s and 70s. Up until recently, the majority of medical isotopes were produced from high-enriched uranium (HEU). Defined as having an enrichment of ^{235}U above 20% (usually around 90% ^{235}U), HEU sources pose a global threat, as rogue states and terrorists could use it for malicious reasons. Already in 1978, the Reduced Enrichment Research and Test Reactor program (RERTR) was launched. The mission of the program was "to minimize and, to the extent possible, eliminate the use of HEU in civil nuclear applications by working to convert research reactors and radioisotope production processes to the use of low enriched uranium (LEU, <20 % ^{235}U) fuel and targets throughout the world." For many decades, the emphasis of the program was on converting the research and material testing reactor but since 2010 increased pressure was on elimination the use of HEU targets for radioisotope production by replacing it with an LEU variant. However, a simple replacement of the HEU by LEU is not possible as this would reduce the amount of ^{99}Mo that can be produced. To maintain the level of ^{99}Mo production, the amount of uranium in a target must be increased. This can be done either by changing the dimensions of the targets or by using a more dense uranium alloy.

The research performed here is focused on LEU based medical isotope production and to increase isotope production. The first part of the thesis is focused on improving techniques that already exist while the second part is focused on developing a next generation method. This research can help the medical sector as well as contribute to global security by reducing HEU radiological material to be in line with the Global Threat Reduction Initiative (GTRI).

Now that the general context for this research is set, the rest of the introduction serves to outline what challenges are considered in this thesis. A brief explanation of the different types of isotopes are given along with their area of use. Current and competing production models are considered as a broad overview of the field in general. A focus on the plate targets from which isotopes are made and the ROMOL-99 extraction process is given, as they form key considerations for this research, and for the results to be useful to industry.

After the introduction, the core of the research is presented in two parts. Part 1 is a study on the digestion of UAlx fuel. Chapters 2 and 3 explore how pure components of UAlx targets turn into a "yellow cake" which releases

isotopes into solution. Chapter 4 explores how whole targets get dissolved and how components in chapters 2 and 3 relate to a whole target scenario. Part 2 investigates the digestion of U_6Mn. Chapter 5 through 7 explores a potential new way to produce medical isotopes through U_6Mn targets. The results from chapter 5 - 7 can be compared to chapters 2 - 4 to see how these two processes compare and to demonstrate the possible future for these high U-density targets.

2 Radioisotopes used for medical purposes

2.1 History

The ^{99}Mo-^{99m}Tc-^{99}Tc family emerged as the most important medical isotope for a few reasons. When the scintillation camera by H.O.Anger was invented in 1957, researchers started to analyze the table of nuclides to determine the best radionuclide for *in vivo* applications [2]. Among the thousands of nuclides, ^{99}Mo-^{99}Tc emerged as the most suitable. There are three arguments what supported the research and use of ^{99}Mo. The first reason is that its nuclear decay energy (141 keV photon) is sufficiently high for penetrating biological tissue while the photo energy is sufficiently low to be absorbed with a high efficiency in a sodium iodide detectors used in scintillation cameras and SPECT technology. On this point alone, no other radio nuclide can compare. This was the main driving factor for molybdenum/ technetium chemistry research. Secondly, ^{99}Tc can be continuously supplied as it can be handled by its longer lived mother nuclide ^{99m}Tc. Finally, the third aspect is the chemistry aspect of technetium. At the time, little was known about the chemistry of these elements as it is not abundantly found in nature. However, its favorable physical properties drove research in the 1960s. In order to bring ^{99m}Tc into a chemical state that would allow it to be complexed with a ligand, for example, it needs to be reduced from its primary oxidation state from +7 down to +5, +3 or +1. With the breakthrough of a stannous reduction technique (Sn^{2+}), the development of the ^{99}Mo/^{99m}Tc generator could advance and the demand for the isotope ^{99}Mo exploded. The techniques used today are based on developments made in the 1970s, which made the production of ^{99}Mo more efficient to meet the word demand.

2.2 Generation of ^{99}Mo and medical isotopes

^{235}Uranium is the only naturally occurring fissile nuclide and it is routinely used to make medical isotopes through thermal fission stimulated by neutron capture. Unlike other decay reactions, thermal fission produces

large nuclear fragments. Although there are many isotopes used in medicine, the radioisotopes which are most applicable in the medical sector are ^{99}Mo, ^{99m}Tc, ^{33}Xe, ^{131}I, ^{201}TI, ^{153}Sm, ^{177}Lu, ^{186}Re, ^{12}5I, ^{192}Ir and ^{60}Co (see Figure 2).

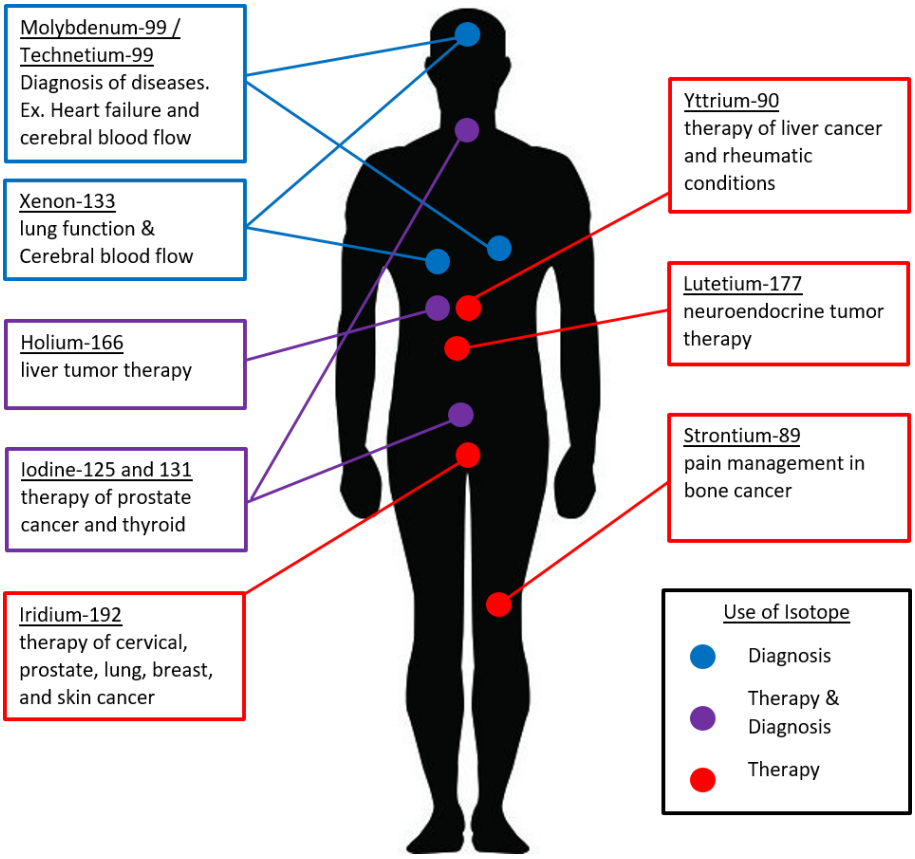

Figure 2) Radioisotopes and their uses in diagnosis and in therapy.

As mentioned, the ^{99}Mo-^{99m}Tc-^{99}Tc family is the dominant medical isotope in radio-pharmaceuticals. ^{99}Mo itself is the mother isotope that undergoes beta decay with a half-life of 66 hours. About 88% of these decays result in the production of the metastable ^{99m}Tc., which subsequently decays to the ground state ^{99g}Tc with a half-life of 6 hours (Figure 3). Because there are many steps before getting the isotopes to hospitals, this product is handled and shipped as ^{99}Mo. Because of their half-lives, ^{99}Mo is sold based on units of activity calibrated for this decay. The unit of activity is a curie (Ci) equal to 37 billion disintegrations per second. Most producers calibrate sales to the number of curies present in a shipment after 6 days after leaving the production facility, known as a 6-day curie. The delivered 6 day curies to

hospitals and end users are about 17 percent of the ^{99}Mo present in the targets at the end of bombardment (EOB).

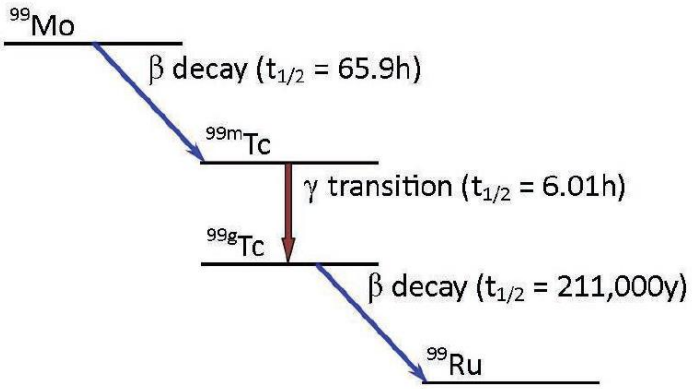

Figure 3) Decay and lifespans of ^{99}Mo family.

There are several ways to produce the ^{99}Mo- ^{99}Tc family (Figure 4) [3]:

1) Fission of ^{235}U with neutrons produced in deuteron and proton accelerators through (D, n) and (p, n) reactions on heavy targets. More than 95% of ^{99}Mo is produced through fission or uranium-235 because fission ^{99}Mo have a very high specific activity (~10^4 ci/g) than those that are produced through any other method and is considered the gold standard.

2) Neutron activation of ^{98}Mo (i.e. ^{98}Mo (n,γ)^{99}Mo) where the energetic photons used in this production scheme are obtained by irradiating heavy targets with an electron beam produced by a linear accelerators.

3) Photofission of ^{100}Mo (i.e. ^{100}Mo (γ,n) ^{99}Mo). The energetic photons used in this production scheme are obtained by irradiating heavy targets with electron beams produced by linear accelerators.

4) ^{99m} Technetium can also be produced through (p, 2n) reaction on targets containing ^{98}Mo. This production scheme eliminates intermediate steps involving the recovery and purification of ^{99}Mo. However, it is only suitable for immediate use because of its short half-life.

All of these methods involve the use of a target, or a vessel to hold the fissile or active component. All four large-scale producers still obtain ^{99}Mo from HEU targets, but are in the process of conversion [4].

The two other major groups of medical isotopes can be divided into fluorine-18, made by accelerators, accounts for about 4.2 million procedures and the other medical isotopes combined account for about 3.8 million procedures.

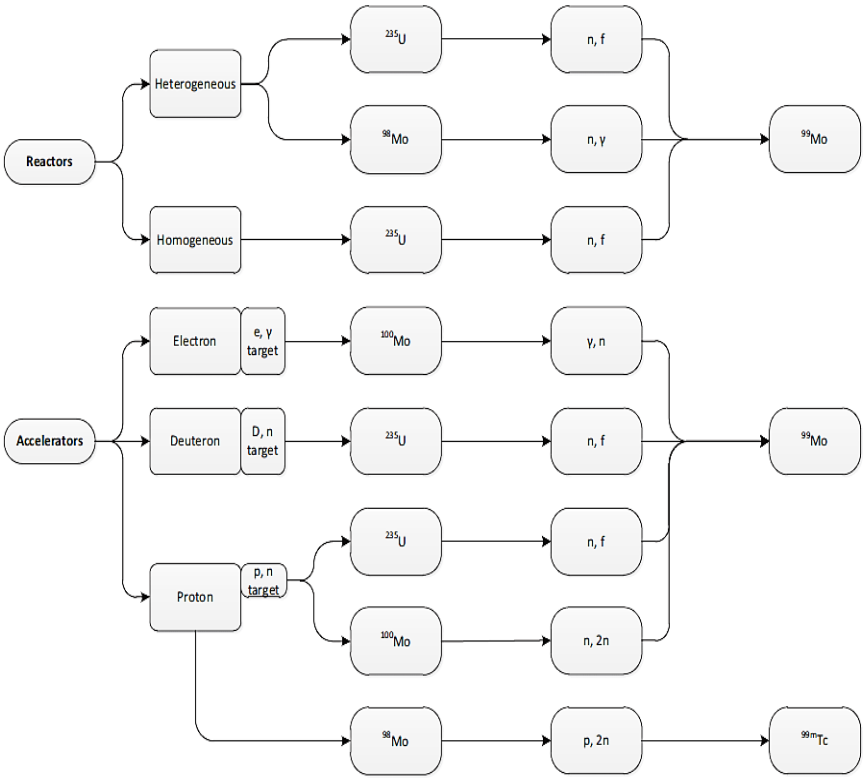

Figure 4) Reactor and Accelerator paths to the production of Mo99 [3]

2.3 Supply chain of medical isotopes

The production of fission based medical isotopes starts by the irradiation of a target in research reactors (Figure 5)[5]. These targets, in general, have a uranium based core cladded in aluminum. Multiple targets are loaded into a basket and are irradiated from 3 to 7 days, at the point where Mo^{99} reaches its maximum population. After irradiation and cooling, targets are sent to a processing facility that will extract and purify the medical isotopes. At these facilities, the multiple targets are put into a cell to be processed using either an acidic or alkaline dissolution method. They go through a series of radiochemical separation and purification steps afterwards. The purity requirement for medical isotopes are very high as the end user is a patient in a hospital, and extensive quality controls are essential.

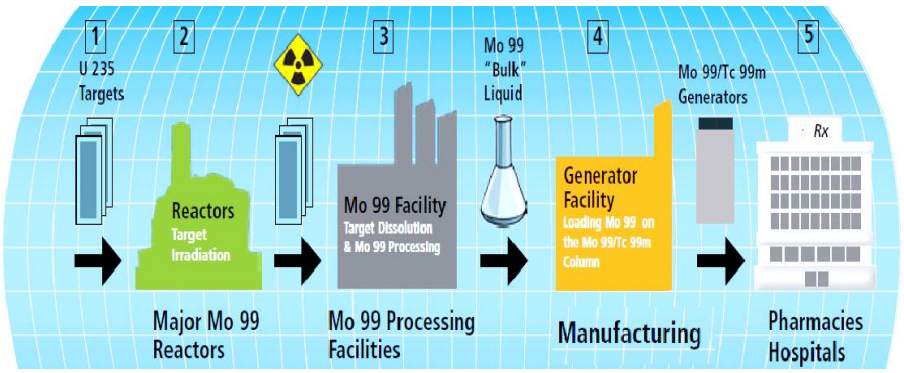

Figure 5) Global supply chain of ^{99}Mo production and subsequent utilization [2].

Currently, there are five major producers of medical isotopes using fission based targets, which include the facilities: Nordion (Canada), the Institute for Radioelements (IRE, Belgium), Covidien/ Mallinckrodt (Netherlands), NTP Radioisotopes (South Africa) and the Australian Nuclear Science and Technology Organization (ANISTO, Australia)[4]. The National Atomic Energy Commission (CNEA) in Argentina was the first ^{99}Mo producer to make large scale quantities using LEU targets, followed by ANSTO and NTP radioisotopes.

This PhD is performed with the consideration of the BR2 reactor at SCK●CEN in Mol, Belgium. The BR2 is one of the major players in isotope production in the world [6]. It can operate at 100 MWs and provides a high flux of thermal neutrons up to 10^{15} n/cm^2.s, and fast neutrons up to 6^{14} n/cm^2.s while operating 140-200 days per year. Altogether, the BR2 has an irradiation capacity of 7,800 6-day Ci per week, supplying 25% of the global Mo-99 demand in average or 65% in peak periods. In addition ^{99}Mo, the targets that are irradiated at the BR2 are processed at outside agencies for the production of other medical isotopes such as ^{125}I, ^{131}I, ^{192}Ir, ^{177}Lu, ^{186}Re, ^{153}Sm, ^{133}Xe, ^{99}Mo and ^{99m}Tc.

3 Targets for fission isotopes

3.1 Design

A target used for isotope production must include a fissile material encased in a protective barrier. In almost all cases, the fissile material is ^{235}U that will be irradiated in a nuclear reactor. Although there are several designs for a

target, they must all conform to these general specifications:

1) They must be fitted into a basket that will be loaded and unloaded into a reactor.

2) It must contain a sufficient amount of ^{235}U to produce the desired amount of isotope.

3) It must have good heat transfer properties to prevent overheating.

4) A target must provide a barrier for the release of radioactive products, especially fission gasses.

5) A target must be compatible with the chemical processing steps used for isotope extraction.

Typical target designs can be seen in Figure 6. In Figure 6A and B, a plate type target are shown. Image A, shows a "picture frame" target and its separate components. Here, the center of the target is called the "meat" which holds the fissile material. The meat is a dispersion of around 50% aluminum and 50% fissile material. The fissile material comes in a powdered particle form, with a ratio of fine particles (diameter below 40µm) and large particles (diameter between 40µm and 150µm) that is set by the manufacturer. The cladding and frame is made out of an aluminum alloy, which is most often Al6061. Although other metals have been used as cladding material, especially in fuel targets, aluminum is the preferred material in isotope

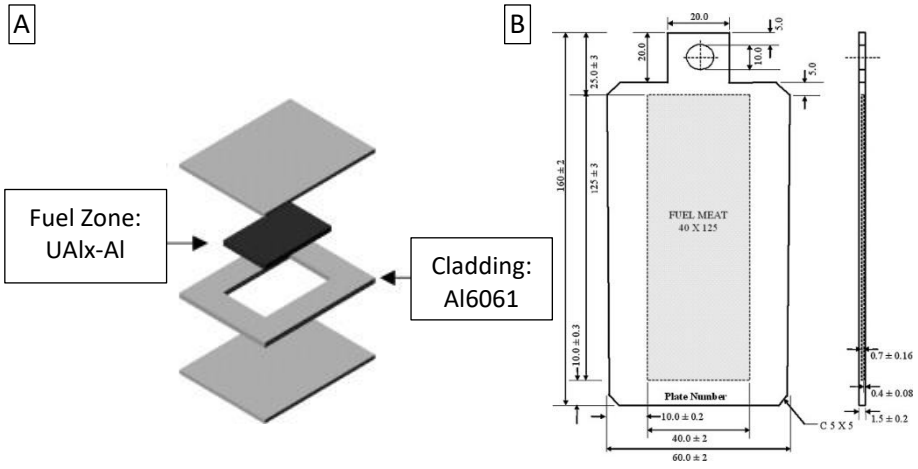

Figure 6) Targets and target designs for Mo99 production. A) Picture frame target B) Schematic and dimensions of a plate target.

targets because of its low capture cross section of neutrons, its ability to thermally conduct heat, and its ability to chemically dissolve readily in acidic or basic media. Image B shows the schematic of a mini-plate, where the thickness of the meat is 0.7±0.16mm and the thickness of the cladding is 0.4±0.08mm. The experiments performed in this thesis is focused on plate type targets although the results apply to all types of target geometries.

Figure 7 shows a competing target that is currently used for isotope production. Figure 7 shows the schematic of a target that is used in a the Cintichem process [7]. This target is known as a "foil" target, which can contain up to 100 g of 130µm foil. The uranium foils have a fission fragment barrier made of either nickel or zinc (>7 µm thickness) to prevent bonding of the foil to the outside walls. Finally, the outer and inner layer of the cylinder can be either zirconium, 304 stainless steel, or aluminum.

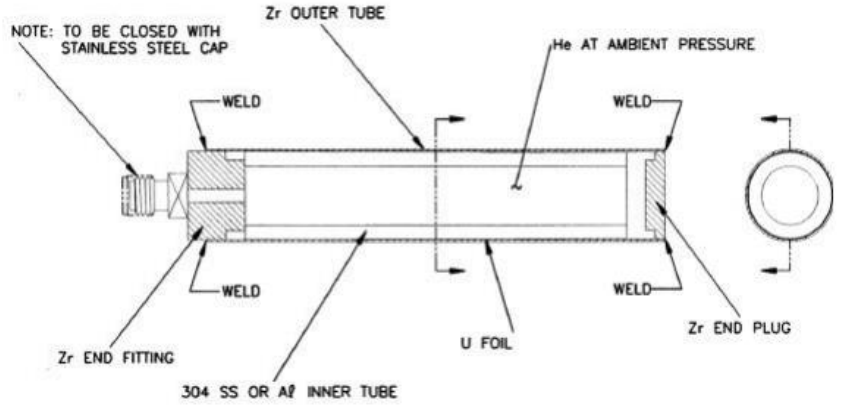

Figure 7) Competing target design – foil target

3.2 Irradiation

Medical isotopes are produced in the uranium-bearing targets by irradiating them with thermal neutrons, which is a low-energy neutron of about 0.025 electron volts at room temperature [1]. When the neutron is absorbed by a ^{235}U nuclei, a fission event occurs producing two or three lower-mass nuclei referred to as fission fragments. Approximately 6 percent of this fragments will be ^{99}Mo (Figure 8**)**. The amount of isotope produced is a function of irradiation time, thermal neutron fission cross section for ^{235}U, thermal

neutron flux, mass of ^{235}U present in the target, and the half-life of the isotope. For typical reactor thermal neutron fluxes on the order of 10^{14} neutrons per square centimeter per second, irradiation times of about 5 to 7 days are required. After this equilibrium time point, the amount of ^{99}Mo created is approximately equal to the amount lost to decay.

Due to irradiation and the fission events, the target produced heat. The lowest melting temperature for any of the target components is the aluminum cladding, whose melting temperature is 660°C. Therefore, 330°C is the maximum allowed temperature for LEU targets in most cases as a safety precaution [8]. Depending on the coolant and the coolant velocity, target central temperature and cladding temperature are kept between 100 and 200°C throughout its irradiation time.

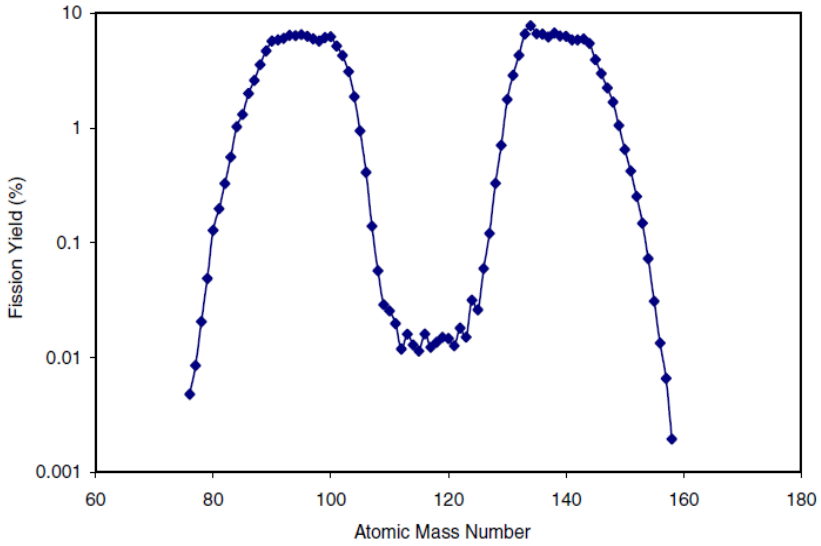

Figure 8) Fission yield for thermal neutron fission of U-235

4 Extraction of ^{99}Mo

The first chemical process for the separation of ^{99}Mo from fission products was demonstrated by Brookhaven National Laboratory (BNL)[9]. They demonstrated this process with a 93% enriched ^{235}U alloy with aluminum, and dissolved it in 6M nitric acid catalyzed by mercuric nitrate. The dissolved solution was passed through an alumina column to separate ^{99}Mo from the acidic solution containing other fission products. The original design was actually for the isotope ^{132}Te and for the production of $^{132}Te/^{132}I$ generator,

which played a pioneering role in nuclear medicine at the time. Shortly after, the Central Institute for Nuclear Research (CINR) in Germany developed the LITEMOL process, which used the solution of fission products after the separation of ^{132}Te and passed it through an alumina column to separate ^{99}Mo by adsorption. The ^{99}Mo obtained from the LITEMOL process was the basis for the first commercially available fission based ^{99}Mo/^{99m}Tc generator in Europe in 1964. Since then, many different processes have been made or adapted to bring this process to the industrial scale where it is today. In general, all of these processes can be classified into either an acidic dissolution process or a basic separation process.

4.1 Acidic and basic digestion processes

A notable acidic dissolution process is the CINTICHEM process. This process is still in operation at the BATAN Institute in Indonesia, which uses tubular targets whose inner surface contains UO_2. After dissolving the target in nitric acid, ^{99}Mo is separated by precipitation with alpha-benzoxime. A modified CINTICHEM process is also known using a uranium metal foil target, where the fission products are released by mechanical removal of the aluminum capsule, and the uranium metal foil is dissolved in nitric acid and a high-pressure, and high-temperature vessel.

In contrast to an acidic method, a pure alkaline digestion process was developed in 1976 by Sameh and Ache to process HEU targets containing uranium-aluminum alloy cladded with aluminum. This was a breakthrough technology of the time that allowed producers to meet the global demand of ^{99}Mo. Because government policy at the time forced a limited production in Karlsruhe, Germany, Sameh transferred the technology to Mallinckrodt at Petten in 1996. This became the most reliable and safest production site for ^{99}Mo with a market share of around 40%.

There are advantages and disadvantages for selecting either an alkaline or an acidic isotope purification pathways [1]. For example, the alkaline processes produce very pure ^{99}Mo, solid waste that is suitable for storage, and the fission gases from this process can be readily isolated for sale and for storage, such as iodine and xenon. However, the alkaline processes produce larger volumes of processing solutions that require more time to dissolve a target than an acidic process. Some ^{99}Mo can also be lost and incorporated to the solid residues. Finally, hydrogen gas production in the alkaline process is a major concern and requires additional chemicals and safety procedures. The advantage of the acidic processing is that, it generally requires shorter

processing times, produces smaller volumes of waste and has a slightly higher Mo-99 yield. However, additional separation steps are necessary, and there needs to be a separate treatment route for the nitrogen oxide gases that are created during the process.

Outside of these to general types of isotope purification, the separation of ^{99}Mo from a fission based target can fall into these classical chemistry strategies:

1) Co-precipitation: Precipitation of ^{99}Mo with alpha-benzoximine is used in the CINITICHEM process

2) Extraction: ^{99}Mo from a nitric acid processing solution with di-(2-ethylhexyl)phosphoric acid (HDEHP) is applied at the Karpov Institute, Obinsk, Russia.

3) Anion exchange: Separation of ^{99}Mo using anion exchange from an alkaline process solution was introduced by Sameh. This process is used in Peten, INVAP (Argentina), NTP (South Africa) and ANSTO (Australia).

4) Adsorption: The adsorption of ^{99}Mo an alumina column (Al_2O_3) from a weak acid process has been demonstrated by Stang [9]. This process is used in most acid digestion routes.

5) Volatilization: Volatilization can be used for ^{99}Mo separation from uranium and the fission products because MoO_2Cl_2 is a volatile compound. General Atomics published a patent that describes this approach and related research is underway [10].

4.2 ROMOL99 method

Special attention is made here to the ROMOL99 method of separating and purifying ^{99}Mo, as it is a central consideration of this thesis. The ROMOL99 method was based on the experience built in the radio-Isotope department of the former Rossendorf institute ZfK, which designed a new fission based

^{99}Mo production method. The basic principles of this process are as follows (Figure 9) [11]:

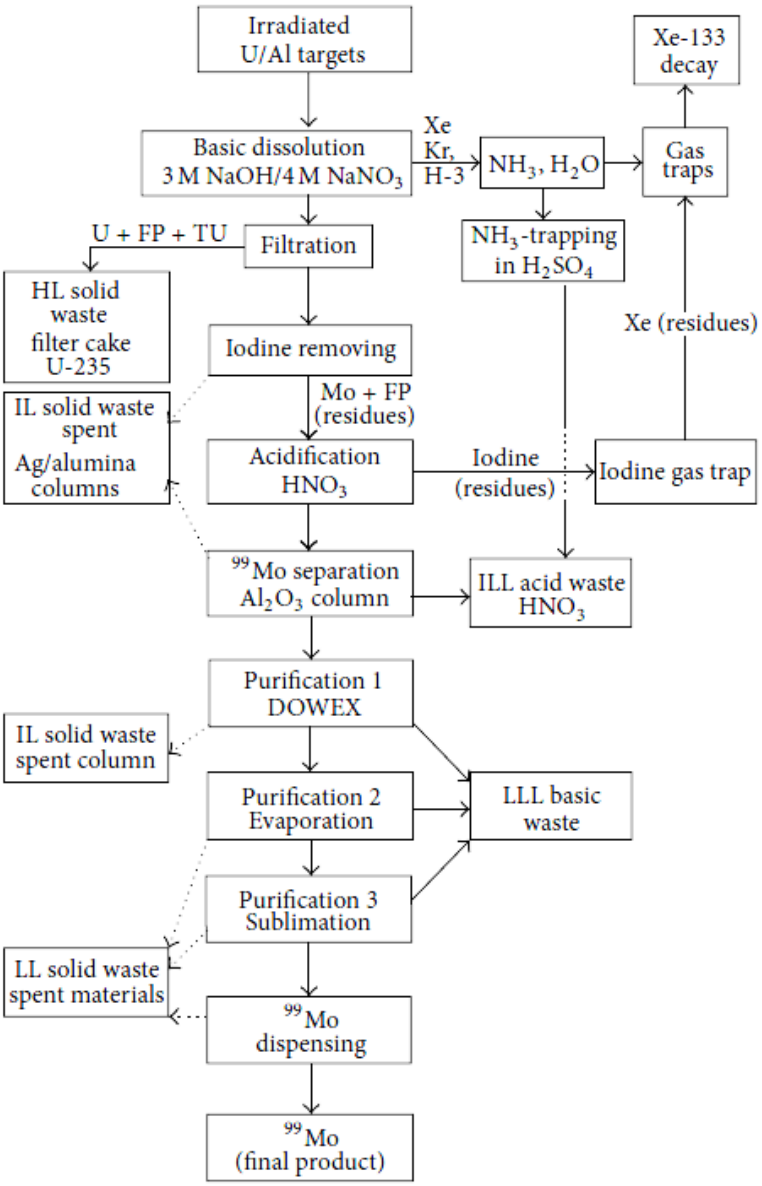

Figure 9) ROMOL99 flow chart for Mo99 isotolation [11]

i) The dissolution of the UAlx/Al-cladded target is performed in a mixture of $NaOH/NaNO_3$ without H_2 generation, under reduced pressure conditions.

ii) Xe is trapped cryogenically after passing a gas treatment line

iii) The NH_3 generated in the dissolution process and the radio iodine, shall be separated prior to Mo separation.

iv) During the dissolution process, nitrite is generated which shall be eliminated prior to ^{99}Mo separation.

When dissolving the target plates in a solvent of ~3M NaOH/ ~4M $NaNO_3$ the following three reactions must be considered:

Eq. 1) $8Al + 3NaNO_3 + 5NaOH + 2H_2O \rightarrow 8NaAlO_2 + 3NH_3$

Eq. 2) $Al + 1.5NaNO_3 + NaOH \rightarrow NaAlO_2 + 1.5NaNO_2 + 0.5H_2O$

Eq. 3) $Al + NaOH + H_2O \rightarrow NaAlO_2 + 1.5\ H_2$

The most important and dominating reaction (Eq. 1) occurs where aluminum reduces the nitrate ion down to NH_3. Responsible for about 10 to 15% of the reaction is (Eq. 2) where the nitrate is reduced to nitrite close to the end of the dissolution process. Finally, a theoretical possibility is reaction (Eq. 3) where the generation of hydrogen becomes available. In general the upper limit of H_2 generation is <2% and is kept low for safety considerations.

With the consideration that x represents the mass of the target matrix that undergoes nitrite formation and consequently (1-x) represents the mass of the target matrix that undergoes NH_3 formation, we consider the "master equation" for dissolving targets:

Eq. 4) $Al + 0.0085U + (0.3814 + 1.125x)\ NaNO_3 +$

$(0.6271 + 0.375x)\ NaOH + (0.2585 – 0.75x)H_2O \rightarrow$

$NaAlO_2 + 0.00425Na_2U_2O_7 +$

$(1-x)0.3814NH_3 + 1.5NaNO_2$

The value x, representing the fraction of the aluminum that is dissolved under nitrite formation, ranges between $0.1 < x < 0.16$.

The solvent volume needed for the dissolution process is determined by the solubility of sodium aluminate ($NaAlO_2$) which is 57g/l or 2.1M/l. Furthermore, the sodium concentration should be kept as high as possible in

order to reach a saturation condition for the precipitate of $Na_2U_2O_7$, in a final compound known as “yellow cake”. The uranium after dissolution must be exclusively in the chemical form $Na_2U_2O_7$ at the end of the process, because it is well known that uranium species of lower oxidation stages absorb ^{99}Mo and therefore reduce its recovery yield. A high nitrate concentration is needed to avoid the formation of hydrogen (Eq.3) while the viscosity of the solution should still be suitable for filtration.

Two other important parameters to consider are the temperature and pressure. Dissolving Al is strongly exothermic with around 600kcal generated from dissolving 100g Al. Additionally, the dissolving speed increases to the second power of the temperature, and is thus self-accelerating. The

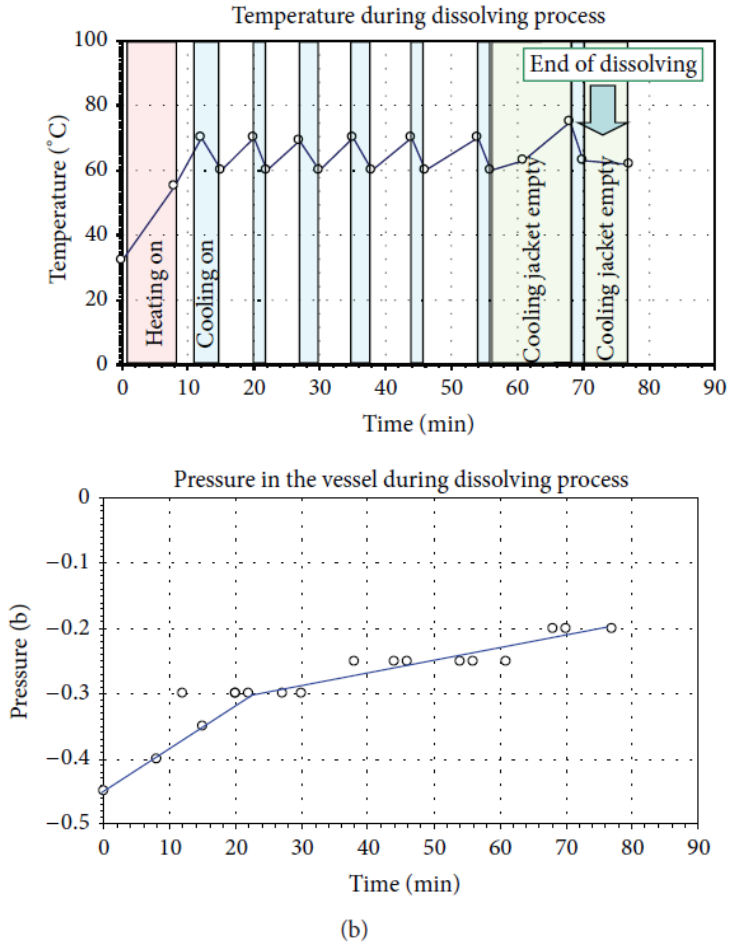

Figure 10. A) Temperature and time of dissolution process. B) Pressure and time of dissolution process [11].

"reaction crest", or the point where this self-acceleration occurs is around 60°C. In practice, a digestion vessel is made safe with a heating and cooling jacket which give short heating and cooling pulses. The reaction vessel is kept between 60 and 80°C and at a reduced pressure for about 80 or 90 minutes before the reaction is complete and filtration of the uranium cake begins (Figure 10).

4.3 Modifying the ROMOL99 process – choosing the oxidant $KMnO_4$

The use of a chemical oxidant or accelerant is found in various processes to convert uranium to a yellow cake. The four major challenges while considering an oxidant or accelerant are:

1) Retention of functionality in basic media

2) Modify the purification process as little as possible

3) Assuring high yield and purity of ^{99}Mo

4) Limiting economic disadvantages.

A table of standard oxidation/ reduction potential is shown in Figure 11 [12], which are commonly found in all industries. Of the strongest oxidizing

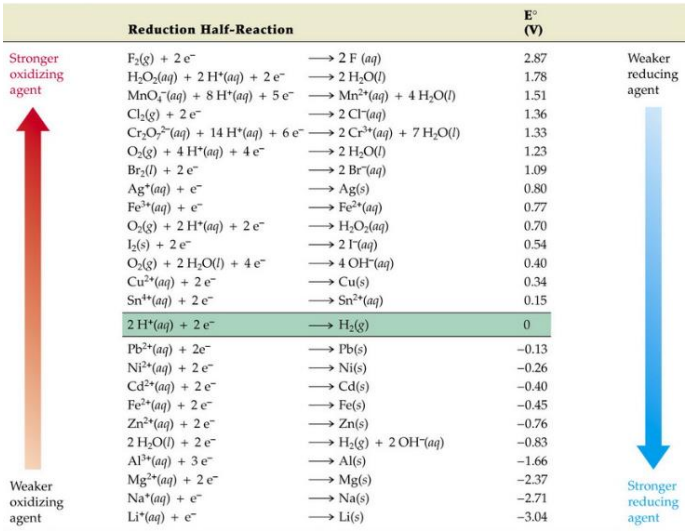

Figure 11) Table of oxidants at 25°C along with reduction/oxidation potentials

reagents, hydrogen peroxide (H_2O_2) has been used to modify the ROMOL99 process on uranium silicide fuel [13, 14]. Research using hydrogen peroxide for dissolving LEU targets have been focused on the rate and mechanism of dissolution, effects of hydroxide concentration, and temperature on dissolution rate. Difficulties in using peroxides were in destroying remaining peroxides after dissolution, remove the hydrated hydroxide precipitate containing uranium and insoluble fission products, and recovery of molybdenum from the filtrate [13].

Potassium permanganate ($KMnO_4$) was studied by Argonne National Laboratory to modify the digestion process on UAlx based LEU foil targets [15, 16]. Uranium metal reacts with potassium permanganate according to the following reaction

Eq. 5) $U + 2KMnO_4 + 2H_2O \rightarrow UO_2(OH)_2 + 2MnO_2 + KOH$

Through their research on U foils and UAlx fuels, there are many outcomes to consider and are applicable when using $KMnO_4$ to accelerate the digestion of uranium alloys. Firstly, hydrogen gas, generated from the digestion of the cladding, can react to permanganate according to the reaction:

Eq. 6) $2MnO_4^- + H_2 + 2OH^- \rightarrow 2MnO_4^{2-} + 2H_2O$

The product $2MnO_4^{2-}$ can further be reduced to MnO_2. Therefore, the amount of potassium permanganate used must account for both the oxidation of uranium in the metallic alloy and for the hydrogen gas. If not, the reaction 1 will be incomplete and Mo99 recovery yield will not be sufficient. The manganese oxides from Eq. 1 and 2 will need additional filtering and contributes to the yellow cake upon filtering. It was found that the stirring was required to mitigate the cake sticking to the digester wall and to have consistent drainage of the digester.

Secondly, the effects on permanganate on iodine must be examined, as Iodine is another major medical isotope that comes from this process. There are a few isotopes of iodine during the fission of ^{235}U which have high specific activities and which may also be used for medical purposes. The two major chemical forms of iodine in alkaline media are an oxidized ion and a reduced I^-. Iodine reacts with $KMnO_4$ to produce iodate. However, IO_3^- is unstable under beta radiation and is reduced to iodide.

Based on a literature of the available modifications to the ROMOL99 process, potassium permanganate was selected as an accelerant to study the

digestion of U_6Mn for several reasons. Of the common oxidizing reagents (Figure 11), only strong oxidants are considered to help ensure oxidation of the fuel (as an intermediate towards its conversion to $Na_2U_2O_7$). Gaseous fluorine (the strongest oxidizing reagent) or chlorine would be potentially dangerous in the same way gaseous hydrogen is, and is forbidden in the ROMOL99 process. Finally, difficulties in using hydrogen peroxide i.e. removing remaining radical species in solution and removing uranium precipitates that were discovered in digesting silicide fuels are a foreseeable event in digesting U_6Mn and these complications could stunt the development of this modified ROMOL99.

Using potassium permanganate could have many other advantages regarding impurities. The reduced product of the permanganate ion (MnO_2 from eq.5) is likely to be a product of manganese in digested U_6Mn, as the digestion solution is at a pH of 14 or higher (Figure 12). The potassium cation has the same charge as the sodium ions in solution and in fact can be

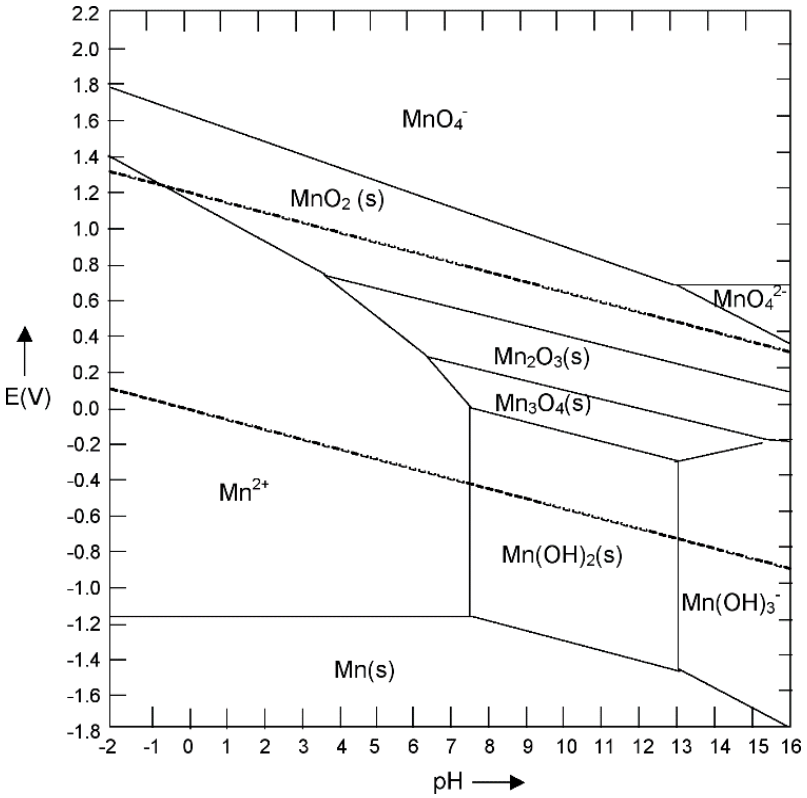

Figure 12) Pourbaix diagram of Mn. Oxidation products of Mn at pH values higher than 14 are MnO_2, Mn_2O_3, and Mn_3O_4..

exchanged to make sodium permanganate ($NaMnO_4$) and is a bystander ion. As both of the reaction products from potassium permanganate has either no effect on the products (K+) or is an impurity that could exist from the fuel itself (MnO_2, Mn_2O_3 and Mn_3O_4), the additional purification from using this oxidant is minimal. It is therefore strategically chosen as viable accelerant for the oxidation of U_6Mn.

A search through open literature found no results on digesting U_6Mn. However, the simultaneous dissolution of uranium and manganese in a closed system has been performed in different conditions and described by Wang *et al [17, 18]*. Their research was performed to study the geochemical cycles of U and Mn, in concern of uranium contamination of soil and grain water. Their results suggests that in general, "manganese oxides can act as a powerful oxidant that accelerates the oxidative dissolution of UO_2" (Figure 13A) and that with sodium carbonate, "UO_2 oxidation by MnO_2 was faster and less U(VI) was adsorbed to MnO_2" (Figure 13B). A key difference with their method in studying the nature of ground water and an industrialized ROMOL99 method, is that their method is working on a nanomolar concentrations during a period of days (200 hours) versus the molar concentrations and hour time scale required in isotope production. The results given here can suggests two things: Firstly, that dissolved inorganic carbon (sodium carbonate) itself would help dissolve uranium oxide, a known properties in uranium chemistry and carbonate leaching [19]. Secondly though, that an oxidation product of manganese in U_6Mn, manganese oxide, would itself help the oxidation rate of uranium,

which may create a synergistic effect when manganese oxide is produced during the dissolution process.

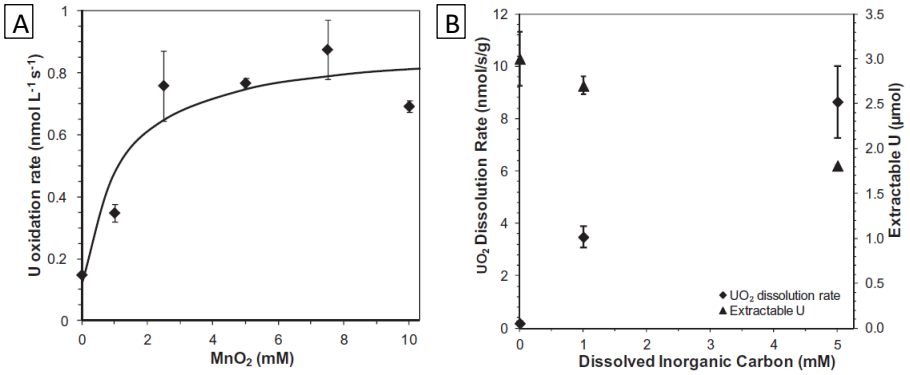

Figure 13) Results of simultaneous dissolution of uranium, manganese oxides, and sodium carbonate [17].

5 International efforts to convert HEU to LEU

A driving force behind this research is to be in-line with international efforts to eliminate all use of HEU in reactor fuel, reactor targets, and medical isotope production facilities. Currently, the Department of Energy's (DOE's) and Europe's HEU elimination efforts are being carried out under the Global Threat Reduction Initiative (GTRI). This initiative is focused on the minimization of HEU in civilian research and test reactors fuels and targets. The GTRI became a vital part of the U.S. National Security Strategy in 2004:

> *To keep fissile material out of the hands of rogue states and terrorists . . . we must address the danger posed by inadequately safeguarded nuclear and radiological materials worldwide. The Administration is leading a global effort to reduce and secure such materials as quickly as possible through several initiatives including the Global Threat Reduction Initiative (GTRI).*

During the same period, the IAEA's director general also announced that the agency's position on HEU elimination during this period:

> *The countries involved should join forces to step up their efforts towards minimizing and eventually eliminating the civilian use of HEU. Joint research should be conducted to address the remaining technical hurdles involved in converting from HEU to LEU the operations of facilities*

(including research and large pulse reactors as well as critical facilities) and the production processes for medical isotopes.

Research reactors have become indispensable for the production of medical isotopes to supply a rapidly increasing demand for diagnostic and therapeutic procedures. However, the commerce in HEU for research reactors was recognized as a potential source of nuclear weapons-usable materials since the mid-1970s. Increasing concerns about the proliferation of HEU prompted the formation of the Reduced Enrichment for Research and Test Reactors (RERTR) program in 1978. The International Nuclear Fuel Cycle Evaluation (INFCE) sponsored by the International Atomic Energy Agency (IAEA) joined the global efforts following the DOE's lead. During this era, a somewhat arbitrary definition of HEU as uranium enriched in ^{235}U percent or more (≥20 percent) was internationally adopted.

As was the case for reactor fuel elements, it was recognized that conversion requires the development of new target designs to accommodate the five-fold isotope loss in converting to LEU from HEU. By the mid-90s, all four large-scale producers of ^{99}Mo were using HEU targets, and are still doing so: Mallinckrodt and the Institut National des Radioéléments (IRE) obtain Mo-99 from HEU targets that are irradiated in the Belgian Reactor II (BR2), the High Flux Reactor in the Netherlands, and the Osiris reactor in France; MDS Nordion obtains ^{99}Mo from HEU targets that are irradiated in the National Research Universal (NRU) reactor in Canada; and Nuclear Technology Products (NTP) Radioisotopes obtains ^{99}Mo from targets that are irradiated in the Safari-1 reactor in south Africa.

Two important conversion actions were accomplished and marks a proof of concept and capability in the field. First, ANL in connection with research reactors in Indonesia and Argentina, began a program to develop higher density LEU targets made of uranium metal foil. Second, the Comisión Nacional de Energía Atómica (CNEA) based in Argentina, converted to LEU-based ^{99}Mo using higher density uranium-aluminum dispersion targets in 2002.

5.1 Considerations for a successful LEU conversion

There are many ways to meet the demands of the IAEA and DOE to convert from HEU to LEU for isotope production and each path starts with the target itself. Three basic approaches exist [1] for the conversion of these targets to LEU:

1) Direct replacement of the HEU in the target with LEU, while increasing the number of targets that are irradiated;

2) Increasing the mass of ^{235}U in the LEU target by increasing the target size;

3) Increasing the mass of ^{235}U in the target by changing the composition of the meat.

The first option, or the direct replacement of HEU and LEU has a great short term appeal as it requires the least amount of changes to the downstream purification processes. HEU and LEU essentially have identical chemical properties, so a direct replacement of the meat to LEU would require no new design considerations, fabrication, testing challenges, legal barriers or regulations to overcome. If the target keeps the same geometry and only converts the meat to LEU, the target would also keep the same heat transfer properties, chemical processability and could be irradiated in the same baskets and same manner as HEU targets. However, if all parameters of the target are kept in an LEU conversion, the yield of ^{99}Mo would be about 20% of the HEU target it replaces because of the reduced ^{235}U mass and its increased neutron capture from the presence of ^{238}U. Consequently, five times as many LEU targets would need to be irradiated to match the yield of a similar HEU production scheme. This would inherently lead to five times as much volume of waste from the extraction process. This waste would contain radioactive material and is not economically advantageous.

The second option is a natural first step in LEU conversion. Just by increasing the volume of meat in the target, or the amount of fuel particles in the meat zone, would also recover some of the yield loss without changing anything inherent to the target. This would lower the amount of waste compared to the first option. However, there are limitations on the dimensions of the meat zone (for thermal reasons) and the amount of particles that can go into the meat (for target fabrication reasons). Even maximizing the amount of fuel particles and fuel zone would not be sufficient to recover the loss in isotope yield.

Finally, the third option would be to increase the mass of ^{235}U by changing the composition of the meat. The current HEU targets (~90 % U^{235}) used to make medical isotope are made of uranium-aluminum alloys and have U-densities of around 1.4 to 1.6 g cm^{-3}. To obtain the equivalent mass of ^{235}U in an LEU (<20% U^{235}) target of the same dimensions, the U-density would have to be about 6 to 8 g cm^{-3}. The major disadvantage to this option would be that it would change any isolation and purification process that happen downstream, and would involve re-applying to any and all regulations thereof. A potential advantage to this option is that it could reduce the amount of waste, as the number of targets that would need to be processed is decreased. However, a new meat composition does not necessarily mean the same or less amount of steps in purification. In pursuing a new meat composition to isotope production, one would have to consider the volume, composition and treatment of waste as new variables to optimize. In this light, it is understandable why changing the meat composition can seem daunting and economically risky. However, keeping the current scheme leads to a financial loss in waste treatment from increasing the amount of targets and in the decrease in product yield.

5.2 High U-density alloys

Conventional HEU and LEU based isotope production targets are made out of U-Al alloys cladded in pure aluminum or Al alloys (e.g. 6061). Uranium forms three intermetallic compounds with aluminum; UAl_2, UAl_3, and UAl_4 (also written as $U_{0.9}Al_4$) (Figure 14), where the ratio of these three compounds are around 0.6%, 61% and 31% respectively in a typical target. The uranium density of an UAlx alloy with this composition is approximately 1.6 g cm^{-3} when the volume fraction in the U-Al alloy is approximately 30 vol% [20].

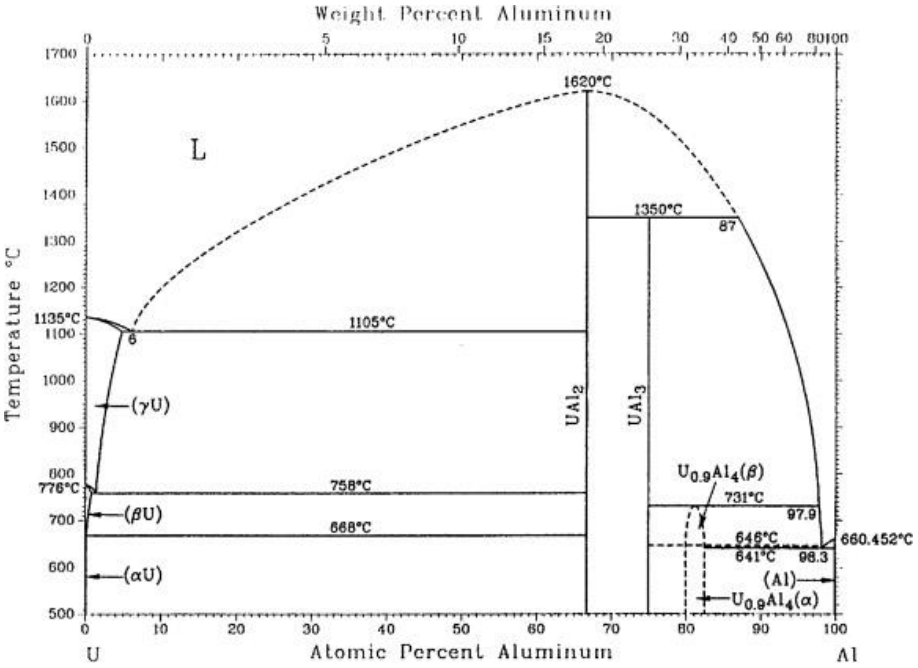

Figure 14) Uranium- Aluminum binary phase diagram.

A competing target, or "next generation target" needs to have a higher density compared to the current UAlx targets. As the alloys of uranium have been studied since the 1950s [21-23], a vast amount of literature exists about the different compounds that could be used in the meat, and no fundamental research has to be done on starting materials. However, the amount of uranium in a target is not just the amount of uranium in the alloy. Considering a dispersion target, the U-loading is calculated using:

$$\rho_U = w_V^D \rho_D v_f^D$$

With ρ_U = density of uranium in the meat (in g/cm^3)

w_V^D = weight fraction of U in the dispersed phase

v_f^D = volume fraction of the dispersed phase

ρ_D = density of the dispersed phase (in g/cm^3)

For each compound, the weight percentage of U in the dispersed phase (w_V^D) is calculated and its density of the dispersed phase (ρ_D) can be found in the

literature. Table 1 shows the results for compounds which are considered in the literature dealing with LEU fuel conversion:

Table 1) Weight fraction of U in high density alloys and density of uranium in the dispersed

	Weight fraction of U in dispersed phase (in %)	**Density of the dispersed phase ρ_D (in g/cm^3)**
U	100	19,1
U_6Fe	96,2887	17,7
U_6Ni	96,0526	17,6
U_6Co	96,0371	17,7
U_6Mn	96,2958	17,8
UAl_2	81,5199	8,1
UAl_3	74,6246	6,7
UAl_4	68,8047	6,0
U-Mo (9%)	91	17,0
U-Mo (5%)	95	17,9
U_3Si	96,2165	15,6
U_3Si_2	92,7077	12,2
USi	89,4480	10,4
U_3SiAl	92,8414	15,34
UN	94,4414	14,3
U_3O_8	84,8007	8,40
U-6Nb-4Zr	88	17,3
U-5Nb-3Zr	94	16,2
$U_{75}Ga_{15}Ge_{10}$	90,9696	15,8
$U_{75}Ga_{10}Si_{15}$	94,1044	15,6

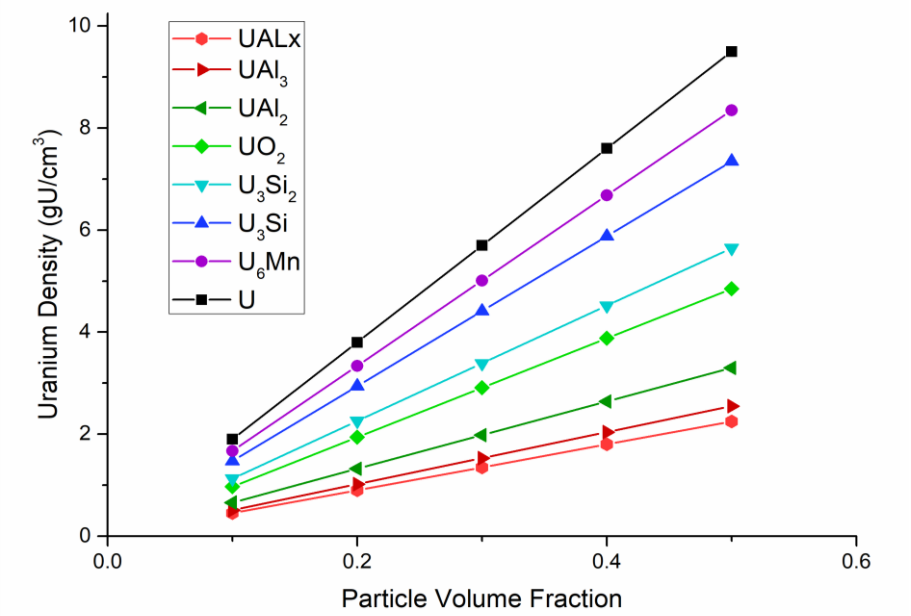

Figure 15) Uranium densities and their volume fraction within a target.

To be considered a viable candidate for LEU conversion, the alloy must have a U-density above ~2 g/cm^{-3} with a maximum volume fraction of the dispersed phase being around 55%. Above this volume fraction, a target is more difficult to fabricate due to the hardness of the fuel particles and the aluminum matrix becomes too small. Therefore, alloys shown in Figure 15 are considered as possible candidates for LEU isotope targets. In this graph, the alloys that has the highest densities are the U_6Metals (U_6Fe, U_6Co, U_6Ni and U_6Mn). U-Mo9%, U-Mo5%, U_3Si_2, and USi also meet the requirements.

5.3 Additional requirements of high-density fuels

In general, the irradiation of ^{99}Mo targets takes only a few days to one week, with low-burn[3] ups of only 3 to 10 %^{235}U. Relatively little physical or chemical changes occur in the target at this range of burnup. Although these targets will not experience high burnups, especially when compared to a fuel target,

[3] Burn up is a measure of how much energy is extracted from a nuclear source. It is measured both as the fraction of fuel atoms that underwent fission in %FIMA (fissions per initial metal atom) and as the actual energy released per mass.

its irradiation behaviors must be taken into consideration. As UAlx are originally designed as fuel targets, many of them are qualified for high burnups (> 30 $\%^{235}U$), although this is three times the amount of burn up it will experience as an isotope target. The stability or behavior of these fuels and targets in low burnup conditions must considered, and many of them have already been investigated [24]. A stable behavior under irradiation for a target means:

- No breakaway swelling: fuel can swell during irradiation for 2 possible reasons. The first one is a modification of the crystal structure due to temperature changes (ex: gamma U ➔ alpha U with an anisotropic swelling). The other is the development of fission products (solids or gases) that have a significant volume difference from the original material. Breakaway swelling which is an excessive exponential swelling could lead to severe issues (blockage of the cooling gap between plates and consequently plate failures).
- No delamination. When delamination occurs, the cladding detaches from the meat, which will lead to severe problems such as overheating due to loss of thermal conductivity;
- The fission gases should be contained within the plate and any release into the environment should be avoided;

An example of fuel particle swelling of a few fuel materials as a function of the fission density or burnup is presented in Figure 16. The graph shows that there is no breakaway swelling at low burnups (lower than 2×10^{21} fissions/cm^3 which corresponds to burnup of ~28 $\%^{235}U$) for U_6Metals and uranium silicides.

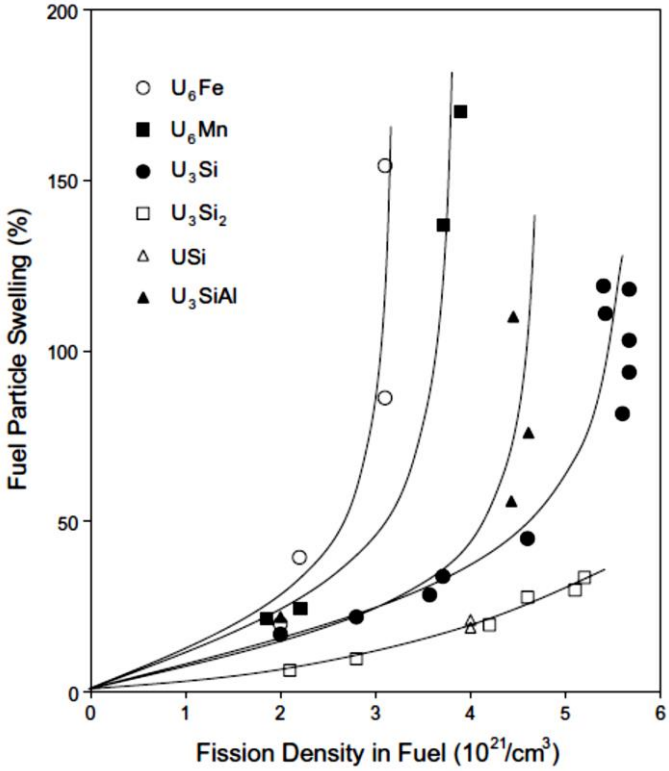

Figure 16) Fuel particle swelling as a function of fission density [24]

5.4 Processability of high-density compounds

Outside of fuel performance under irradiation, a major consideration in choosing material for isotope production is its chemical processability. As mentioned in the "chemical limitation" section, either an acidic or basic route is used to extracting the medical isotope from targets. However, in contrast the physical properties of U-alloys, very little research has been performed on the chemical processability of these materials. The extraction of isotopes from irradiated targets most likely represents the biggest unknown for the conversion of HEU targets to LEU targets.

A considerable mention and a template for this area of research is the study of uranium silicides in the form U_3Si_2. Silicides have been heavily researched by Argonne National Laboratory for its potential use in isotope production [14]. Their research concluded that ROMOL like conditions (NaOH or NaOH/ $NaNO_3$) cannot dissolved uranium silicide alone. The addition of peroxides

was required in order to dissolve silicides at an acceptable rate, but agglomerates formed and were problematic. A nitric acid route could be used but silicic acid became problematic as it formed a gelatinous slurry. Additionally, fluoride ions dissolved uranium silicides but the resulting waste and disposal became extremely corrosive. Finally, Although it has been noted that the chemistry of irradiated and un-irradiated targets are essentially the same due to low burnup [1], this seemingly obvious outcome should not be taken for granted. In the case of U_3Si_2, irradiated silicide has a slow dissolution rate compared to un-irradiated counterpart, owing to the bonding of silicide particles during irradiation [3, 25].

Argonne's investigation of uranium-silicide fuels demonstrates an exhaustive but necessary efforts to understand the feasibility of using new fuel for isotope production. They investigated both major routes of extracting isotopes, with additives and extra steps, and with different concentrations and reaction conditions. Most importantly, it demonstrates how some research paths can lead to an unfavorable conclusion but yielded many valuable lessons along the way. Clearly, having a high U-density and sufficient physical properties are not the only prerequisites that must be considered. However, they are an indispensable and essential attribute in order to make a conversion to an LEU target worthwhile.

6 Models of dissolution and digestion of solids

6.1 Introduction to digestion and dissolution mechanisms

There are many ways in which solids and liquids can interact with one another. In industry, the conversion of UAlx fuel to a yellow cake within the ROMOL99 method, has been referred to as either a "dissolving process" or "digestion". Both terms are in some ways misnomers and lack in specificity. To call it a dissolving process, the products should at some point be "dissolved" in solution, where the fuel would be incorporated into the liquid phase either by interactions with ions or non-charged molecules. However, the yellow cake reaction products are composed of solids and is separated by

physical filtration methods. There is not an intermediate that goes into solution, and therefore to classify this as a dissolving process is misleading and erroneous. The word digestion is normally reserved for a biochemical process where insoluble food molecules are broken down into water-soluble units so they can be absorbed. This word may have been adapted to this industry, as again it is certainly not a dissolution process, but the fuel does change chemically, physically, and in oxidation state. Although the term "digestion" can embody a solid-solid transformation, it does not describe any mechanism which it does so.

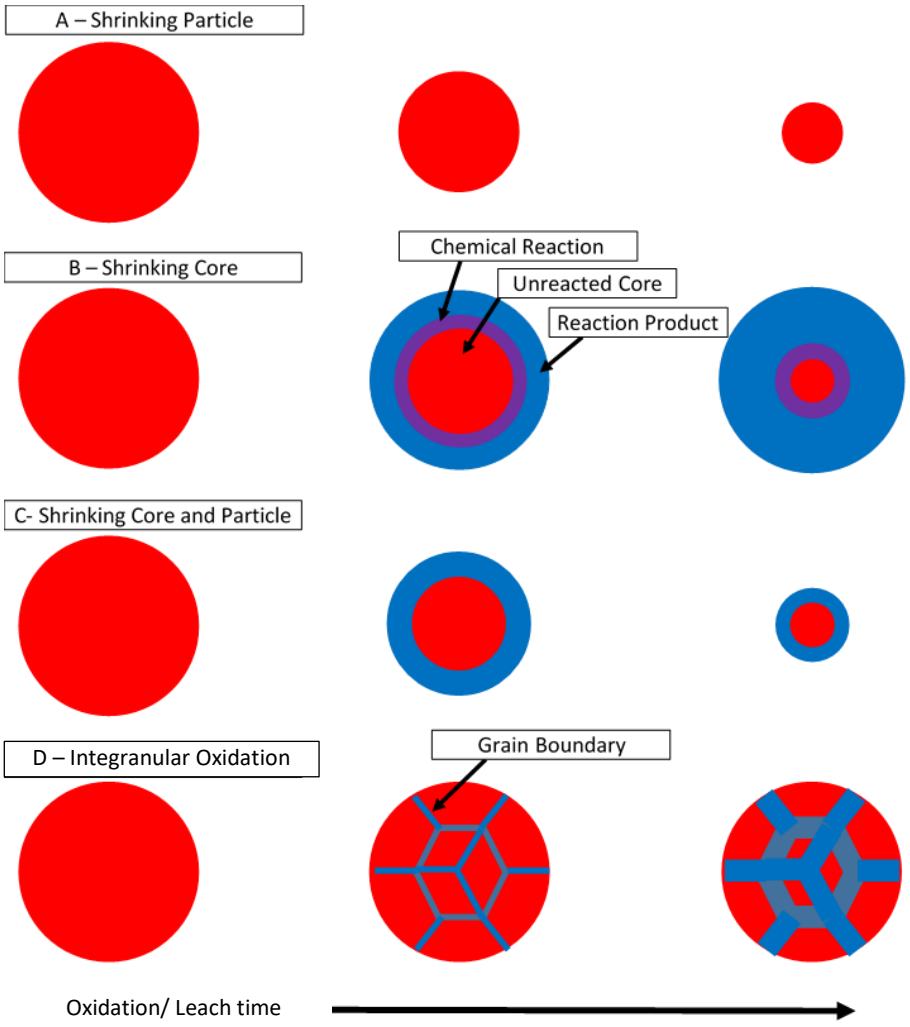

Figure 17) Models of oxidation and leaching. A – particle shrinking; B – shrinking core; C – shrinking core and particle; D - intergranular oxidation.

This thesis seeks to identify which mechanisms are responsible for the digestion of isotope production targets and to further define what digestion means from a chemical, physical, and metallurgical perspectives.

There are a few mechanisms that could be responsible for the conversion of fuel to yellow cake (Figure 17).

- Shrinking particle: Figure A, The surface of particle interacts with a reagent, and slowly shrinks as it is dissolves into solution.
- Shrinking core: Figure B, shows a shrinking core model, where the particle size stays the same. The reaction front penetrates into the particles, but the reaction products stay on the particle, forming a "shell" layer. This model often assumes an "ash" or porous shell, which allowed the reactants to penetrate the shell and get to the core. In this model, diffusional coefficient and mass transfer are important characteristics to consider.
- Shrinking core and particle: Figure C, shows the combination of the shrinking core- and shrinking particles, where the shell layer can break off or comes a state where it can dissolve.
- Intergranular oxidation: Figure D, shows intergranular oxidation or corrosion along grain boundaries.

Although there are more ways for solids to interact with liquids, and more modes of corrosion, the ones presented here are a good starting point for this analysis. Knowing which type of mechanism controls the "digestion" rate of UAlx fuel would give us the ability to optimize the design of fuel particles and to increase digestion speed.

The following experiments presented in this chapter are therefore performed to address the following:

- What model of oxidation correctly describes the digestion of UAlx?
- At what rate does UAlx fuel digest in alkaline media?
- What role does the microstructure of the fuel have on the type and rate of digestion?
- Can we improve the digestion rate without adding an accelerant?

6.2 Oxidation events in digestion

Within this thesis, many forms of oxidation are explored within the U-Al and U-Mn alloying systems. In particular, the oxidation of aluminum and uranium occurs with the production of hydrogen via the following reactions:

Eq 7) $Al + 3H_2O \rightarrow Al(OH)_3 + 3/2\ H_2$

Eq 8) $U + 2H_2O \rightarrow UO_2 + 2H_2$

Additionally, it is predicted that the use of potassium permanganate results in the oxidation of uranium via the following reaction:

Eq 9) $U + 2KMnO_4 + 2H_2O \rightarrow UO_2(OH)_2 + 2MnO_2 + 2KOH$

The techniques used in this thesis are suitable to detect changes in chemical composition, oxidation, and microstructure, including energy dispersive spectroscopy (EDS), x-ray diffraction (XRD) and electron backscattered diffraction (EBSD). Oxidation can be used as a sign of other physical-chemical events, such as electron transfer and potential differences, corrosion, electrochemical dissolution, and energy minimization, to name a few. To further differentiate this oxidation process as a corrosion process, scanning electrochemical microscopy (SECM) and electrochemical scanning tunneling microscopy (EC-STM) are needed. Similarly, cyclic voltammetry and inductively coupled plasma mass spectrometry (ICP-MS) are needed to classify this process as active electrochemical dissolution or electro catalytic dissolution [26-28]. These techniques are not used in this thesis. Therefore, surface oxidation and intergranular oxidation are used throughout the body of the text to describe the digestion phenomena. As this is the first in-depth study of the subject, and without looking further at a local electrochemical potential for instance, there is missing information to have a complete picture. Therefore, the oxidation that is observed in this thesis is inviting for further analysis to be done.

7 Research area, strategy, and philosophy

The scope of this PhD project is based in practical, economical, and physical considerations. Firstly, this thesis has been performed at Belgium's Studiecentrum voor Kernenergie Centre d'Étude de l'énergy Nucléaire (SCK•CEN) and the BR2 reactor. Therefore, fission based medical isotopes

production methods will be studied. Secondly, most ^{99}Mo extraction facilities use the ROMOL99 process or slight variation of it. Therefore, it is a combination of new target meat in combination with the ROMOL99 process that will be studied.

The overall objective in this thesis is to improve low-enriched uranium based medical isotope targets and to discover how to design them. Designing a next generation target must include a high U-density fuel to increase the isotope yield of a target, as is discussed in "Considerations for a successful LEU conversion". Special attention will be made on its ability to digest, dissolve, or whichever mechanism is most successful at releasing medical isotopes and with an understanding that next generations must outcompete the UAlx targets that are currently in use (Figure 18).

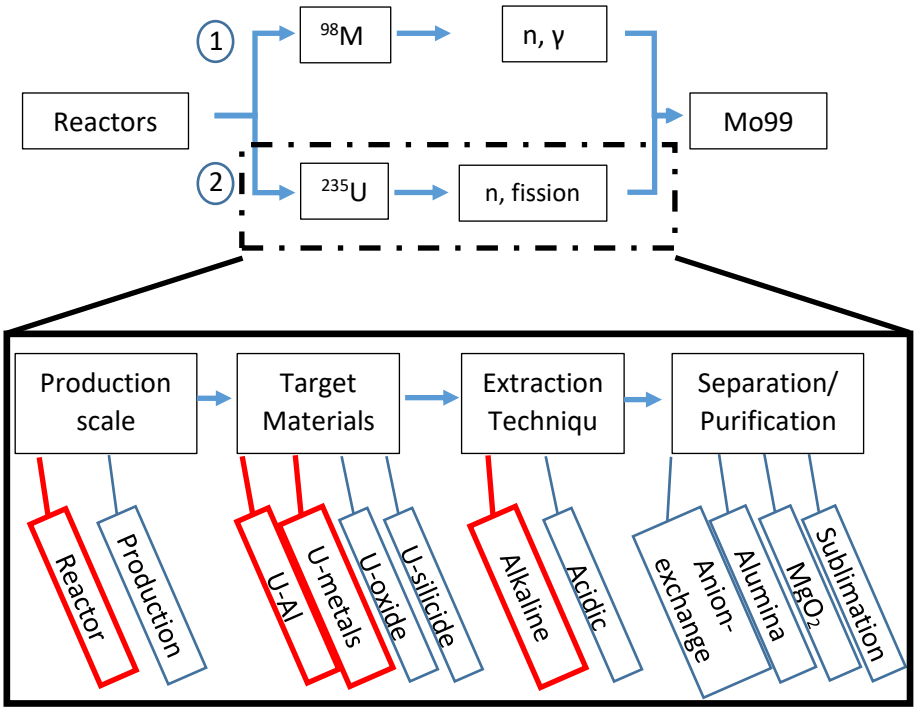

Figure 18) Techniques of isotope production and extraction. Highlighted in red are techniques that will be considered for experimental design.

However, finding a way to compare the digestion of next generation target with the current UAlx targets is in and of itself a non-trivial task. Despite the fact that these chemical processes have existed since the 1960s, and that they are used in facilities around the world every day, not much is known

how isotopes that are made from UAlx fuel, are release into solution. It is understood that isotopes are released when the uranium turns in to other oxidation states (UO_2 and $Na_2U_2O_7$) and that most facilities can complete this step in 90 minutes. However, what happens during this 90 minutes and how this transformation occurs is unknown. Essentially, this reaction is "black box" chemistry where only the initial and end products are analyzed with no understanding of any intermediate. Optimization can and has only been performed before and after the "black box" but not within the black box itself, and with no understanding of the physical-chemical phenomena involved. Consequently, a comparison of performance cannot be made if the standard itself is not understood. Therefore, the research that is performed here will take two homologous routes in tandem (Figure 19):

Part 1) Understanding the digestion of UAlx fuel

How UAlx transforms into UO_2 and $Na_2U_2O_7$ within the scope of a ROMOL99 extraction process is the focus of the first part of this thesis. As is mentioned in "ROMOL99 method", the main reactants, products, and parameters to consider are UAlx, $Na_2U_2O_7$, NaOH, $NaNO_3$, temperature and pressure. To be in agreement with the ROMOL99 standards, the concentration of NaOH will initially be tested at 4M NaOH but higher concentrations will be explored. Additionally, the volume of solution will be kept well above the solubility of sodium aluminate ($NaALO_2$) of 57g/l

First, pure UAl_2, and UAl_3 will be tested in these conditions. A fundamental understanding of how these two intermetallic phases react to the solution in a pure form will be the basis in understanding how these targets as a whole react. Although it would be advantageous to study pure UAl_4, preparing such a sample proved to be difficult as will be explained below and is omitted.

Following, eutectic or mixed phased particles will be studied. Particles composed of UAl_2-UAl_3 and UAl_3-UAl_4 are often found in actual targets and represent majority of particles within the meat. A comparison of pure particles and eutectic particles can be analyzed to see the influxes one phase has over another.

Finally, how HEU and LEU targets dissolves will be studied. How actual targets digested can be compared to the model pure and mixed phased particles alone. The effects of the dispersant aluminum phase, and cladding have on the meat particles can be compared and would give insight into how digestion works in an industrial setting.

Part 2) Qualification and understanding the digestion of U_6Mn fuel

In "Considerations for a successful LEU conversion", increasing the mass of ^{235}U is considered for next generation medical isotope targets and is the focus of the second part of this thesis. As is demonstrated in Figure 15, the best candidates for increasing the uranium mass is U_6Metals (U_6Mn, U_6Fe, U_6Co, and U_6Ni), U-Silicides (USi, U_3Si, and U_3Si_2), and U-Molybdenum (U-Mo5% and U-Mo9%). Of these, U-Mo alloys are unsuitable for isotope production because the high ^{98}Mo would dilute the ^{99}Mo produced during irradiation, reducing its specific activity and make it unusable[1]. Uranium-silicides have been heavily studied and could be an area of research. Research in this area would have to be focused on breaking up the reacted U-Si-Al interactions that happen during irradiation and breaking up the silicic acid slurry that occurs during digestion. However, many methods have already been investigated by Argonne National Laboratory and many potential dead-ends have already been identified, making this a risky option.

U-Metals on the other hand is a promising family of intermetallics that fit many criteria. Its U-density (17.8 g cm^{-3}) is close that of pure uranium (19.1 g cm^{-3}), and above U-silicides (15.3 g cm^{-3}). It can withstand a burn up of around 30%, well above the 5-10% that most isotope targets receive. However, no

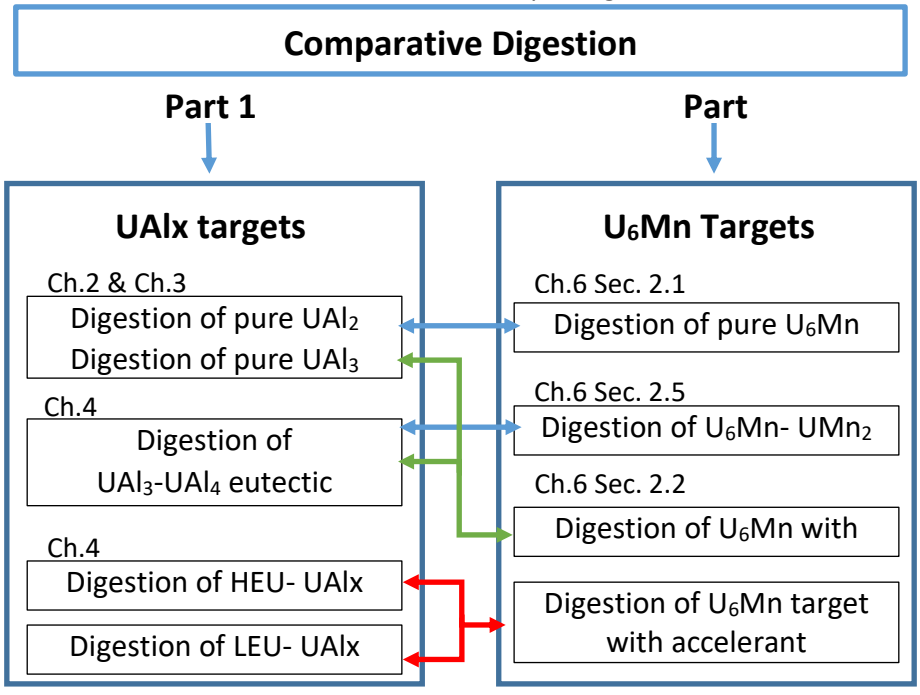

Figure 19) Comparative digestion and thesis outline.

research has been published in open literature regarding U-metals and its ability to digest or dissolve in ROMOL99 conditions. For all of these reasons mentioned, it has been chosen as the focal point of this part of the thesis and will be compared against UAlx targets.

To begin this research, pure U_6Mn will be studied as a pure form in digestion. Digestion conditions will firstly be identical to the UAlx digestion experiments, to see if this material is suitable for this process without any changed. The results of these experiments will be compared to pure UAl_2 and UAl_3 particles. Oxidants and accelerants will be tested to optimize this process in the event that digestion does not occur within an industrially suitable time frame. Next U_6Mn-UMn_2 eutectic will be studied for a few reasons. U_6Mn is often formed with UMn_2 along its grain boundaries, and required a long annealing to produce a pure sample. Practically, UMn_2 is almost always present and its digestion must also be considered. Secondly, the digestion of U_6Mn-UMn_2 eutectic can be compared to the digestion of UAl_3-UAl_4 eutectic. If a combination of a high U-density target (such as U_6Mn) and its successful digestion outperforms the current UAlx system, then a new path towards an LEU based medical isotope production is opened.

With this comparative, two path approach to investigate LEU based medical isotope production, a broad range of ideas and strategies can be investigated and cross examined, with applicable results to both current and future methods of isotope production. As change in industry tends to take time to meet regulation requirements and testing standards, an optimization of the currently used method would be more pragmatic. Seeing into the “black box” of digestion UAlx targets in the ROMOL99 method could allow us to optimize this crucial step in isotope recovery. On the other hand, finding a way to separate isotopes from irradiated high-density LEU targets would provide a more optimum and superior solution to the current method. This thesis therefore seeks to advance both methods of radioisotope production using low-enriched uranium.

References

1. *Medical Isotope Production Without Highly Enriched Uranium.* National Academies Press (US): p. 220.
2. Lee, S.-K., G.J. Beyer, and J.S. Lee, *Development of Industrial-Scale Fission 99Mo Production Process Using Low Enriched Uranium Target.* Nuclear Engineering and Technology, 2016. 48(3): p. 613-623.
3. *Non-HEU production Technologies for Molybdenum-99 and Technetium-99m.* IAEA Nuclear Energy Series, 2013(No.NF-T-5.4).
4. *Feasibility of producting Molybdenum-99 on a Small Scale Using Fission of Low Enriched Uranium or Neutron Activation of Natural Molybdenum.* IAEA Technical reports series, (no. 478).
5. IAEA, *Feasibility of Producting Molybdenum-99 on a Small Scale Using Fission of Low Enriched Uranium or Neutron Activation of Natural Molybdenum.* Technical Reports Series no. 478, 2015.
6. Ponsard, B., *Medical Radioisotope production at BR2.* MEDICIS - Promed Specialized Training on Radioisotope Production, 2017.
7. Vandegrift, G.F., et al., *Full-Scale Demonstration of the Cintichem Process for the Production of Mo-99 Using a Low-Enriched Target.* 1998 International Meeting on Reduced Enrichment for Research and Test Reactors, 1998.
8. Domingos, D.B., et al., *Comparison of low enriched uranium UAlx-Al and U-Ni) targets with different geometries for the production of molybdenum-99.* 2016.
9. Stang Jr, L., *Manual of isotope production processes in use at Brookhaven National Laboratory*. 1964, Brookhaven National Lab., Upton, NY.
10. *Methods and Apparatus for Selective Gaseous Extraction of Molybdenum-99 and Other Fission Product Radioisotopes.* EP 2580763 B1 20150722 (EN), 2015.
11. Muenze, R., et al., *The Fission-Based 99Mo Production Process ROMOL-99 and Its Application to PINSTECH Islamabad.* Science and Technology of Nuclear Installations, 2013. 2013: p. 1-9.
12. *The socratic.* https://socratic.org/questions/how-do-you-rank-oxidizing-agents.
13. Snelgrove, J.L., et al., *Development and Processing of LEU Targets for Mo-99 Production -- Overview of the ANL Program.* RERTR, 1994.
14. Buchholz, B.A. and G.F. Vandegrift, *Processing of LEU targets for 99Mo Production -- Dissolution of U3Si2 Targets by Alkaline*

Hydrogen Peroxide. (INIS-XA-C--2005). International Atomic Energy Agency (IAEA), 2004.
15. A. V. Gelis, et al., *ANL progress in developing an leu target and process for mo99.* RERTR 2003, 2003.
16. Gelis, A.V., et al., *ANL progress on the Cooperation with CNEA for the MO99 Production.* RERTR 2004, 26 International meeting on Redduced Enrichment for Research and Test Reactors, Jan 2004.
17. Wang, Z., et al., *Uraninite oxidation and dissolution induced by manganese oxide: A redox reaction between two insoluble minerals.* Geochimica et Cosmochimica Acta, 2013. 100: p. 24-40.
18. Wang, Z., et al., *Oxidative UO2 dissolution induced by soluble Mn(III).* Environ Sci Technol, 2014. 48(1): p. 289-98.
19. Grenthe, I., Drozdzynski, J., Fujino, T., Buck, E., Albrecht-Schmitt, T.E., Wolf, S.F, *The Chemistry of the Actinide and Transactinide Elements, Chapter 5.* 2006. 1.
20. Ryu, H.J., et al., *Metallurgical considerations for the fabrication of low-enriched uranium dispersion targets with a high density for 99Mo production.* Journal of Radioanalytical and Nuclear Chemistry, 2014. 305(1): p. 31-39.
21. Baenzinger, N.C., et al., *Compounds of uranium with the transition metals of the first long period.* Acta Crystallographica, 1950(3): p. 34-40.
22. *Gmelin Handbook of Inorganic Chemistry U Supplement Volume B2 Alloys.* 1989: p. 333.
23. Thaddeus B. Massalski, H.O., P.R. Subramanian, Linda Kaaprzak, *Binary alloy phase diagrams 2nd ed*. Vol. 3. 1990.
24. Finlay, M.R., G.L. Hofman, and J.L. Snelgrove, *Irradiation behaviour of uranium silicide compounds.* Journal of Nuclear Materials, 2004. 325(2-3): p. 118-128.
25. Sameh, A. *Production of fission Mo-99 from LEU uranium silicide target materials*. in *Invited Papers on Symposium on Isotope and Radiation Applications*. 2000. ROC.
26. Walther, B., et al., *Electrochemical dissolution of hard metal alloys.* Electrochimica Acta, 2007. 52(27): p. 7732-7737.
27. Gilbert, J.A., I.A. Shkrob, and D.P.J.J.o.T.E.S. Abraham, *Transition metal dissolution, ion migration, electrocatalytic reduction and capacity loss in lithium-ion full cells.* Journal of the Electrochemical Society, 2017. 164(2): p. A389.
28. Łukaszewski, M. and A.J.J.o.E.C. Czerwiński, *Dissolution of noble metals and their alloys studied by electrochemical quartz crystal microbalance.* Journal of Electroanalytical Chemistry, 2006. 589(1): p. 38-45.

Part I

Digestion of UAlx fuel

Chapter 2

Extraction of medical isotopes from UAlx fuel

Summary

A solution of sodium hydroxide and sodium nitrate is used worldwide to digest uranium aluminide targets to extract medical isotopes. This digestion process turns UAlx fuel to an oxide and a yellow cake of sodium diuranate, which allows the isotopes to be released and separated out in solution. Despite its wide use, relatively little is known about how the fuel converts into an oxide. This chapter explores the rate and mechanism at which the fuel turns into an oxide as a function of time.

Scanning electron microscopy (SEM) coupled with energy-dispersive x-ray spectroscopy (EDX) is used to image cross sections of digested fuel particles to evaluate the progression of oxidation. X-ray diffraction (XRD) is used to determine the composition of the fuel and the chemical products at the end of the digestion process. During the digestion process, samples are taken at 5 minute intervals, quenched and purified to track the progression of oxidation in these particles.

It is found that UAl_3 fuel has three different stages of digestion. The first stage is surface oxidation, where a layer of UO_2 develops on the surface of digested particles reaching a thickness of 10μm. The second stage is the oxidation of triple junction. The third stage is the oxidation of the grain boundaries. Discovered for the first time is that this digestion is a form of intergranular oxidation and not a surface oxidation process.

Additionally, the effects of two common types of impurities are also investigated. The first type of impurity is phases of UAl_2 and the second type is an aluminum phase present at the grain boundaries. UAl_2 is found to not only be resistant to oxidation itself but it also prevents the intergranular oxidation along neighboring UAl_3 phases. In contrast, aluminum rich grain boundaries enhance intergranular oxidation. Oxidation fronts penetrate over 100μm within 20 minutes in particles with aluminum GB, where only triple junctions are oxidized in grain boundaries without an additional aluminum phase, and with the same concentration of reagents and digestion time.

With the experimental evidence presented here, junction types are classified based on their response to oxidation. Oxidation resistant and oxidation susceptible designs are presented as a network of junction types and are demonstrated with digested fuel particles meeting these design specifications. An oxidation resistant design with R0 and R1 resistant junctions stops the oxidation front at its surface while an oxidation

susceptible design with R2 and R3 susceptible junctions allows for the penetration of the digestion solution into the fuel particle. The results presented here allows us to design better fuel particles for the digestion and extraction of medical isotopes from UAlx fuel particles.

Table of Contents

1 Introduction 48

1.1 Background 48

1.2 Digestion experiments 49

2 Experimental methods 50

2.1 Fabrication of fuel particles 50

2.2 Digestion of fuel particles 50

2.3 Sample preparation 51

2.4 Analysis technique – scanning electron microscopy 51

2.5 Particle classification, cross-sections and limitations 55

3 Results 56

3.1 Experiment 1: Digestion of annealed UAl_3, ROMOL-99 conditions 56

3.1.1 Sample preparation and characterization of the UAl_3 button 57

3.1.2 Sample preparation before digestion 59

3.1.3 Digestion – Experiment 1 61

3.1.3.1 Phase 1 - Surface oxidation 61

3.1.3.2 Phase 2 - Oxidation at triple junction 65

3.1.3.3 Phase 3 - Oxidation at grain boundaries 67

3.1.3.4 Final Stages 68

3.1.4 Impediment of UAl_2 on percolation networks in UAl_3 68

3.1.5 Discussion – Experiment 1 70

3.2 Experiment 2 Digestion of as-cast UAl_3 70

3.2.1 Sample preparation and characterization 71

3.2.2 Digestion – Experiment 2 78

3.2.2.1 Small particles – 20 minutes of digestion 78

3.2.2.2 Large Type 4 Particles – 20 minutes of digestion 78

3.2.2.3 Particles at 30 minutes of digestion 79
3.2.3 Discussion – Experiment 2 81
3.3 Experiment 3: Digestion of annealed UAl_3 in 8M NaOH 81
3.3.1 Digestion – Experiment 3 82
3.3.1.1 Surface oxidation 82
3.3.1.2 Final digestion products – filter cake analysis 84
3.3.2 Discussion – Experiment 3 85
4 Discussion – towards optimized digestion of UAl_3 86
4.1 Oxidation behavior and junction classification in UAlx fuel 86
4.2 Optimally designed grain boundaries for the controlled oxidation properties of UAlx Alloys 90
4.3 Strategies for the production of oxidation susceptible UAlx alloys and its successful digestion 91
4.4 Further discussion on selective oxidation 93
5 Conclusion 94

Table of Experiments

Identification	Sample	Solution	Temp (^oC)	Time (min)
Experiment 1	Annealed UAl_3	4M NaOH, 4M $NaNO_3$	95	90
Experiment 2	As-cast UAl_3	4M NaOH, 4M $NaNO_3$	95	30
Experiment 3	Annealed UAl_3	8M NaOH, 4M $NaNO_3$	95	90

1 Introduction

1.1 Background

Uranium-aluminum (UAlx) dispersion targets comprised of High-Enriched Uranium (HEU) to Low-Enriched Uranium (LEU) are currently used worldwide to produce medical isotopes. Dispersion targets begin with UAl_2 particles in a matrix of aluminum powder, which transform into UAl_3 and UAl_4 during the target fabrication process. The final composition of UAl_3 and UAl_4 varies from one manufacturer to another, with almost no UAl_2 remaining in the final target. After being irradiated and the isotopes are formed, these targets are dissolved or digested to extract and isolate the isotopes.

All current ^{99}Mo producers who use LEU UAlx targets use an alkaline digestion chemical process [1]. Multiple targets are digested in a dissolver containing various concentration of NaOH and $NaNO_3$. This alkaline digestion step converts UAlx to a yellow cake of $Na_2U_2O_7$ (NaDU), releasing the isotopes from the fuel and into solution. In particular, the well-known ROMOL-99 process [2] uses a solvent of 3M NaOH and 4M $NaNO_3$, and completely dissolves targets within 90 minutes, as mentioned in chapter 1.

Although the corrosion and digestion of UAlx intermetallics is well studied, relatively little is known about the mechanism that converts the UAlx fuel into an oxide or the rate that it happens. The aqueous corrosion of UAlx fuel [3] for example, has been well characterized for testing conditions that might exist in a waste repository. The oxidation of UAlx intermetallics for power reactors [4, 5], has been studied by gravimetric methods to understand its oxidation behavior between 350-600^{o}C, using an atmosphere of pure oxygen.

However, the development of UAlx to NaDU as a function of time is elusive. After a typical digestion of UAlx fuel, an analysis of the filter cake is performed with XRD and EDX to ensure that the reaction went to completion [6-8], but any intermediate step is not well documented in public domain. This study seeks to understand how UAlx fuel evolves during the digestion process. An understanding of this process can help to optimize or redesign the digestion step to ensure the complete extraction of medical isotopes from irradiated UAlx fuel.

1.2 Digestion experiments

The digestion experiments performed in this chapter consider two design aspects. The first is to convert an industrial ROMOL-99 digestion process to a lab scale digestion. The second is to digest samples that represent a variety of different microstructural types. The first design aspect affects how much reagents and fuel is used in each experiment and is kept constant for most experiments. The second is varied to investigate how different microstructural types are affected by the digestion bath.

In a lab scale digestion, the digestion bath is kept to 250ml of solution in a borosilicate reaction vessel. The solvent volume needed for a digestion of a target piece is determined by the solubility of sodium aluminate ($NaAlO_2$) which is 57g/L. The amount of sodium hydroxide in the digestion bath could theoretically react with more than 200g of UAl_3 fuel. For the experiments performed in this chapter, only a few grams of fuel were digested in each experiment to be well below either limit. The reaction vessel is equipped with a condenser to trap escaping gasses and to keep the concentration of reagents constant. External heating is applied by a water bath and a heating plate. A solution of ethylene glycol 60 vol% at 4°C was used to chill the reaction vessel or halt the reaction when needed.

There are three experiments that were performed to represent three different morphologies:

Experiment 1 – Digestion of an ascast UAl_3 sample. This experiment is performed to understand how pure UAl_3 digests. Not only does annealing relieve crystals of dislocations and internal stress, but it also allows for the development of strain-free grains and grain growth. Digestions with annealed samples used UAlx fuel that was annealed at 650°C for 72 hours.

Experiment 2- Digestion of an as-cast sample. In as-cast samples, an excess of aluminum is found at grain boundaries, forming a discrete aluminum phase at the boundary. This experiment is performed to see the effects of these aluminum-boundaries and how they compared to grain boundaries without aluminum. In experiment 1 and 2, the effects of minoring amounts of UAl_2 is also observed.

Experiment 3 – Digestion of UAl_3 using 8M NaOH. This experiment is performed to see the effects of doubling the concentration of the driving reagent in order to reduce the digestion time.

2 Experimental methods

2.1 Fabrication of fuel particles

All fuels in this study were produced by arc melting in an Arc 200 cold crucible arc melting furnace under highly pure argon gas. Before melting, metals are stripped of their surface oxide layers with a solution of 60% vol nitric acid and rinsed with acetone. Once the precursors are loaded into the copper hearth, the furnace chamber is put under vacuum of 4 x 10^{-3} mbar, backfilled with argon, then vacuumed down a second time to 2.3 x 10^{-4} mbar for 1 hour to ensure as little oxygen is present in the chamber during arc melting.

The uranium provided was depleted in pellet form that were around 19 grams each. The aluminum provided came in atomized form from the company Alpoco. The composition of the powder as specified by the manufacturer is 99.67% aluminum with major impurities of: Cu 0.163%, Si 0.047%, Fe 0.082% and Zr with 0.012%. To prevent the aluminum powder from being ejected from the copper hearth upon arc-melting, the aluminum was first pressed into pellets with an average of 5 grams each. The press exerted 10 tons of pressure on a cylindrical pellet with a diameter of 8.6mm.

2.2 Digestion of fuel particles

Digestion of UAlx particles followed similar ROMOL-99 conditions. The digestion solution was prepared in a borosilicate reaction vessel, externally headed in a water bath and magnetically stirred. The water bath was held at 95^{o}C for the duration of the experiment (Figure 1, Step 1). Five to seven grams of fuel was digested either with 4 M NaOH and 1.6M $NaNO_3$, or with 8M NaOH in 250ml of solution. At designated time points, 3 ml of solution was aliquoted from the reaction vessel to a specimen vial. In the vial, the specimen was diluted to below 0.4M NaOH and immediately cold quenched to 4^{o}C (Figure 1, Step 2). After the experimental run, the samples were further diluted until the solution reached a neutral pH and no NaOH could be detected (Figure 1, Step 3). A GE healthcare Whitman acid/alkaline test paper

were used to measure pH values. The samples were then dried under ambient conditions.

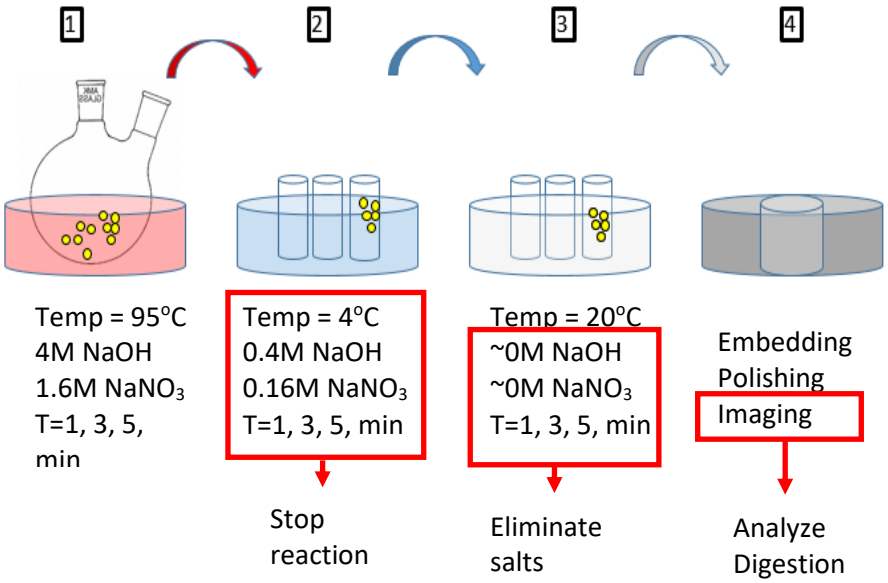

Figure 1) Experimental layout for timed digestions. Step 1) Digestion at 95°C with timed aliquoted samples. Step 2) flash quenching to stop the reaction in a cold bath. Step 3) Dialysis to eliminate salt crystals from solution. Step 4) embedding and polishing for SEM imaging.

2.3 Sample preparation

Cross-sectional imaging were taken from the digested particles by embedding them in epoxy resin, which were cured into a puck. The puck was ground and polished with dry and wet methods. For the initial grinding stages to produce a flat specimen, pucks were ground using SiC papers with grit sizes 320 (35 µm), 600 (15 µm), 800 (13 µm), 1200 (8 µm). The duration of each of the grinding steps was 5 minutes. For SEM quality images, 3 steps using diamond suspension (3 µm, 1µm, 0.25 µm) was used. The samples were rinsed with water between polishing steps and cleaned with ethanol.

2.4 Analysis technique – scanning electron microscopy

Scanning electron microscopy (SEM) coupled with energy dispersive x-ray spectroscopy EDX is used to image and analyze samples and their microstructure. In both techniques, an incident electron beam causes the excitation of secondary electrons, backscattered electrons and characteristic

X-rays. Depending on which type of electron or x-ray is detected, different information about its microstructure or chemistry can be inferred. When both techniques are coupled together, localized chemical composition can be obtained on micro- or nano-scaled features of a flat polished sample. This information can be used to detect, for example, localized oxidation, physical-chemical transformations, and structural changes to a material.

Primary electrons (PE)s: produced by the filament of a Shottky field emission gun, the primary electrons originate from the SEM and interact with a sample surface to produce a number of secondary interactions (Figure 2A) that can be detected and used for imaging. These secondary interactions are produced when the primary electrons lose energy by repeated random scattering and absorption within a teardrop shaped interaction volume (Figure 2B). This interaction extends from a few nanometers to 5 µm into the sample surface and define the resolution limit of the SEM.

Secondary electrons (SE) micrographs: SE imaging mode collects low energy SE (<50 eV) that are ejected from the valance or conduction bands by inelastic scattering from the incident beam. Because of their low energy, these electrons originate from just a few nanometers within the surface of the specimen. These electrons are topographically sensitive and have a high spatial resolution. This makes them the most frequent choice for microscopic imaging. The drawback is that they carry little information about the elemental compositions of the sample. As well, this technique is not particularly good for flat polished samples, as are the majority of the samples in this thesis. Although different material compositions polish differently, and structural features can still be seen using this imaging mode, it must be remembered that an imaging originating from topographical information may not differentiate between chemical compositions.

Backscattered electrons (BSE) micrographs: BSE are much more energetic than secondary electrons and originate from a larger depth. These electrons originate in the electron beam, and are back-scattered or reflected out of the specimen by elastic scattering. Since elements with a higher atomic number backscatter electrons more strongly, and thus appear brighter in an image, BSE imaging can be used to detect contrasts between areas of different chemical compositions and densities. In contrast to SE images, BSE images will have less spatial resolution and less topographical information. For flatly polished samples, this can be useful to detect chemical changes to a samples microstructure.

Energy-dispersive X-ray (EDX): In contrast to SE, where the PE interact with valence or conduction band electrons, in EDX spectroscopy, the PE interacts with ground state (unexcited) electrons in discrete energy levels. If an inner shell electron is ejected, a hole will be created and filled from a higher-energy election. The difference in energy between the high-energy shell and low energy may be released in the form of an x-ray and detected. As these X-rays are characteristic of the difference in energies between the two shells, and of the atomic structure of individual elements, EDX allows the elemental composition of the sample to be measured. Combining EDX imaging with a SE or BSE image allows for an elemental composition to be defined, for a specific microstructure on a sample.

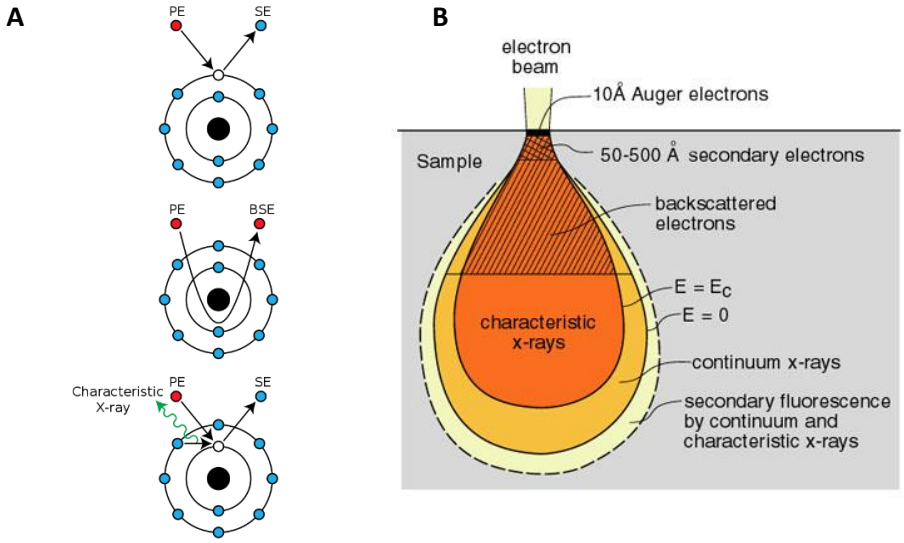

Figure 2) A- types of electron interactions within an SEM. B - Information depths of secondary electrons, backscattered electrons, and x-rays

The SEM that is used in this work is a JEOL JSM 7100 LV, Field Emission Gun (FEG) SEM is installed augmented with a Bruker EDS detector. The SEM is coupled to a stainless steel glovebox and mounted inside a concrete hot cell, allowing for the examination of radioactive specimens up to an activity of 4.44 MBq. Detailed specifications of the SEM can be found in Table 2[4].

[4] Provided by Jelle Van Eyken

JEOL JSM6610 LV	
Filament	Schottky Field Emission Gun (FEG)
Acceleration Voltage	0.1 – 30 kV
Probe Current	1 PA – 200 nA
Magnification	x 10 – x 1 000 000
Stage	5-axes (X,Y,Z,R,T) mechanically eucentric stage
Max specimen size	Ø < 100 mm h < 40 mm
Max specimen weight	2 kg
Low Vacuum	Variable pressure: 10 – 300 Pa
Pixels	1280 x 960 – 5120 x 3840
Resolution High Vacuum	1.2 nm at 30 kV, WD 10 mm, secondary electrons 2 nm at 1 kV, WD 10 mm, secondary electrons
Resolution Low Vacuum	3 nm at 30 KV, WD 10 mm, 30 Pa backscattered electrons 3 nm at 30 KV, WD 10 mm, 60 Pa secondary electrons

Table 2) Specification summary of JOEL JSM 7100 LV

For the analysis of digested particles, SEM images were taken in secondary electron configuration, to see topographical differences across the oxidized fuel particle, and in backscatter electron configuration, to see grain boundaries through channeling contrast. EDX was used to analyze the elemental composition of the fuel and oxidation phases identified in the SEM images. X-ray intensity profiles (or X-ray map) show the measured intensity of a single X-ray wavelength (or energy), corresponding to a specific element, as a function of the sample feature. Since the measured intensities are not corrected for local density, absorption, fluorescence, etc. they only provide qualitative information on the local and specific elements in the samples. Quantitative elemental information cannot be derived from these maps, as differences in intensities do not necessarily signify a difference in concentration. However, variations in X-ray intensity of a specific element in an area that are known to be of a similar composition, do give an indication on the relative elemental concentration. In addition to EDX mapping, X-ray diffraction (XRD) is performed to help identify the phases present in the digested sample.

2.5 Particle classification, cross-sections and limitations

As mentioned above, SEM images were taken of the digested fuel particles in order to visualize the digestion process. In particular, this is done to see the development of the NaDU layer against the undigested fuel. SEM and EDX are two dimensional analysis techniques with which is used to characterize 3D objects. Measured thickness and diameters of particles are not absolute and measured thickness values are taken as though they are connected around the particle.

In the following analysis, particles are analyzed at a cross-section and by its Feret diameter[5]. To analyze the development of the UO_2 or NaDU, EDX elemental maps were processed with SigmaScan Pro Version 5.0.0. All EDX scans show aluminum in red, oxygen in blue, and sodium in green. In the case of fuel particles (Figure 3 A, B and C) the area of fuel or oxide layer is taken as the number of red (fuel) or blue (oxide) pixels over the total number of colored pixels. In the case of large particles (defined as cross-section

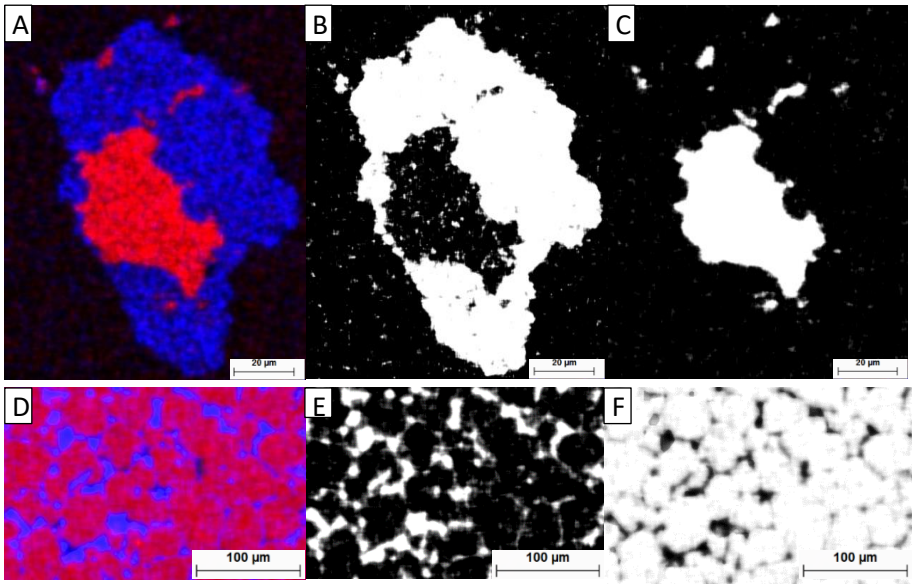

Figure 3) Image analysis through SigmaScan Pro. Image A shows an EDX map of a digested fuel particle with aluminum in red, and oxygen in blue. The image is RGB separated from its blue oxide (B) and its red aluminum fuel core (C). For large particles, representative areas were taken (D) with its oxide (E) separated from its fuel (F).

[5] Feret diameter calculates, for each object, the theoretical diameter of the object if it were circular in shape.

radius>100µm) an area fraction of fuel or oxide growth is taken in section (Figure 3 D, E and F).

Finally, the measurement of surface oxydation was also performed on EDX color maps of particles. This oxidation layer is measured as a function of the cross section by partitioning the image into a 4µm by 4µm grid (Figure 4). A distance measurement was taken of the oxide every 4µm in areas where the oxide layer exists. Zero values were disregarded in the analysis below. In general, this measurement of surface oxidation is limited in accuracy by the effects of sample preparation and potential breakage. However, as will be evident below, the oxidation thickness becomes consistent enough to make a discussion on it and its characteristics possible. This analysis is used as a first approximation.

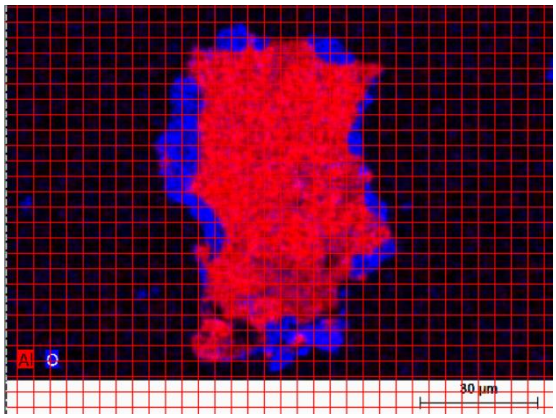

Figure 4) Measurement of surface oxidation by gridding.

3 Results

3.1 Experiment 1: Digestion of annealed UAl_3, ROMOL-99 conditions

UAl_3 phases in fuel particles can be found in all UAlx targets. They can be found as pure UAl_3 phases, UAL_3 with minoring amounts of UAl_2, or UAl_3 mixed with UAl_4 phases. The objective of this first experiment is to see how pure UAl_3 digests in a caustic digestion solution. To achieve a highly pure sample, an UAl_3 button[6] was prepared according to the procedure described

[6] A button is a small ingot. Metallic precursors are heated past its melting point and then cooled to make a small sample.

in the Gmelin handbook of inorganic chemistry volume 2B [9]. The procedure for the production of pure UAl_3 calls for arc melting stoichiometric amounts of uranium and aluminum metal in argon atmosphere. To obtain a metallurgical recovery yield of 97-99%, the sample has to be melted several times and annealed for homogenization [10-12]. In making UAl_3 from stoichiometric amounts of uranium and aluminum, an excess amount of aluminum can be found at the grain boundaries. In annealing, the grain sizes grown and the segregated grain boundaries become a part of the grains with UAl_3 phases come into direct contact with each other.

3.1.1 Sample preparation and characterization of the UAl_3 button

A secondary electron (SE) image of the UAl_3 sample surface that was used in these experiments is shown in Figure 5. This button was annealed at 650^{o}C for 72h. Holes or voids can be observed in the post annealed button as black spots with white edges (Figure 5A). Additionally, cracks can be seen in connection with the holes. EDX analysis over large areas (Figure 5, point 100)

indicates that the majority of the composition is 25±2 at% U and 75±1 at% Al. In some small places, pure uranium (point 38, Figure 5) was identified.

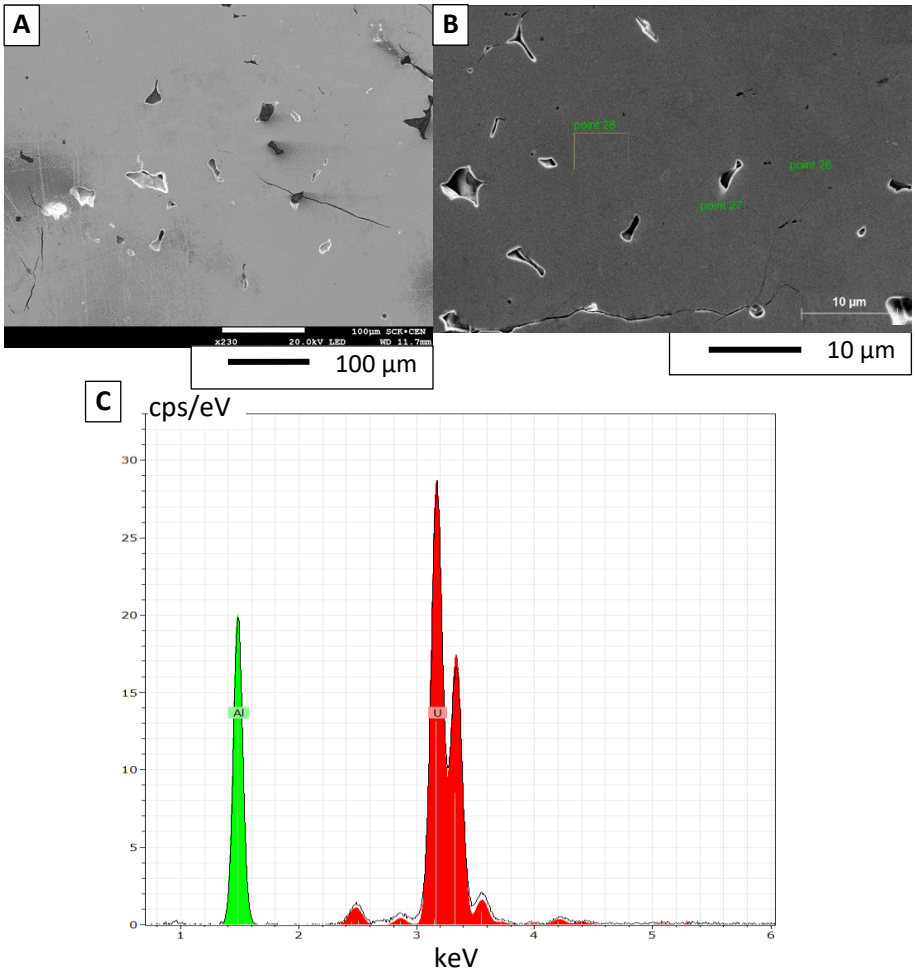

Figure 5) SEM image of UAl3 button after 650°C anneal for 72 hours. A- SE image and an overview of the ingot showing voids. B – BSE image indicating point of analysis. C – EDXS of point 28 indicating uranium in red and Al in green. Accelerating voltage of 20kV, 13mA probe current, acquisition time 30 minutes.

A XRD analysis was performed to confirm which phases were present in the ingot. A diffractogram of the ingot from 15° through 150° in 2θ is shown in Figure 6. When compared with the ICSD patter of UAl_3 (00-007-0301), there is a strong match is observed. Furthermore, the remaining small-intensity peaks are matched to the three most intense peaks of UAl_2 (ICSD pattern 00-019-0053). The button of the post-annealed UAl_3 is qualitatively quite pure.

Nevertheless, it should be noted that there were pieces of segregated uranium in the SEM images that did not appear on the diffractogram.

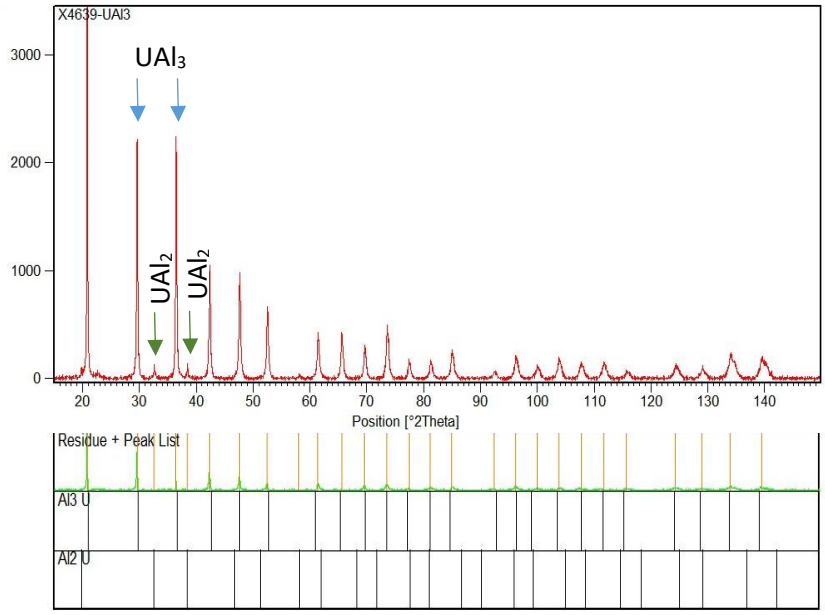

Figure 6) XRD of UAl_3 button after annealing at 650°C for 72 hours. Selected UAl_3 peaks are indicated in blue. Selected UAl_2 peaks are indicated in green.

3.1.2 Sample preparation before digestion

Particles were examined before digestion occurred, to examine the effects of grinding. These particles were prepared by manually crushing the ingot of UAl_3 in ambient conditions. The surface oxidation of uranium and its alloys leads to surface passivation of a few nanometers [13] but does not interfere with the oxidation processes studied here.

The particles after grinding exhibit a wide range of sizes from 1µm to several hundreds of microns, most of which were pure UAl_3. Figure 7 A shows the native oxide layer (arrow 2) with a thickness around 100µm of UAl_3 particles (arrow 1). Figure 7 B is a BSE image of a large cross section of an as-ground fuel particle. Large cross sections feature grain boundaries (BG, arrow 4) and triple junctions (TJ, arrow 5). Also visible are voids or cracks (arrow 6). Finally, some particles contain grains of UAl_2 (arrow 3). These grains are checked independently with EDX, but can also be identified as brighter grains in BSE images due to its heigher density.

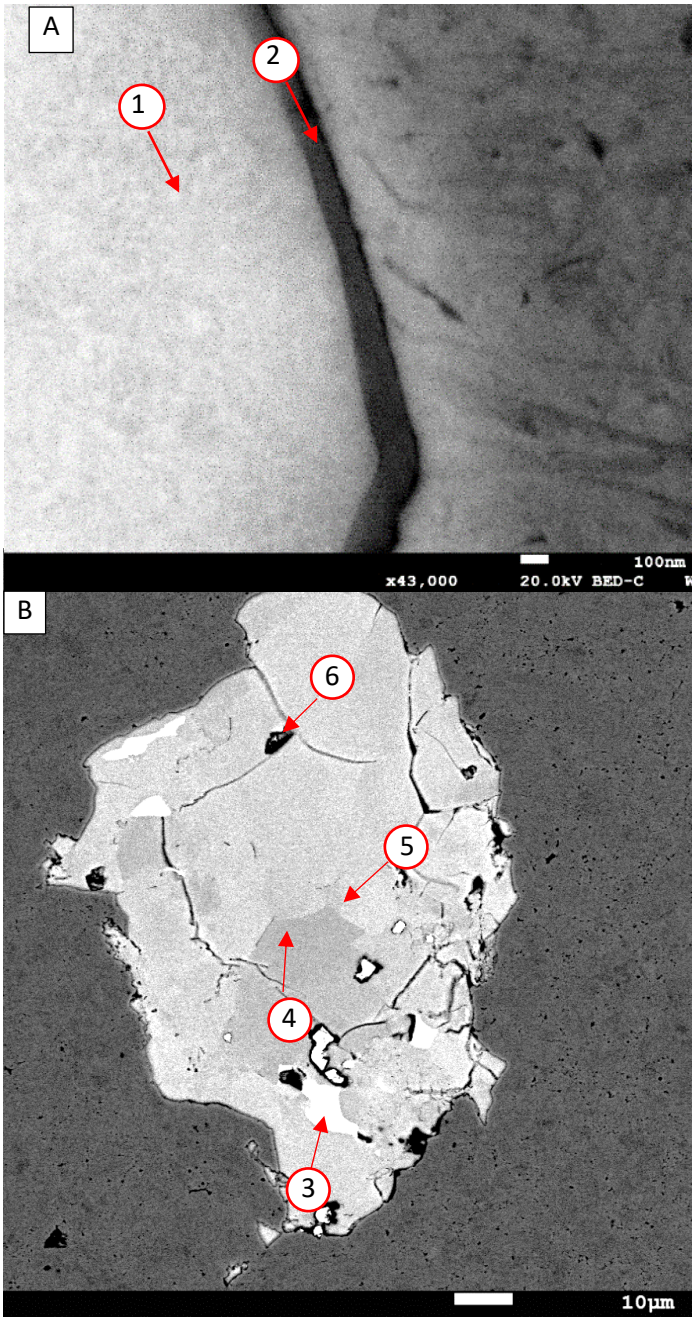

Figure 7) Annealed UAl_3 particles. A,1) BSE image of an UAl_3 particle edge before digestion with; 2) a native oxide layer; B) A cross section representing a fuel particle; C) BSE image of a large cross section and fuel particle; 3) light regions are impurities of UAl_2 with its corresponding phase boundaries against UAl_3; 4) grain boundary of UAl_3. 5) triple junction of UAl_3; 6) voids and stress cracks.

3.1.3 Digestion – Experiment 1

The digestion of UAl_3 was performed in a 4M NaOH and 4M $NaNO_3$ bath at 95°C. Samples were taken after 3 and 5 minutes of digestion, with subsequent samples taken at 5 minute interval after that. The samples were quenched by immersing the sample in a water bath cooled by a 4°C ethylene glycol solution. The samples were dried as prepared for SEM imaging, as described in section 2.3.

3.1.3.1 Phase 1 - Surface oxidation

Samples taken from the first 10 minutes of fuel digestion show oxidation primarily at the sample surface. Figure 8 shows EDX map measurements of particles digested for 3 minute (Figure 8A) 5 minutes (Figure 8B) and 10 minutes (Figure 8C). The oxidation of UAl_3 is reflected by the increased oxygen content (blue) on the outside of the particle core (in red). Surface oxidation occurs equally for small cross sections (Figure 8B) medium cross sections (Figure 8C).

During the first 10 minutes, relatively little oxidation or digestion occurs internally or inside the fuel particles. Figure 8D, a BSE image of Figure 8C, shows channels that are fully oxidized at 10 minutes. Within the same particle, voids, grain boundaries, and triple junctions show no signs of oxidation. Figure 8 E shows a cross section with UAl_2 as lighter grains. Again, only surface oxidation is visible while grain boundaries, or phase boundaries, and triple junctions are fully intact.

Some surfaces (Figure 8C and E) show no signs of oxidation. This is likely to be an artifact of sample preparation. As sample preparation for SEM imaging analysis is an abrasive process, some of the oxidation layer can break off. Favorable oxidation could happen, for example, on a closed packed plane of a crystal structure. However, as UAl_3 has a symmetrical structure in the class Pm-3m (group 221), and it is unlikely that favorable oxidation against any plane can occur. Additionally, a surface with no signs of oxidation could be a sign of a shrinking core and shrinking particle. However, this process is not known to dissolve any of the uranium and is therefore unlikely to be an explanation as well.

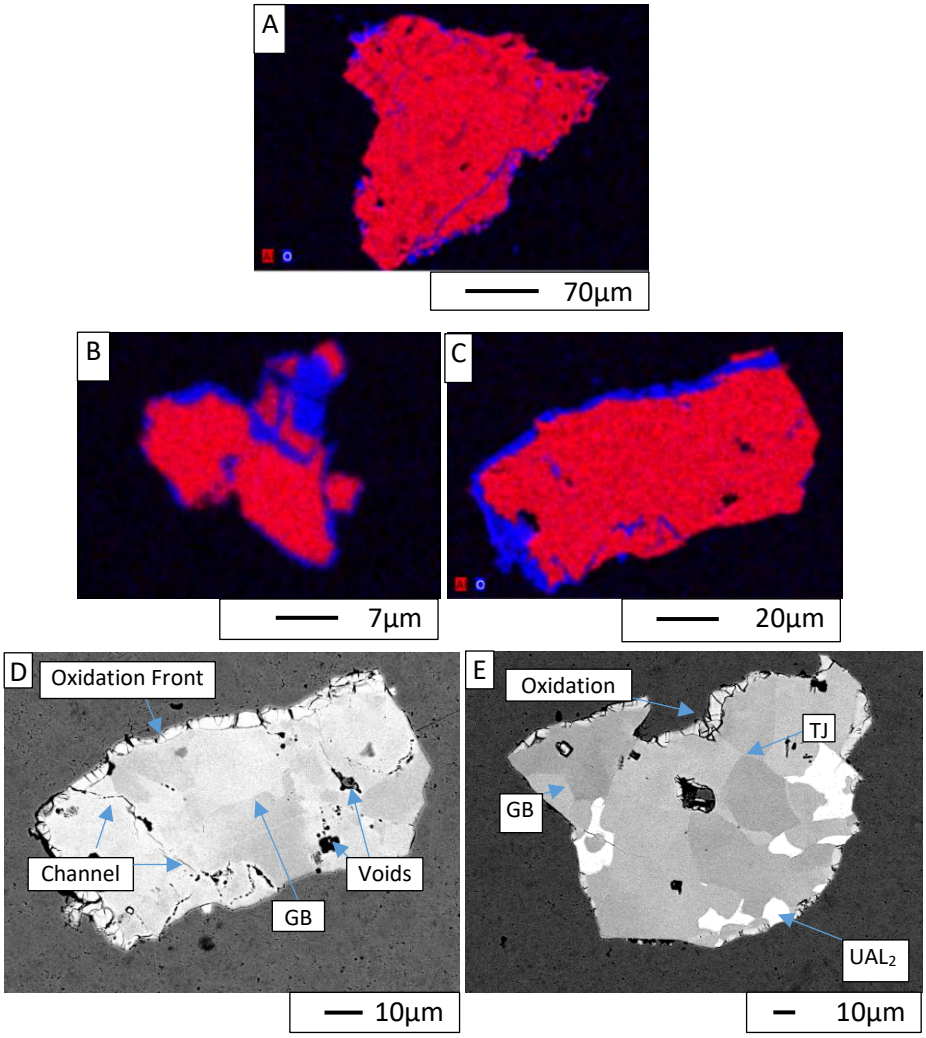

Figure 8) stage one surface oxidation. A-C are combined EDX images. A) particle after 1 minute B) after 5 minutes and C) after 10 minutes of digestion. Aluminum from UAl_3 is represented in red and oxygen from UO_2 is represented in blue. D and E) BSE images of particles digested for 10 minutes.

The development of the surface oxidation was evaluated by measuring the thickness of the oxide layer. For each time point, 20 to 40 particles were evaluated and the results are displayed in Figure 9. Particles digested for 3 minutes had a mean oxide thickness of 0.89µm. Particles digested for 5 minutes had a mean thickness of 1.39µm and particles digested for 10 minutes had a mean oxide thickness of 3.2µm.

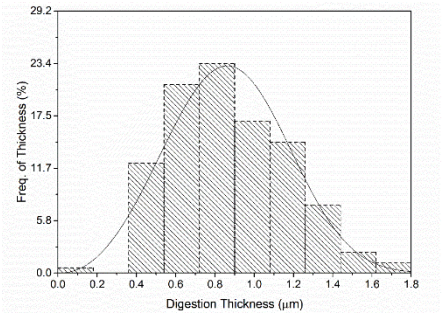

	NaOH	Mean	STD
T=3	4M	0.89	0.29

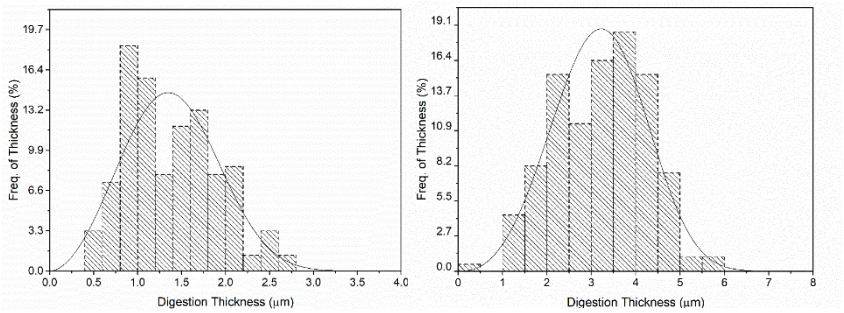

	NaOH	Mean	STD
T=5	4M	1.39	0.522

	NaOH	Mean	STD
T=10	4M	3.21	1.02

Figure 9) Oxide thickness after 3, 5 and 10 minutes of digestion.

A few patterns are still observed across all particles that were imaged. Upper limits to the oxide thickness, for example were consistent. Particles digested at 3 minutes showed no oxide thickness above 2.3 μm, and particles digested at 10 minutes showed no oxide above 10μm (with one outlier).

Oxidation in small cross sections at 30 minutes

Small particles that are digested for 30 minutes show surface oxidation that does not advance much further than for particles that were digested for 10 minutes. Figure 10 A and B shows and EDX and SE image of a small cross section digested for 30 minutes. The average thickness here is 10.2 µm with an oxide area fraction of 77.95 percent. All small cross sections at 30 minutes were more than 75% oxidized. The amount of oxidation was independent of shape factor[7] in the sample size range 0.33-0.61.

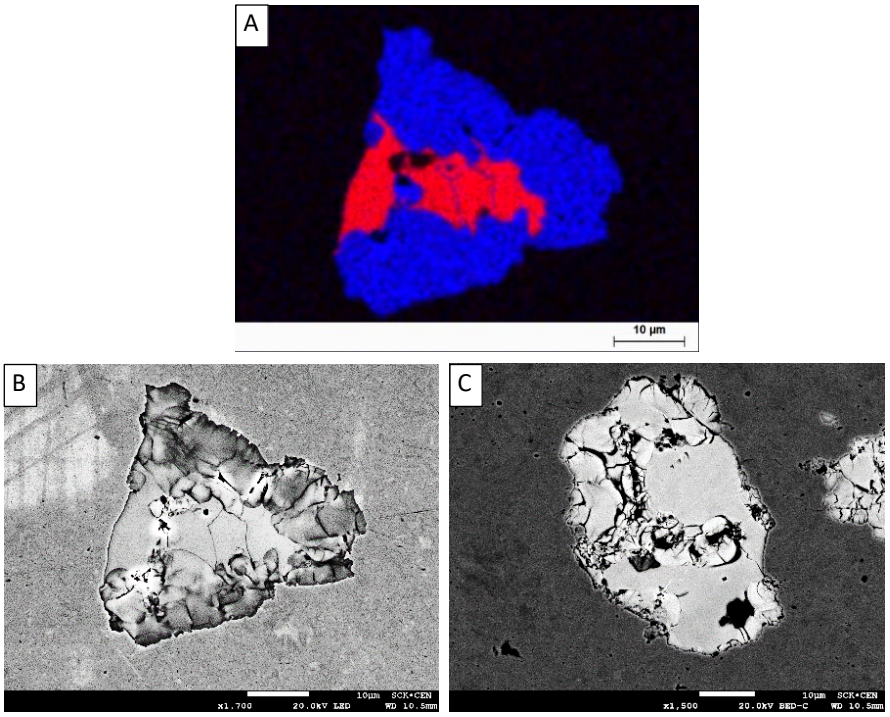

Feret Diameter	Avg. Thickness	Shape Factor	Long Axis µm	Area % Fuel	Area % Oxide
36.1µm	10.2±2 µm	0.55	39.1	22	78

Figure 10) digestion of small particles at 30 minutes. A) EDX map of aluminum (red) and oxygen (blue); B) an SE image of A; C) BSE image. Small cross section of a digested particle.

[7] Shape factor used here is a measure of sphericity. It is a dimensionless measure equal to 4π times the area divided by its perimeter squared. A perfect circle has a shape factor 1 while a line has a shape factor approaching zero.

3.1.3.2 Phase 2 - Oxidation at triple junction

In the early stages of particle digestion, it was discovered that surface oxidation is the only mechanism operating to convert UAl_3 to UO_2. This mode of oxidation was active between the starting time and 10 minutes into digestion, in a 4M NaOH bath at 95°C. As will be made evident, new modes of oxidation become apparent for large polycrystalline particles. These modes occur within the fuel particles. In general, internal oxidation begins to occur between 10 and 15 minutes of digestion and is able to penetrate all particle size at least within a particle radius of 500μm.

Large particles or cross-section

Large particles are considered separately not only because of their classification in target production, but because the particles are much larger than the grain size, or polycrystalline. This allows the effects of grain size, boundaries and triple junctions to play a role. A particle with a large cross section can be seen in Figure 11. In addition to surface oxidation, particles after 30 minutes show internal oxidation at triple junctions. In Figure 11A shows a BSE image of large particle cross section, where grain boundaries are visible. Black areas can be seen at each intersection of grain boundaries or at triple junctions. Figure 11B presents an EDX color map of the same cross section. Here the color map shows that these locations have been oxidize, unlike the voids in particles digested for 10 minutes (Figure 8 B, C). At this stage, sodium is also detected in the oxidation layer, unlike particles analyzed at earlier time points. Oxidation of triple junctions without affecting grain boundaries must be due to the availability of digestion solution to the junction. It is speculated that this mode is made possible due to voids and intraparticle cracks that are present throughout the particles, or some other pathway for the solution to move throughout the particle.

The progress of oxidation or digestion has two notable differences when observing larger cross section. Unlike smaller fuel particles, the fuel area in larger particles is more dominant than the oxide area. The fuel area for the particle displayed in Figure 11 A-C has a fuel area fraction of 84% and an oxide area fraction of 15.7%, almost the inverse of Figure 10. Additionally, it is evident that the surface oxidation thickness does not develop significantly past 8 to 10µm. If surface oxidation developed at the same rate as particles imaged between 1 and 10 minutes, than we would expect a surface oxidation on the scale of 30µm. surface oxidation developed fully developed at 10 minutes. This limitation of surface oxidation highlights the importance of internal oxidation or different modes of digestion.

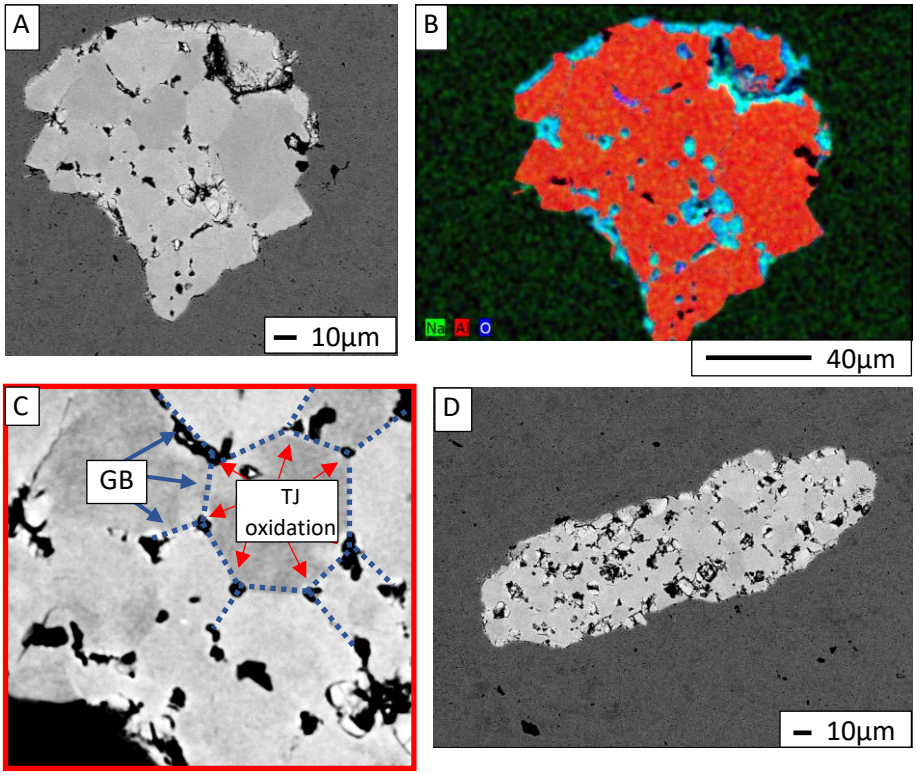

Figure 11) Large particles digested at 30 minutes: A) BSE image of a large particle with corroded TJs; B) EDX elemental map of A. O in blue, Al in Red, and Na in green; C) a focused section on GBs and TJs; D) BSE image. An additional large particle with corroded junctions. Feret diameter is 111µm, shape factor 0.38, long axis 113µm, area% fuel 84, area% oxide 16.

3.1.3.3 Phase 3 - Oxidation at grain boundaries

Following surface oxidation and oxidation at triple junctions, a new mode of oxidation becomes evident. Between 30 and 60 minutes, oxidation at triple junctions proceeds through grain boundaries. Figure 12 shows a BSE image of a large particle cross section at 60 minutes of digestion. Within this particle, unconnected triple junctions can be oxidized, without any link to another triple junction through a grain boundary in the same plane. Additionally, there are three types of grain boundaries. Grain boundary 1 in Figure 12 is not-oxidized and intact, grain boundary 2 is in an early onset of oxidation, and grain boundary 3 is fully oxidized. All three stages of grain boundary oxidation are seen on all images of pure UAl_3, independent of its distance to the particle edge.

Because it is impossible to see the particle above and below the cross section, it is also not possible to prove oxidation pathways and dynamics. However, the "random" distribution of oxidized and non-oxidized GBs constitute a clear indication and existence of "special" fast oxidation GBs. To classify GBs, and to determine which are more vulnerable to oxidation, a technique such as Electron Backscatter Diffraction (EBSD) would have to be used. The use of EBSD to identify which grain boundaries oxidize faster will be covering in a following chapter.

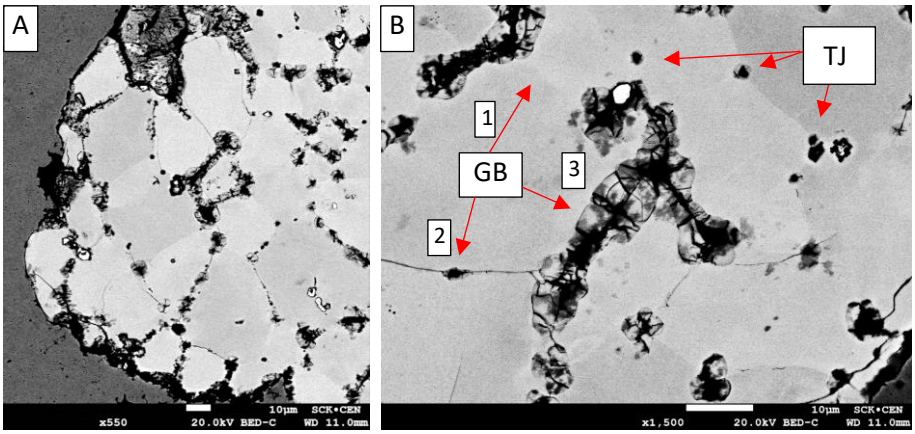

Figure 12) BSE image of particle with a large cross section. Corrosion can be seen not only at triple junction but also at grain boundaries.

3.1.3.4 Final Stages

After grain boundaries are oxidized, a percolation network forms to make a continuous path for digestion. Figure 13A shows a BSE image of a large cross section with Figure 13B its EDX elemental map. The area is 33% oxidized, with the oxidation pathways laying on grain boundaries. The fuel that remains undigested are the centers of grains. This is in contrast to having the particle surface digested and the core of the particle undigested. Finally, particles with small cross sections such as in Figure 13C, are fully digested. The EDX point analysis of small particles indicate that they are rich in sodium, oxygen and uranium.

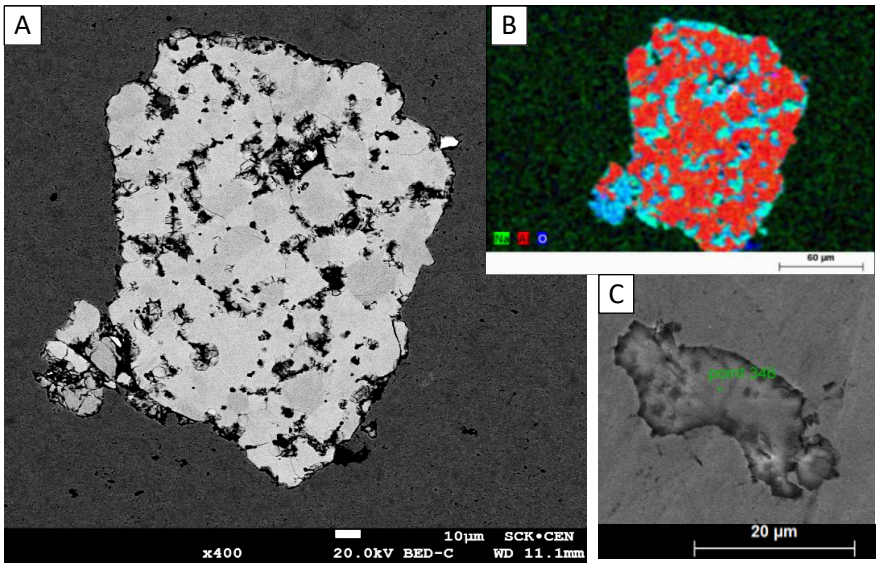

Figure 13) Corroded particles at 90 minutes. A) BSE image of a large particle with percolating network; B) EDX elemental map of particle A. The feret diameter is 166µm, shape factor 0.607, area %fuel 67, area %oxide 33; C) particle with small cross section that is fully digested.

3.1.4 Impediment of UAl_2 on percolation networks in UAl_3

Finally, the digestion of non-pure UAl_3 particles are analyzed. It is already stated in literature that UAl_2 [14] itself does not digest well compared against UAl_3 and UAl_4 (see appendix I). However, the literature lacks detailed information about the digestion kinetics when a fuel particle is mixed with different phases. Figure 14 demonstrates the effects of UAl_2 within a digested fuel particle after 90 minutes. Figure 14 A and D show a large dual

phase particle cross section after 90 minutes of digestion. Only the surface of the particle is digested. In image A, the interior of the particle remains undigested. This is in huge contrast to particles examined at the same time point in Figure 13, where only the cores inside the grains remain intact. Not only is UAl_2 itself hard to digest, but it stops the digestion process in the of UAl_3 phases. In essence, surface oxidation is the only available digestion mechanism available to mixed phase particles. Mixed particles of UAl_2-UAl_3 are therefore capable to survive the ROMOL-99 digestion conditions for an extended period of time.

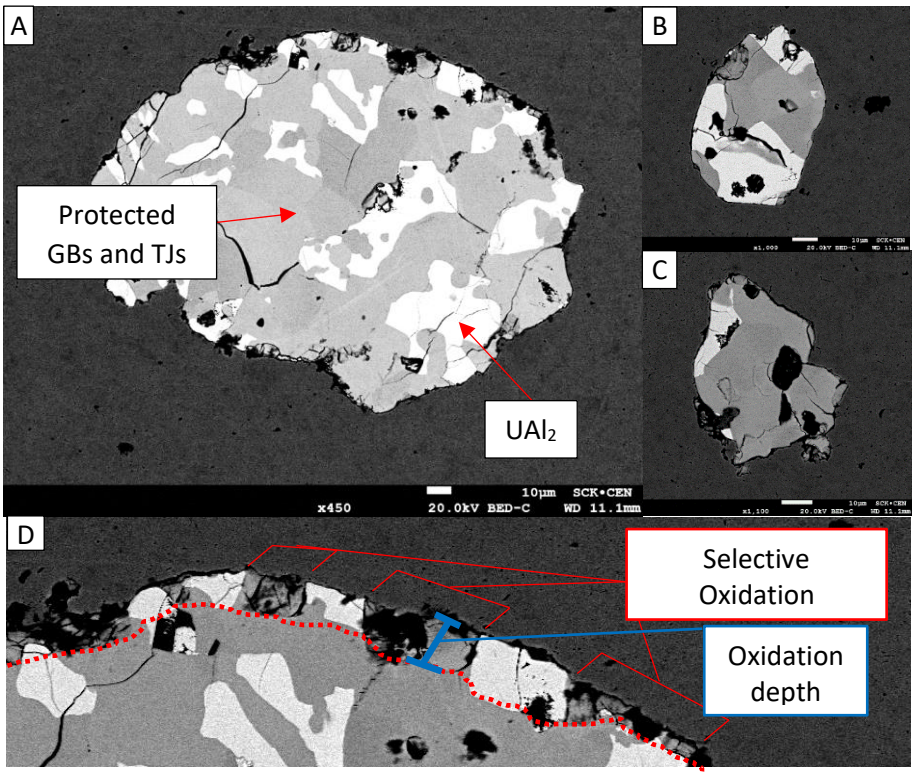

Figure 14) Digestion of mixed UAl_2/ UAl_3 fuel particles after 90 minutes of digestion. A) BSE image. Large particle cross section with UAl_2 as light grains. GB and TJs within UAl_3 phases are protect as pathways are blocked. B and C) BSE images of particles with small cross sectiond. D) focus of image A. selective surface corrosion of UAl_3 with protected UAl_2 barriers.

3.1.5 Discussion – Experiment 1

The current understanding of the uranium-aluminum alloy dissolution process is based on surface digestion [2, 15-18] (Figure C). In a caustic system, the kinetic interpretation of the solution on U-Al alloys is that it is a heterogeneous, first-ordered kinetic reaction, with a rate law that may be written as [15]:

Eq1) $$-\frac{dc}{dt} = k\frac{s}{v}\,c$$

Where *c* is the caustic molar concentration at time *t; s* is available surface area of the alloy in square centimeters; *t* is time in minutes; and *v* is the dissolvent volume in liters. The results of this experiment makes evident that this interpretation is limited when digesting pure UAl_3. Surface oxidation does occur but only in the first stage of the digestion process. Therefore, only considering the surface area *s* in equation 1 is only valid for this stage of the digestion.

The reaction that is occurring in pure UAl_3 in this digestion is also not a dissolution. It has been discovered that UAl_3 undergoes intergranular oxidation, shown in Figure D. More specifically, the second stage of digestion is the oxidation of TJs while the third stage of intergranular oxidation is the oxidation of GBs. Particles that exhibit intergranular oxidation must be manufactured differently than particles that only undergoes surface oxidation. Particles that only undergo surface oxidation should be engineering to have optimal surface to volume ratio, or shape factor, or aspect ratios. For UAl_3 particles, the density of triple junctions and the number of grain boundaries will play a more important role. This topic will be investigated more in-depth in the following chapter.

Finally, the digestion effects of UAl_2 phases on UAl_3 is reported here for the first time. It has been known that UAl_2 does not digest, but the fact that it can impede on ability for UAl_3 to digest was unknown. As intergranular oxidation is the key digestion UAl_3, then it follows that blocking a junction or pathway will also stop digestion. This component of blocking digestion is explored in more detail below.

3.2 Experiment 2 Digestion of as-cast UAl_3

The interest of studying as-cast samples is that they exhibit significantly different grain sizes, grain boundaries, and microstructural properties compared to annealed samples. Although the overall composition is the

same (total amounts of uranium and aluminum), it is these changes that influence oxidation and therefore need to be studied independently. In the arc-melter, a sample solidifies in approximately 15 minutes which produces an as-cast microstructure with solidification defects such as voids and cracks. The consequences are that grain sizes are smaller in as-cast samples and grain boundaries are less developed i.e. high-energy grain boundaries more prominent in as-cast samples, and solute segregation or aluminum along grain boundaries) is also a common attribute.

This experiment on as-cast samples is to study aluminum-grain boundaries in particular. Identified in the previous experiments is that grain boundary oxidation plays an important role in the oxidation of pure UAl_3. Grain boundary properties such as impurities and second phases along the boundary has been known to affect oxidation and corrosion properties of metals [19-23]. The effects of these phases on UAlx alloys is not available in the literature. Here, the effects of aluminum phases present at the grain boundaries, on the oxidation of as-cast UAl_3 is presented.

3.2.1 Sample preparation and characterization

An EDX analysis of the ingot surface is presented in Figure 15. The area labeled “Point 92” indicates that the majority of the ingot was UAl_3. An analysis at Point 93 show that the triple junctions, and the grain boundaries, are rich in aluminum and has a discrete phase present. Finally, uranium rich phases appear throughout the ingot, indicated at point 94.

Due to the variation of microstructure across an as-cast sample, there are many different types of fuel particles that can be made from this ingot. Four different fuel particles have been categorized based on the type of grain boundaries (discrete phase on grain boundary or well defined[8]), if there are phases of UAl_2 present, and how large the fuel particle is. The following sections defines these fuel particles from an as-cast ingot and how they oxidize in a digestion bath.

[8] Well defined grain boundary means in this context, is a grain with little to no discrete phases at the boundary. It is where two crystalline grains meet. “well defined” is a reference to the grain’s crystallinity.

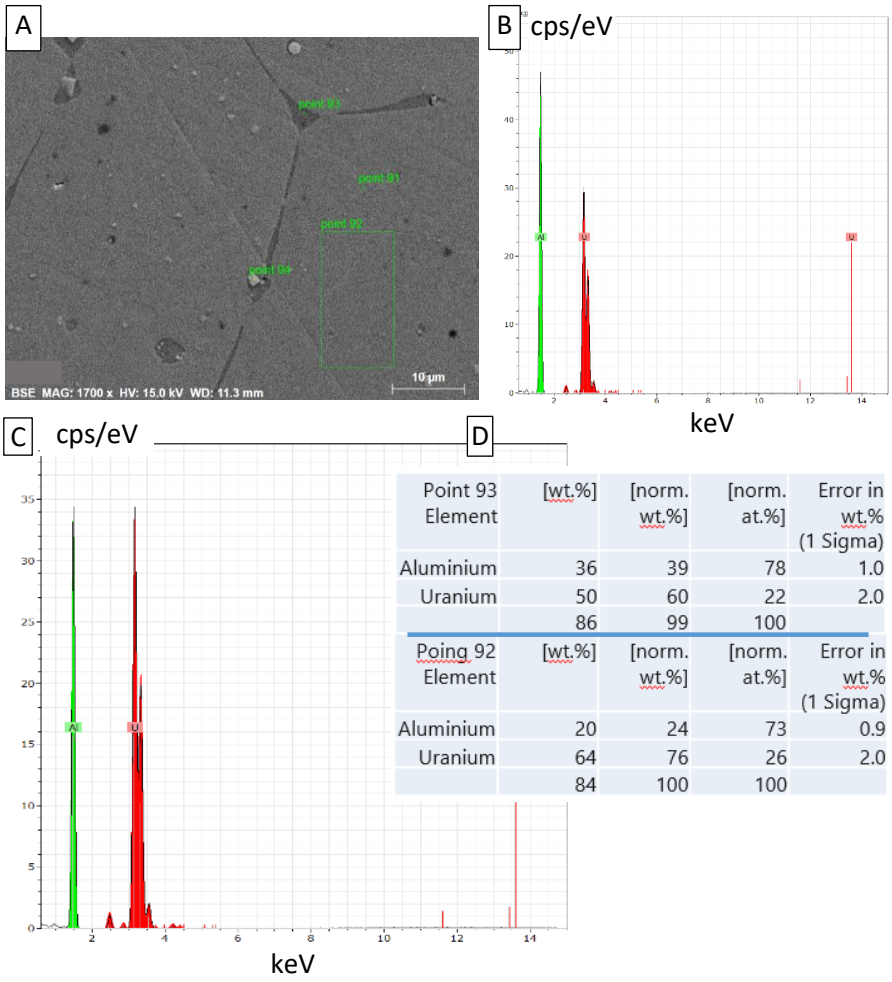

Point 93 Element	[wt.%]	[norm. wt.%]	[norm. at.%]	Error in wt.% (1 Sigma)
Aluminium	36	39	78	1.0
Uranium	50	60	22	2.0
	86	99	100	

Poing 92 Element	[wt.%]	[norm. wt.%]	[norm. at.%]	Error in wt.% (1 Sigma)
Aluminium	20	24	73	0.9
Uranium	64	76	26	2.0
	84	100	100	

Figure 15) EDXS analysis of As-cast UAl_3 ingot. A; BSE image of the as-cast surface, with labels of areas taken for EDXS analysis. B;EDX spectrum of point labeled 93. Uranium is indicated in red and aluminum is indicated in green. C; EDS spectrum of point labeled 92. D; results of the EDS analysis for point 93 and 92. An area analysis labeled "Point 92" shows the majority of the ingot is UAl_3. Point 93 shows a discrete phase at the triple junction and along the grain boundaries. Point 94 corresponds to a phase of pure uranium.

Type 1) well defined GB

Type one particles in as-cast fuel have GBs that are visible due to channel contrasting. These samples are likely to have originated in the center of the button or ingot. Figure 16 shows type one particle with well-defined grain boundaries and triple junctions. Additionally, some UAl_2 phase is present in this cross section. This particles are similar to annealed samples in appearance.

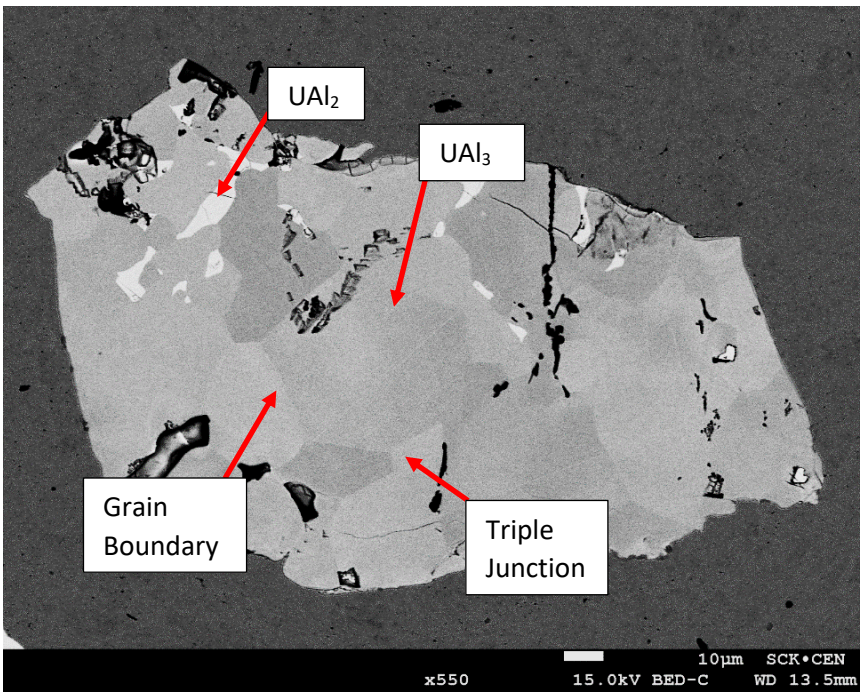

Figure 16) BSE image of a type one particle of an as-cast sample. Grain boundaries are visible through channel contrast. UAl_2 phase is visible as light regions. Voids and cracks are visible as darker regions.

Type 2) Aluminum phase at Grain Boundaries

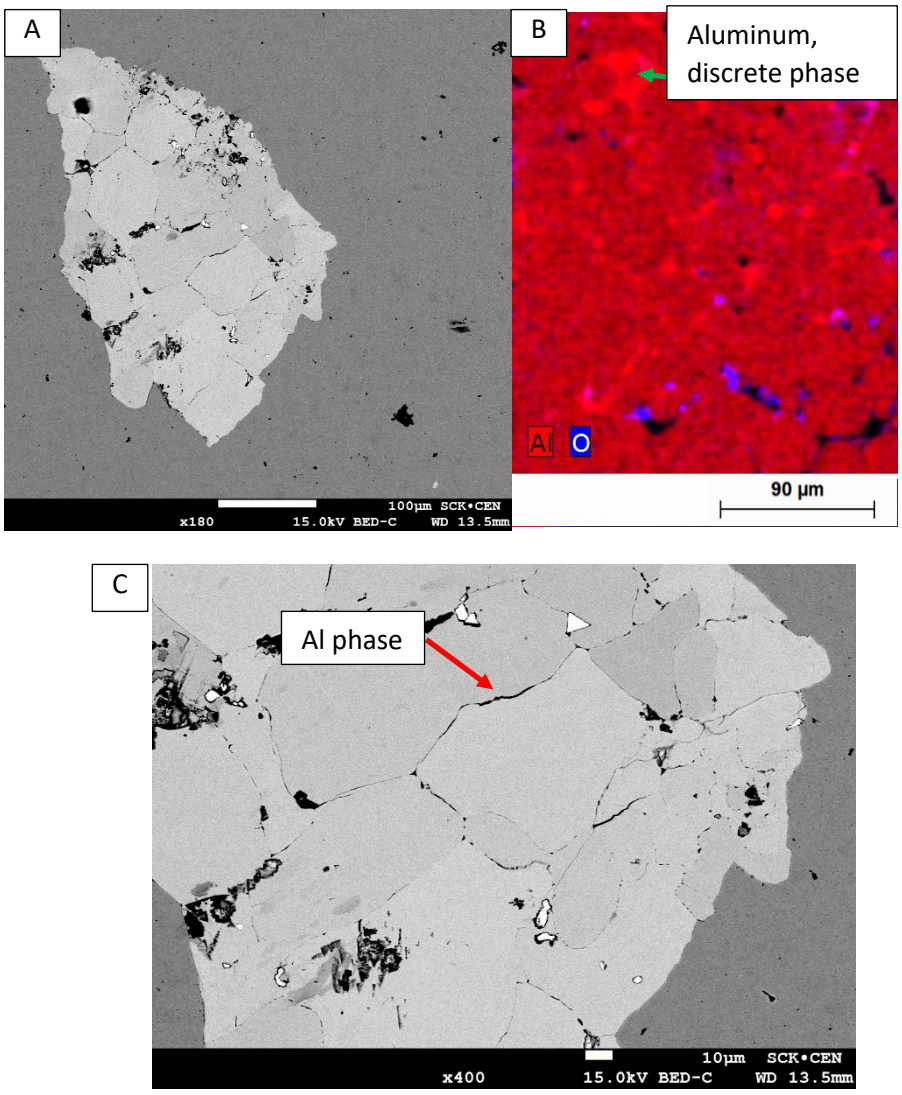

Figure 17) A; BSE image of a Type 2 particles with an aluminum rich, discrete phase at the grain boundaries. B; EDS elemental map, with oxygen in blue and aluminum in red. C; close up of image A, with indicated discrete phase.

Another prominent group of particles have a discrete second phase at the grain boundaries. In these particles, the grain boundaries did not have time to form and the grain boundaries are rich in aluminum forming a second phase. This is demonstrated in Figure 17, showing a BSE image of a UAl_3 particle. In this particle, grain boundaries are clearly visible as a dark line.

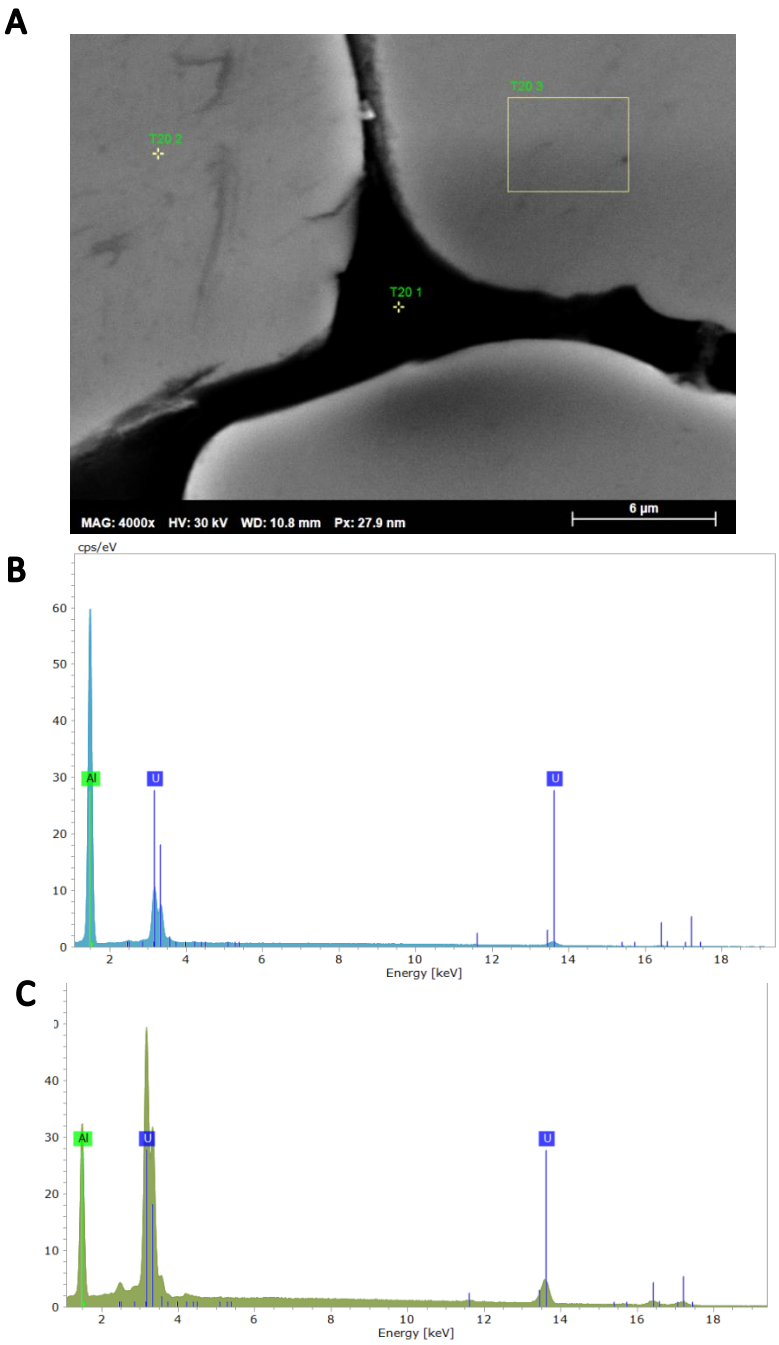

Figure 18) Analaysis of the discrete phase present at grain boundaries taken at 30kV accelerating voltage, probe current of 11. A- BSE image of the the aluminum phase at the boundaries and junction. B – EDX spectrum taken from the center of the junction labeled T20 1 with a dwell time of 10 min. C – EDX spectrum taken on the interior of a UAl_3 cell, labeled T20 3 with a dwell time of 20min.

This is in contrast to particles like in Figure 16, where GBs are marked by the meeting of two different shades of gray.

An examination through EDXS of the discrete phase is presented in Figure 18. A BSE image is presented focused on a junction and grain boundaries with the discrete boundary phase present. An EDX point analysis is taken at the center of the junction, with an acceleration voltage of 30kV, probe current of 11µA, and a dwell time of 10 minutes, and is presented in Figure 18 B. The composition of this point is 95±2 at%Al, 5±1 at%U. An EDX spectrum is taken of the interior of the grain and is presented in Figure 18 C. The composition was found to be 24±2 at% and 75±1 at%Al, or UAl_3. This analysis indicates that the phase present at the grain boundaries is aluminum. It is unknown if the uranium is actually present in this phase due to uncertainty in the special resolution of this technique. Further experimental evidence is needed to confirm the exact nature of the phase presented here. For the remainder of the thesis, it will be referred to a discrete aluminum phase at the grain boundary.

Type 3) Cross section mixed with UAl_2 and UAl_3

Type 3 particles (Figure 19) have a significant fraction (above 10%) of UAL_2. As discussed in (sec 3.1.4), these particles will have different characteristics due to the difficulty of digesting UAl_2. As-cast mixed particles digested will be

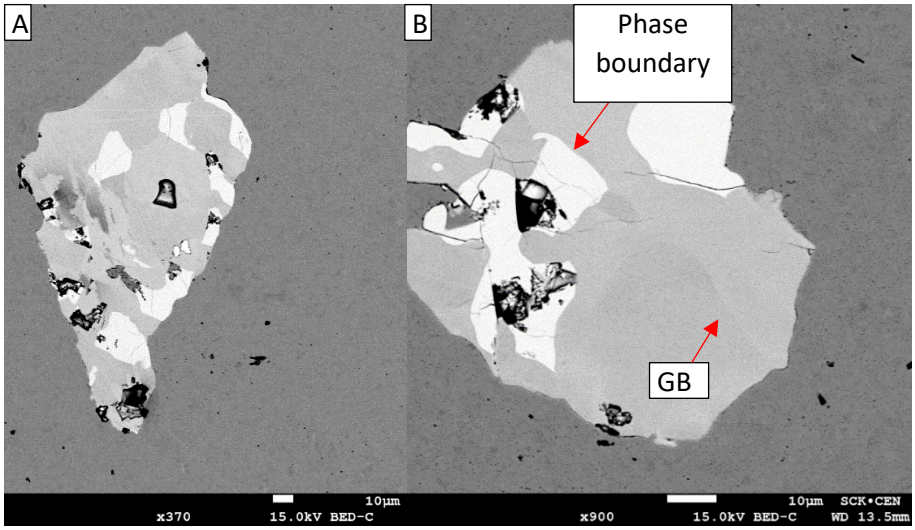

Figure 19) BSE imagees with a discrete second phase. Type 3 particles with UAl_2 present in the cross section.

monitored in the same way as annealed samples. These particles can have phase boundaries (UAl_2-UAl_3), grain boundaries (UAl_x-UAl_x) and triple junctions composed of any combination thereof. The surface of these particles will have regions of exposed UAl_2 or UAl_3 as well. Type three particles are unique in that the effects of mixed phases on the oxidation of UAlx can be studied.

Type 4) Large particles with FD> 100µm

In this experiment, many samples of significantly large particles were studied. These particles are designated as having a Feret diameter significantly larger than 100 µm. The goal in studying these particles is to see if there is a penetration depth limit of oxidation at TJs and BGs. Previously, this limit was never reached, as all particles imaged had oxidized TJs (at 30 minutes) and GB (at 60 minutes).

An aspect to consider with large as-cast particles is that they contain variations in the as-solidified microstructure, possibly due to the variation of the cooling rate. Figure 20 shows a typical large particle. The right area of the particle Figure 20 B shows a second phase at the grin boundaries with significant amounts of aluminum. There are more developed GBs, although still some second phase occurs. The effects of a second GB phase can therefore be analyzed at the same time in the same particle.

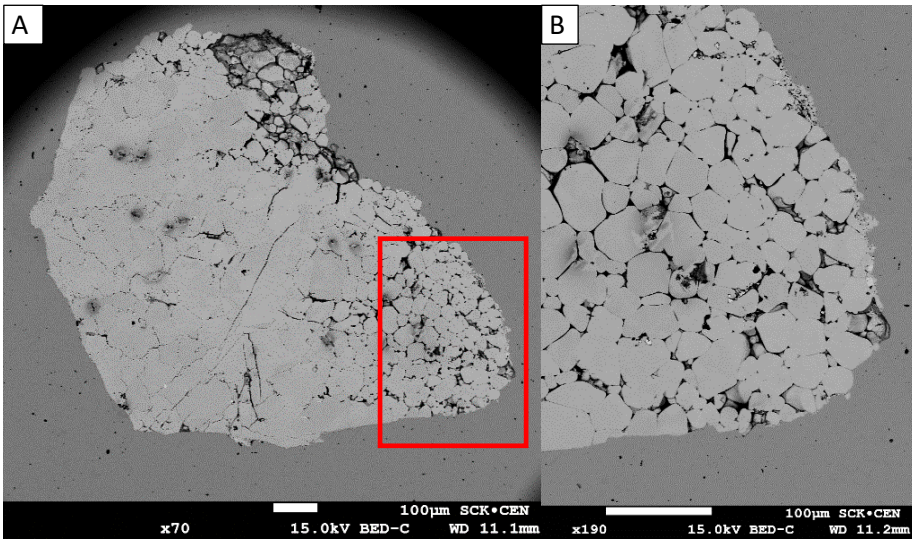

Figure 20) A) BSE images of a Type 4 particles of cross sections with FD> 100µm. B) Focused section with second phase along GBs.

3.2.2 Digestion – Experiment 2

3.2.2.1 Small particles – 20 minutes of digestion

At 20 minutes of digestion, cross sections with Feret diameters less than 40 µm were significantly digested. Figure 21A, demonstrates a cross section with a FD of 32.5µm were 94.8 of its area is oxidized and Figure 21 B demonstrates a cross section with a FD of 53.1 µm were 74.2 percent of the area is oxidized. An average of 17 "fine" or small FD (22-34µm) had a 90±7% average area of oxidation. The area of oxidation for larger particles significantly varies, as discussed in more details below.

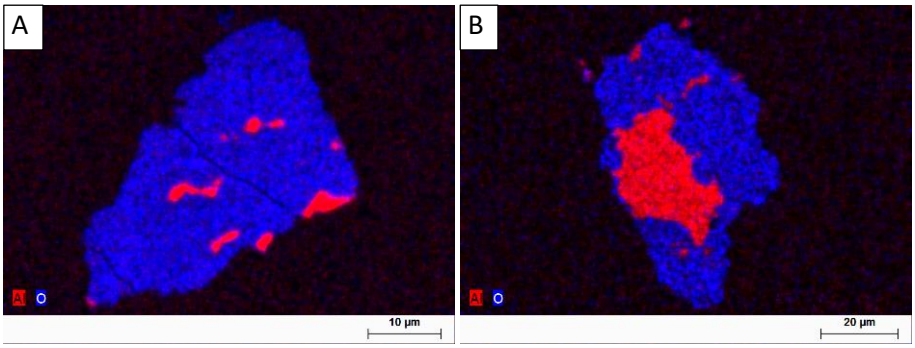

Figure 21) EDXS elemental maps of digested particles of small cross section at 20 minutes.

3.2.2.2 Large Type 4 Particles – 20 minutes of digestion

A large particle containing different grain boundary characteristics was digested for 20 minutes. Figure 22 A shows a BSE image of a particle with a Ferret diameter >>100µm. Top edge has well defined GBs (Figure 22C) while the bottom edge has aluminum present at its boundaries (SS GB) Figure 22 D. The elemental mapping of this particle Figure 22B showing the aluminum rich, second phase GBs on the left of the oxidation front, and oxidation to the right of the oxidation front.

Here, the effects of GB characteristics can be compared directly. The oxidation front has penetrated the large particle by about 200µm through the aluminum GB side, while almost no internal oxidation is evident in the well-developed GB region. Surface oxidation is visible in both regions of the particle (Figure 22 B). In the oxidation region, the area fraction that is oxidized is 16.7% (Figure 3 D). This particle again demonstrated the limitations of surface oxidation or a shrinking-core model. Although surface oxidation is the dominant form of oxidation during the first 10 minutes of digestion, its penetration depth is halted after a few micrometers. Surface

oxidation may be the only form of oxidation for small particles or particles that are not polycrystalline or without grains and GBs. However, to efficiently digest large particles, its network of grain boundaries are its primary mode of digestion.

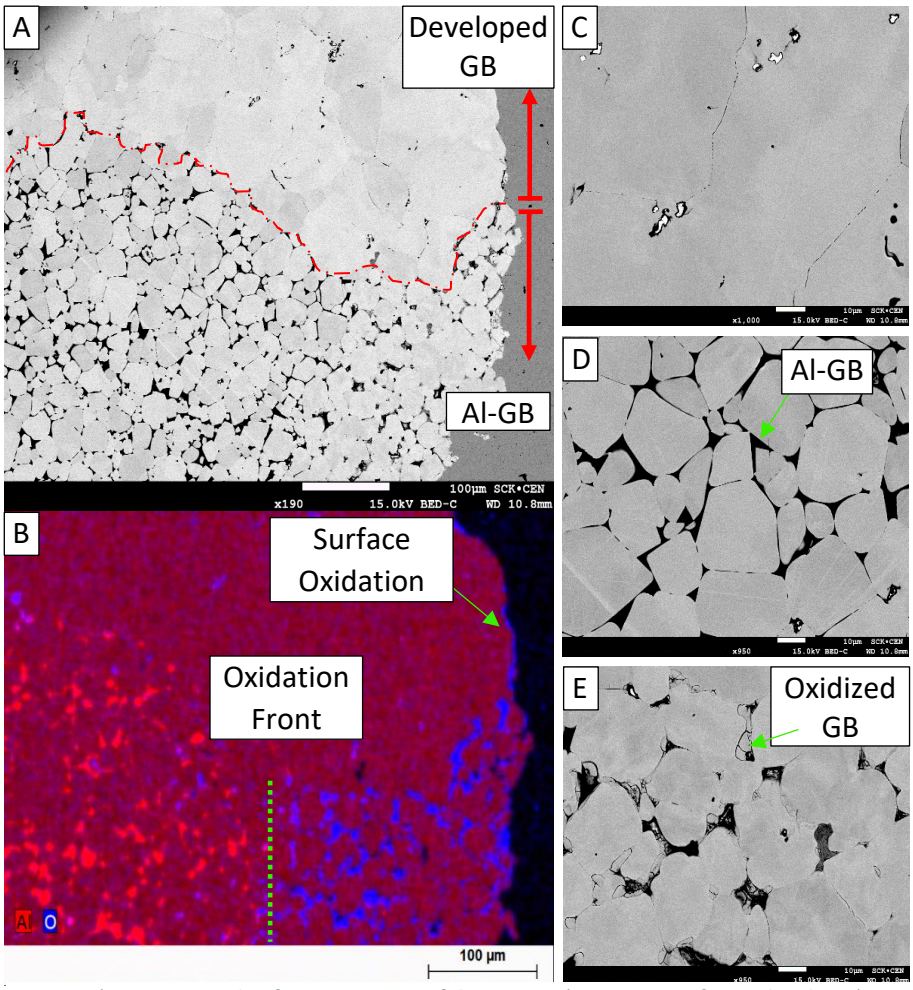

Figure 22) Type 4 particle after 20 minutes of digestion. A) BSE image of particle edge B) EDS mapping of the particle presented in A. Oxygen is seen in blue and Aluminum in red. C) Area of particle with well-defined GB. D) area of particle of aluminum rich GB. E) area of particle with corroded or digested GB.

3.2.2.3 Particles at 30 minutes of digestion

Because as-cast particles have a variation in microstructure, their digestion patterns start to very significantly after 20 minutes. Figure 23 shows three different particle types, all digested for 30 minutes. Of the same particle,

Figure 23 A and B shows a BSE-image and an EDX elemental map respectively. All triple junctions have been attacked with some connecting through a grain boundary. This is similar to the digestion of annealed samples at 30 minutes (Figure 11). Surface oxidation is presented in Figure 23 C where two aluminum cores surrounded by an oxidized layer. These cores do not have GB or TJs, and the oxide layer never goes exceedingly past 10µm. Again, this oxide layer resembles the thickness found at 10 minutes of digestion or longer (Figure 21 B, Figure 8 C, and Figure 10). Finally, Figure 23 D shows a particle that is a type 3 particle, mixed with UAl_2. Unlike Figure 23 B, this particle only shows surface oxidation and only along the UAl_3 phases. The surface oxidation layer of this particle also abruptly stops once it reaches a UAl_2 phase. Internal oxidation is not found in this particle despite having the same digestion time.

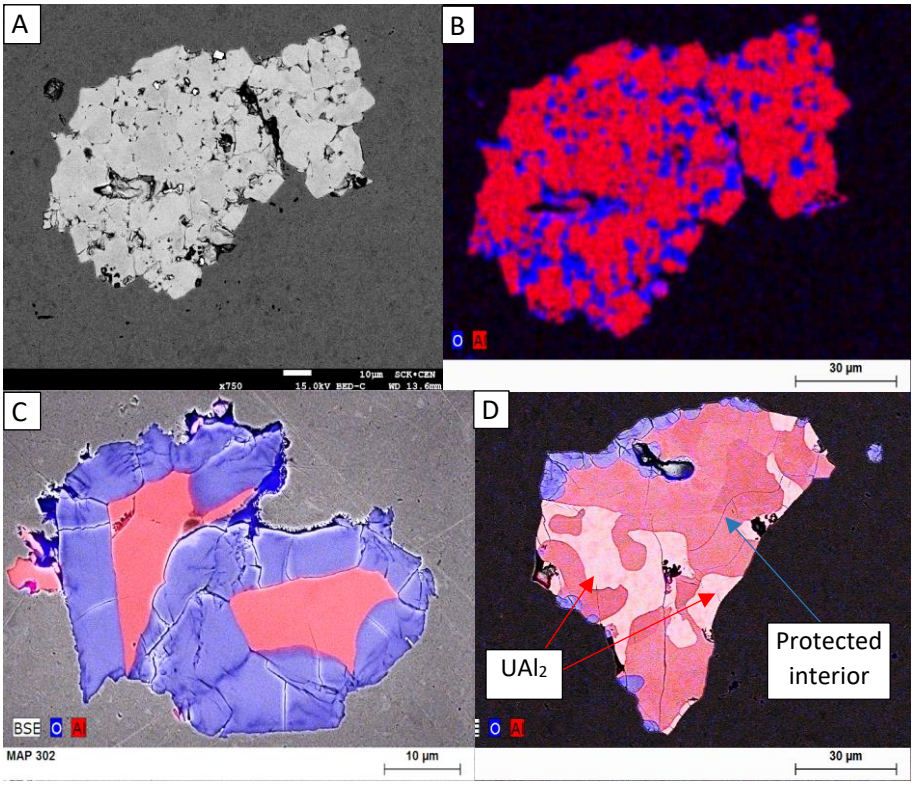

Figure 23) Particles after 30 minutes of digestion A) BSE image of digested particle with its elemental EDX map B. C) Fine particle with surface oxidation. D) BSE-EDS compositve image. Particle with UAl_2 phase and protected GB network.

3.2.3 Discussion – Experiment 2

Presented here is the digestion results of as-cast UAl_3 particles. There are many significant differences in the rate of digestion when compared to as-cast samples in experiment 1. In as-cast samples, the oxidation front along boundaries with a second phase can penetrate over 100µm into the fuel particle at 20 minute (Figure 22 B). In the same concentration and at the same digestion time, fuel particles of annealed samples were beginning the second phase of TJ digestion. Second phase boundaries are not found to undergo a separate TJ oxidation phase but instead, the oxidation front proceeds along GB and TJ at the same time. UAl_2 phases were again found to protect the interior of the particles and surface oxidation was again found to only penetrate the first few microns of the particle.

The results presented here add to a body of literature on the effects of an impurity or second phase and intergranular oxidation. Although this effect is studied to help improve metals against oxidation [19-23], this would be an instance where it should be used to enhance oxidation. As the objective is to convert uranium aluminides into oxides to release isotopes, then it would be advantageous to have altered GBs in isotope production targets. As-cast fuel is a way to achieve this effect and would reduce the production time of the fuel. Adding a hyper-stoichiometric amount of aluminum might also achieve a similar results. However, the formation of UAl_4 would also develop. The effects of UAl_4 on digestion is explored in a separate chapter (see also appendix II).

3.3 Experiment 3: Digestion of annealed UAl_3 in 8M NaOH

In this experiment, digestion was performed on annealed UAl_3 particles with double the amount of sodium hydroxide, at 8M NaOH. This digestion was performed to evaluate the concentration effect on the oxidation of UAl_3. The concentration of reagents, temperature, particle and grain sizes, are variables that are responsible for the digestion time. In the previous experiments, oxidation of UAl_3 was not complete after 90 minutes (Figure 13), despite digesting at the same concentration and temperature reported in literature [2]. The reason for this discrepancy is unclear. The effects of microstructure is discussed in this chapter and the following two chapters. However, a difference in the digestion solution is investigated in this experiment

3.3.1 Digestion – Experiment 3

3.3.1.1 Surface oxidation

The early oxidation stages of UAl_3 particles in an 8M solution of NaOH resembles the early stages of digestion at 4M NaOH. In particles that were digested for up to 10 minutes, only surface oxidation occurred. Figure 24 shows UAl_3 particles digested for 3, 5, and 10 minutes at 8M NaOH. At 3 minutes, the oxide layer reaches a mean thickness of 1.38±0.5µm, at 5 minutes the mean thickness is 2.0 µm ±0.64 µm, and at 10 minutes the mean

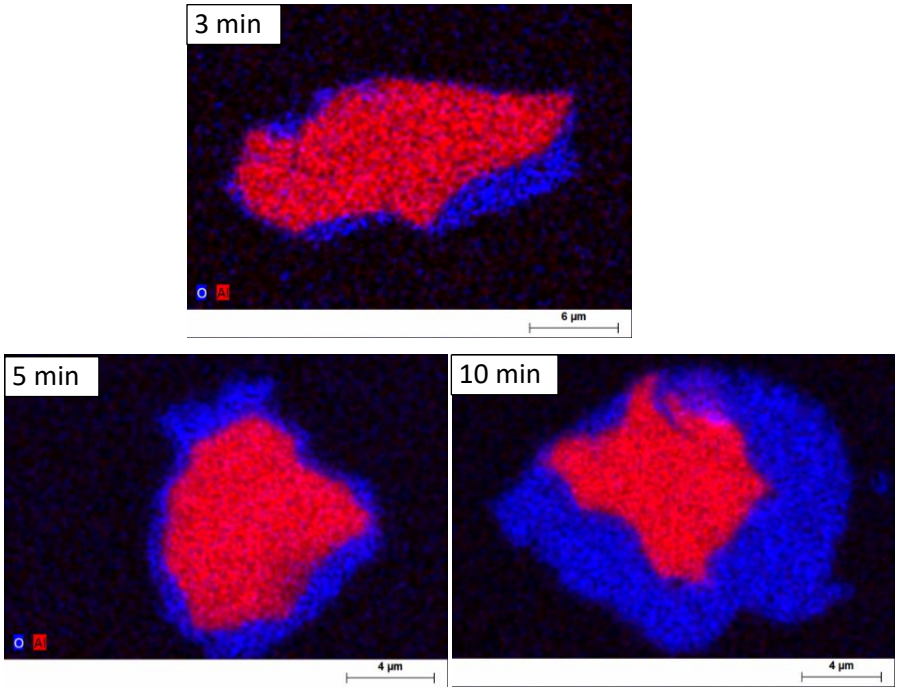

Figure 24) EDS maps of digested UAl_3 particles at 3, 5, and 10 mintes of digestion. Oxygen is indicated in blue and aluminum is indicated in red. The surface oxide layer develops and is measured in figure 25.

thickness is 3.66±1.3 µm. In comparison to fuel particles that were digested at 4M NaOH, the growth rate of the oxidation layer was twice as fast for the first 5 minutes. However, the surface oxide thickness approached the same thickness after 10 minutes Figure 25

T= 3 minutes
4M NaOH) Mean =0.87µm STD = 0.29
8M NaOH) Mean = 1.38 µm STD = 0.45
T= 5 minutes
4M NaOH) Mean = 1.39 µm STD = 0.52
8M NaOH) Mean = 2.03 µm STD = 0.645
T= 10 minutes
4M NaOH) Mean = 3.21 µm STD = 1.02
8M NaOH) Mean = 3.66 µm STD = 1.35

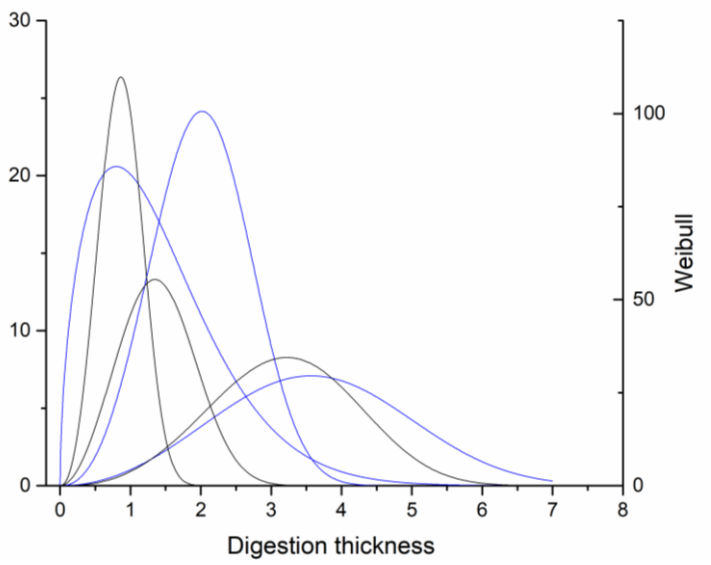

Figure 25) Comparison of oxide thickness of fuel particles at 3, 5 and 10 minutes and with 4M and 8M NaOH.

3.3.1.2 Final digestion products – filter cake analysis

An analysis was made of the filter cake after 90 minutes of digestion. Figure 26 shows an XRD diffractogram of the filter cake, along with an EDX map of a large digested fuel particle. Both XRD and EDX maps show that even very large particles were digested to completion. Additionally, the particles were not UO_2, but they had developed fully into $Na_2U_2O_7$. This is a huge contrast

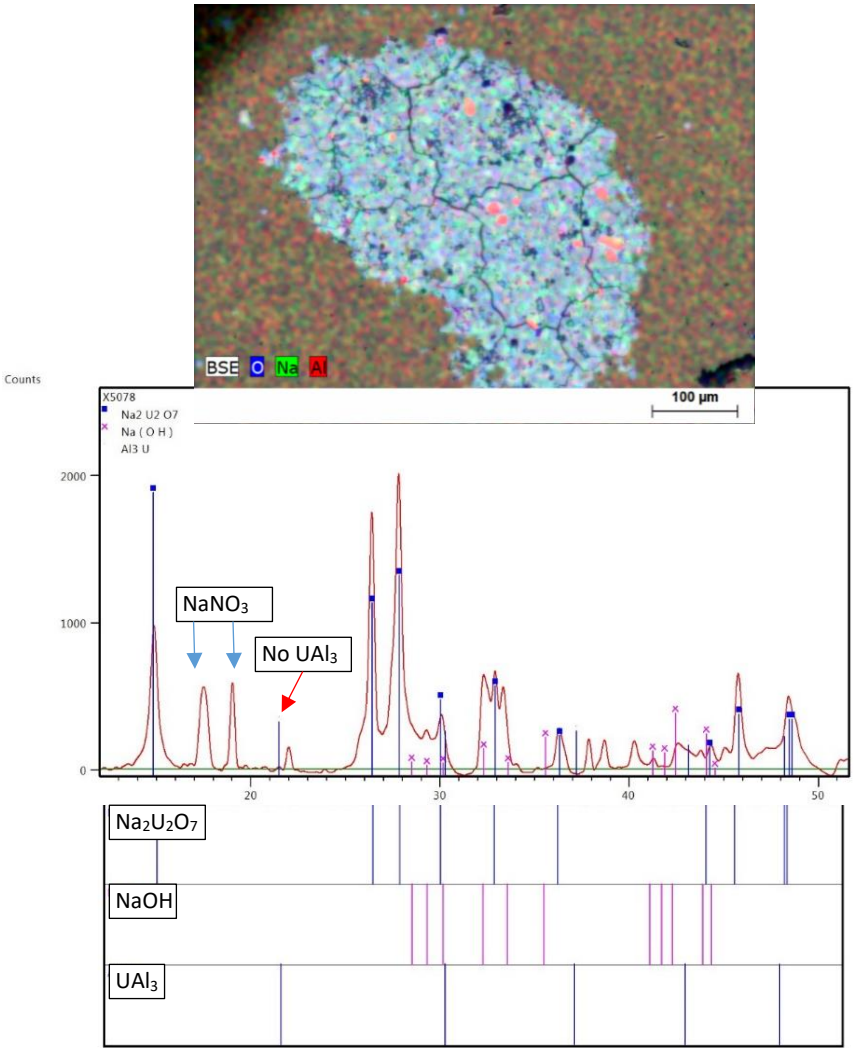

Figure 26) Above; combined EDX map of large digested fuel particle after 90 minutes of digestion, 8M NaOH. 20kv accelerating voltage, 13 probe current, 4hr acquisition time. Oxygen is indicated in blue, sodium in green, and aluminum in red. The EDS map is superimposed on a BSE image. Below; XRD of filtercake indicating $Na_2U_2O_7$, NaOH, and UAl_3

to particles that were digested with 4M NaOH, where the UO_2 phase present, even after a 90 minutes of digestion.

3.3.2 Discussion – Experiment 3

Although standardly, a concentration of approximately 3M or 4M NaOH is used to digest UAlx targets and yields $Na_2U_2O_7$ as yellow cake, the experiments here failed to fully digest UAl_3 fuel in 4M NaOH and within 90 minutes. There are many possibilities that can explain this discrepancy. A major notable discrepancy is that these experiments were digesting pure UAl_3 fuel without any cladding. The dissolving of the Al6061 is extremely exothermic (close to 600 kcal is generated for dissolving 100g Al)[2] and that energy could speed up the digestion process of the fuel. The digestion of UAl_4, that is in the meat as well, is also likely to give off an excess energy that could help speed up the digestion process.

The digestion of UAl_3 in 8M concentration of NaOH on the contrary, was very successful. Even large very large particles (FD>>100µm) were fully digested. The accompanying XRD scan also shows the successful conversion of UAl_3 to $Na_2U_2O_7$ (Figure 26). The concentration of reagents seems to be important for digesting large particle within 90 minutes, but small particles (FD≥ 40µm) seem to be digested by either 4M or 8M concentration of NaOH within 90min.

What is also unclear, is exactly when UO_2 converts to $Na_2U_2O_7$. The detection of UO_2 is evident at least up to 30 minutes of digestion, but the conversion to $Na_2U_2O_7$ seems to be abrupt. The experimental techniques here are clearly not suitable to detect the transition and would perhaps require an *in situ* XRD experiment. The EDX mapping alone is not sufficient as well, as it is not a quantitative technique, especially with light elements such as sodium.

4 Discussion – towards optimized digestion of UAl_3

4.1 Oxidation behavior and junction classification in UAlx fuel

The oxidation behavior of UAl_3 has been studied as a function of time to determine what mechanisms of oxidation are active during its digestion. As is presented through the present studies, fuel particles undergo surface oxidation for the first 10 minutes (Figure 8), oxidation at TJs (Figure 11) followed by GB oxidation (Figure 12).

It has been established that the grain boundary degradation phenomena take place as a percolation process in the network of high energy random boundaries in polycrystalline materials. Therefore, the percolation-controlled intergranular oxidation can be suppressed by the connectivity of intergranular degradation-susceptive random boundaries, and suppressed by the elimination of voids and intraparticle cracks. It has been demonstrated that a fraction of 50%-75% of percolation-resistant low-Σ CSL boundaries is required to interrupt the network of degradation susceptible random boundaries.

In literature [24], the maximum random boundary connectivity (MRBC) is determined in materials to find the threshold at which a oxidation front can fully penetrate the system. The types of junctions are classified in terms of the connectivity of low-Σ coincidence site lattice (CSL) to random orientated GB (R) as the following (Figure 27): (1) R0 type with no random boundaries, (2) R1 type with 1 random boundary and 2 CSL boundaries, (3) R2 type with 2 random boundary and 1 CSL boundaries and (4) R3 type with 3 random boundaries. In Figure 27, MRBC is composed of R2 and R3 type tripple junctions.

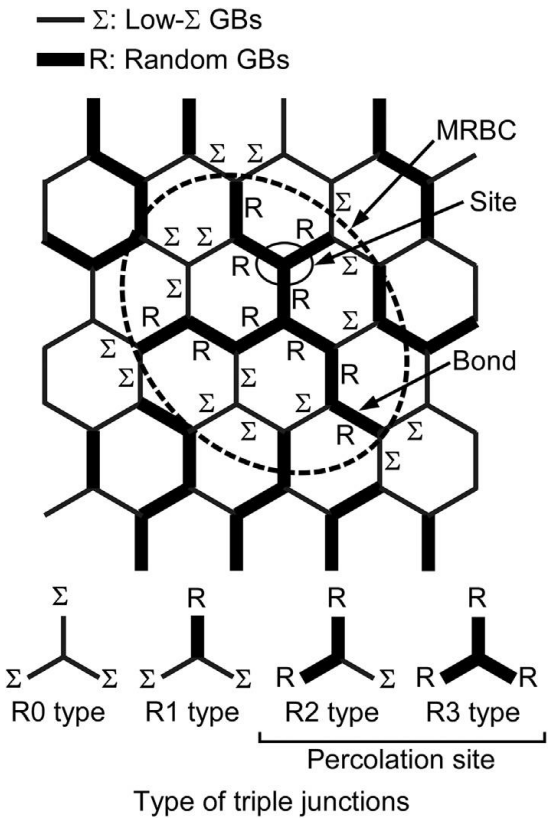

Figure 27) Definition of four different types of triple junctions in terms of the percolation probability based on the maximum random boundary connectivity [10]

For the digestion of UAl_3 with UAl_2 as an impurity, there are additional considerations for maintaining a percolation network. In the table below, new junction types are considered for the materials digested in this study. Specifically, UAl_2 is seen as the equivalent to two low-CSL boundaries, while aluminum-grain boundary is also considered to be a "random" grain boundary, in that it oxidizes in the same way, if not more efficiently, than a random grain boundary (Figure 22). For the fuel described in this chapter, boundary types can be classified in the following way: (1) protected R0 type with three UAl_2 phases and no UAl_3 phase, or two UAL_2 phases and one UAL_3 phase. (2) Termination pattern where Al-GB or R grain boundary meets a UAl_2 phase. A pathway R2 type where two of the positions are either R or Al-GB, and R3 type were all three boundaries are either R or Al-GB in character.

Here, the difficulty in digesting UAl_2 itself is not only the problem, but also that it prevents a percolating pathway, or neighboring GB and TJs for oxidation. As surface oxidation is very limited for UAl_3 particles, this can have significant consequences.

Classification	Group	Junction Type
Protection pattern R0 Type	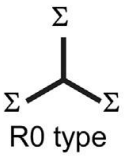	
Terminal pattern R1 type	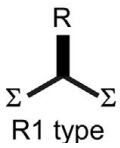	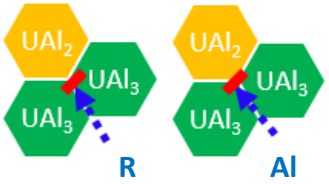
Pathway pattern R2	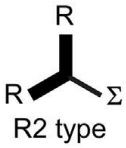	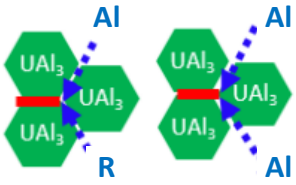
Un-obstructed pattern R3	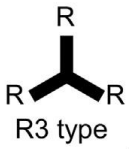	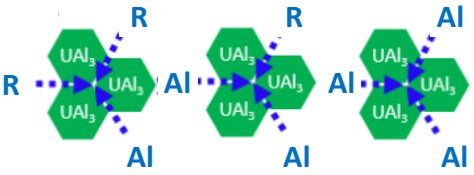

Figure 28) Classification of junction types in UAlx in correlation to classical junction types. R0 – protection pattern. R1 – Terminal Pattern. R2 – Pathway pattern. R3 – un-obstructed pattern

4.2 Optimally designed grain boundaries for the controlled oxidation properties of UAlx Alloys

The oxidation properties of UAlx fuel as a function of its GB and TJ properties is considered and can be used to strategically engineer UAlx alloys for digestion environments. Figure 29 demonstrates two particles that have been digested in a 4M solution of NaOH for 120 minutes in a 95^{o}C bath, featuring different oxidation properties. Design type A is an oxidation resistant design with R0 and R1 type triple junctions. This alloy only undergoes surface oxidation with a thickness of 10µm. This oxidation layer is the same thickness as is observed in particles that have been digested for 10 minutes (Figure 8 C and D). The majority of TJs and GBs are preserved. In contrast, a type B alloy (Figure 29 B) is designed to be oxidation susceptible. This design is, for example, favorable for a ROMOL-99 digestion process that is used to convert UAlx into UO_2 and finally into $Na_2U_2O_7$. This particle originally has R3 type junctions composed of Al-grain boundaries or random grain boundaries. The penetration depth of oxidation here is around 90µm. Notably, this is in the same range of oxidation depth as a particle digested for 20 minutes (Figure 22). This can be an indication that, oxidation via aluminum-GBs also has its limitations and that this oxidation pathway is less efficient after about 90µm. As UO_2 develops at the GBs, the transport of the driving reagent along these paths could become inhibited.

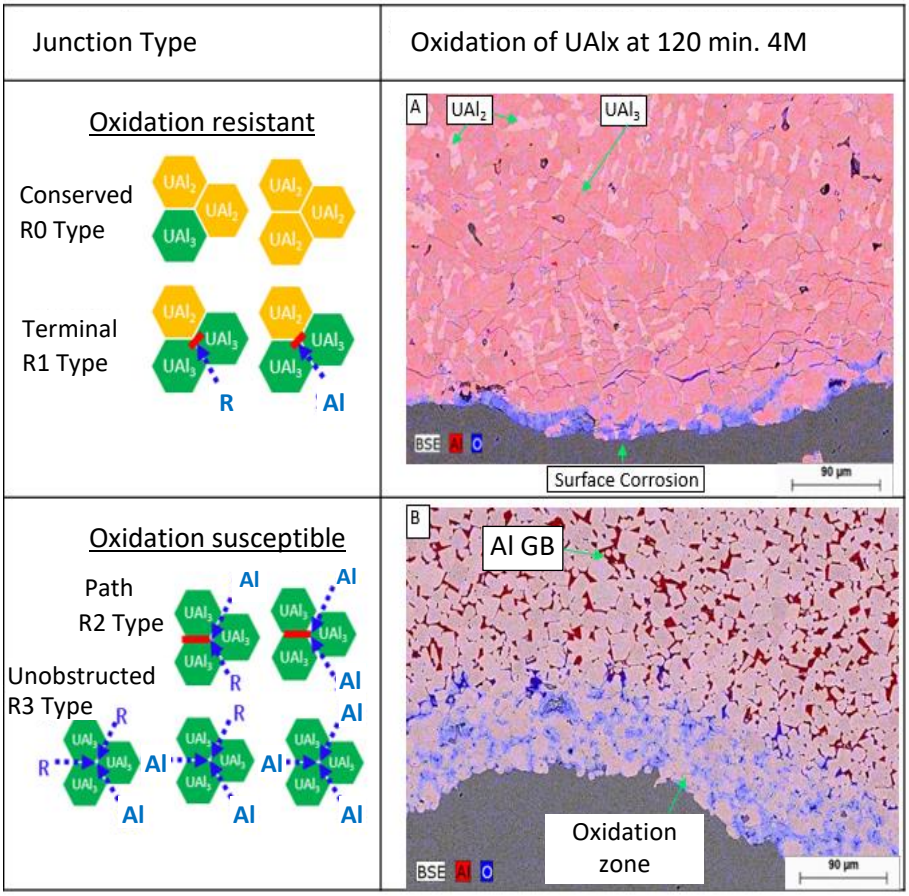

Figure 29) Fuel performance in caustic media is influenced by phase type and boundary type. Oxidation resistant UAlx fuel (A) have junction that have one or more boarders of the UAl_2 phase (in yellow). Oxidation susceptible design (B) have junctions composed of UAl_3 phases (green), and have a discrete second phase at the boundaries or have randomly orientated grain boundaries.

4.3 Strategies for the production of oxidation susceptible UAlx alloys and its successful digestion

Strategies to produce oxidation susceptible UAlx alloy should go against more traditional studies in improving materials against oxidation. In particular it would be important to decrease the fraction of low Σ CSL boundaries, a topic that is discussed in chapter 3. Also, it can focus on increasing the fraction of voids in a material, as well as intraparticle cracks. This is accomplished by not giving the polycrystalline alloy enough energy

and time for grains to form energetically stable boundaries. Once boundaries are formed, an immediate quenching would produce the most grain boundaries with random orientations and solute segregation or Al-GBs. Additionally, using an as-cast alloy or applying as little heat or annealing has an additional advantage of increasing the amount of secondary phases at the grain boundary. As is demonstrated in (Figure 22 and Figure 29) aluminum phases at GBs oxidize the most favorably compared to any other form of GB. Additionally, the effects of grain size is also discussed in chapter 3 and is included in grain boundary engineering.

The effects of particle size on oxidation can be carefully inferred on the basis of cross sections that have been imaged in this study. All cross sections of UAlx particles with a Feret diameter lower than 40µm were fully oxidized after 60 minutes, in 4M or 8M concentration of NaOH. These cross sections can represent fine particles with the equivalent Feret diameter. To digest larger particles, digestion parameters have to be optimized to ensure that the conversion of UAlx to NaDU goes to completion. For example, large particles of UAlx were able to digest in 8M solution of NaOH for 90 minutes. As surface oxidation becomes limited after 6-10 µm, strategies for intergranular oxidation become necessary for a complete digestion in addition to the concentration of reagents.

Perhaps, a better standard to abide by concerning oxidation susceptible UAlx alloys is the maximum connectivity for random boundary network (MRBC) Figure 27, and the fraction of randomly orientated GBs. To interrupt the network of degradation susceptible random boundaries, it has been found that a fraction of 50-75% of percolation resistant low-Σ CSL boundaries are required for Fe-6.5%Si alloy[24] and 70±5% for austenitic stainless steels[25]. A similar study would have to be performed to determine a tolerant threshold for the MRBC of UAlx alloys, although the complete elimination of low-Σ CSL boundaries would be optimal. Elimination of UAl_2 alone would help ensure a MRBC, not only because it is itself hard to digest, but also by reducing the amount of R0 and R1 TJs. A hyper-stoichiometric amount of aluminum should be added in making UAl_3 to help ensure no UAl_2 is present in the alloy. Additionally, this might help with the formation of aluminum phases at GBs.

4.4 Further discussion on selective oxidation

The patterns of oxidation demonstrated in this chapter, and specifically intergranular oxidation, could be an indication of an electro-chemical phenomena that underlies this chemical transformation. Specially, intergranular oxidation is normally an indication of a galvanic coupling or a microgalvanic coupling, where a potential difference between the grain boundaries and the grain interior and can facilitate an electron transfer, oxidation, and degradation. A galvanic couple can occur in between an anodic point with a “lower electrode potential” and a cathodic point or a “higher electrode potential”. In this this chapter, two sources of potential differences can be identified.

The first source of a potential difference is the aluminum phase at the grain boundary or any other precipitates that may have occurred along the grain boundaries. In most cases, intermetallic particles or secondary phases found along grain boundaries takes on the role of a cathode in relation to the surrounding matrix, which becomes the anode [26, 27]. The effect of the coupling leads to a preferential oxidation at the interface between the intermetallic particle and the matrix. The results presented in this chapter give a promising indication that this process could be occurring and would require further techniques to confirm exact nature of this intergranular oxidation. More in-depth EDXS maps could be performed to see if there are more impurities along these boundaries or if there are depletion regions surrounding them.

The second source of intergranular oxidation could be due to the different orientation of the grains that make up the boundary. The oxidation differences on boundaries can sometimes be attributed to the different anodic/ cathodic nature of differently orientated grain and to a galvanic coupling effect when they appear together in a microstructure. Depending on grain orientation at an interface, a partial anodic exchange current will be given by a grain with a lower potential while the partial cathodic exchange current will be given by the higher electrode potential[28] in much the same way that an impurity can also act as a potential difference. To confirm this phenomena, techniques such as scanning electrochemimcal microscopy (SECM) and electrochemical scanning tunneling microscopy (EC-STM) are required to evaluate local potential differences that would facilitate localized oxidation. However, in the following chapter electron backscattered

diffraction (EBSD) is used to identify patterns in grain orientation and preferential oxidation within UAl_3 samples.

5 Conclusion

The current understanding of the digestion of UAl_2 and UAl_3 to extract isotopes is limited. Until now, it was assumed that the conversion of this material into an oxide was a surface reaction making the particle size, surface area, Feret diameter, and shape factor an important focal point in target production. The importance of having a high fraction of small particles (diameters below 40μm) and minimizing the amount of UAl_2 are currently the main strategies to produce targets suitable for chemical break down. An analysis of the digestion of targets is an examination of the final ^{99}Mo yield and the resulting yellow cake that is filtered from the solution.

The results presented here is the first demonstration of UAl_3 converting into an oxide as a function of time and how the microstructure of the material plays a central role in this process. The digestion as a surface reaction is only valid for the first stage of the reaction, which lasts for the first 15 to 20 minutes in standard ROMOL99 conditions. Beyond this amount of time, this model is not valid as the particles undergo intergranular oxidation (Figure D). Specially, oxidation of TJs represent the next stage of digestion followed by the oxidation of GBs. Engineering particles that undergo intergranular oxidation demands a different set of rules to be considered, to makes these particles more digestible. The results here demonstrate that the density of TJ, grain sizes, and types of grain boundaries are more likely to play an important role in digestion than surface area. This topic is discussed in chapter 3.

The results here further demonstrates the impact of impure phases, such as UAl_2 and other secondary phases have on the digestion of a particle as a whole. As it was unknown that GB oxidation played a central role in digestion, it was also unknown that UAl_2 prevented its neighboring network of GBs from oxidation. Functioning like a dam, the impact of UAl_2 on the network of GBs makes this phase much more problematic than previously known. The volume of material that goes undigested could reach at least one to two TJs away from a UAl_2 phase making the total loss in extraction more than the amount of isotopes present in the UAl_2 phase alone. On the other hand, Al-GBs outperform regular grain boundaries and function like an open valve.

The used of having secondary phases in UAlx fuel is not reported in open literature but it is demonstrated to decrease the digestion time of a particle.

Finally, the classification of junction types to promote or prevent oxidation gives developers tools to design fuels that suits their needs in a strategic manner. R0 and R1 type junctions can be used to make oxidation resistant fuel while R2 and R3 type junctions can be used to make fuel susceptible to digestion and isotope extraction (Figure 29). Although this classification has demonstrated that the oxidation properties of UAl_3 can be controlled it must be further developed. For R1-R3 junction types, a random "R" grain boundary can be at least one GB that forms the junction. In the following chapter 3, a random grain boundary is further defined as a high angle grain boundary with certain conditions. Furthermore, there are two GBs that are oxidation resistant. Oxidation resistant grain boundaries will reduce the junction number by 1 (e.g. R3 to R2). In general, the junction classification system provided here must be developed further but is demonstrated to be a working principle in designing UAl_3 with predictable digestion properties.

References

1. *Non-HEU production Technologies for Molybdenum-99 and Technetium-99m.* IAEA Nuclear Energy Series, 2013(No.NF-T-5.4).
2. Muenze, R., et al., *The Fission-Based 99Mo Production Process ROMOL-99 and Its Application to PINSTECH Islamabad.* Science and Technology of Nuclear Installations, 2013. 2013: p. 1-9.
3. Kaminski, M.D., *Aqueous Corrosion of Aluminum-Based Nuclear Fuel.* ANL-CMT-03/1, 2003: p. 133.
4. Openshaw, P.R. and L.L. Shreir, *Oxidation Of Uranium-Aluminum Intermetallic Compounds I. Kinetis Studies.* Corrosion Science, 1963. 3: p. 217-273.
5. Openshaw, P.R. and L.L. Shreir, *Oxidation of Uranium-Aluminum Intermetallic Compounds II, Nature and Surface Topography of Oxide Films.* Corrosion Science, 1964. 4: p. 335-344.
6. Lee, S.-K., G.J. Beyer, and J.S. Lee, *Development of Industrial-Scale Fission 99Mo Production Process Using Low Enriched Uranium Target.* Nuclear Engineering and Technology, 2016. 48(3): p. 613-623.
7. A. V. Gelis, et al., *ANL progress in developing an leu target and process for mo99.* RERTR 2003, 2003.
8. Mondino, A.V., M.V. Wilkinson, and A.C. Manzini, *A new method for alkaline dissolution of uranium metal foil.* Journal of Radioanalytical and Nuclear Chemistry, 2001. 247(1): p. 111-114.
9. *Gmelin Handbook of Inorganic Chemistry U Supplement Volume B2 Alloys.* 1989: p. 333.
10. Giessen, B.C., *Developments in the structural chemistry of alloy phases*. 1969: Springer.
11. Thümmler, F., H. Lilienthal, and S.J.P.M. Nazaré, *UAl2-Al INSTEAD OF UAl3-Al IN FUEL-ELEMENT PLATES FOR ADVANCED TEST-REACTORS.* 1969. 12(23): p. 1-22.
12. Thümmler, F., S. Nazare, and G.J.P.M. Ondracek, *THE TECHNOLOGY OF UAl3–Al IRRADIATION TEST-PLATES.* 1967. 10(20): p. 264-287.
13. Davis, N.E., *Modeling the oxidation surface reaction on uranium metal*. 2013, University of Illinois at Urbana-Champaign.
14. Conturbia, G.R. and M. Durazzo, *Study of Thermomechanical Treatment for Manufacturing UAlx/Al Dispersionn Targets.* RRFM Conference Proceedings, 2017.
15. Wymer, R., R.J.I. Blanco, and E. Chemistry, *Uranium-aluminum alloy dissolution.* 1957. 49(1): p. 59-61.

16. Almond, P.M., et al., *Dissolution and off-gas results for U-Al and Al alloys representative of MURR-type used nuclear fuels.* 2015. 50(18): p. 2790-2797.
17. Crooks III, W., et al., *Mercury-free dissolution of aluminum-based nuclear material: from basic science to the plant.* 2003. 48(4): p. 163-169.
18. Vandegrift, G., et al., *CONTINUING INVESTIGATIONS FOR TECHNOLOGY ASSESSMENT OF" Mo PRODUCTION FROM LEU TARGETS.* 1989: p. 115.
19. Joshi, A. and D.F.J.C. Stein, *Chemistry of grain boundaries and its relation to intergranular corrosion of austenitic stainless steel.* 1972. 28(9): p. 321-330.
20. Viswanadham, R., et al., *Grain boundary segregation in Al-Zn-Mg alloys—Implications to stress corrosion cracking.* 1980. 11(1): p. 85-89.
21. Scamans, G., N. Holroyd, and C.J.C.s. Tuck, *The role of magnesium segregation in the intergranular stress corrosion cracking of aluminium alloys.* 1987. 27(4): p. 329-347.
22. McMahon Jr, C., L.J.J.o.V.S. Marchut, and Technology, *Solute segregation in iron-based alloys.* 1978. 15(2): p. 450-466.
23. Joshi, A., C. Shastry, and M.J.M.T.A. Levy, *Effect of heat treatment on solute concentration at grain boundaries in 7075 aluminum alloy.* 1981. 12(6): p. 1081-1088.
24. Kobayashi, S., R. Kobayashi, and T. Watanabe, *Control of grain boundary connectivity based on fractal analysis for improvement of intergranular corrosion resistance in SUS316L austenitic stainless steel.* Acta Materialia, 2016. 102: p. 397-405.
25. Tsurekawa, S., S. Nakamichi, and T. Watanabe, *Correlation of grain boundary connectivity with grain boundary character distribution in austenitic stainless steel.* Acta Materialia, 2006. 54(13): p. 3617-3626.
26. Larsen, M.H., et al., *Intergranular Corrosion of Copper-Containing AA6x xx AlMgSi Aluminum Alloys.* Journal of the Electrochemical Society

2008. 155(11): p. C550.
27. Murer, N., N. Missert, and R. Buchheit. *Towards the Modeling of Microgalvanic Corrosion in Aluminum Alloys: the Choice of Boundary Conditions*. in *Proceedings of the COMSOL Users Conference Boston*. 2008.

28. Martinez-Lombardia, E., et al., *Use of Local Electrochemical Methods (SECM, EC-STM) and AFM to Differentiate Microstructural Effects (EBSD) on Very Pure Copper.* 2017. 16(1): p. 1-7.

Chapter 3

Grain boundary engineering for enhanced extraction of medical isotopes

Summary

The digestion of UAl_3 fuel particles is studied with Electron backscattered diffraction (EBSD) to determine the relationship that grain sizes and coincident site lattice (CSL) have on oxidation. Previously, it was found that intergranular oxidation played an important role on the digestion of UAl_3. However, it is unknown if there are certain types of grain boundaries that are more susceptible or resistant to oxidation. In this chapter, concepts of grain boundary engineering are explored to optimize the digestion of UAl_3 particles.

UAl_3 particles are digested in a bath of 4M NaOH for 120 minutes. Cross sections of the particles are taken at different depths with scanning electron microscopy (SEM) and EBSD to assess the progress of oxidation. Over 10,000 grains were analyzed for their sizes, orientation, and CSL boundary. The oxidized boundary length of each CSL boundary was measured as a fraction of the total boundary length.

It was found that random high angle grain boundaries were more susceptible than low angle grain boundaries, when it comes to oxidation. Two special boundaries, Σ3 and Σ9 boundaries, were found to be significantly resistant to oxidation. It was also found that grain sizes play a large role in predicting how well particles digest. Particles with large average grain sizes above 40μm showed almost no sign of digestion while particles with lower average grain sizes were susceptible to digestion.

Based on the data presented here, recommendations are given on the optimal microstructure of UAl_3 particles for the extraction of medical isotopes. Suggestions on how to keep grain sizes small and how to minimize low-angle grain boundaries are given. The strategy of using CSL theory to increase oxidation susceptibility may be the first instance where grain boundary engineering is used to enhance, rather than prevent, oxidation.

Table of Contents

1 Introduction 102

2 Grain boundary engineering.....103

3 Electron Backscatter Diffraction (EBSD).....104

3.1 Background 104

3.2 Coincident site lattice in cubic materials 106

4 Experimental Methods 107

4.1 EBSD specifications and sample preparations.....107

4.2 Cleanup of low confidence index patterns in EBSD maps 109

4.3 Experimental outline.....111

5 Results.....113

5.1 Grain Boundary Analysis at 120 minutes of digestion.....113

5.2 Analysis of an aluminum phase along the grain boundary.....116

5.3 Effects of grain size on oxidation rate 118

6 Discussion 124

7 Conclusions and outlook 126

1 Introduction

The experiments in Ch.2 have revealed many new ideas on the "digestion" of UAlx fuel. Mainly, it has revealed that fuel digestion is actually a type of oxidation or corrosion process, similar to that of steels [1-3]. In this oxidation process, it is found that oxidation of triple junctions and grain boundaries, play a central role in converting UAlx to UO_2 and finally $Na_2U_2O_7$. The identification of this type of oxidation process or mechanism is significant in that we can engineer fuel particles optimized for "digestion" purposes. For example, if the oxidation would proceed only via surface reactions, where a shrinking core model can be applied, then improving the surface area to volume ratio of these particles would be necessary. However, as is clearly demonstrated in chapter 2, we must consider intergranular oxidation as an integral part of the conversion of UAlx fuel to a yellow cake. In intergranular oxidation, triple junctions and grain boundaries must be optimized to favor certain material properties. For example, oxidation resistant grain boundaries for robust structural materials and oxidation susceptible grain boundaries for conversions to a yellow cake.

Grain Boundary Engineering (GBE) is the appropriate method to use in order to understand and to optimize a material to be oxidation susceptible. Already identified in chapter 2 is the fact that aluminum enhanced grain boundaries can significantly enhance the oxidation rate of UAl_3. This "sensitization" of grain boundaries is already a demonstration of a common phenomenon in GBE [4]. Although normally, sensitization of grain boundaries to oxidize and intergranular stress corrosion cracking is view negatively in structural materials, it can be used increase digestion here.

GBE is a method of changing grain orientations and grain boundaries in a polycrystalline solid to affect its materials performance. To further our understanding on intergranular oxidation in UAl_3 fuel, digested samples will be analyzed using electron backscattered diffraction (EBSD) to determine which, if any, grain boundaries are more or less susceptible to digestion. This chapter is dedicated to deepening our understanding of intergranular oxidation on UAl_3 using EBSD.

2 Grain boundary engineering

Over the past several decades, grain boundary engineering (GBE) has been developed to enhance several materials properties of metals such as susceptibility to corrosion, cracking, sliding, segregation and precipitation [5, 6]. The goal of the emerging technology of GBE is to improve grain-boundary-controlled properties of polycrystalline materials by increasing the fraction of so-called special boundaries at the expense of random boundaries. “Special grain boundaries” are referred to in literature as the formation of annealing twins (bounded by coherent $\Sigma 3^n$ boundaries), which have been shown to substantially decrease corrosion, particularly in steels, Cu, Ni, Cr, and alloy 600.

Equally important in developing corrosion and oxidation resistant material is not only increasing “special grain boundaries” but also controlling grain boundary triple junctions (GBTJ). Triple junctions composed entirely of three low-Σ Coincident site lattice (CSL) boundaries, or two low Σ CSL boundaries and a single random high-angle grain boundary are classified as “special” because they will usually possess enhanced resistance to intergranular degradation. Not only are triple junctions the meeting points of “special” boundaries, but they themselves have unique properties due to excess energy, vacancy binding energy, and activation energy for vacancy migration [7]. GBTJ are often the initiating site for intergranular corrosion.

All research on GBE is focused on improving the polycrystalline materials against oxidation corrosion. However, what if we would like to increase the oxidation rate? In the case of ROMOL-99 technology, the fuels and materials involved in isotope production should be designed to be digested within 90 to 120 minutes [8], or as fast as possible.

The following experiments presented here are performed to address the following:

- Are some grain boundaries in UAlx more susceptible to oxidation than others without the use of aluminum grain boundaries?
- Is there an optimum grain size for digestion?
- Can we improve the digestion rate with only GBE and without catalysts or oxidants?

3 Electron Backscatter Diffraction (EBSD)

3.1 Background

Electron Backscatter diffraction (EBSD) is a technique which combines microstructural and crystallographic analysis to study crystal orientation, phase, or strain in a crystalline material. A polished sample is placed in the SEM chamber tilted to 70° from the horizontal stage towards the diffraction camera (Figure 1, A). The tilt increases the yield of BSE and thus increases the intensity of the EBSD signal while only probing the sample surface. With the surface tilt and considering the typical electron voltage employed (20-30kV), the surface depth from which an EBSD pattern is generated is roughly a few tens of nanometers [9]. Because this technique is a surface sensitive and

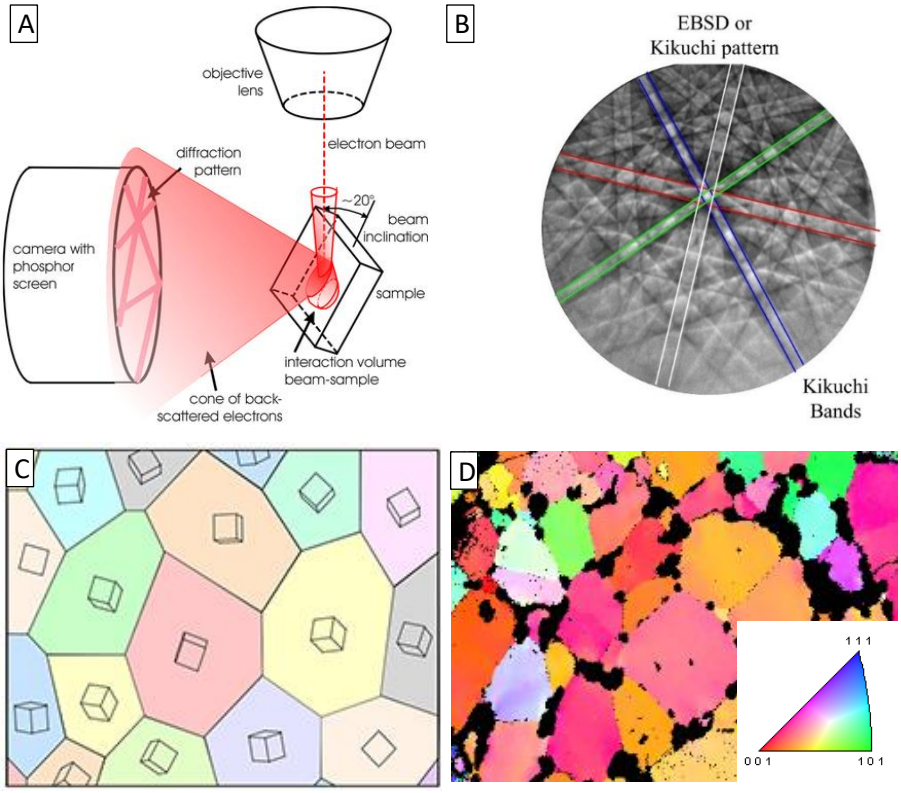

Figure 1) Electron Backscatter Diffraction. A) Geometry of sample to electron beam and phosphor screen; B) escaping electrons forming kikuchi bands; C) representation of grains in different orientation; D) inverse pole figure with an orientation key.

probing technique, polishing of the sample is important. Mirror quality polish of a flat surface are required to avoid deformation of the top layer due to mechanical polishing, an oxide layer, residue from etching, and internal strain. Inside the SEM, an electron beam is focused onto the sample, where they can either enter, escape, or reflect. Escaping electrons near the Bragg angle can diffract to form Kikuchi bands (Figure 1, B), which correspond to the lattice diffracting planes. The width of the Kikuchi band is dependent on the spacing of a lattice plane family that generated the band. If the crystal structure is known, it is possible to relate the bands present in the kikuchi pattern to the underlying crystal phase and orientation within the electron interaction volume. Each band can be individually mapped to a Miller indices of the diffracting plane which it came from. For most crystal structures, only three bands or planes which intercept are required to describe a unique solution to the crystal orientation.

To study how oxidation effects grain boundaries, EBSD can be used to find the crystal orientation of each point that the incident beams interacts with, and thus each grain within a crystal. Scanning the beam across a sample surface results in a rich microstructural map where each orientation is identified with a color (Figure 1C and D), creating a 2D map of the whole illuminated area. By identifying the orientation of each crystal, each boundary that is formed at the interface of two grains can also be uniquely described based on the two planes in contact and an axis of rotation and misorientation. This is a particular advantage of an inverse pole figure (IPF) presented in (Figure 1D). An IPF displays a specific sample direction within the crystal system, based on crystal symmetry. For a cubic class system, the IPF can be reduced to a triangle (Figure 1). In this orientation, which is used throughout this chapter, the following color key is used:

- red represents a grain where the [001] of the crystal is parallel to the assigned sample direction
- blue represents a grain where [111] of the crystal is parallel to the assigned sample direction
- green represents [101] of the crystal is parallel to the assigned sample direction.

3.2 Coincident site lattice in cubic materials

Boundaries between two grains can be described to have a structural unit which depend on both the misorientations of the two grains and the plane of the interface. The structural unit that exists is related to the concept of coincident site lattice (CSL), where repeated unites are formed on the boundary interface from points where the two misorientated lattices happen to coincide [10]. This is demonstrated in Figure 2A. where the blue dots represents atoms that are aligned from the lattices of the green and red dots, perpendicular to the interfacial plane. In CSL theory the degree of fit, denoted by Σ, between the two lattices is described by the reciprocal of the radio of coincidence sites to the total number of sites [11]. For example, When Σ=5 there will be one atom for each five atoms that will be shared between the two lattices (Figure 2B). Thus a boundary with a low Σ is expected to have lower energy due to the higher coincident sites, than a high Σ boundary. Low Σ boundaries, having lower energies, tend to have special properties like corrosion and crack resistant.

Each Σ type is calculated differently for each crystal class system. Uranium trialuminide (UAl_3) is a cubic crystal system that is isomorphic with $AuCu_3$ in the space group Pm-3m no.221. For a cubic system there are 50 Σ types and are described in Figure 2C [12-14]. UAL_4 on the other hand, has a body-centered orthorhombic structure with the space group of either I2ma (no.46) or Imam (no74). CSL for orthorhombic structures known [15], there is little evidence thus far that UAl_4 undergoes intergranular oxidation, and is therefore omitted in this analysis (see appendix II on the digestion of UAL_4). Therefore, this study will focus on UAl_3 exclusively.

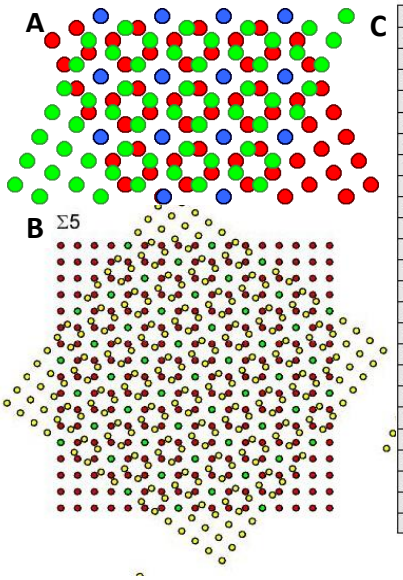

C

Σ Type	Angle	Axis
1	0	1 1 1
3	60	1 1 1
5	36.86	1 0 0
7	38.21	1 1 1
9	38.94	1 1 0
11	50.47	1 1 0
13a	22.62	1 0 0
13b	27.79	1 1 1
15	48.19	2 1 0
17a	28.07	1 0 0
17b	61.92	2 2 1
19a	26.53	1 1 0
19b	46.83	1 1 1
21a	21.78	1 1 1
21b	44.41	2 1 1
23	40.45	3 1 1
25a	16.26	1 0 0
25b	51.68	3 3 1
27a	31.59	1 1 0
27b	35.43	2 1 0
29a	43.60	1 0 0
29b	46.40	2 2 1
31a	17.90	1 1 1
31b	52.20	2 1 1

Σ Type	Angle	Axis
33a	20.05	1 1 0
33b	33.56	3 1 1
33c	58.99	1 1 0
35a	34.05	2 1 1
35b	43.23	3 3 1
37a	18.92	1 0 0
37b	43.14	3 1 -
37c	50.57	1 1 1
39a	32.20	1 1 1
39b	50.13	3 2 1
41a	12.68	1 0 0
41b	40.88	2 1 0
41c	55.88	1 1 0
43a	15.18	1 1 1
43b	27.91	2 1 0
43c	60.77	3 3 2
45a	28.62	3 1 1
45b	36.87	2 2 1
45c	53.13	2 2 1
47a	37.07	3 3 1
47b	43.66	3 2 0
49a	43.57	1 1 1
49b	43.57	5 1 1
49c	49.23	3 2 2

Figure 2) Coincident site lattice for cubic materials. A- demonstration of coincident atoms in of two lattices, highlighted as blue dots. B – Demonstration of Σ5 grain boundary, with overlapping atoms in green. C – list of Σ types in cubic systems.

4 Experimental Methods

4.1 EBSD specifications and sample preparations

In the experiments presented in this chapter, the electron backscatter diffraction (EBSD) maps were recorded using an EDAX TEAM Pegasus system with a Hikari XP EBSD detector. The EDAX system is installed on a ThermoFischer SCIOS focused ion beam and scanning electron microscope (FIB/SEM) with a Schottky-type field emission gun (FEG). The spectra were recorded at 20kV with a beam current of 6.4nA. The EBSD results were analyzed using the TSL OIM Analysis 8 software package. For these measurements 4x4 or 8x8 pixels were binned for the 14 megapixel EBSD camera. The raster step size used during the EBSD measurements was 50 nm at the speed of around 100 patterns per second with a hexagonal raster pattern.

To prepare a sample for EBSD measurements, a sample is initially prepared similarly to those prepared for SEM/ EDX analysis. Samples were either digested fuel particles or a small piece of a target. Digested fuel particles

were first mixed with silver particles in a 1%wt by volume mixture. The powdered mixtures were compacted with 10 tons of pressure to make small pellet with a diameter of ~8.6 mm. This pellet would then be embedded into an epoxy resin. If the sample was a small piece of a target, it was directly imbedded into an epoxy resin to make a mount. The mount was ground and polished with dry and wet methods. For the initial grinding stages to produce a flat specimen, the pucks were ground using SiC papers with grit sizes 320 (35 μm), 600 (15 μm), 800 (13 μm), 1200 (8 μm). The duration of each of the grinding steps was ~5 minutes. To obtain a mirror finish of the surface, 3 steps using diamond suspension (3 μm, 1μm, 0.25 μm) is used. The samples were rinsed with water between polishing steps and cleaned with ethanol.

In order to get consistently good confidence indexing during the EBSD measurement, a focused ion-beam (FIB) was used to further polish the sample surface in-situ in the vacuum chamber (Figure 3). Similar methods have been reported [16] to obtain high quality EBSD measurements, and is needed in samples that oxidize quickly, such as metallic samples. A Ga ion source was employed at an ion acceleration voltage of 20kV, to perform an additional, in-situ polishing step. The sample was orientated in the vacuum chamber so that the ion beam would impinge on the surface at roughly a 1^{o} grazing angle (Figure 3C). The working distance for EBSD measurements, or the distance at which the beam is focused, used in all samples was 10 mm while the sample was tilted 70 degrees (Figure 3D)

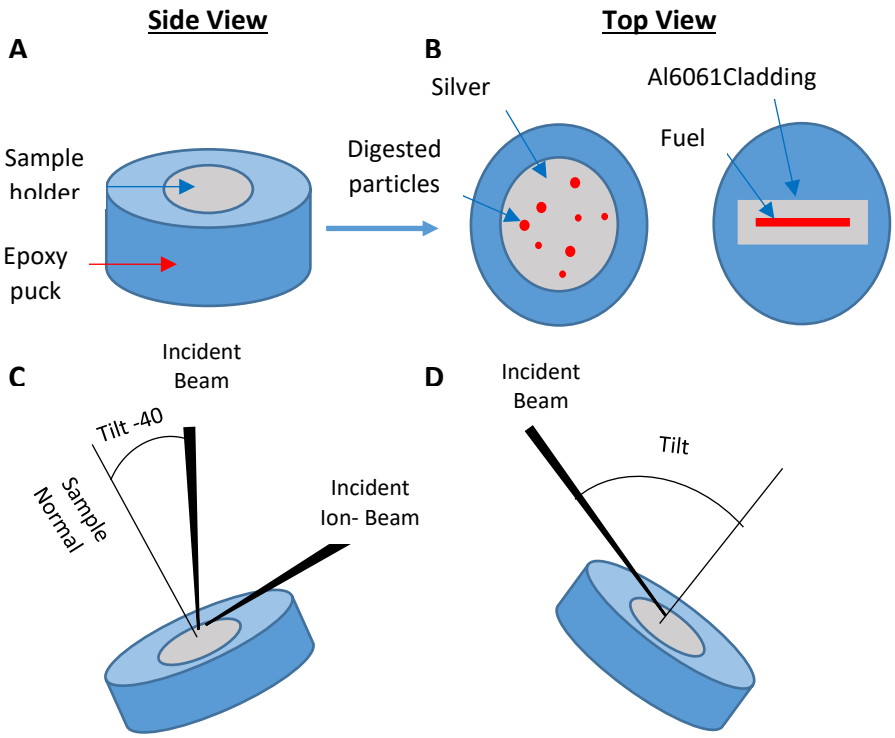

Figure 3) EBSD samples and sample configuration. A- General sample model used in EBSD analysis. B - visualization of digested fuel particles embedded in silver or fuel target embedded in epoxy resin. C – Ga ion polishing D – EBSD measurement

4.2 Cleanup of low confidence index patterns in EBSD maps

Studying the grain boundaries of digested samples is not as straight forward as studying as-fabricated samples. Due to the intergranular oxidation itself, the grain boundaries that are to be studied may or may not exist, if the boundary is oxidized or not. Furthermore, because the samples has to be embedded and polished, as described in the previous section, it is impossible to study a sample either *in situ* or to retrieve the same sample, put it back into a digestion bath, and polish it again. Additionally, the oxidized surfaces and boundaries will have a different crystal structure, leaving their original crystal orientation ambiguous. Due to all of these physical and chemical changes, an area can give rise to a low confidence indexed patter. Generally, a pattern must have a confidence index (CI) above 0.1 in order for the calculated orientation to be considered correct. Because of all of these shortcomings, calculating original boundary lengths and oxidation lengths

directly is not possible. Data cleanup is necessary in order to evaluate the progress of digestion in a sample.

a “clean up” is performed to fix areas that are missing due to digestion, or have low confidence indexes due to being near a grain boundary or oxidation. Before “holes” of oxidation were filled in via dilation of high confidence indexed points, and before an error could propagate, low confidence points were corrected by associations with its neighbor. Neighbor orientation correlation is only performed on data points with CIs less than the chosen value of 0.2 (slightly above the standard 0.1). If a point has a CI less than this minimum value, it is checked to see if the orientation is different from its immediate neighbors. The second condition is to determine if the orientation is different from its immediate neighbors. A clean up “level 0” requires all nearest neighbors must be different more than the tolerance angle, for cleanup level 1, all but one of the nearest neighbors must be different and so on until level 5. If the first requirement is meet, a third requirement is tested. This requirement determines the number of neighbors which represent like orientations to within a given tolerance angle. For level 0 an all neighbors have a similar orientation, cleanup requires all but one of the nearest neighbors to be of like orientation and so on until cleanup level 5. If all conditions are meet, the orientation of the low confidence area is changed to one of the neighbors involved in meeting condition 2 and 3, at random. The effect can be seen in Figure 4 under neighbor orientation. In this view, “dead pixels” within a grain are corrected to match the grain. Pixels at grain boundaries are smoothened to match the majority of its neighbors as well through a “neighbor orientation correlation. For a sample of multiple phases, a similar cleanup is applied for a phase correction.

A final step in a cleanup procedure is to perform grain dilation. This is an iterative method and only acts on points that do not belong to any grain yet have neighboring points that are indexed. If the majority of neighbors of a point belong to the same grain, then the orientation of that point is changed to match that of the majority that surrounds it. Otherwise, the orientation is matched to any of the neighboring points which belong to grains. This can be seen in Figure 4 under the grain dilation column. Grain boundaries and junctions that are digested and absent are filled in until all boundaries are connected. Grain boundary lengths are calculated based on these corrections.

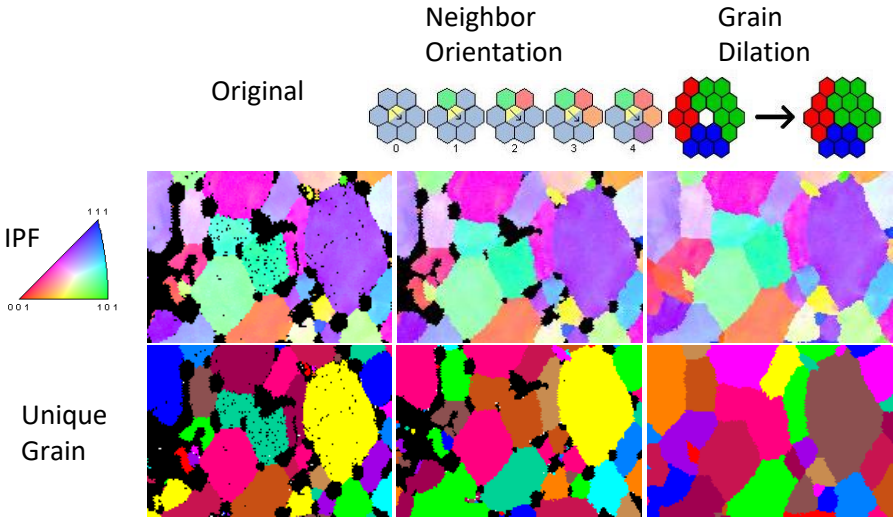

Figure 4) Cleanup of a corroded UAl_3 sample demonstraiting neighbor orientation and grain dilation.

4.3 Experimental outline

Digestion of annealed UAl_3 particles followed similar ROMOL-99 conditions described in Chapter 1 and 2. The particles digested in this experiment were taken from the same UAL_3 particles as analyzed in Ch.2 section 3.1 and 3.1.1. The digestion solution was prepared in a borosilicate reaction vessel, externally headed in a water bath and magnetically stirred. The water bath was held at 95°C for the duration of the experiment. Five to seven grams of fuel was digested in 4M NaOH and 3M $NaNO_3$ in 250ml of solution. At 120 minutes, 20 ml of solution was aliquoted from the reaction vessel to a specimen vial. In the vial, the specimen was diluted to below 1M NaOH and immediately cold quenched to 4°C. After the experimental run, the samples were diluted further until the solution reached a neutral pH and no NaOH

could be detected. The samples were then dried under ambient conditions. Prior to EBSD analysis, samples were prepared as described in sample preparation section (chapter 2 section 2.2.2 and 2.2.3).

During digestion and polishing, the fuel particles are randomly orientated and are not fixed. Because of these conditions, oxidation cannot be studied as a function of some defined surface, when it comes to digesting fuel particles outside of a target. It cannot be known on what plane in the particle observation are made. The initial polishing steps taken in these experiments remove up to 60 µm of the initial puck. Therefore the plane at which the first images are taken can lie somewhere between the particle surface and 60 µm into the particle.

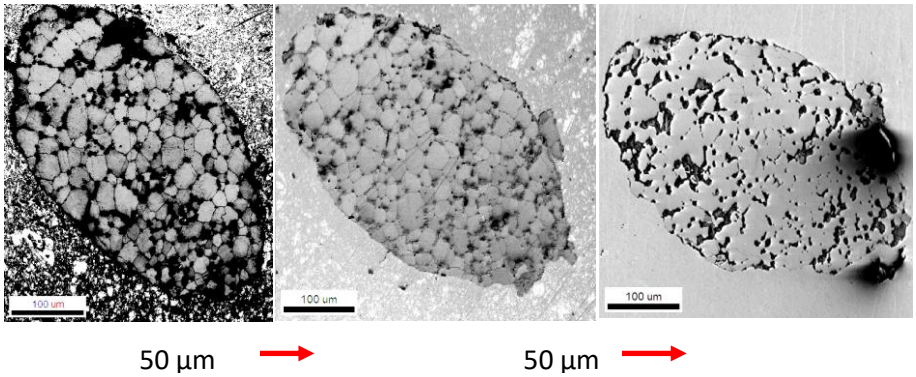

Figure 5) Depth analysis of a digested fuel particle.The first image is a BSE image with the two following images are SE images. EBSD measurements were performed on the same sample and different depths. The oxidation measurements can be compared over a span of 100 µm.

Finally, it is important to study the digestion deep into the particle and to be certain that an analyzed particle is not just a surface effect. Although it is possible to use a FIB to etch surface and continue to do EBSD, this process would be too time consuming for large areas that would be necessary to achieve a statistically relevant results. To study the digestion deep into a fuel particle, a sample was re-polished with SiC paper outside of the FIB to take off another ~50 µm (Figure 5). This depth was chosen as it is above the average grain size of all of the samples but going any further often leads to particles to be pulled out of the mount during polishing. A particle was analyzed with EBSD at least on 3 different planes using this method.

5 Results

5.1 Grain Boundary Analysis at 120 minutes of digestion

20 fuel particles were analyzed with diameters above 100µm, to analyze the relationship between oxidation and coincident site lattice. Over 10,000 grains were analyzed for their orientation, or disorientation, grain size, and the boundaries formed between them through inverse pole figures (IPFs).

Figure 6 is the result of the analysis of a digestion fuel particle that has been digested for 120 minutes, at 95°C in 4M NaOH. Figure 6A, represents the IPF, showing the grain orientations of the fuel particle. The oxidized areas (Figure 6A, inset) have been filled in (as described in section 4.2) to calculate the boundary length that was originally there. The total length of each grain boundary, or CSL, is compared to the oxidation length along that boundary type within the particle (Figure 6B). The graph of Figure 6B is the summary of three different EBSD analysis and is the fuel particle shown in Figure 5. Additionally, the average grain in this particle has a diameter 13.3µm or 28.5µm by area. For the analysis of CSL boundaries, Brandon's criterion was followed which premises a deviation given by an equation of the form $\Delta\theta=\theta_0(\Sigma)^{-n}$ where $\theta=15$ and $n=0.5$.

The total lengths of each grain boundary varies from 100 to 800µm. All low angles were above 450µm, while higher angles varies from 100µm to 800µm. The characteristic distribution of boundary misorientations in a completely random oriented set of grains in a cubic system normally peaks around 45 degrees and decreases to either 0 or 60 degrees. In this sample, the slightly high number of low angles can be due to the fact that the sample was annealed for 3 days at 800°C. The long lengths of 43b and 45a could be a remnant of the random distribution, as is the distribution overall.

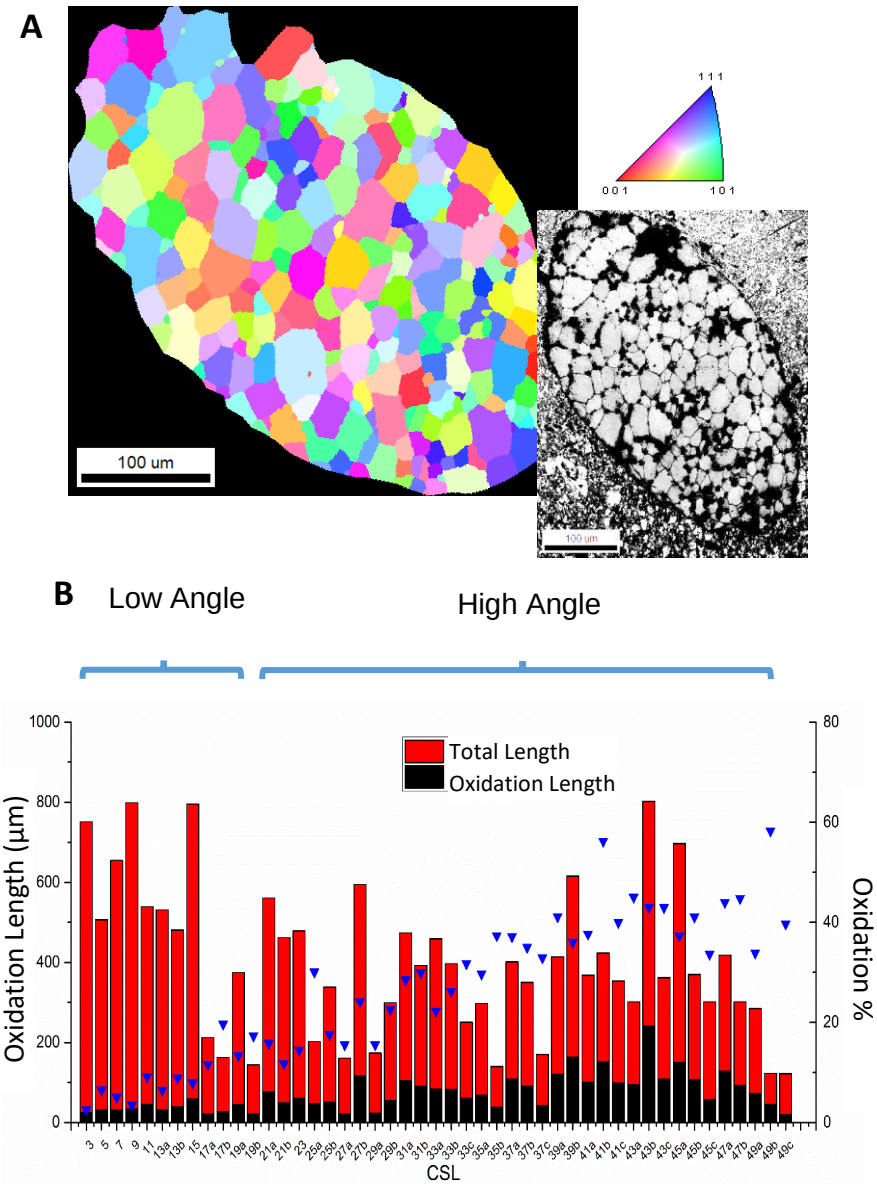

Figure 6) EBSD analysis on a UAl_3 particle, digested for 120 minutes in 4M NaOH. A; BSE image of a digested fuel particle, with oxidation at TJ and GB. Accompanying IPF with a clean up of the oxidized areas. B; analysis of CSL boundaries and their oxidation length.

The percentage of oxidation along each CSL can be seen in blue triangles in Figure 6C. In general, it can be seen that lower angle (Σ1-15) are much more oxidation resistant than high or random grain boundaries (Σ17a-49c). In particular, Σ3 and Σ9 boundaries demonstrate a considerable resistance to the digestion bath (Figure 7). With only a few exceptions, digestion paths can be seen to permeate throughout the UAl_3 particle and stop once it reached a Σ3 or Σ9 boundary. These boundaries are a part of the so called "special"

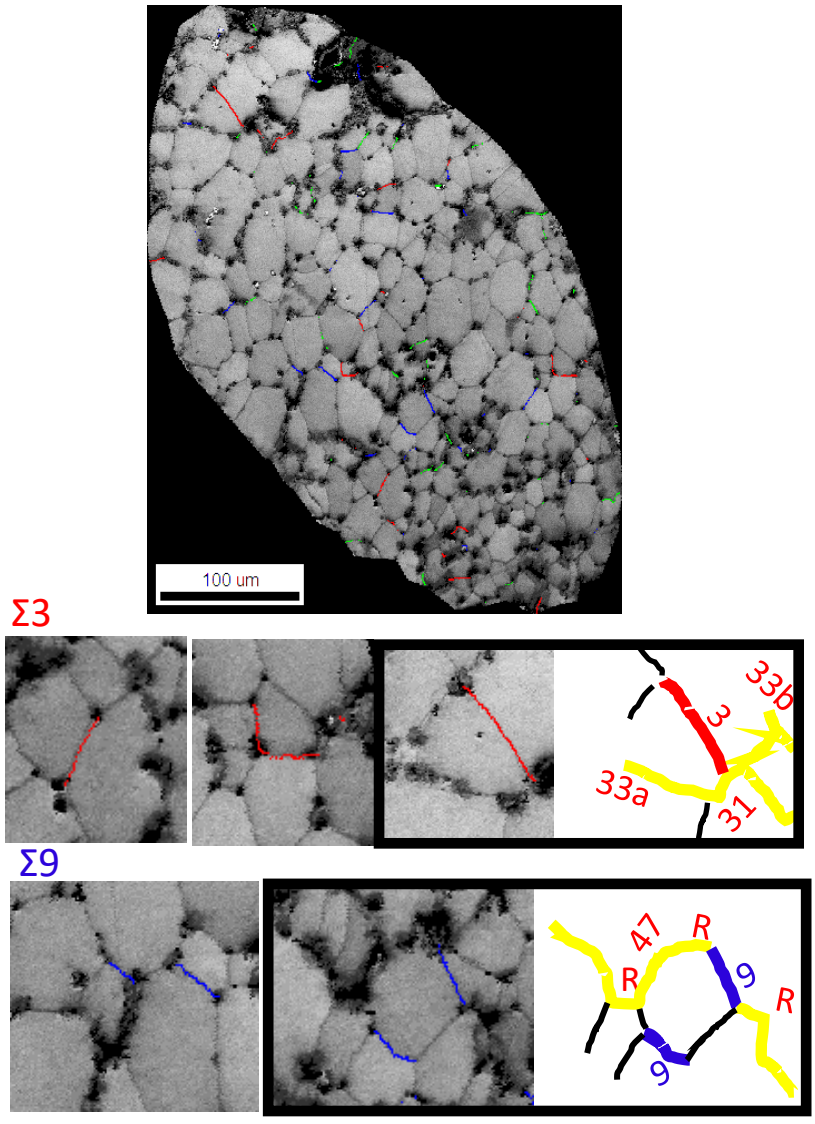

Figure 7) BSE image - corrosion resistant $\Sigma 3^n$ boundaries. Boundaries Σ3 and Σ9 show resistance to corrosion while Σ27 does not.

grain boundaries, where it is predicted that $\Sigma 3^n$ boundaries would have special physical properties due to their low energy and high coincidence. In this analysis, Σ27, where n=3, did not show an enhanced resistance to oxidation (Figure 6).

5.2 Analysis of an aluminum phase along the grain boundary

Previously in chapter 2, aluminum phases along the grain boundary were discovered in the samples used for this thesis. Furthermore, it was also discovered that an additional aluminum phase on GBs significantly enhances the digestion of these particles. It is therefore important to estimate the amount of aluminum at the grain boundaries that can affect the results presented in this chapter.

An estimation of the amount of grain boundaries that had an aluminum phase present was performed using image analysis of the starting UAl_3 ingot. Several images of the ingot were studied to calculate the length of aluminum phases per square area Figure 8A. The dark lines found in these micrographs were analyzed with EDXS to determine if they have more aluminum than in the center of the grains. As the information volume of EDXS spot analysis is larger than the width of a GB or volume of a junction, this technique was used to check if these features found in this analysis are similar to those found in Chapter 2. In Figure 8B, an analysis of a triple junction (Figure 8C) showed that this area is 83±2 at%Al and 16±2 at%U, which is similar to the analysis presented in Chapter 2 Figure 18. It is estimated that approximately 2.5µm of GB length per $100\mu m^2$ have aluminum at their boundaries. This is equal to approximately 12% of the grain boundaries in Figure 6 and Figure 7 have aluminum at their grain boundaries. It is unknown if this is distributed equally along all grain boundary types, or if it accumulates at high angle grain boundaries. A future analysis using EBSD would have to be used to assess if a relationship exists.

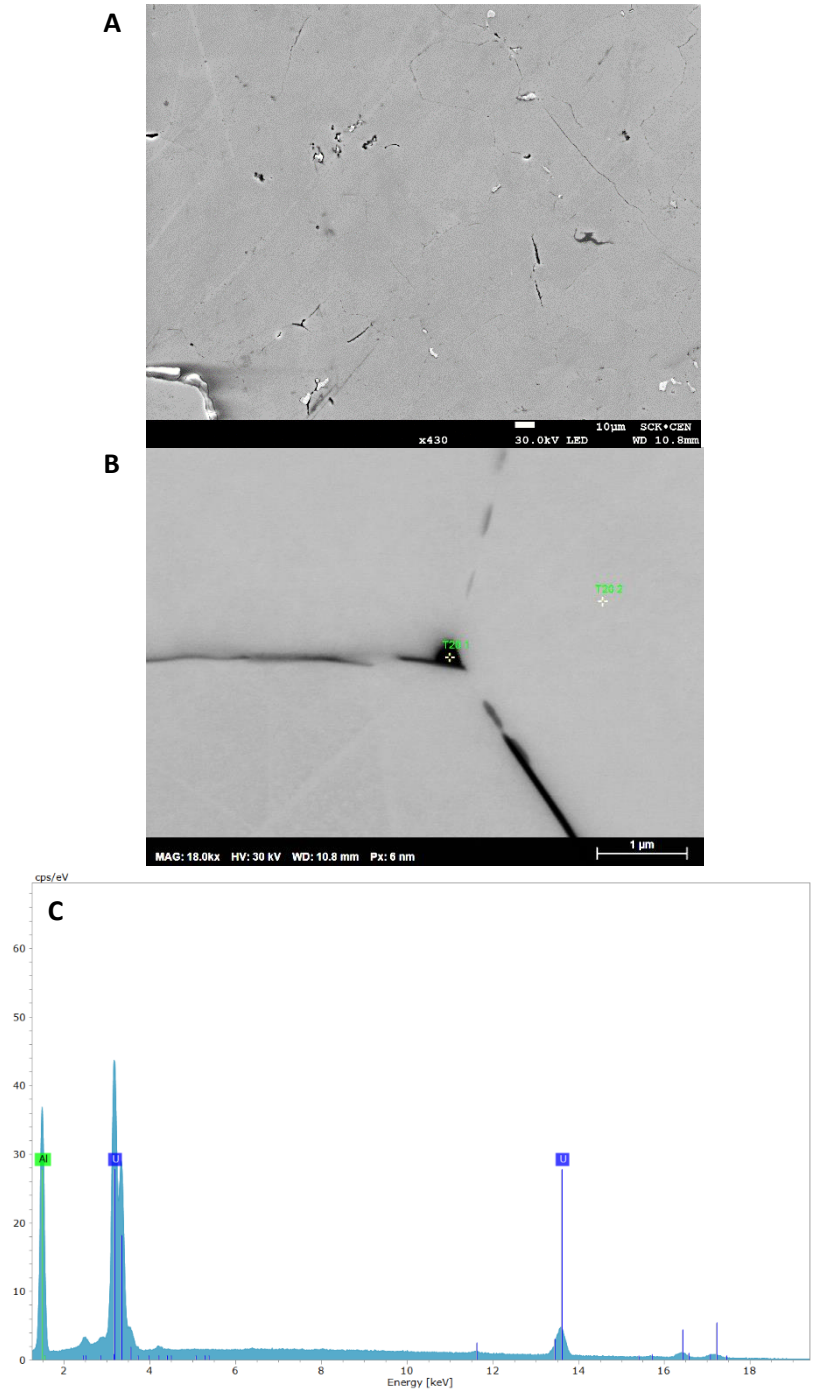

Figure 8) Aluminum phase along the grain boundary. A; BSE image of the starting UAl3 ingot. B; BSE image of a triple junction with aluminum on the boundarys and junction. C; EDXS point analysis of the junction. Aluminum is more abundant at the junction than in the center of the grain.

5.3 Effects of grain size on oxidation rate

An analysis of several particle did not yield the same amount of oxidation, even when the particle composition (UAl_3) and digestion conditions (95°C, 4M NaOH, 120min) were the same. A dramatic difference can be seen in Figure 9. In these particles, a minimal amount of oxidation can be seen. In this image, even the grain boundary triple junctions are well preserved. In Figure 9, high CSL boundaries are indicated in red while low boundaries are indicated in blue. In this particle, even high angle boundaries are not oxidized, even when there is a pathway along high CSL boundaries throughout the particle. In comparison with the particle analyzed in Figure 7, the average grain size in this particle is 45µm, which is significantly higher than well digested particles.

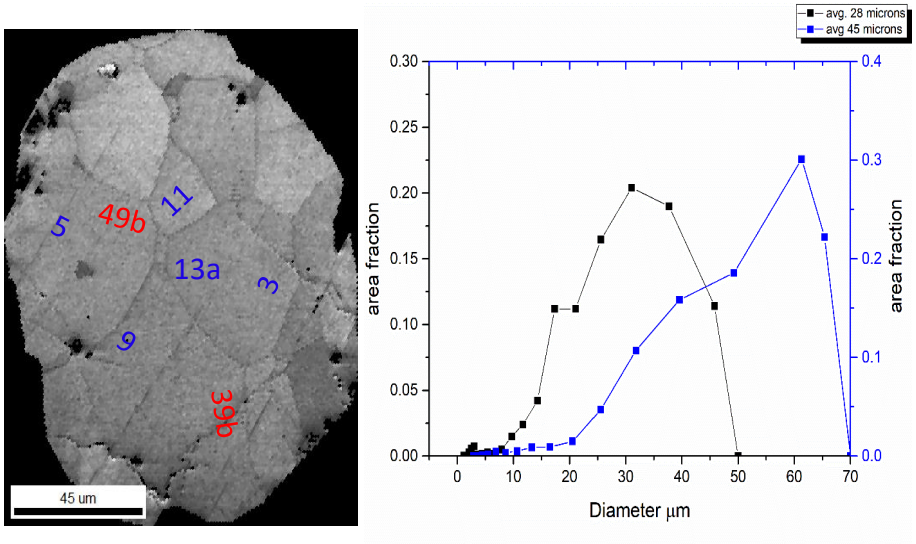

Figure 9)Left- BSE image. Digested UAl_3 particles with large grain boundaries, at 120 min, 95°C, 4M NaOH. Low angle boundaries are indicated in blue, while high angle boundaries are indicated in red. Right- comparison of grain sizes of particles digested in the same conditions. Black line represents the grain size distribution of the particle in figure 7 with an average diameter of 28 microns, while the blue represents the grain size distribution of the particle on the left.

To investigate this effect further, several particles were digested in the same condition. Although several particles have been examined, only those that were able to be polished and reanalyzed at several depths are considered for a complete analysis that can be compared too. Two examples are seen in Figure 10, which compares a sample with a grain size of 18µm (sample A, analyzed over 200 µm) and 40µm (sample B, analyzed over 150µm). In

sample A, almost all triple junctions are oxidized. Furthermore, almost all grain boundaries have been oxidized indiscriminately. In this particle, Σ3 and Σ9 boundaries are more oxidized than those in Figure 7. The sample in Figure 10A, has a smaller average grain size than the sample in Figure 7

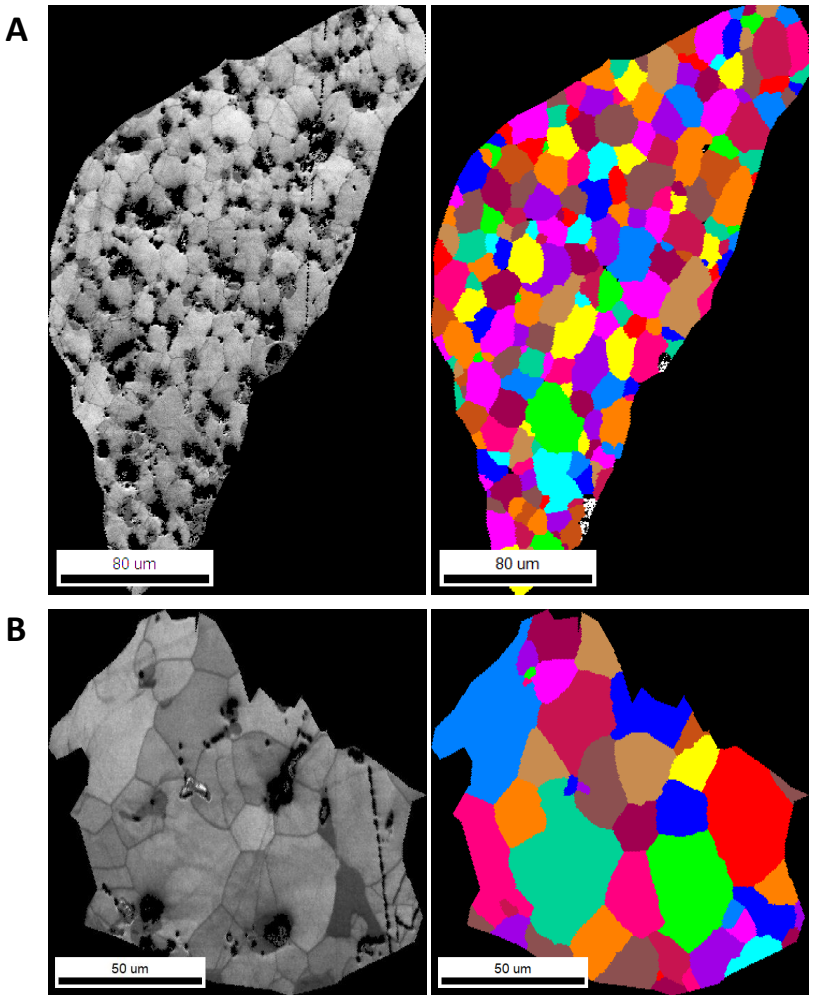

Figure 10) BSE images of digested particles with their corresponding grain maps. Effects of grain size and corrosion. A – small grain size particle with an average grain size of 18µm. B – large grain size particle with a large grain size of 40µm.

The effects of coincident site lattice and grain size on the oxidation rate is made evident in Figure 11 - Figure 15. In these figure, four samples are compared for the amount of intergranular oxidation along different grain boundaries within an average grain size (in units of 1/µm). Starting with the same with the smallest average grain size of 18 µm (0.056 μm^{-1}) in Figure 11, all grain boundaries show oxidation. Even low angle grain boundaries are oxidized around 15% of the total length. High angle grain boundaries were oxidized up to 80% of the length.

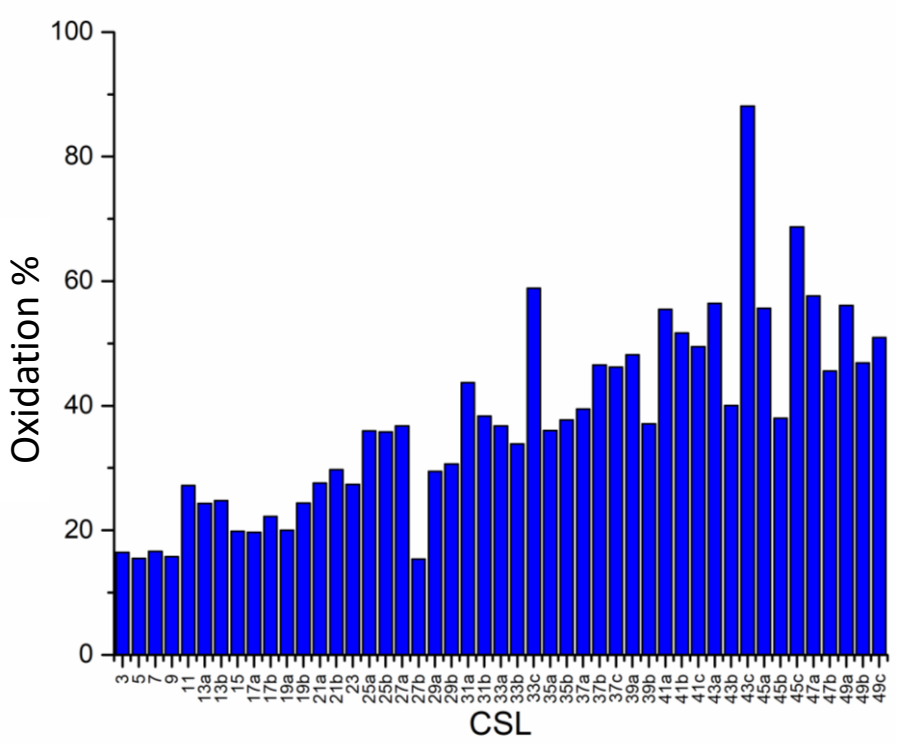

Figure 11) Oxidation percentages of CSL boundaries in a UAl_3 particle, with an average grain size of 18µm.

When there are slightly larger grains (28µm or 0.036μm^{-1}), the low angle boundaries start to become digestion resistant, with Σ3 and Σ9 boundaries having a distinct ability to be resistant. Somewhere between an average grain size of 28µm and 40µm, there is a drastic change where UAl_3 particles become digestion resistant. Particles with average grain sizes above this range show a drastic change in its ability to oxidize, and are very resistant to digestion.

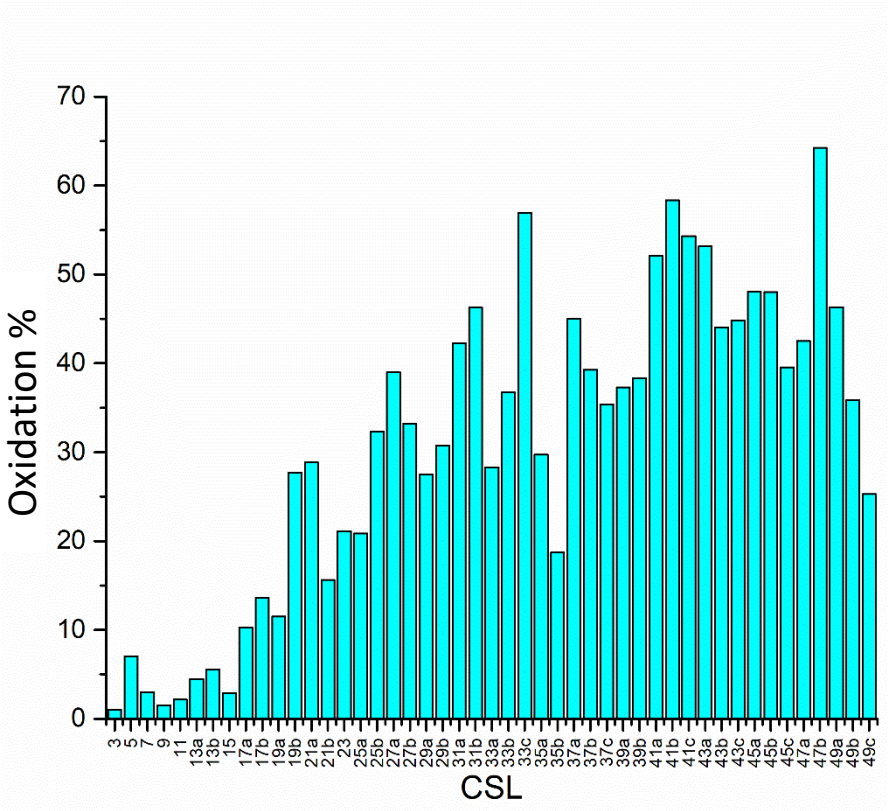

Figure 12) Oxidation percentages of CSL boundaries in a UAl_3 particle, with an average grain size of 35µm.

Figure 13 and Figure 14, shows the oxidation of a UAl_3 particle with an average grain size of 40µm and above. All boundaries are comparable to low angle grain boundaries shown in Figure 12. Even high angle grain boundaries have only oxidized up to 14%.

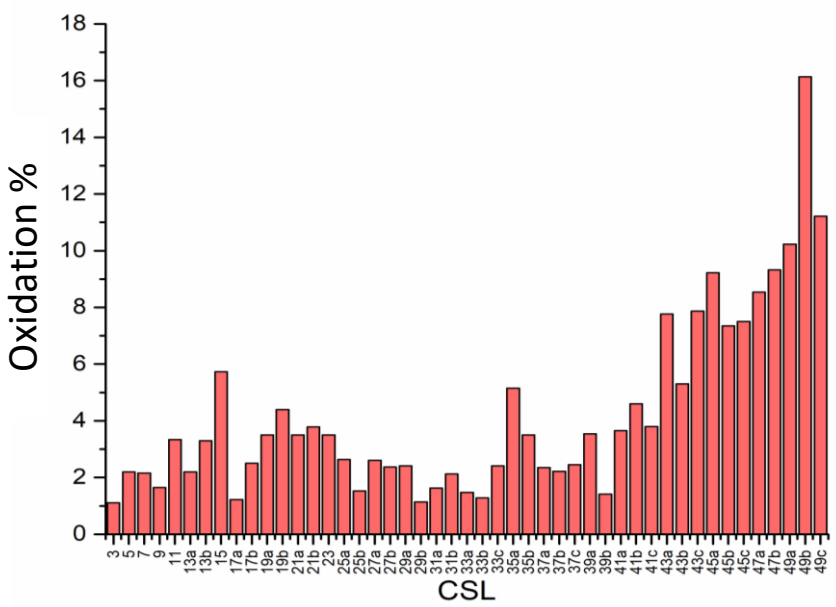

Figure 13) Oxidation percentages of CSL boundaries in a UAl_3 particle, with an average grain size of 40µm.

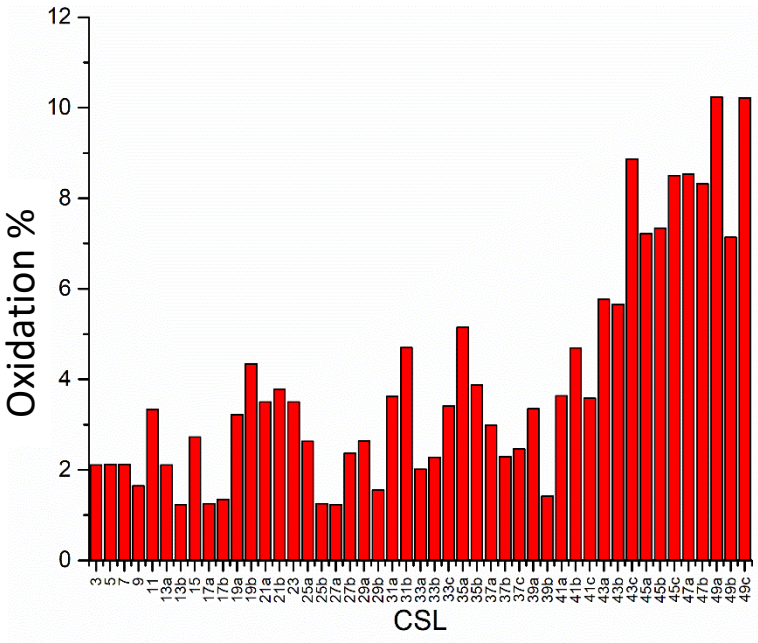

Figure 14) Oxidation percentages of CSL boundaries, of a UAl_3 particle with an average grain size of 45.5µm

Finally, a summary graph is put together in Figure 15. This graph demonstrates that grain sizes have a more important role to play on the digestion of UAl_3 particles, than grain boundary type. Although special grain boundaries exist in this material, it is a short lived effect and not applicable to all average grain sizes or grain networks. For a comparison of grain sizes found in targets and in fuels, see appendix III.

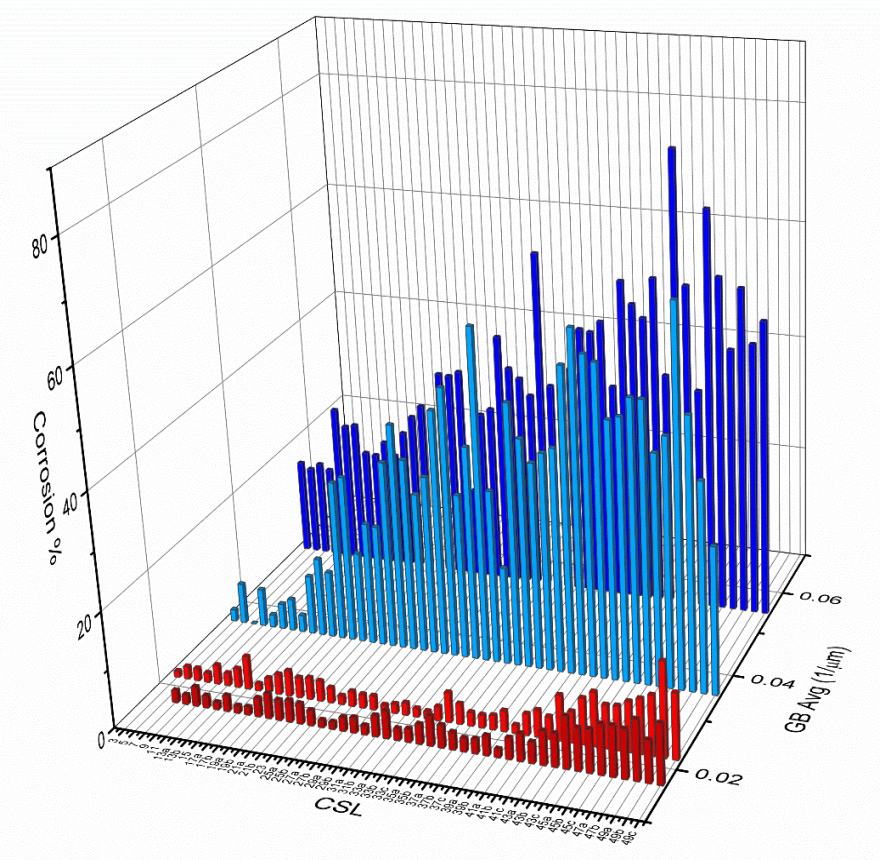

Figure 15) Effects of grain size on oxidation of UAl_3 particles, at 4MNaOH, 120 minutes, and at 95°C.The average grain boundary axis is presented in reciprocal units (1/µm) to display the larger average grain boundaries with lower amounts of oxidation first.

6 Discussion

Compiling this analysis together, a conceptual graph on the effects of grain size, CSL and boundary length is proposed in Figure 16. In this graph, the x-axis represents the degree of misorientation, or CSL boundary, and the Y axis represents the average grain size of the grain next to the grain boundary of interest. Indicated above each picture is the boundary type and the length of the grain boundary. It can be seen that grain boundaries with high angle CSL oxidize the most efficiently, if they belong to a network where the average grain size is below 40µm. Low angle boundaries are more resistant to oxidation, but can oxidize if they are in a network of small grain sizes. In contrast if the average grain size of the particle are above 40µm, then all boundary types are protected, even if the boundary itself is small with high angled misorientation (Σ33b-4.97µm in Figure 16).

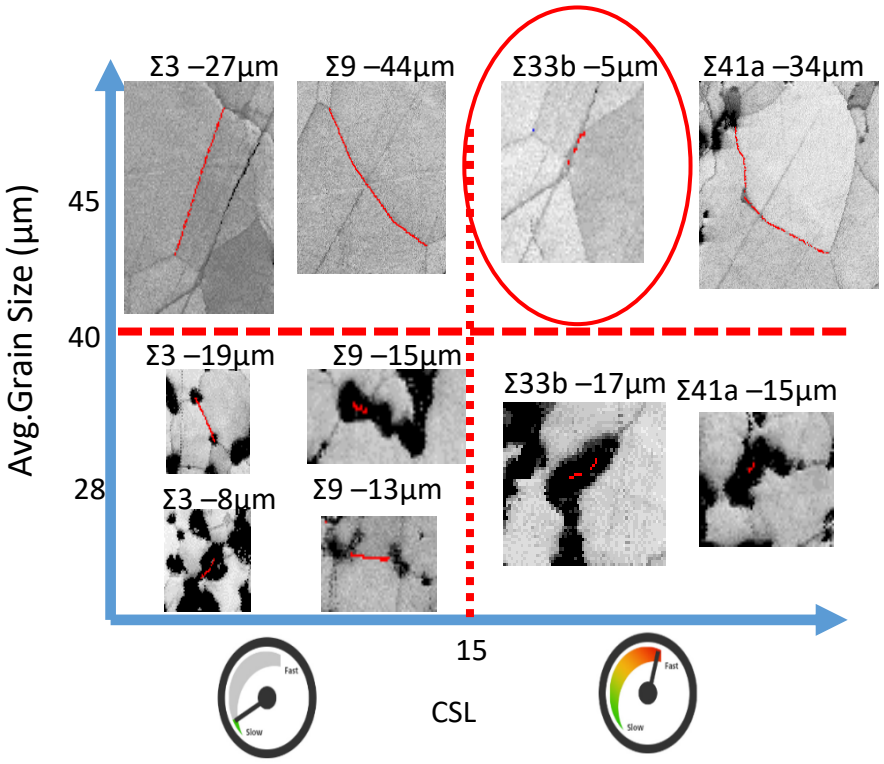

Figure 16) Conceptual graph on the effects of grain size and oxidation. X-axis represents CSL, Y-Axis represents grain size. Each picture is labeled with its CSL assignment with its boundary length.

The fact that the grain size has an influence on the oxidation or corrosion rate has been known for some time. However, the relationship between grain size and oxidation has very little consensus. A variation on the relationship between grain size and oxidation depends on the alloy system. However, in many cases there is a discrepancy within the same system [17]. Contradictory conclusions have been published claiming that increasing size can either increase and decrease corrosion resistance. Contradictory claims can be associated with the difficulty in isolating size effects from other microstructural changes that are caused by thermomechanical processing used to achieve various grain sizes [18-20]. Grain size variation can be achieved using different common metallurgical methods such as hot and cold rolling, working, extraction, severe plastic deformation, milling and pressing. Different processing routes simultaneously lead to microstructural changes, such as increasing special boundaries, in addition to changing grain sizes. Both factors play a role in a material's corrosion response. Given these apparently inseparable variables, it is not unwarranted that a consistent picture of the effects of grain size on corrosion has yet to be established.

The effects of grain size on the oxidation of UAl_3 presented here are in some ways idealized from a real digestion of UAl_3 in a target (see appendix III). In this chapter, the fuel particles are made in an arc-melter and annealed for three days. An arc-melter produces an ingot with variable grain sizes, likely due to the fact that the surface of the ingot in cooled rapidly via direct contact with a chilled copper hearth, while the inside of the ingot is left to cool at a slower rate. Even after annealing, the effects of the initial size distribution is retained. Forming pure UAl_3 without annealing is difficult as it is formed by a peritectic reaction (UAl_2 + L) which often leads to a saturation of aluminum at the grain boundaries if there is no annealing. In fact, a 3 day anneal duration was determined to be needed for producing a sample with highly pure UAl_3 [21]. However, annealing also leads to a higher amount of low-angle grain boundaries simultaneously. In this case, making a pure UAl_3 sample without anneal, to study grain size effects without further heat treatment, is almost impossible.

In a realistic situation, UAl_3 that is found in a target undergoes metallurgical treatment that can affect grain sizes, grain boundaries, intergranular phases, and precipitates. In a plate type target, the fuel is pressed with aluminum into a briquette, welded into an aluminum frame, and undergoes several rounds of hot and cold rolling until it reaches its final specifications. Finally, there is a "blister" test where a target is held for more than an hour at various

temperatures to ensure that it will to undergo failure during its irradiation due to heat stress. This effects of all of these metallurgical processes would also have to be studied independently.

The effects of "special grain boundaries", in particular $\Sigma 3^n$ where n=1 or 2 in the case of UAl_3, is to be anticipated. This phenomena is well document, for example, in steels [1] where this fact is used to make corrosion resistant steels. Low-energy and special grain boundaries of metallic grains have a high resistance to corrosion [22] and the number of low-angle special boundaries leads to a rise of the metal corrosion resistance [23]. What is perhaps surprising is these properties exist inside of a "window" of average grain boundary sizes, as is shown in Figure 15 and Figure 16.

7 Conclusions and outlook

Grain boundary engineering has been long used as a way to optimize material properties in polycrystalline materials. It has been used in fuel targets as well. Note that controlling the grain size leads to an efficient release of fission gas to avoid the growth of void regions that can lead to failure [24]. As the design of medical isotopes targets are originally the same used for fuel, perhaps these targets were unknowingly a proper microstructure to also extract these isotopes. However, it is important that these mechanisms are revealed if new targets are to be designed, and the new design to be compatible with digestion methods. In a similar scenario, there are times in industry where digestion does not go to completion, when all concentrations, reactants, and products seem to be the same. With the insight of the in depth analysis here, new variables, i.e. high energy grain boundaries, grain sizes, and triple junction densities, can be considered in this process to help ensure that a digestion of UAlx fuel particles will proceed to completion.

The images provided here in Chapters 2 and 3 are the first in open literature to show the inside of digested fuel particles. They reveal for the first time that these oxidation pathways are the way by which uranium from UAlx fuel evolves into yellow cake. With these new mechanisms in mind, new techniques can be envisioned to help enhance the digestion properties of these targets. These recommendations comes in two themes: 1) Grain size control and 2) minimize low angle grain boundaries.

1. Grain Size Control - For grain size control: Zener pinning is a known technique to influence the grain size of a material. Zener pinning is the influence of a dispersion or fine particles in an alloy. Small particles act to prevent the motion of such boundaries by exerting a pinning pressure which counteracts the driving force pushing the boundaries. Both low- and high-angle boundaries are retarded by the presence of particles via Zener pinning (see Figure 17). The effect is often exploited in commercial alloys to minimize or prevent recrystallization or grain growth during heat treatment. In our case, it could be used to maintain small grain size well below 40µm. Although not mentioned by its academic name, this is clearly the method used in an IAEA report on target production where it is mentioned "to achieve a smaller grain size … we added small amounts of iron and aluminum to produce an "adjusted" uranium alloy containing ~450 ppm iron and ~1000 ppm aluminum" [25] (pg. 37 ¶2). However, this is claimed to have been done to produce a "more-uniform dimensional change in the uranium during irradiation", and may have inadvertently helped with digestion as well.

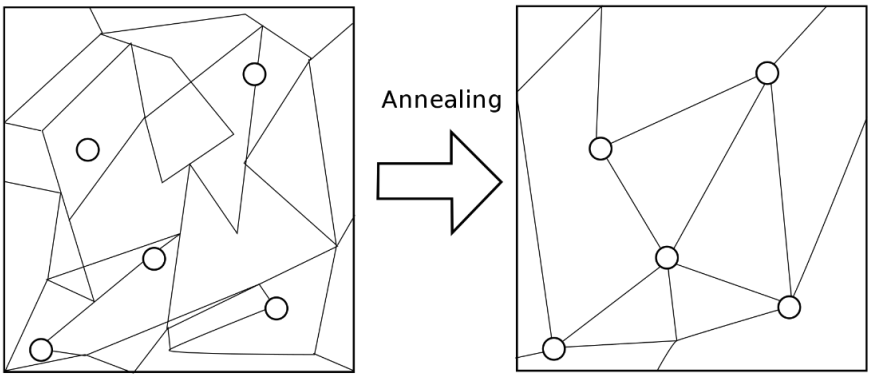

Figure 17) Effects of Zener pinning and annealing on grain growth

Another technique that can be used to modify the grain size can be found in the claims of ultrafine-grained (UFG) and nanocrystalline (NC) material fabrication methods. Over the past decade, research has been done on nano-crystalline material (grain size below 100nm) and ultra-fine grain material (1µm-100nm). The most common method to produce UFG and NC metallic alloys is through severe plastic deformation (SPD) under high hydrostatic pressure to avoid failure problems, sometimes at high strain rates [26]. Such techniques are able to decrease grain size significantly to the nanoscale and could improve its digestion, which is favorable for isotope extraction.

2. Minimize low-angle grain boundaries - Additional recommendations affect the distribution of special grain boundaries. For example, the grain boundary microstructure in SUS316L stainless steel has been shown to have oxidation resistance once created with a series of cold rolling of 2%, 3%, and 4% reduction ratios with a subsequent treatment of annealing at 1273K (approx. 70% of its melting temperature) for 10 or 72 hours, with the best results being a combination of low reduction ratios and short anneal times[2]. Similarly, hot rolling is used to produce isotope targets with the last steps being a cold rolling [27] before cutting down to its final dimensions. Follow-up studies should be carried out on the effects of hot and cold rolling of these targets on the microstructure and the grain boundary network of these fuel particles. Additionally, EBSD has been recently been coupled to additional techniques such as an in-situ tensile stage to demonstrate how stress affects texture evolutions and grain boundaries directly and can be used to study stress on UAlx materials [28].

Finally, the identification of this “digestion” process as an oxidation process, and specifically intergranular oxidation, opens up many doors to the advanced studies of LEU UAlx based isotope production targets. Having correct nomenclature or further refining a definition for a process opens up a library of information that already exists to help engineer a better product. The oxidation presented here, that is similar to oxidation and corrosion, has existed for a long time and it is advantageous to merge the “digestion” of targets with this already established field. Reciprocally, corrosion science can expand its scope of use by including processes like isotope extraction. This is perhaps the first, if not one of the very few times, where it is favorable to engineer a material to increase oxidation rate. Oxidation studies are normally categorized under “failure analysis” but in this case it is desirable. A new, if not underdeveloped branch of materials science should include the advancement of corrosion or oxidation for extraction, leaching, and purification processes.

References

1. Chezganov, D.S., M.A. Borovykh, and O.A. Chikova, *Prediction of steel corrosion resistance based on EBSD-data analysis.* IOP Conference Series: Materials Science and Engineering, 2017. 192.
2. Kobayashi, S., R. Kobayashi, and T. Watanabe, *Control of grain boundary connectivity based on fractal analysis for improvement of intergranular corrosion resistance in SUS316L austenitic stainless steel.* Acta Materialia, 2016. 102: p. 397-405.
3. Hu, C., et al., *Improving the intergranular corrosion resistance of 304 stainless steel by grain boundary network control.* Corrosion Science, 2011. 53: p. 1880-1886.
4. Kocsisová, E., et al., *Study of the sensitization on the grain boundary in austenitic stainless steel AISI 316.* 2014. 22(341): p. 131-136.
5. Randle, V., *Grain boundary engineering: an overview after 25 years.* Materials Science and Technology, 2010. 26: p. 253-261.
6. Schuh, C.A., M. Kumar, and W.E. King, *Analysis of grain boundary networks and their evolution during grain boundary engineering.* Acta Materialia, 2003. 51(3): p. 687-700.
7. Adlakha, I. and K.N. Solanki, *Structural stability and energetics of grain boundary triple junctions in face centered cubic materials.* Sci Rep, 2015. 5: p. 8692.
8. Muenze, R., et al., *The Fission-Based 99Mo Production Process ROMOL-99 and Its Application to PINSTECH Islamabad.* Science and Technology of Nuclear Installations, 2013. 2013: p. 1-9.
9. Schwartz, A.J., et al., *Electron backscatter diffraction in materials science*. Vol. 2. 2009: Springer.
10. Pan, Y. and B.L.J.S.M.e.M. Adams, *On the CSL grain boundary distributions in polycrystals.[Coincidence site lattice].* 1994. 30(8).
11. Cayron, C.J.A.m., *Quantification of multiple twinning in face centred cubic materials.* 2011. 59(1): p. 252-262.
12. Gertsman, V.J.A.C.S.A.F.o.C., *Geometrical theory of triple junctions of CSL boundaries.* 2001. 57(4): p. 369-377.
13. Reed, B.W., et al., *The structure of the cubic coincident site lattice rotation group.* 2004. 60(3): p. 263-277.
14. Sharma, N.K. and S.J.P.M. Shekhar, *Cut-off deviation for CSL boundaries in recrystallized face-centered cubic materials.* 2017. 97(23): p. 2004-2017.
15. Fortes, M.J.p.s.s., *Coincidence Site Lattices in Non-Cubic Lattices.* 1977. 82(1): p. 377-382.

16. Jadernas, D., et al., *Microstructural characterization of as-fabricated and irradiated U-Mo fuel using SEM/EBSD.* Journal of Nuclear Materials, 2018. 509: p. 1-8.
17. Ralston, K.D. and N. Birbilis, *Effect of Grain Size on Corrosion: A Review.* Corrosion Science, 2010. 66.
18. op't Hoog, C., N. Birbilis, and Y.J.A.E.M. Estrin, *Corrosion of pure Mg as a function of grain size and processing route.* 2008. 10(6): p. 579-582.
19. Ralston, K., N. Birbilis, and C.J.S.M. Davies, *Revealing the relationship between grain size and corrosion rate of metals.* 2010. 63(12): p. 1201-1204.
20. Zhao, M.C., et al., *Influence of Microstructure on Corrosion of As-cast ZE41.* 2008. 10(1-2): p. 104-111.
21. *Gmelin Handbook of Inorganic Chemistry U Supplement Volume B2 Alloys.* 1989: p. 333.
22. Watanabe, T., *Grain Boundary Design for Desirable Mechanical Properties.* Le Journal de Physique Colloques, 1988. 49(C5): p. C5-507-C5-519.
23. Lin, P., et al., *Influence of grain boundary character distribution on sensitization and intergranular corrosion of alloy 600.* Scripta Metallurgica et Matcrialia, 1995. 33(9): p. 1389-1392.
24. al., A.e., *Nuclear Fuel and Method of Fabricating The Same.* Pat. No.: US 2012/0257707 A1, Pub. date: Oct. 11, 2012.
25. IAEA, *Production technologies for molybdenum-99 and technetium-99m.* IAEA-TECDOC-1065, 1999.
26. Pineau, A., A. Amine Benzerga, and T. Pardoen, *Failure of metals III: Fracture and fatigue of nanostructured metallic materials.* Acta Materialia, 2016. 107: p. 508-544.
27. Ryu, H.J., et al., *Development of High-Density U/Al Dispersion Plates for Mo-99 Production Using Atomized Uranium Powder.* Nuclear Engineering and Technology, 2013. 45(7): p. 979-986.
28. Liu, F., et al., *Evaluation of the reliability of twin variant analysis in Mg alloys by in situ EBSD technique.* Journal of Magnesium and Alloys, 2019. 7(2): p. 258-263.

Chapter 4

Digestion of mixed UAl_3-UAl_4 fuel and target analysis

Summary

The majority of fission based medical isotopes are made from uranium-aluminide targets. The majority of the fuel particles within these targets are a mixture of UAl_3 and UAl_4, in either pure forms or a mixture of the two. In this chapter, the digestion of UAl_3-UAl_4 mixed particles is studied. Two sample types are digestion: HEU target pieces and UAl_3-UAl_4 as-fabricated fuel particles. In both sample types, UAl_4 forms a continuous phase with UAl_3 phases as "islands". The weighted average diameter of the UAl_3 phase size within the target is 3.5µm while the weighted average in the as-fabricated fuel is 10.9µm. In the experiments performed here, the digestion of these particles are evaluated by the oxidation depth in the UAl_4 phase and the phase size of UAl_3. Target pieces or as-fabricated fuel were digested in 4M NaOH and taken out at different stages of digestion. Cross sections of the samples were taken to evaluate the progression of the digestion solution within the material.

In the digestion of targets, it was found that digestion occurs in three phases. The first phase is when the cladding is breached by the digestion solution. At this moment, the fuel within the target is exposed to sodium hydroxide and starts to occur around 15 minutes of digestion. The second stage is the advancement of the solution along the dispersed aluminum phase. The aluminum oxide reaches a thickness of 46µm before the fuel falls off into solution and can be digested further. The last stage is the digestion of the UAlx fuel particles. It is found that digestion proceeds along the UAl_4 phase but any further analysis is limited due to the small phase sizes.

In the digestion of as-fabricated particles, it is evident that the oxidation front proceeds along the continuous phase. UAl_3 phase sizes below 2µm are oxidized at the same rate as the UAl_4 phase. After 120 minutes of digestion, the average weighted diameter was reduced to 3.4µm where the cores of the UAl_3 phases are left undigested within the oxidation zone.

Table of Contents

1 Introduction 134

2 Materials and experimental procedure 135

2.1 Sample description and characterization 135

2.2 Experimental procedures.....139

3 Experimental Results.....139

3.1 Digestion of UAl_3-UAl_4 target: stage 1 - target breach.....139

3.2 Digestion of UAl_3-UAl_4 target: stage 2- Advanced oxidation front 141

3.3 Digestion of UAl_3-UAl_4 target: stage 3 – Indiscernible digested fragments.....142

3.4 Digestion of large single grain UAl_3 phases inside a target.....143

3.5 Digestion of UAl_3-UAl_4 fuel – as fabricated.....144

3.6 Summary of results.....147

4 Discussion 149

5 Conclusion.....151

Table of Experiments

Identification	Sample	Solution	Temp (^oC)	Time (min)
Experiment 1	HEU Target	4M NaOH, 4M $NaNO_3$	95	45
Experiment 2	Annealed UAl_3	4M NaOH, 4M $NaNO_3$	95	120

1 Introduction

In the previous chapters, the digestion of UAl_3 fuel particles in caustic media was explored as a function of time. For the first time, an in-depth analysis of how UAl_3 develops into an oxide is revealed by imaging cross sections of digested fuel particles. The way that this process proceeds (surface, triple junction, and grain boundaries), the effects of secondary phases (UAl_2 and aluminum-grain boundaries) and that some grain boundaries are more vulnerable than others, are all valuable information that can be used to optimize the extraction process.

However, the fuel that exists in current targets is more complex in its microstructure and phase morphology. In current isotope production targets, UAl_3 and UAl_4 intermetallics form the majority of the target meat. UAl_3 and UAl_4 are the desired phases because they have been reported to dissolve more readily than UAl_2 in alkaline solutions, which defines the processing yield after irradiation [1, 2]. Therefore, a study of how UAl_3-UAl_4 mixed phase particles would complete the representation of fuel particles in a modern target.

A final target containing predominantly UAl_3 and UAl_4 fuel particles is achieved after a long process of hot rolling and annealing an initial briquette[9] encased in aluminum cladding. The initial target starts with particles of UAl2 dispersed in a pure aluminum phase [3-7]. The use of UAl_2 as a starting material is done as it is easier to synthesis due to its congruent melting point, or that it forms directly from its liquidus, and because it has a higher U-density than UAl_3 and UAl_4. A briquette of UAl_2-Al is transformed into UAlx-Al through a series of hot-rolling steps that is performed to meet the final dimensions of a target [8-10]. In general, fuel particles in a target can have one of five forms: pure UAl_3, pure UAl_4, phases of UAl_4 in a continuous phase of UAl_3, phases of UAl_3 in a continuous phases of UAl_4, or a bi-continuous system.

The conversion of UAl_3-UAl_4 mixed phase particles into an oxide or a yellow cake has not been reported in open literature. Again, this is the case where only the initial products and the end products are reported without any

[9] Briquette is an initial compact composed of fuel and pure aluminum particles. It becomes the fuel zone, also referred to as the meat, once it is encased in cladding and rolled into a target.

knowledge of an intermediate [11-14]. However, there are many ways in which a biphasic solid or eutectic composition can undergo a chemical transformation process. It can undergo a shrinking core model or grain boundary oxidation, like pure UAl_3 fuel particles. Additionally, biphasic material can undergo a dealloying process [15, 16], where one phase is selectively leached or etched away from the more stable phase. Without knowing which process is occurring during digestion, it is impossible to optimize the microstructure of a fuel particle for isotope extraction.

In this chapter, the oxidation of UAl_3-UAl_4 particles is investigated as a function of digestion time. In particular, samples where the UAl_3 phase forms "islands" in a continuous UAl_4 phase is studied. This morphology is chosen as it represents the majority of UAl_3-UAl_4 particles found in targets. The oxidation of the UAl_3 phase is monitored by analyzing the phase sizes at different time points. Samples with different phase sizes are studied to help visualize the effects of oxidation. For large phase sizes, samples were made in an arcmelter and annealed to obtain phase sizes. Additionally, an HEU target was digested to study how this process occurs in a target with small phase sizes. The transformation of UAl_3-UAl_4 fuel into an oxide is studied by SEM cross-sectional image analysis of the fuel particles at different digestion times. The results are analyzed and discussed in order to unravel the dominating mechanism and to propose a model for the digestion process.

2 Materials and experimental procedure

2.1 Sample description and characterization

The digestion of UAl_3 "islands" within a UAl_4 continuous system is studied based on two samples involving different phase sizes. One sample is of UAl_3-UAl_4 fuel particles as found in an HEU fuel plate, while the other is of UAl_3-UAl_4 particles prepared by an arc-melter and annealed. The two sample types represent the ratio of UAl_3 to UAl_4 found in targets, which can vary from 0.33 to 0.66 of UAl_3 by volume [1, 7].

In the first set of samples, pieces of an HEU target were used for the digestion of fuel with small phases. The fuel within a target has particle sizes that range from 1µm to 300µm (Figure A). In Figure A, the lights phases are determined through EDX to be UAl_3 while the dark phase is made of UAl_4. The majority of the particles in the micrograph in Figure 1A are particles where the UAl_4 phase is the continuous phase, with phases of UAl_3 forming islands within the UAl_4 phase.

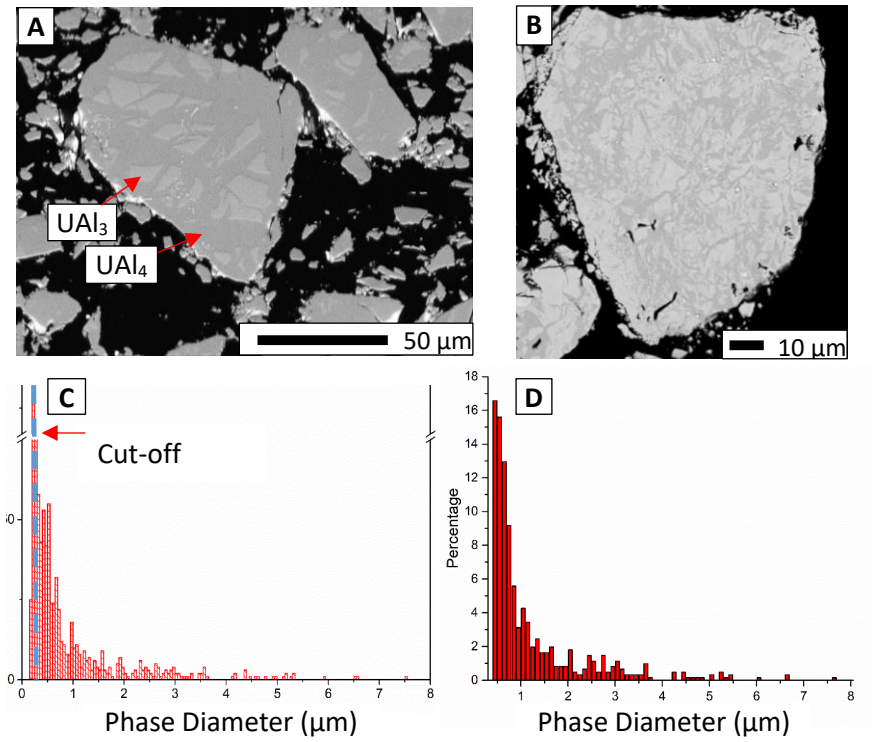

Figure 1) Analysis of fuel in an HEU target. A and B – BSE images of typical UAl_3-UAl_4 mixed particles found in a HEU target; C – raw data of phase sizes with cut-off threshold as suggested by Shannon's theorem; D – UAl_3 phase diameter in percentages.

Quantitative image analysis was performed to characterize the size distribution of the UAl_3 phase. During the digestion process of mixed particles, the evolution of UAl_3 phase size is evaluated as a function of digestion time. To estimate the sizes, SEM images were analyzed through the program Sigma Scan Pro 5 [17]. Backscattered images were used, as voids, UAl_3, and UAl_4 are visible as different intensities due to their different densities. First, a histogram stretch that optimizes the contrast and brightness was performed to isolate the UAl_3 phases, from the UAl_4 phase

and voids. Intensity thresholding method was applied to identify UAl_3 phases, and edge features were eliminated from the data. Fuel particles from the middle and edges of the target were evaluated and the total area analyzed is above 100,000 μm^2.

According to Shannon's sampling theorem, the smallest measurable detail in an image should be at least twice the spatial resolution of the image [18, 19]. To ensure no false UAl_3 areas were counted, the area of 3 pixels was taken to be the smallest measurable feature. At the lowest magnification of 500x, this was found to be 0.3µm which was taken as the threshold limit and the standard for the analysis performed here. Figure 1C, shows the raw distribution obtained from image analysis performed on the fuel particles within the target. The dotted blue line represents the threshold that is permissible in this analysis. Figure 1D shows the corrected distribution. Through this analysis, it was found that the average equivalent diameter of a UAl_3 phase in this HEU target was 1.1 µm while the average weighted diameter was 3.5 µm.

For large UAl_3 phase size fuel particles that are as-fabricated from an arc-melter and annealed was analyzes. This fuel was made by arc-melting natural uranium with aluminum. The ingot was annealed at 700°C for 72 hours. The resulting microstructure can be seen in a BSE image in Figure 2A. In this ingot, the UAl_4 constitutes the continuous phase with areas of UAl_3 (Figure 2B), as it is in an HEU target (Figure 1). Through image analysis, it was found that the ingot is composed of 36±1 vol% UAl_3 and 64±1 vol% UAl_4. Additionally, voids can be seen in the UAl_4 phase, which were calculated to be 5±1% of the ingot by volume. To calculate UAl_3 sizes, an image analysis was performed (Figure 2C), where edge phases and the residuals were omitted. The raw count of UAl_3 diameters are presented in Figure 2E with the corresponding cut-off threshold. The corrected distribution of equivalent phase diameter is presented in Figure 2F. It was found that the average equivalent diameter in this ingot is 3.2 µm with an area weighted diameter of 10.9 µm. When examining the UAl_3 phase, it is found that there are two types of UAl_3 phase sizes which can be distinguished by its size class, shown in Figure 2 D. Type 1 (Figure 2D) are small satellites that make up 60% of UAl_3 phases with equivalent diameters below 2 µm, making up the majority of the UAl_3 phase by number. However, a second population of larger UAl_3 phase (labeled type 2 in Figure 2D) raise the average weighted diameter to 10.9 µm. When comparing sizes, the UAl_3 phase sizes in the as-cast ingot were 3 times larger

in its equivalent diameter size than the ones found in targets both in number and by weighted average.

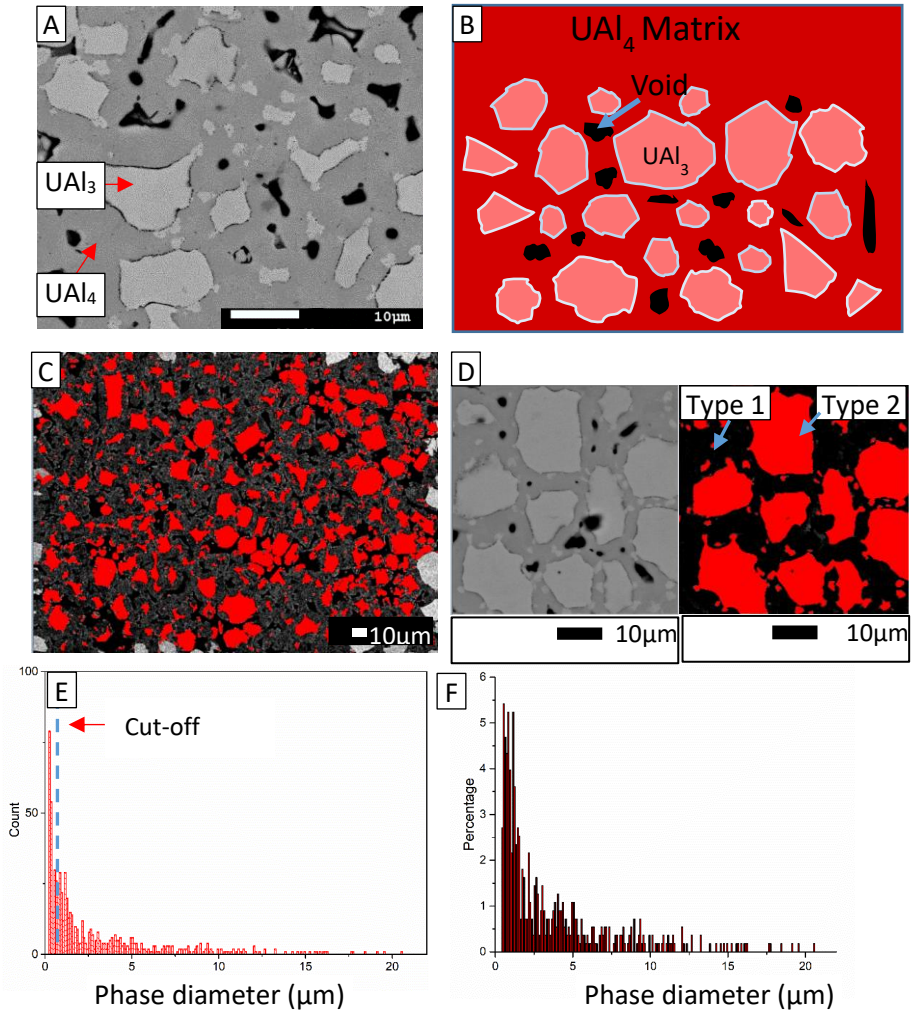

Figure 2) SEM- BSE images of an ingot and UAl_3 phase size analysis. This sample has a continuous phase of UAl_4, with islands of UAl_3 A- BSE image of the ingot, with UAl_3 visible as lighter phases in a darker UAl_4 continuous phase; B- representation of the microstructure; C – image analysis demonstrating the thresholding to identify UAl_3 phase; D – Type1 and Type 1 UAl_3 phase; E – raw data including the cut-off limit; E – UAl_3 phase diameter as percentages in the ingot; F – phase diameter as percentage.

2.2 Experimental procedures

The digestion of target pieces is handled with more care than the digestion of as-fabricated fuel. The digestion of target pieces are performed between 55 and 60°C, i.e. at a temperature which is lower than the near boiling temperature of pure fuel digestions. As mentioned in Chapter 1, the digestion of Al is strongly exothermic (close to 600kcal per 100g Al [11]) as is autocatalytic above its reaction crest of 60°C. Because of this decrease in temperature, the reaction rate of the experiment is much slower than experiments performed at near boiling temperatures. However, this temperature range is more representative of real digestions and is safer to perform. Additionally, the digestion is performed in 4M NaOH and 4M $NaNO_3$ in a digestion bath of 250ml. Four target pieces, each weighing approx. 5 grams were placed in the digestion bath at the same time. One Target piece was taken out at designated time points and was rinsed in a cooling bath of pure water to stop the reaction. The target pieces were prepared for SEM analysis as is demonstrated in Chapter 3.

3 Experimental Results

The digestion of targets have three distinct phases. The first stage is the breach of the target, where the digestion solution breaks through the cladding and can interact with the fuel zone. The second stage is the advancement of the oxidation front along the pure aluminum phase with partial oxidation of the UAlx fuel. The third stage is the final stage, where fully oxidized particles can be found among mixtures of UAlx-UOx particles that have recently passed the oxidation front.

3.1 Digestion of UAl_3-UAl_4 target: stage 1 - target breach

The first stage happens 20 minutes after the emersion of the target pieces into the digester, where the cladding of the target is breached by the digestion bath (Figure 3). In a breach, the meat of the target is exposed to the digestion bath but the UAlx fuel particles have not undergone any digestion. Cracks and voids within UAlx fuel particles are not oxidized at this stage. The dispersant aluminum immediately in contact with the exposed surface and immediately surrounding UAlx particles have started to oxidize. However, most of the dispersant aluminum has not reacted (Figure 3 B). Meat exposure to the digestion bath is a gradual process that occurs around 20 to 25 minutes of digestion.

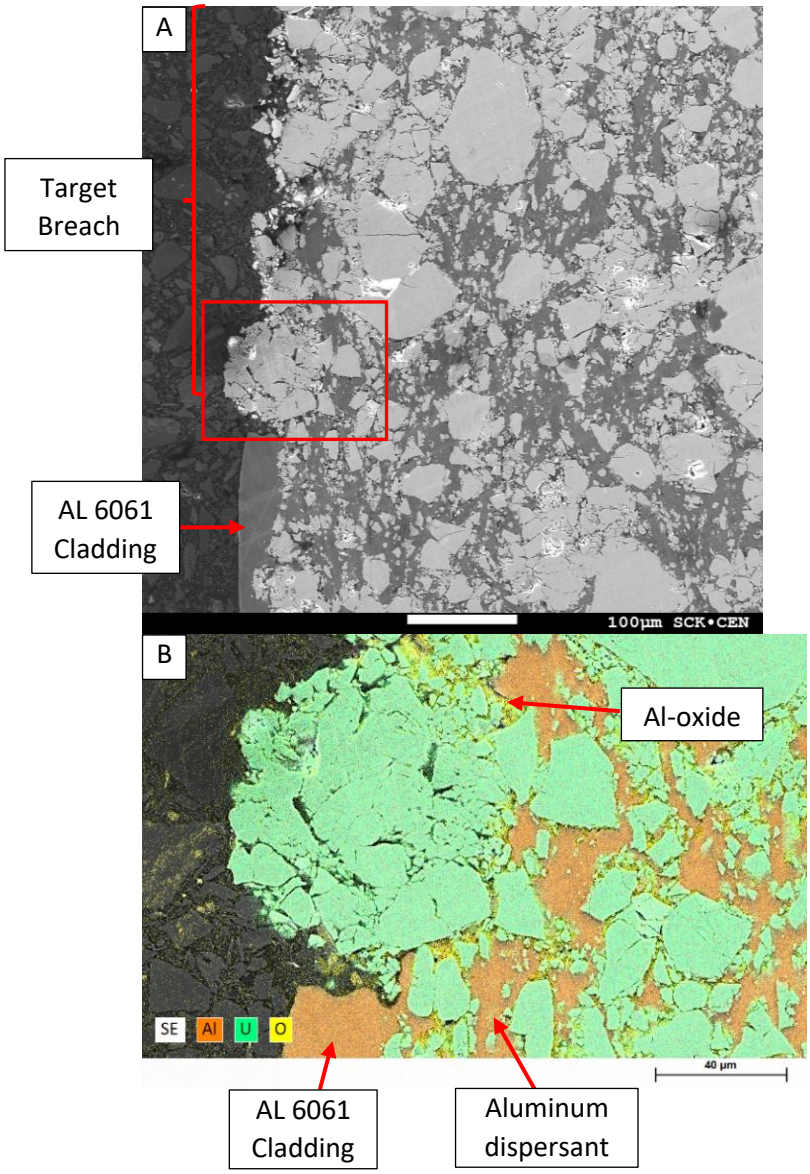

Figure 3) In situ digestion of UAl_3-UAl_4 target. 20 minutes into digestion, a breach of the cladding allows fuel to come into contact with digestion solution. A – SEM image of the target breach, indicating the breaching event and the edge of the AL 6061 cladding. B – EDX elemental map on an SE image of the edge of the breaching event. In this image, Aluminum is orange, uranium is green, and oxygen is yellow.

3.2 Digestion of UAl_3-UAl_4 target: stage 2- Advanced oxidation front

During stage 2 of the digestion process, the digestion solution moves through the dispersed aluminum phase through the target. Stage 2 is distinguished from Stage 1 by the presence of an alumina zone that demonstrates the advancement of the digestion bath (Figure 4A). The alumina oxide originating from the dispersant Al had an average thickness of 31.8 ± 6 µm. The average meat thickness at this stage is 870 ± 4 µm (Figure 4B). The fuel particles on the surface of the alumina-oxide zone can break from the target and can continue to digest in solution. Unlike stage 1 UAlx fuel particles, the fuel particles within the aluminum zone of stage 2 have undergone surface oxidation. In Figure 4C and D, the oxidation of a fuel particle at the edge of the digestion front is presented. In the EDX elemental map (Figure 4D) the oxide has penetrated the UAl_3-UAl_4 fuel particle. The leading edge of the digestion front proceeds through the continuous UAl_4 matrix quicker than

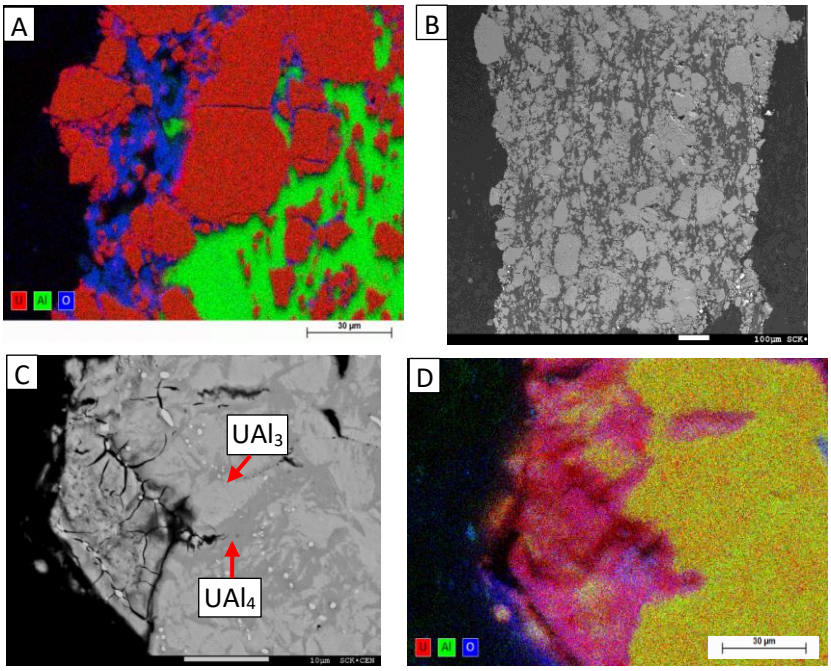

Figure 4) Target corrosion – 15 minutes after breach. A – combined SEM-EDX elemental map of the corrosion zone for U, Al and O. O on the map is associated with the digestion reaction. ; B – BSE image demonstrating the width of the fuel zone; B and C – BSE image of a digested UAl_3-UAl_4 particle at the edge of the digestion front. D combined BSE-EDX elemental map of the particle in image C, of U, Al, and O.

the UAl_3 phases. This behavior is examine more thoroughly in the next section of digested particles with larger phase sizes.

3.3 Digestion of UAl_3-UAl_4 target: stage 3 – Indiscernible digested fragments

30 minutes after the target breach (45 minutes into digestion), the digested fuel particles become mixed oxides. Figure 5A shows that the target meat is reduced to a thickness of 607.5±15µm. Figure 5 C shows the thickness of the aluminum oxide thickness at 45.9±8µm (Figure 4A). This indicates that the digested meat disintegrates after 45 µm past the digestion front. Fuel particles along the leading edge of the digestion front become indiscernible particles of UAlx with UOx in-between them (Figure 5B). This phenomena will be looked at more closely in 3.5.

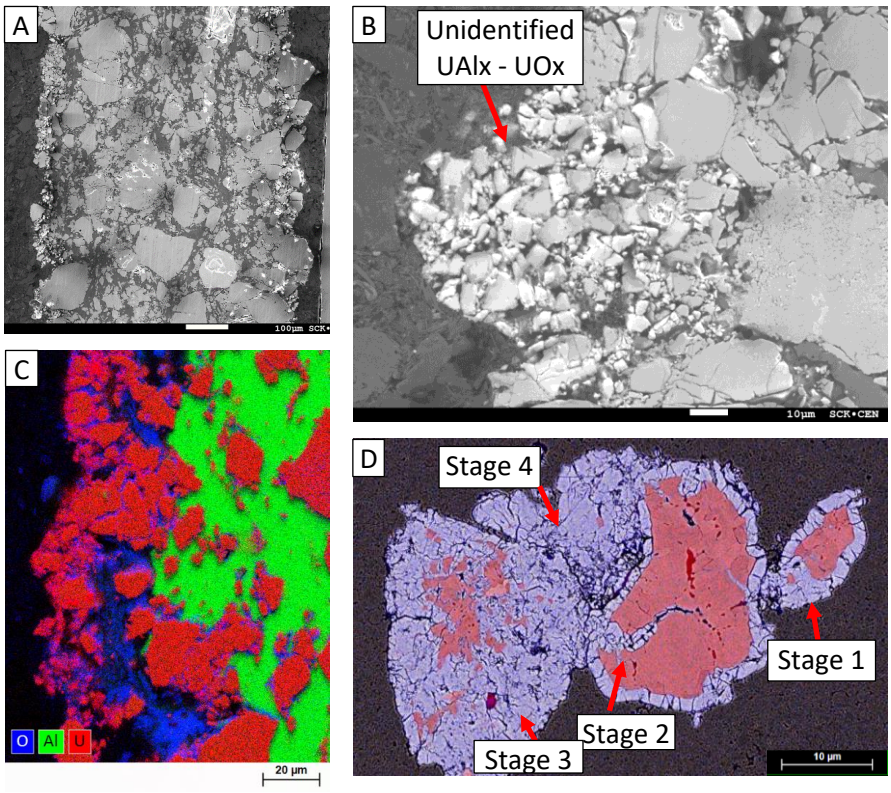

Figure 5) Target corrosion – 30 minutes after breach. A – BSE image demonstrating the thinning of the fuel zone; B – BSE image of an oxidized UAlx particle, with unidentifiable fragments; C – EDX elemental map, demonstrating the oxide front; D – BSE-EDX elemental mapparticles found in the digester, freed from the target. Aluminum is in red and oxygen is in blue. All stages of the corrosion are found at the same time.

Finally, the fuel particles that can be found in solution and free of the target, exhibit all stages of the oxidation process depending on when they were released from the target. Figure 5D shows a BSE image of freed UAlx particles that were in solution 45 minutes after the start of the digestion. Within one sample, we have a fuel particle that has undergone surface oxidation (stage 1), intergranular oxidation at grain boundaries and triple junctions (stage 2), advancement inside the grain (stage 3) and complete oxidation (stage 4).

3.4 Digestion of large single grain UAl_3 phases inside a target

The small UAl_3 phase sizes made the oxidation of mixed particles difficult to analyze. The digestion of mixed UAl_3-UAl_4 particles resulted in mixed UOx phases (Figure 5B) with some indication that the digestion front advances through the UAl_4 phase before the UAl_3 phases turn into an oxide. However, an analysis of the conversion to an oxide is difficult as the phase and grain size of the fuel approaches the minimum detectable feature size when abiding by Shannon's sampling theorem, the oxidation width, or the detection limit of an EDX or EBSD detector. Therefore, an examination of oxidation on larger phase sizes during the same time point of digestion (as Figure 5) was performed.

The digestion of large UAl_3 phases at the edge of the digestion front at 45 minutes of digestion can be seen in Figure 6A. A BSE image of phases labeled 4 and 6 is presented in Figure 6B. UAl_3 phase 4 and 6 have equivalent diameter of 78.3µm and 72.4µm respectively, well above the target average number 1.1µm and weighted average 3.5µm. The phases can be seen to have a uranium rich core (Figure 5 A) with two distinct oxide layers surrounding the particle. An EDX elemental analysis indicated that the layer closest to the phase had an approximate composition of Al: 67 at%, U: 17 at% and O: 15 at%. This layer is designated as $U_xAl_yO_z$. The outer most layer was found to have the composition; U: 33at% and O: 66 at%, indicated as UO_2. The thickness of the UO_2 layer was found to be 2±0.5µm while the $U_xAl_yO_z$ layer was found to be 3.5±1.5µm (Figure 6B).These particles also do not show any internal oxidation, such as those demonstrated in Figure 5D, stages 2, 3 and 4. The absence of any observable oxidation for large phases of UAl_3 was contrary to what has been observed previously in the digestion of UAl_3 of similar phase sizes. With EDX and SEM imaging alone, it cannot be determined if the UAl_4 phase prevented the internal oxidation of the UAl_3 phases, if all of the internal grain boundaries were oxidation resistant or if

another microstructural difference was responsible. EBSD analysis was performed to examine the grains of these phases.

An inverse pole figure (IPF) and a unique grain map of 8 UAl_3 "Islands" shown in Figure 6 A is presented in Figure 6C and D. These maps demonstrate that these phases are large and single grained. These phases do not have any internal triple junctions or grain boundary to oxidize and therefore only underwent surface oxidation. The smaller phases surrounding the "islands" in Figure 6 A are in the oxide phase and are not UAl_3 phases.

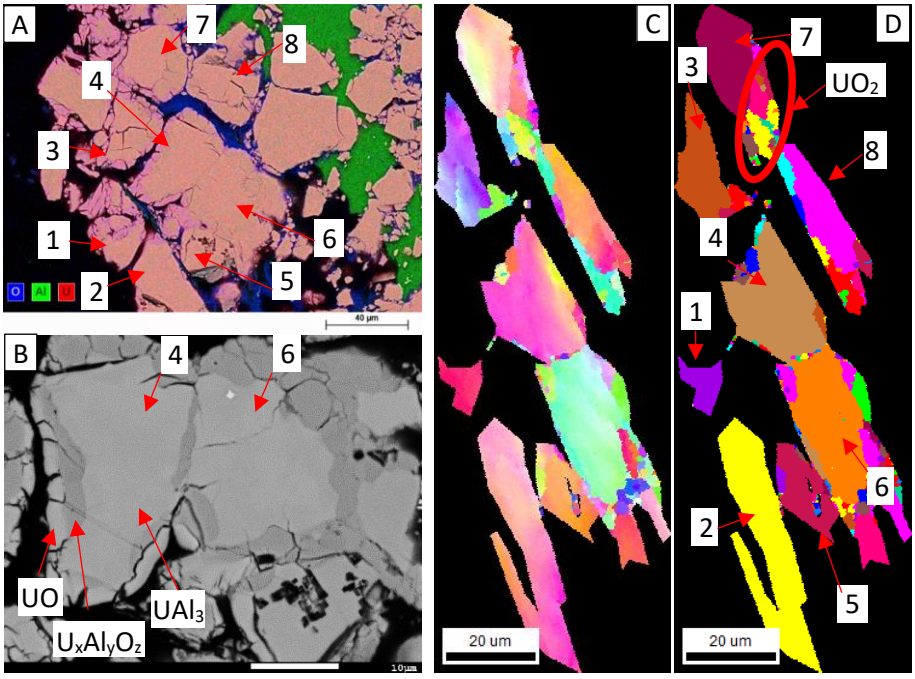

Figure 6) Oxidation of Large UAl_3 phases. A – BSE-EDX elemental map with phase number labeled. B – BSE close up of UAl_3 phases 4 and 6. C – IPF and D -unique grain map of UAl_3 phases.

3.5 Digestion of UAl_3-UAl_4 fuel – as fabricated

In order to see if there is a selective digestion or selective oxidation effect in mixed UAl_3-UAl_4 fuel particles, digestion of fuel with larger phase sizes was needed to be performed in-order to see the different phases that remained after oxidation. To achieve this, a digestion of as-fabricated UAl_3-UAl_4 was performed.

A digestion was performed with particles made from the ingot presented in Figure 2. The digestion solution was identical to the digestions of the target

pieces presented above. The digestion was performed in 250 mL solution of 4M NaOH and 4M $NaNO_3$. Samples were taken out at 20 minutes, 60 minutes, and 120 minutes. The samples were quenched, rinsed, embedded and polished, as demonstrated in chapters 2 and 3. Results from this digestion can be seen in Figure 7.

The digestion of these fuel particles were again found to have three distinct phases. Stage one occurs within the first 20 minutes, where it can be seen that oxidation has predominantly occurred at the surface. Oxidation occurs more favorably on the surface of the continuous UAl_4 phase, while the surface of the UAl_3 phases show little oxidation. Void surfaces within 20µm of the surface were also oxidized.

Stage two occurs between 20 and 60 minutes, where the oxidation front has progressed beyond 30µm within the continuous UAl_4 phase. Within 40µm of the surface, phases of UAl_3 are surrounded by uranium oxide. To quantify this, phase sizes were measured from within 40 µm from the surface of the fuel. The distribution of particle sizes is presented in Figure 7 B in black. The number average was found to be 7.5µm, which is 6.4µm larger than the number average of the whole ingot, while the average weighted diameter was 8.9 µm or 2µm smaller than the average weighted diameter of the whole ingot.

Finally, at 120 minutes, it can be seen that the digestion zone appears as a uniform oxide. In this stage, the UAl_3 phases have also undergone oxidation. The UAl_3 phases are reduced to a few microns in radius. Again, quantification of the UAl_3 phases were performed and its size distribution shows in red, in Figure 7 E. The average phase diameter in number was 2µm while the weighted average was 3.9µm. The weighted average is 7µm smaller than the weighted average of the whole ingot. Voids that are more than 40µm past the digestion front do not show significant signs of oxidation, indicating a limit of the void pathway for reagents to enter the fuel.

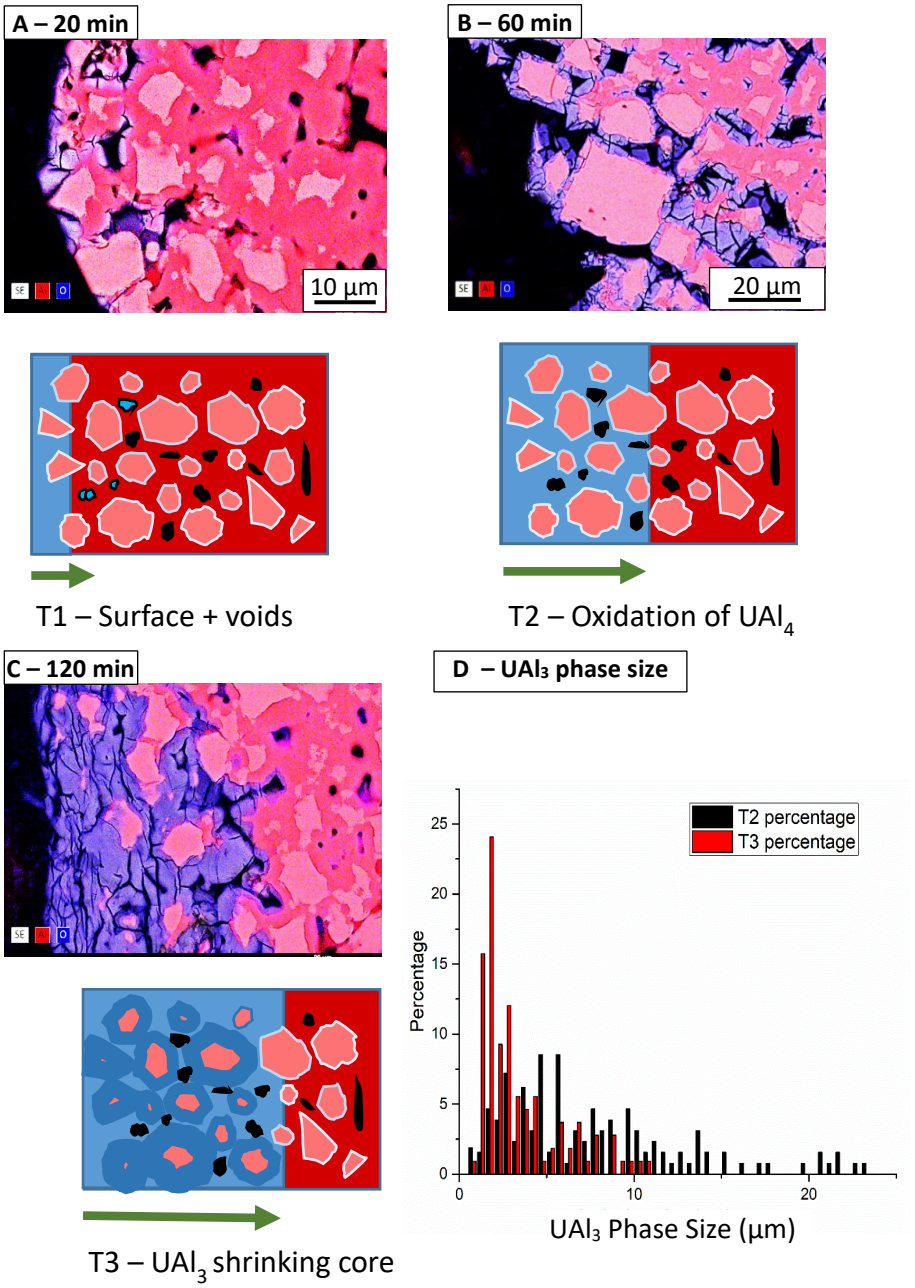

Figure 7) SE-EDX images with its representations of a digestion of mixed UAlx particle. Time of digestion are T1 – 20 min. T2 – 60 min and T3 – 120 min. Oxygen is indicated in blue and aluminum in red. E – UAl_3 phase sizes at T2 and T3 as a percentage of its frequency.

3.6 Summary of results

The digestion of the UAl_3-UAl_4 mixed parties showed significantly different results than UAl_2-UAl_3 mixed particles, and of pure UAl_2 or UAl_3 particles. Unlike UAl_2-UAl_3, The presence of the UAl_4 phase did not stop the digestion of UAl_3 particles, as UAl_2 phases did. In fact, oxidation proceeded along the continuous UAl_4 phase, up to 40µm before the UAl_3 phase started to oxidize. Unlike pure UAl_3 particles, intergranular oxidation, oxidation at GB or TJs, did not play a significant role even for large UAl_3 phase sizes (see also appendix IV).

The digestion of UAl_3-$UAlAl_4$ fuel particles within a target demonstrated many distinct stages of digestion. The first phase is when the solution has digested the cladding and the fuel zone is exposed. From the moment that the target is breached, the aluminum matrix in the meat becomes the first to oxidize. This aluminum oxide layer can penetrate 45µm into the meat before the fuel particles fall off into solution where it can further digest. Once the target is breached and the solution is in contact with the meat, the oxidation front can advance at approximately 8.8µm per minute through one surface of the fuel zone. Once the fuel starts to digest, the oxide of the fuel particle proceeds from the surface of the particle to its interior, having a preference for the UAl_4 phase (Figure 4 B). For particles with small UAl_3 phase sizes, the resulting phases are a mix of UOx and UxAlyOz, or follows the stages of intergranular oxidation, as discussed in chapter 3 (Figure 5).

The examination of large UAl_3 phases within the oxidation zone of a digested target allowed for a better insight into the conversion of the meat into an oxide. The large phases within the oxidation front only underwent surface oxidation, with either one or two layers of oxide. If one oxide layer was present, then it developed as a UO_2 phase. If there was an oxide layer between the UAl_3 phases and the uranium dioxide, it was a found to contain a non-stoichiometric amount of U, Al, and O, likely a UAl_4 phase that has converted into an oxide. All of the phases presented in Figure 6 A, including the one on the leading edge of the digestion front, were single grained UAl_3 phases, with only surface oxidation. The surface oxide thickness on these phases, and of UAl_3 particles presented in chapter 2 and 3, were less than 10µm. This demonstrates that single grained phases and particles of UAl_3 need to have diameters less than 20µm in order to be fully digested. Once the diameters of these phases become larger than this radius, then the

center of the grain becomes immune to digest, and would make medical isotopes unable to be extracted.

The digestion of the as-fabricated particles showed how the oxidation front along the different phases occurred. In as-fabricated particles, there were also three distinct stages of digestion. The first stage, designated T1, showed only oxidation along the UAl_4 at the surface of the particle. During a second stage, designated as T2, there is a preferential oxidation of the UAl_4 phase. This preferential oxidation lead to the oxidation of UAl_4 well before UAl_3 (0-60 minutes) and up to 40 or 50µm into the particle surface. During the last stages of digestion, designated as T3, the UAl_3 phases started to oxidize from its surface to the core.

The evolution of the UAl_3 phase diameters throughout the digestion process was evaluated through imaging analysis. An analysis of the initial ingot showed that the average UAl_3 phase diameter was 1.1µm while the average weighted diameter was 10.9µm. After 60 minutes of digestion the average weighted dimeter decreased by 2µm, which is expected as the digestion solution oxidized the sample. It is at first surprising that the average diameter by number increased to 7.5µm. However, 60% of the phases by number had a diameter below 2µm in the original ingot (Figure 2, E). Effectively, the phase size within the oxidation zone was homogenized by eliminating the smaller but more represented sizes in favor of phases that were larger in diameter than the average surface oxidation of 2µm. The fact that small UAl_3 phase sizes oxidized faster maybe the reason that the oxidation front in UAlx particles in targets do not show a strong selective leaching effect (Figure 4 D) as large phase sizes (Figure 7 C) found in an ingot.

After 120 minutes of digestion, the oxidation of UAl_3 phases progressed. Both the average diameter by number and by weighted averaged reduced to 2µm and 3.9µm respectively. Again, any fuel that does not turn into an oxide or a yellow cake will hold the isotopes in its place and cannot be collected. Although UAl_3 is considered an ideal intermetallic for a production target, large phases or grain sized UAl_3 phases is demonstrably unfavorable for isotope production.

4 Discussion

The research presented here only explores the morphology of UAl_3 phases within a continuous network of UAl_4. A future analysis of UAl_3-UAl_4 particle should include different ratios of UAl_3-UAl_4 phases to complete the analysis that was performed here. Although almost all of the fuel in the examined UAlx target has a UAl_4 continuous phase, it is not the only geometry that can exist. In particular, the effects of a continuous UAl_3 phase with UAl_4 phases should be studied. An understanding of the geometric effects can be aided by this model of oxidation in Figure 8. created by František Štěpánek [20] to demonstrate oxidation or corrosion of a material of two phases. In this model, voxels were randomly arranged with blue cells having a corrosion rate 10 times of the red cells. If we imagine UAl_3 as red voxels and UAl_4 as blue, then we have a picture of the geometric consequences of corrosion or digestion on different phase compositions. In Figure 8A, there is an equal amount of blue and red material as the phases are bi-continuous. Similarly to the sample in Figure 7, the UAl_4 phase, oxidizes through the sample leaving islands of the slower UAl_3 phase creating a "worm effect". If on the other hand, the faster dissolving phase is surrounded by the slower-dissolving phase, it has to wait for the solid-liquid interface before it itself can dissolve, which leads to "surface roughening". This could be an effect if the UAl_3 was the continuous phase with UAl_4 phases. Needless to say, model A in Figure 8 is favorable when it comes to digesting fuel to extract medical isotopes, and model C should be avoided. A future study should include different ratios of UAl_3 to UAl_4 phases to determine the optimum and the cut off ratios suitable for isotope extraction.

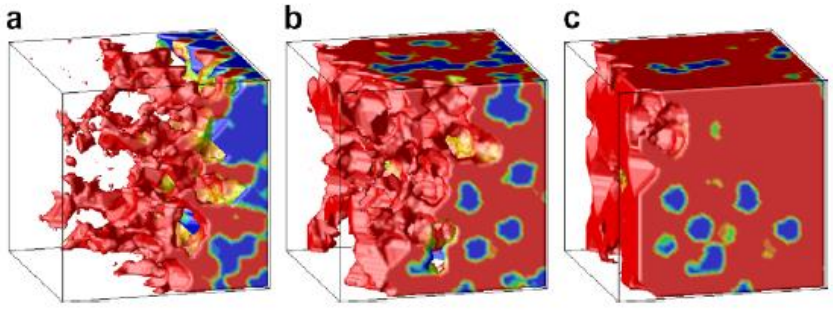

Figure 8) Digestion of a composite material.Partially dissolved samples should the evolution of surface roughness. The red phase has a dissolution rate that is 0.1 of the dissolution rate of the blue phase, and with different compositions of a) x_α = 50%, b), x_α = 70% and c) x_α = 90%

All of the samples in this analysis and the previous chapters were done with cold samples. Cold samples are not irradiated, non-radioactive, and are made with natural or depleted uranium. Because they are cold samples, there are a few crucial parameters that cannot be assessed with these samples. Two main issues to address are the effects of irradiation damage on the digestion of the material and the tracing of molybdenum-99 leaving the fuel and into solution.

Irradiation damage is likely to have little impact on the digestion process, but will create defects that can affect the oxidation process. Target burnups or isotope production are around 3 to 5% leaving most of the microstructure intact. Although interactions between the fuel and the dispersant aluminum or cladding have been found to affect digestion in other alloys [21], the effects in an UAlx fuel and a dispersion of aluminum would also be minimal. Besides UAl_2, all other known alloys or intermetallics of uranium and aluminum can digest and would not impede the process.

However, the tracing of ^{99}Mo during the digestion process should be studied in detailed. As this thesis is the first to present cross sections of digested particles at a function of time, and is done with cold samples, there are no demonstrations in the literature that traces how ^{99}Mo leaves the fuel. Currently, ^{99}Mo yields are commonly calculated by taking the ratio of ^{99}Mo activity in the filtrate to the sum of the activity in the filtrate and the sludge or yellow cake [13], but how it leaves is not reported. The techniques provided here are a crucial step in understanding how this process happens and where ^{99}Mo is left behind in the microstructure. Repeating the experiments performed here with irradiated samples could reveal how ^{99}Mo and other isotopes leave the fuel during digestion. It would be important to couple this analysis to a technique that would be sensitive enough to detect the isotopes in trace amounts, such as electron probe microanalysis (EPMA). Techniques that can detect low concentrations would be required for detecting ^{99}Mo in a target as approximately 6.1 percent of the fissioned uranium result in ^{99}Mo and only a small fraction of the uranium undergoes fission. It is certain that analyzing irradiated and digested particles would show that ^{99}Mo would be left in un-oxidized fuel, such as the center of large UAl_3 phases. However, it may reveal if ^{99}Mo is trapped in oxidized fuel, such as in the center of grains or deep in the fuel particle.

5 Conclusion

Until now, there has been no proposed mechanism on how UAl_3-UAl_4 mixed phase particles digest. In particular, the digestion of UAl_3 phases with a continuous UAl_4 phase was unknown, despite it being the most common morphology within a UAlx isotope production target. It was found that selective oxidation of UAl_4 phase proceeded first, before the oxidation of the phases, and that phase sizes above a few microns took a longer time to digest. Different strategies can be made knowing that selective oxidation is a key step in the digestion of mixed phase particles.

Dealloying or selective oxidation, is known in many industries including drug delivery of pharmaceuticals, detergents, or agrochemicals into a solution. All of these products are composite materials with an active component that needs to be released (radio isotopes, antibiotic, surfactants, and fertilizers respectively) and an auxiliary element (excipients, fillers, and binders) [20]. In medicine for example, a filler might be added to slowdown the release of the active component, which can be in a separate phase that readily dissolves in the stomach. When other components (including porosity) are present, the release rate will generally be different from that of the pure phases separately. The effective digestion rate may be increased or decreased, depending on the intrinsic dissolution rate of the other components, their amount in the volume of space, and their relative spatial arrangement in the material microstructure.

In the case of UAlx fuel particles, there are many strategies in microstructural engineering to either enhance or decrease the oxidation rate. Already covered on decreasing the oxidation rate is the addition of UAl_2 phases, the addition of low-energy grain boundaries, and the addition of large grains in pure UAl_3 fuel. In this analysis of UAl_3-UAl_4 fuel, large UAl_3 phases and single grained phases are added to this library of digestion resistant UAlx designs. Although these strategies are not good for isotope production, it may find its use in fuel targets. UAlx plates have been known to fail due to pin-hole corrosion where UAlx fuel was lost during irradiation [22]. To help reduce the amount of fuel that is lost in an incident, Accident tolerant fuel (ATF) is being developed. ATF is designed to offer better performance during normal, transient and accident scenarios. Near-term concepts for ATF, which provide short-term and fast implementing solutions, include additives to standard fuel pellets to improve performance, the addition of coatings, or improved

steel cladding [23-25]. Perhaps, a near-term solution could be in the improved microstructure of the fuel itself. In the case of UAlx fuel targets, large single-grained phases could be a near-term solution.

For the purposes of isotope production, digestion susceptible fuel needs to be designed in order to extract isotopes. In previous chapters, it was demonstrated that aluminum rich grain boundaries, small grain sizes in pure UAl_3 fuel, and high energy grain boundaries were found to favor oxidation. To add to the library of digestion susceptibility in UAl_x mixed particles, is that there should be small phases of UAl_3 in a continuous network of UAl_4. The phase size of UAl_3 phase would ideally be below 10μm to ensure its conversion to an oxide. The porosity clearly has an impact in transporting the digestion fluid into the fuel particle. However, a quantitative effect of voids in the advancement of the digestion front is out of the scope of this study.

References

1. Conturbia, G.L.C.R., et al., *Phase quantification in UAlx-Al dispersion targets for Mo-99 production.* Journal of Nuclear Materials, 2018. 509: p. 465-477.
2. Cols, H.J., P. R. Cristini, and A.C. Manzini, *Mo-99 From Low-Enriched Uranium.* International Meeting on Reduced Enrichment for Research and Test Reactors, Las Vegas, Nevada, Outubro, 2000: p. 1-6.
3. Ryu, H.J., et al., *Metallurgical considerations for the fabrication of low-enriched uranium dispersion targets with a high density for 99Mo production.* Journal of Radioanalytical and Nuclear Chemistry, 2014. 305(1): p. 31-39.
4. Ali, K.L., et al., *Development of low enriched uranium target plates by thermo-mechanical processing of UAl2–Al matrix for production of 99Mo in Pakistan.* Nuclear Engineering and Design, 2013. 255: p. 77-85.
5. Ryu, H.J., et al., *Development of High-Density U/Al Dispersion Plates for Mo-99 Production Using Atomized Uranium Powder.* Nuclear Engineering and Technology, 2013. 45(7): p. 979-986.
6. Mushtaq, A., *Specifications and qualification of uranium/aluminum alloy plate target for the production of fission molybdenum-99.* Nuclear Engineering and Design, 2011. 241(1): p. 163-167.
7. *Non-HEU production Technologies for Molybdenum-99 and Technetium-99m.* IAEA Nuclear Energy Series, 2013(No.NF-T-5.4).
8. Souza, J.A.B.d. and M. Durazzo, *Fabrication procedures for manufacturing high uranium concentration dispersion fuel elements.* 2011.
9. Durazzo, M. and H.G. Riella, *Procedures for manufacturing nuclear research reactor fuel elements*. 2015: LAP LAMBERT Academic Publishing.
10. Kaufmann, A.R., *Nuclear Reactor Fuel Elements: Metallurgy and Fabrication*. 1962: Interscience Publishers.
11. Muenze, R., et al., *The Fission-Based 99Mo Production Process ROMOL-99 and Its Application to PINSTECH Islamabad.* Science and Technology of Nuclear Installations, 2013. 2013: p. 1-9.
12. Lee, S.-K., G.J. Beyer, and J.S. Lee, *Development of Industrial-Scale Fission 99Mo Production Process Using Low Enriched Uranium Target.* Nuclear Engineering and Technology, 2016. 48(3): p. 613-623.

13. A. V. Gelis, et al., *ANL progress in developing an leu target and process for mo99.* RERTR 2003, 2003.
14. Gelis, A.V., et al., *ANL progress on the Cooperation with CNEA for the MO99 Production.* RERTR 2004, 26 International meeting on Redduced Enrichment for Research and Test Reactors, Jan 2004.
15. Snyder, J., et al., *Stabilized nanoporous metals by dealloying ternary alloy precursors.* 2008. 20(24): p. 4883-4886.
16. Zhang, Z., et al., *Generalized fabrication of nanoporous metals (Au, Pd, Pt, Ag, and Cu) through chemical dealloying.* 2009. 113(29): p. 12629-12636.
17. *SigmaScan Pro 5, SPSS inc.:2010.*
18. Cappia, F., et al., *Critical assessment of the pore size distribution in the rim region of high burnup UO2 fuels.* Journal of Nuclear Materials, 2016. 480: p. 138-149.
19. Nagabhushana, S., *Computer vision and image processing*. 2005: New Age International.
20. Štěpánek, F., *Effect of microstructure and pure component properties on the dissolution rate of a binary composite material.* Computational Materials Science, 2008. 44(1): p. 145-151.
21. Sameh, A. *Production of fission Mo-99 from LEU uranium silicide target materials*. in *Invited Papers on Symposium on Isotope and Radiation Applications*. 2000. ROC.
22. Kaminski, M.D., *Aqueous Corrosion of Aluminum-Based Nuclear Fuel.* ANL-CMT-03/1, 2003: p. 133.
23. Zinkle, S.J., et al., *Accident tolerant fuels for LWRs: A perspective.* 2014. 448(1-3): p. 374-379.
24. Ott, L.J., K.R. Robb, and D.J.J.o.N.M. Wang, *Preliminary assessment of accident-tolerant fuels on LWR performance during normal operation and under DB and BDB accident conditions.* 2014. 448(1-3): p. 520-533.
25. Savchenko, A. *The issue of novel trends in fuel alloying to reduce interaction*. in *Proceedings of the Research Reactor Fuel Management (RRFM-2018) Conference, Munich, Germany, 11.03-15.03*. 2018.

Part II

Qualification and digestion of U_6Mn fuel

Introduction

Bringing the use of a new fuel from theory to practice in isotope production requires many steps and demonstrations of the whole process line. This includes safety analysis, measurements of its physical properties, proofs of concepts, and much more. Some requirements to bring a new process to the market are more defined, like the guidelines from the International Atomic Energy Agency (IAEA) or the Department of Energy (DoE), and some more practical like specifications from clients and manufacturers. In all cases, the physics and chemistry of a new process must be fully demonstrated to deliver a product that is safe, reliable, and performs consistently to standard.

Examining the microstructure of a new fuel is important as it controls the physical and chemical performance of the material. Understanding the microstructure of a fuel leads to an understanding of its initial physical and chemical properties. It is important in fuel fabrication, irradiation, and chemical processing. In UAlx target that are used for isotope production, the microstructure has already been known through its use as a fuel target. All of the original medical isotope targets are just a conversion of fuel targets used in power plants. As both have to withstand similar conditions, its performance criteria was kept the same and so was its microstructure. The only significant difference is that isotope production targets are irradiated for only a few day where as fuel targets are in operation for months.

In order to make the first steps towards the use of U_6Metals in isotope production, its production via arc-melting, its microstructure, and calorimetry was performed and is presented in chapter 5. This study marks the first in a long set of studies to qualify the fuel. Studying its microstructure together with a calorimetric analysis, can give us many insights into how it will perform in production, irradiation, and digestion

The qualification of fuel requires many demonstrations that will ensure that the fuel, target, and target assembly will perform in a predictable way in both normal and critical conditions. Qualification is normally separated into the categories: Properties of un-irradiated fuel, fuel meat and fuel element as-manufactured properties, fuel meat and fuel element irradiation properties, and fuel assembly properties [1]. Essentially, qualifications are performed to ensure the safety of the all of the components that go into a nuclear reactor.

Good practices for the qualification of high density low enriched uranium for isotope production

The IAEA provides guidelines for the good practices in qualification of high density low enriched uranium for research reactor fuels [1]. These guidelines include the recommendation for measuring the exothermic energy release up heating. This recommendation comes from the point of view of a failure condition, rather than in normal operating conditions. In most cases and in standard conditions, the reaction rate between the fuel and aluminum cladding in a target is exothermic, but small when all components remain as solids. However, if portions of the target become molten, the reaction rate could increase rapidly and be difficult to control. The quantity and rate of heat generation from a fuel-matrix-cladding interaction should be measured as a part of qualification, because exothermic reactions are one source of heat that is considered during the analysis of an accident resulting in fuel element temperatures approaching the cladding solidus temperature. These measurements are normally performed on differential thermal analysis or differential calorimetry techniques to satisfy qualification guidelines for new fuels. A calorimetric analysis of Uranium-Manganese binary alloys are presented in chapter 5 to further our understandings of these alloys and to conform to target qualification standards.

Chemical qualification of new fuel for isotope production

Although the IAEA's recommendation for qualification is thorough and ensures target safety, it is directed towards fuel targets and not isotope production. As such, it does not consider any chemical processing steps needed to extract isotope from the target. Currently, there is no equivalent set of qualification standards for target after irradiation and for extraction.

Regardless if the chemical processing is done in an acidic or basic environment, the microstructure of the fuel will undoubtedly affect its dissolution or digestion process. In chapter 5, the microstructure of uranium-manganese alloys is detailed for this reason. A whole range of compositions from Pure U_6Mn, U_2Mn, and any composition in-between is considered in this study as it is for final target production. This study on its microstructure will be used in the experiments of digestion. The digestion and chemistry of U_6Mn is explored in chapter 6. U_6Mn is first digested in standard NaOH and $NaNO_3$ to see how it performs in a digestion that is identically used for UAlx fuels. Following, U_6Mn is digested with KMnO4 to see how an oxidant can improve the digestion process. To end part II of this thesis, chapter 7 gives guidelines and an outlook on implementing U_6Mn based medical isotope production targets.

References

1. *Good Practices for Qualification of High Denstiy Low Enriched Uranium Research Reactor Fuels.* IAEA Nuclear Energy Series, 2009(No. NF-T-5.2).

Chapter 5

Microstructure and calorimetric analysis of the U-Mn binary system[10]

[10] This chapter is adapted from a published article: Cea, Andrew Ken, et al. "Microstructure and calorimetric analysis of the UMn binary system." *Journal of Nuclear Materials* 514 (2019): 380-392.

Summary

The microstructure, growth kinetics, and the high temperature phase equilibria of the U-Mn binary system are investigated using differential scanning calorimetry, SEM, EDX spectrometry and XRD. Alloys with various compositions are prepared in a positive-pressure arc melting furnace in order to examine all possible phase changes within the system. Phase composition and morphology were analyzed using XRD, SEM and EDX. Transformation temperatures and enthalpies have been assessed pertaining to: (i) allotropic phase changes αMn → βMn → γMn →δMn, (ii) two eutectic isotherms UMn_2 + βMn → L and U_6Mn + UMn_2 → L and (iii) melting transitions as a function of composition. The development of the two intermetallic phases U_6Mn and UMn_2 are observed. UMn_2 formed with a faceted morphology in a matrix of U_6Mn, while grain boundary decomposition is found of UMn_2 in αMn. The transformation temperatures are compared to existing phase diagrams and are slightly higher than reported in literature. Experimental observations of the allotropic transformations of αMn to βMn and βMn to γMn are in agreement with a calculated phase diagram. The eutectic composition for UMn_2 and αMn is found to be 55 wt%Mn, in agreement with previously reported values, while the enthalpy of fusion associated with this eutectic point is found to be 54±6.5kJ mol^{-1}. The enthalpies of formation for the two intermetallic phases U_6Mn and UMn_2 are 71±8.5 kJ mol^{-1} and 42±5 kJ mol^{-1} respectively.

Table of Contents

1 Introduction 164

2 Phase equilibria and thermochemical information on U-Mn 166

3 Experimental Methods 168

3.1 Alloy synthesis and preparation 168

3.2 Microstructural characterization and composition analysis 171

3.2.1 Scanning electron microscopy 171

3.2.2 Image analysis 172

3.2.3 X-ray diffraction 172

3.3 Thermal Analysis 173

4 Results 173

4.1 Microstructure Characterization 173

4.1.1 Sample 2: U-Mn5 174

4.1.2 Sample 3: U-Mn16 174

4.1.3 Sample 4 and 5: U-Mn32 and U-Mn35 175

4.1.4 Sample 6: U-Mn55 176

4.1.5 Sample 7 and 8: U-Mn75 and U-Mn92 177

4.2 XRD 178

4.3 Transformation temperature and U-Mn phase diagram 180

4.4 Effects on heating rates and temperature variations 184

4.5 Enthalpies of transformation 187

5 Discussion 189

6 Conclusion 192

1 Introduction

The search for high-density fuels to convert from high-enriched uranium (HEU) to low-enriched uranium (LEU) fuels has been a long standing issue with global efforts to reduce enrichment for civilian applications [1]. For instance, the conversion of material test reactor (MTR) driver fuel required the development of high U density fuels. Historically, medical-radioisotope targets bear many similarities with regular MTR fuel plates, both in form (a dispersion of U particles in an Al matrix, in Al cladding) and in fuel type. For MTR driver fuel, the development of new high density fuels for the conversion from HEU to LEU is driven by the compensation of loss in neutron flux, while for radioisotope targets it is to compensate for a loss in isotope yield.

However, fuels for isotope production come with different challenges. In addition to needing a high U-density, a newly developed fuel for isotope production must be capable of undergoing chemical digestion and extraction processes, which often disqualifies newly developed LEU MTR driver fuels. Uranium silicide fuel for example was developed for low to moderate power research reactors [2]. However, difficulties in dissolving the fuel after irradiation [3] became problematic and using conventional alkaline or acidic dissolution processes were not efficient. Similarly, uranium-molybdenum alloys, developed for high power research reactors [4, 5], are not suitable for Mo-99 production as the Mo-98 would dilute the Mo-99 produced and reduce its specific activity [6].

The U_6Me intermetallic compounds (Me = Mn, Fe, Co, and Ni) have been considered and experimentally tested for some time already. U_6Me alloys were studied primarily for their density (U density of approx. 17.0 g cm^{-3}). However, their poor irradiation performance disqualified them for high burn-up applications [7, 8]. In light of low-burn up applications, such as medical-radioisotope production, have these compounds resurfaced. For instance, to have the desired burnup of 9-12%, a typical Mo99 targets would have to be irradiated for 200 hours at a thermal neutron flux of approximately 2E14 n/cm^2 -s. UAlx fuel that is currently used worldwide for Mo99 production is qualified to moderate Burnup (approx. 30%)[1]. In comparison, it has been demonstrated that mini-plates made of U_6Mn with 6.3 gU/ cm^3 and a nominal fuel-volume loading of 42% behaved well at 53% burnup (i.e. neither extreme swelling nor delamination was observed) [9]. This preliminary result

demonstrates that U_6Me compounds could be a potential fuel for isotope production.

The alloy systems of uranium with first row transition metals have many similarities both crystallographically and thermodynamically. All systems form a high density intermetallics in the form of U_6Mn, U_6Fe, U_6Co, and U_6Ni. This family of intermetallics are isostructural as tetragonal with the space group I4/mcm. UFe_2, UMn_2 and UCo_2 are also isostructural with the space group Fd-3m. Together with the pure solution phases, the binary diagrams of these alloys are constituently comparable. As U_6Mn has the highest density in this family, it is ideal for future isotope production targets to increase isotope yield.

The U-Fe system is well studied as a component of metallic fuel fast reactors or as an interaction product of fuel and cladding, among other things [10-12]. In comparison, not much has been published on the properties of U-Mn alloys. Because of the lack any characterization on the whole U-Mn binary system, this paper seeks to provide experimentally measured calorimetric data and microstructural analysis on these alloys and to critically discuss these. This is impart to satisfy good practices for qualification of research reactor fuels[13], in understanding basic properties of un-irradiated fuel, and in fuel meat and fuel element as-manufactured properties. A second aspect is to obtain fundamental knowledge about the physical-chemical properties of these alloys, as this knowledge is unavailable. Additionally, the microstructure and composition of the fuel can affect its chemical properties. For example, it may be found that the digestion or dissolution of U_6Mn is more difficult than UMn_2, in the same way that UAL_2 is more difficult to digest than UAL_3 and UAl_4 [14]. For this reason, a broad spectrum of alloys need to be studied to understand the whole system.

To investigate these alloys, buttons will be prepared in an arc melter. The composition of these buttons will be examined with X-ray diffraction (XRD) and imaged with scanning electron microscopy (SEM) together with energy dispersive X-ray (EDX) spectroscopy. Finally, differential scanning calorimetry (DSC) will be used to study transition temperatures and enthalpies of transition. Before further assessment, the existing knowledge of the high temperature phase equilibria and enthalpies of formation of the U-Mn binary system is summarized in the next section.

2 Phase equilibria and thermochemical information on U-Mn

There are only a few publications on the U-Mn binary phase diagram based on experimental research available in open literature. Wilhelm and Carlson (Figure 1)[15] systematically studied the U-Mn system by melting metals with self-induction and analyzed them with XRD and optical microscopy, and with thermal analysis. The resulting experimental phase diagram (Figure 1) shows that:

- The maximum solubility of Mn in αU is negligible at room temperature.
- Mn reaches a maximum solubility of approximately 1%wt in beta and gamma uranium at 745°C, while decreasing in the beta uranium region to 0.25%.
- The addition of 6%wt Mn steeply reduces the melting temperature of U from 1132 to 716°C .
- The Mn rich side of the diagram by contrast has no defined solvus or solidus and the maximum solubility in each Mn allotrope is not indicated.
- There are two stoichiometric intermetallic phases of U_6Mn and UMn_2.
- Eutectic points exist at 6%wt Mn between U_6Mn and UMn_2 at 715°C, and 55%wt Mn at 1035°C between UMn_2 and βMn.

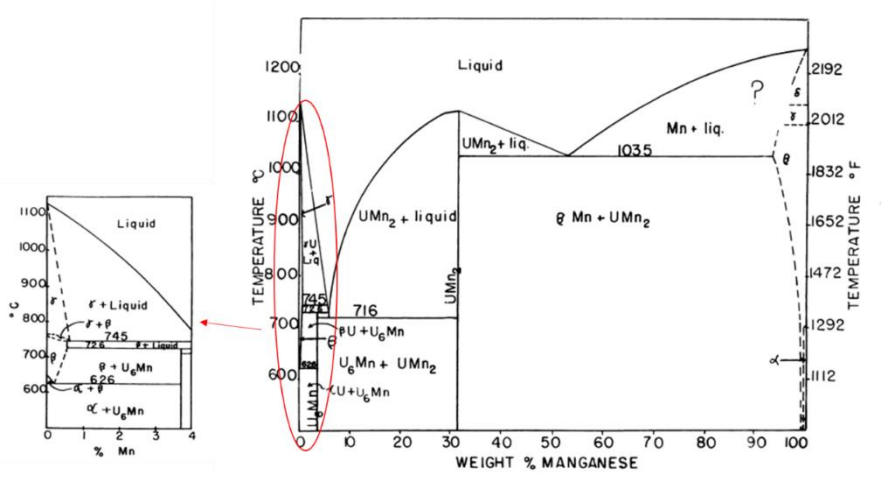

Figure 1) U-Mn phase diagram. The uranium rich region is highlighted [15].

Both sample preparation and experimental conditions can have an effect on measured transition temperatures and enthalpies [16, 17]. However, the study by Wilhelm does not mention how the samples were prepared for thermal analysis measurements, and how the measurements were performed. The effects of sample preparation on thermal analysis and thermal lag on transition temperatures could therefore not be evaluated.

Another phase diagram was published by Hansen [18], primary predicated on Wilhelm's work, with some considerations on other crystallographic studies [19, 20]. Here, it is noted that γMn is stabilized to room temperature by small additions of U, and that βU can be kept metastable at room temperature by small additions of Mn. The Mn rich portion of this diagram is modified from Hansen to reflect the stability of the different Mn allotropes, although no clear values were determined. This diagram was later redrawn by Massalski [21] based heavily again on the experimental work by Wilhelm and Hansen. Here, the allotropic transitions in Mn and U are clearly marked. However, the solvus and solidus on the Mn side are still absent.

Recently, a theoretical phase diagram based on the CALPHAD method has been assessed by Liu *et al* (Figure 2)[22]. The Mn rich portion of the phase diagram was completed and the maximum solubility of U in β-, γ-, and δMn was calculated to be 2.96 wt%, 1.71 wt%, and 1.29 wt% respectively. The

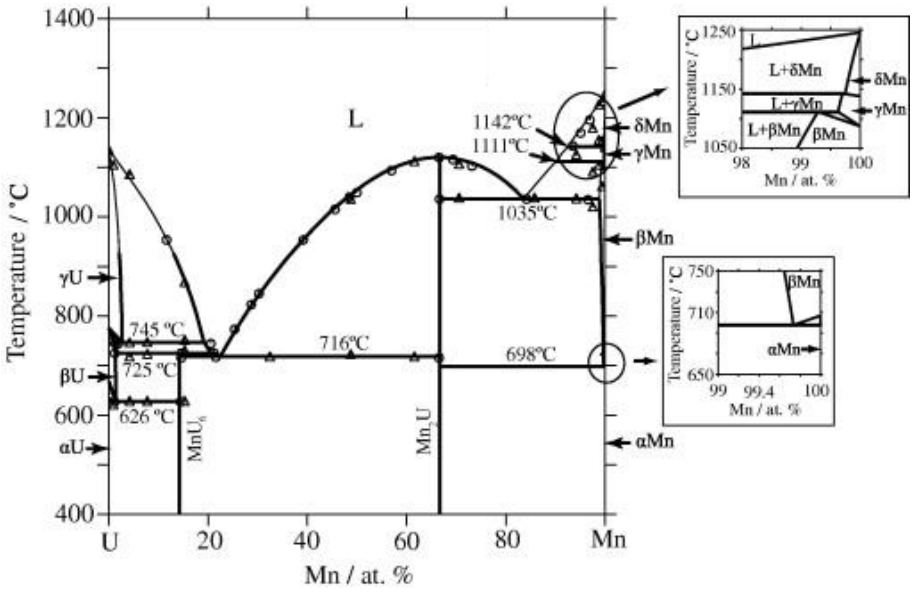

Figure 2) Calculated phase diagram with the Mn rich portion highlighted (encircled) [22]

calculated phase diagram is in agreement with Massalski involving some differences with Wilhelm in the Mn-rich region.

Finally, enthalpies and entropies have been determined for a few U-Mn alloys. Differential Scanning Calorimetry (DSC) experiments on U glasses with first row transition metals has been performed by Northeastern University [23]. Although the crystallization behavior of these glasses was the focal point of their study, their DSC experiments provide estimated enthalpies for the compositional range between U-Mn 20 and 35.3 %wt. Additionally, thermodynamic properties were investigated by Electromagnetic Field (EMF) measurements for the temperature range 660°C to 860°C (Table 1)[24].

Table 1) Table of enthalpies, entropies, and Gibbs free energy, at 700°C as obtained using EMF measurements [16].

U Fraction	Enthalpy	Entropy	Free Energy
U_x	$-\Delta\bar{H}_U$ kJ/mol	$-\Delta\bar{S}_U$ J/mol•K	$-\Delta\bar{G}_U$ kJ/mol
0-0,333	38.07±4.6	12.47±3.9	26.36±1.12
0,333-0,857	12.64±2.9	12.21±3.0	0.79±0.29
U_x	$-\Delta H$ kJ/mol	$-\Delta S$ J/mol•K	$-\Delta G$ kJ/mol
UMn_2 - 0,333	12.68±1.5	4.17±1.9	8.97±0.42
U_6Mn - 0,857	12.55±2.5	10.32±2.2	2.51±0.33

3 Experimental Methods

Sample preparation, characterization, and analysis were performed to examine each step of the alloy fabrication process and analysis.

3.1 Alloy synthesis and preparation

A series of U_xMn1_{-x} binary alloys were made, where compositions are strategically chosen to represent each crystallographic and physical transition in the U-Mn binary phase diagram (dotted red lines in Figure 3). Unless stated otherwise, the alloys in this study will be identified by their composition of Mn by weight or sample number.

Sample 1: U starting on the uranium rich region, the three allotropes of uranium can be observed with a pure uranium sample.

Sample 2: U-Mn5 is an alloy with a composition of 5wt% Mn, representing U_6Mn with minoring amounts of UMn_2.

Sample 3: U-Mn16 represents a composition region that is phase mixture of U_6Mn (72%) and UMn_2 (28%).

Sample 4: U-Mn32 a sample of UMn_2 was made to represent the second intermetallic that can be formed between U and Mn.

Sample 5 U-Mn35 represents the first manganese rich alloy, where manganese saturates the system and can no longer form an intermetallic upon its solidification process.

Sample 6: U-Mn55 represents both an eutectic composition, point, and the second eutectic in the U-Mn system, with UMn_2 (53%) and pure Mn (47%) as its components.

Sample 7: U-Mn75 represents a sample that under goes all allotropic transitions of Mn (75%) and the melting of UMn_2 (25%).

Sample 8: U-Mn90 similar to sample 7 and 6, where the composition is made up of Mn (98%) and UMn_2 (1%).

Sample 9: Pure Mn represents all allotropic phase transformations of manganese.

All samples were made in an Arc 200 cold crucible arc melting furnace under highly pure argon gas. Before melting, both metals (natural uranium and 99%Mn) were stripped of its surface oxide layer. The surface oxidation layer on the uranium was removed with 60 % by volume nitric acid and wiped with acetone while manganese oxide on the manganese chips were sanded with silicon carbide paper and rinsed in acetone. Once the precursors were loaded into the copper hearth, the furnace chamber was put under a vacuum of $4x\ 10^{-3}$ mbar, backfilled with argon, then vacuumed a second time to $2.3\ x10^{-4}$ mbar for one hour to ensure that as little oxygen is present in the chamber while arc melting.

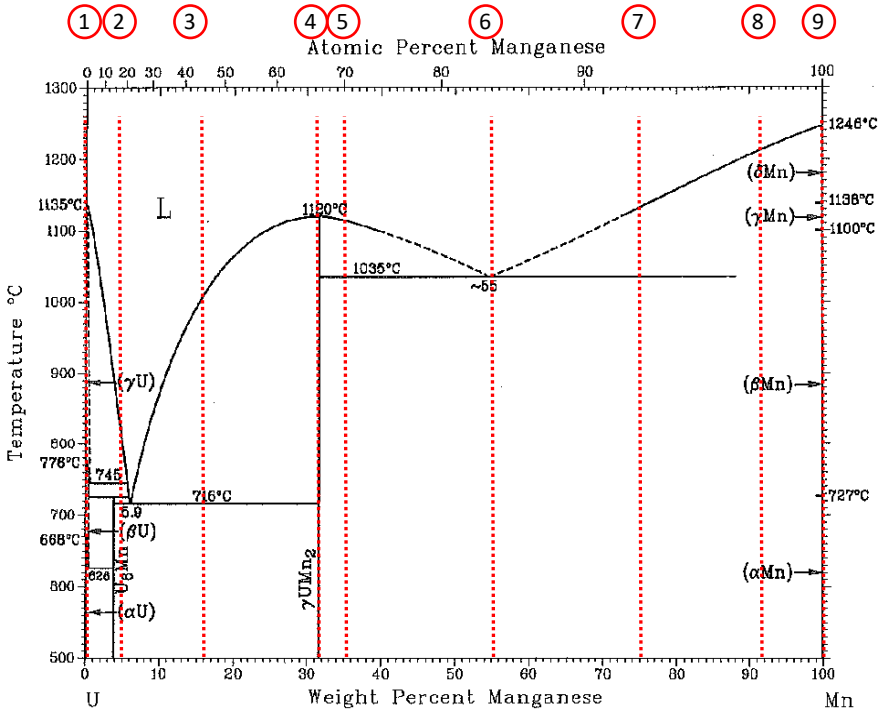

Figure 3) U-Mn Binary Phase diagram with samples and their thermal path in a calorimetry experiment indicated in red. Diagram extracted from [15]

A difficulty in preparing Mn alloys is the loss of Mn by vaporization or distillation, as the vapor pressure of Mn at its melting point is greater than one millimeter Hg. To reduce the loss of Mn, arcmelting was performed in at 150mbar. Some Mn was still lost and a hyper-stoichiometric amount of Mn was added to compensate. To ensure homogeneity, each alloy is flipped and melted three times. Each button is weighed before and after melting and weight loss is considered to be purely Mn in origin.

Each alloyed button was cut in half, embedded, and polished for SEM and EDX analysis. After the buttons were inspected by imaging, samples were prepared in powder form for XRD and TGA analysis. Each button was ground into a powder by either a zirconia coated ball-mill for the alloys with high U content, or crushed in a mortar and pestle for the alloys with high Mn content (Table 2). Initially, samples were ground under argon. However, powders immediately react in air and surface oxidation is found to be inevitable. For the experiments described below, both grinding processes

were performed in ambient conditions. The effects of surface oxidation are taken into account and discussed below.

Table 2 Alloy composition by mass balance experiments performed. Grinding type for XRD and DSC is given for each alloy. Imaging or analysis performed is indicated with an "x".

Sample	Reference Or Id	wt% of Mn by balance	Grinding Type	SEM/ EDX	XRD	TGA/DSC 3K min^{-1}	TGA/DSC 10K min^{-1}
1	U-Mn0	0	Ball Ground	x		x	
2	U-Mn5	5.1	Ball Ground	x	x	x	x
3	U-Mn16	18	Ball Ground	x	x	x	x
4	U-Mn32	33	Crushed	x	x	x	x
5	U-Mn35	37	Crushed	x	x	x	x
6	U-Mn55	57.2	Crushed	x		x	
7	U-Mn75	78	Crushed	x	x	x	x
8	U-Mn92	90	Crushed	x		x	
9	U-Mn100	100	Crushed	x		x	

3.2 Microstructural characterization and composition analysis

3.2.1 Scanning electron microscopy

Microstructure analysis was performed with a shielded JEOL type 7100 field emission gun scanning electron microscope (SEM). Simultaneously, energy dispersive x-ray analysis (EDX) was performed with a Bruker EDX-flash for elemental analysis.

SEM images in both secondary electron and backscatter electron configuration were taken to see if there was any compositional variance across the button. The solidification microstructure of the intermetallic phases and pure phases were characterized and classified according to their morphology. SEM-EDX spectrum imaging are performed simultaneously to generate the 3D datacube from which you extract elemental maps and images and discrete "spot" analysis. EDX spectrometry was used to either analyze the elemental composition of the structures identified in the SEM images or to record X-ray maps. X-ray intensity profiles (or X-ray maps), show the measured intensity of a single X-ray wavelength (or energy), corresponding to a specific element, as a function of the position in the

sample and are two dimensional. Since the measured intensities are not corrected for local density, absorption, fluorescence, peak overlap, etc., they only provide qualitative information on the location of specific elements in the sample. Quantitative information, i.e. differences in element concentration, cannot be derived directly from these maps as differences in intensity do not necessarily signify a difference in concentration. However, variations of X-ray intensity of a specific element in areas that are known to be of similar composition, do give an indication on the relative element concentration.

3.2.2 Image analysis

As stated in the previous section (3.1), Mn vaporization makes it difficult to ensure the final composition of the alloy. A way to assess the amount of dissolved Mn is based on SEM imaging analysis. Over 20 SE and BSE images of each button were taken and processed to ensure a good representation of the button. The images were taken at low magnification and at both the button edges and the bulk, and are processed in SigmaScan Pro version 5, to determine phase and elemental composition. As all alloys in this study are predicted to have only two phases, optimization of contrast and brightness was performed to separate the image into two components, to eliminate any error that could result from polishing or cracks. Intensity thresholding was performed to segment the image into two phases. Erosion and dilation filters are used eliminate false pixels or noise a solution phase, while ensuring that no true phase is eliminated in a grain boundary eutectic. The variation in phase composition before and after applying these filters results in an uncertainty that varied between 1 and 2.1wt% Mn.

The percentage of each phase and elemental composition in each alloy was evaluated by image processing. As each alloy was inspected and demonstrated to be homogenous, it is taken that the 2-dimensional phase composition used for imaging analysis is representative of the 3-dimensional one. Following the analysis of the alloyed buttons, powder samples were made for XRD and DSC measurements.

3.2.3 X-ray diffraction

XRD was performed on a Philips X'pert Pro diffractometer configured in a Bragg-Brentano parafocusing geometry in a θ-θ configuration. Zero point calibration was performed with a sintered Si disk while validation is performed against an Al_2O_3 disc (NIST Standard Reference Material 1976b).

An LFF X-ray tube (Cu Kα1 = 1.54059 Å) was used as a radiation source. A fixed divergence slit is used in combination with a 0.02 rad Soller slits and a copper beam mask to ensure high quality diffractogram. Detection was performed with a position-sensitive PANalytical X'Celerator detector with diffractograms recorded in the range 15-100° (2θ). The recorded pattern was used to confirm which phases are present in the sample. Once the powder was fully characterized from the alloy, with both SEM imaging and XRD analysis, a thermal analysis was performed.

3.3 Thermal Analysis

TGA-DSC was used to determine physical-chemical properties. Transition temperatures were taken as the onset of a thermal event, while the area of endothermic peaks was taken as the enthalpy of transition. Differential scanning calorimetry (DSC) was performed using a Netzsch STA 449 F1 Jupiter equipment to evaluate transition temperatures and enthalpy of transitions. Experiments were performed under high purity argon (99.9992%) with no measurable water content (dew point < -80°C). A 20 mL min^{-1} flow of argon gas was maintained through the balance compartment and leading into the furnace chamber. The flushing gas entering the furnace chamber through a secondary inlet has a constant flow of 80 mL min^{-1} making the total exiting flow rate equal to 100 mL min^{-1}. The instrument is calibrated by melting standards of In, Sn, Bi, Zn, Al, and Au. All DSC runs were corrected for drift and buoyancy by the subtraction of a blank run under identical conditions.

Samples weighing between 45 and 60 mg were used for each DSC experiment. The powder sample was placed in an alumina crucible and the furnace chamber was evacuated down to 6 $x10^{-3}$ mbar. For the first experiments, the sample was heated up to 1185°C with a heating/cooling rate of 10 °C min^{-1}. However, certain peculiarities in the obtained data called for a slower cooling rate. 3°C min^{-1} is further decided from the point of view of having minimal thermal lag and of detecting feeble thermal arrests found during continuous heating and cooling.

4 Results

4.1 Microstructure Characterization

The microstructure of each phase within the composition made in this study exhibit different classical structures of a binary system. The development of any singular phase is decided by the competing forces such as nucleation

sites and nucleation difficulties, presence of impurities, solid-liquid interface energy, among other factors [25]. Although the mechanisms responsible for the microstructural development of U-Mn alloys is beyond the scope of this study, the solidification products can still be observed and are assessed.

4.1.1 Sample 2: U-Mn5

An examination of the phase diagram (Figure 3) indicates that on cooling, U-Mn5 would solidify first as γU and then as βU. At 725°C, a peritectic transformation occurs forming U_6Mn from solid βU and liquid. Following at 716°C, the solidification of γUMn_2 occurs, making the final composition at room temperature a mixture of U_6Mn as a major phase and UMn_2 as a minor phase. Figure 4 shows an SE image and an EDX elemental map of U-Mn5. The dominant U_6Mn phase can be seen as the continuous phase and U rich region indicated in red. UMn_2 can be seen as the Mn rich regions indicated in green. UMn_2 occurs as a eutectic mixture along crystals of U_6Mn. It has been observed that on a macroscopic level, the U_6Metal series forms as highly crystalline needles [15]. This morphology is observed in the microstructure as seen in Figure 4.

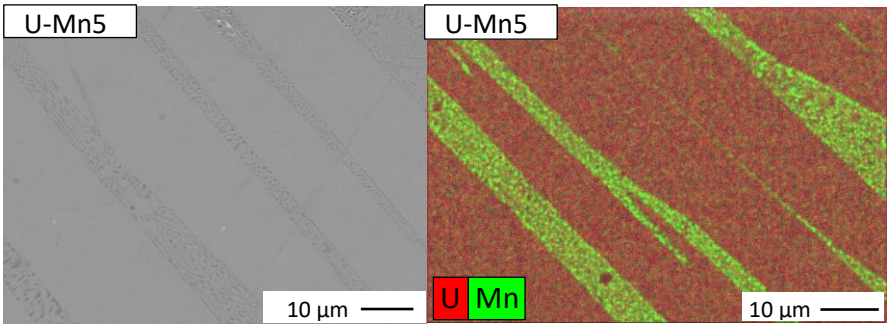

Figure 4) left) SE image of U-Mn5 . Right) EDX mapping with U in red and Mn in green

4.1.2 Sample 3: U-Mn16

The composition of U-Mn16 first solidifies as UMn_2 upon cooling from a pure liquid solution. At 716°C, U_6Mn starts to crystalize in a continuous matrix around UMn_2, forming the final eutectic composition. The two constituents of the alloy can be seen in Figure 5. EDX analysis of the dark region demonstraited that the composition was 34 at% U and 66 at% Mn, forming the compound UMn_2 while the light regions have 86 and 14 at% U and Mn respectively. EDX analysis bears testimony that UO_2 is not formed throughout the alloy and no major impurities can be detected. Faceted domains of UMn_2

can be seen to have formed in a matrix of U_6Mn. The microstructure observed here can be classified as a lamellar with an average domain width of approximately 4 µm and an average matrix spacing between adjacent domains of <1 µm. As the interfacial surface energy is lower along specific planes, the domains grow on a well-defined planes eventually merging.

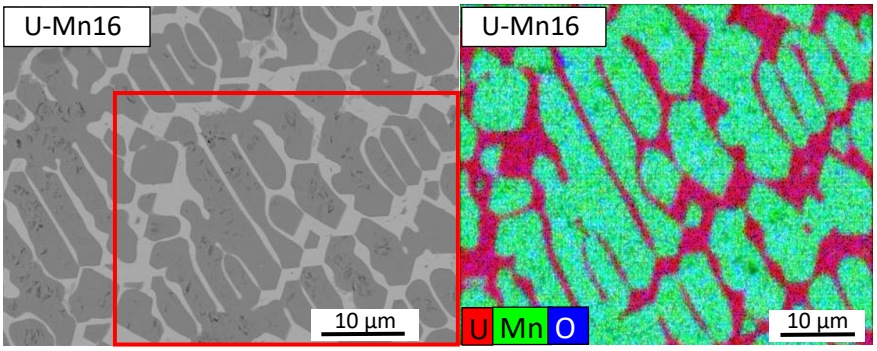

Figure 5) left) BSE image of U-Mn16. Area of EDX map marked in red. Right) EDX mapping combining uranium in red, manganese in green, and oxygen in blue of U-Mn16.

4.1.3 Sample 4 and 5: U-Mn32 and U-Mn35

Alloys containing 32 and 35 wt% Mn form UMn_2 predominantly and are hyper-stoichiometric with respect to Mn. Both of these compounds first solidify UMn_2 as the major phase, with βMn solidifying at 1035°C. The allotropic transformation of βMn to αMn occurs at 698°C. In Figure 6 the alloys containing 32wt% Mn is dominantly a single phase. Regions near the cracks have been identified through EDX elemental maps to be rich in manganese. Within these fractures, U can be seen to precipitate. Similarly, the alloy U-Mn35 cracks that run throughout the button.

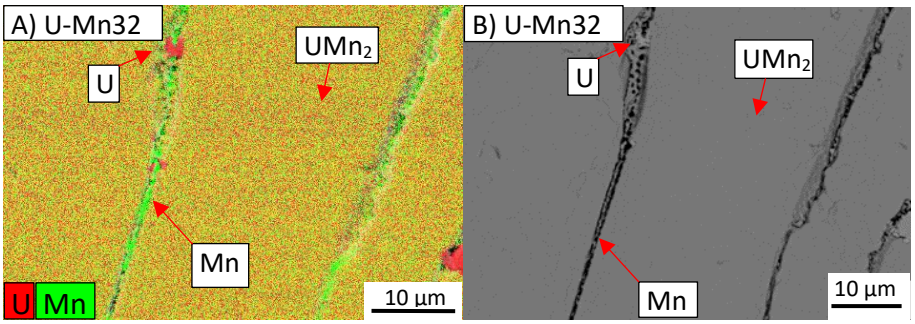

Figure 6)A) Combined EDX elemental map of uranium and manganese of sample 4, U-Mn32. B) BSE images of sample 4

4.1.4 Sample 6: U-Mn55

The second eutectic formed in the U-Mn binary system is a liquid solidifying as UMn_2 and pure Mn, and can be seen in sample 6, U-Mn55. Both UMn_2 and pure manganese solidify or melt at the same temperature Figure 3. Globally, this composition was found to have a varying microstructure, which each phase interlocked with one another. In Figure 7, an EDX elemental map (A) can be compared with a BSE image (B) of the same location. In the BSE image, the microstrucutre shown here can be seen as a lamellar eutectic. The UMn_2 phase is visible as white lamella with a domain width of 0.14±0.03µm and the αMn can be seen as dark lamella with a domain width of 0.12±0.02µm. In the corresponding EDX map (A), the phases are not well defined and the elemental distribution does not match the underlying structure. As the interaction volume of the EDX point (>1µm) is larger than the feature size, this technique is found to be not suitable to analyze this structure. In the SE image C, a classic lamellar eutectic is seen in the same alloy. The UMn_2 phase can be seen to form domains within a continuous Mn matrix. The average

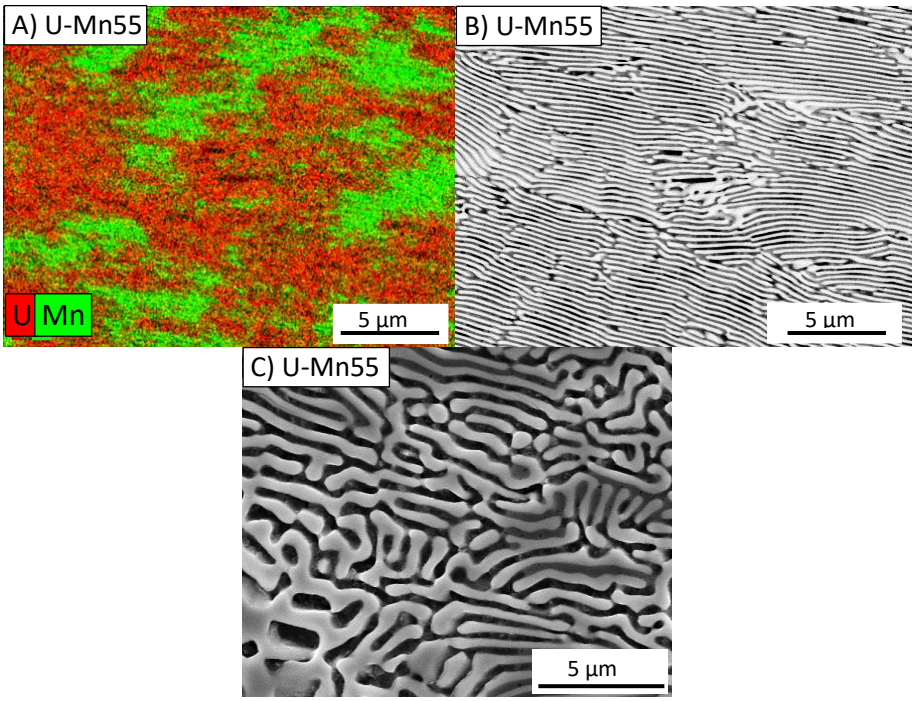

Figure 7)Microstructure of sample 6, U-Mn 55, eutectic composition. A) EDX elemental map of U-Mn55 alloy. U in red and Mn in green. B) BSE images underlying image A. C) SE image of lamellar eutectic microstructure in the same alloy

domain width of the UMn_2 phase was found to be 0.35±0.1µm while the average domain width of the Mn phase was found to be 0.27±0.1µm, with both phases being equally dispersed and double the domein width of the lamellae. This composition (C) can also be defined as a chinese script with clearly defined edges of the UMn_2 crystal. Pockets of pure Mn have been found during imaging analysis, and the exact eutectic point is in agreement with literature.

4.1.5 Sample 7 and 8: U-Mn75 and U-Mn92

Finally, the development of the intermetallic UMn_2 in the remaining interdendritic U-enriched liquid can be assessed. Figure 8 shows EDX elemental mapping, where U is represented in red and Mn is represented in green. Upon cooling and according to the phase diagram, the pure manganese phase solidifies as δMn and undergoes an allotropic transitions to γ and then βMn (Figure 3). UMn_2 nucleates in βMn followed by a final allotropic transition from β to α Mn. The UMn_2 phase nucleates at grain boundaries of βMn in U-Mn92 and resembles eutectic decomposition. Notably in the as-solidified microstructure of U-Mn92, the dendrites form first. Following, the interdendritic U-enriched liquid with a eutectic composition will solidify. The interlamellar spacing of the eutectic will reflect the undercooling, as seen in Figure 8.

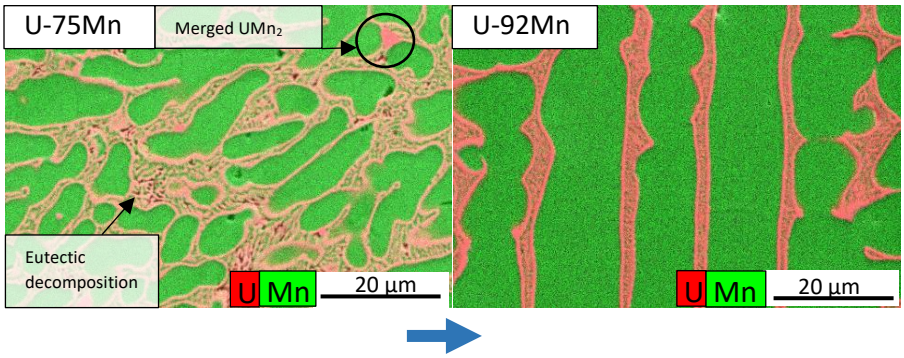

Figure 8) EDX elemental map with uranium in red and manganese in green. Left) U-75Mn and right) U-92Mn. Mn is represented in green and U is represented in red. UMn_2 can be seen to develop and grow along grain boundaries of αMn and grows into an interconnected network

Through image analysis (sec 3.2), the amount of each major and minor phase in each alloy is given in (Table 3).It was found that the estimated amount of Mn that remained in the alloys estimated by image analysis was in good

agreement with what was predicted due to mass loss during arc melting. The values provided by image analysis are taken to be a better representation of the total alloy, as loss of uranium due to distillation or loss of precursors while arc melting is not accounted for in the estimate by weight balance.

Table 3 Alloys produced for this study. Sample number, reference, weight percentage and phase composition are presented.

sample	Reference Or Id	wt% Mn by balance	wt% Mn by Image Analysis	Major phase % at 20°C	Minor phase % at 20°C
1	U-Mn0	0	0	α-U - 100	-
2	U-Mn5	5.1	5.6±2.0	U_6Mn - 92.8	UMn_2 - 7.19
3	U-Mn16	18	16.7±1.4	UMn_2 - 71.75	U_6Mn - 28.25
4	U-Mn32	33	32±1.1	UMn_2 - 98	UMn_2 - 2
5	U-Mn35	37	35±1.5	UMn_2 –95	αMn - 5
6	U-Mn55	57.2	55.1±2.1	UMn_2 – 53.0	αMn – 47.0
7	U-Mn75	78	75.1±1.8	αMn – 74.7	UMn_2 – 25.3
8	U-Mn92	90	92.1±1.3	αMn – 98.03	UMn_2 - 1.97
9	U-Mn100	100	100	αMn - 100	-

4.2 XRD

X-ray diffraction was performed to identify phases present in both buttons and powders in order to evaluate alloy production and sample preparation. For button analysis, the alloy was cut in half and multiple scans were taken on the inside face of the freshly cut surface. Three XRD diffractograms for sample 2 is presented in Figure 9. As the alloy forms a dendritic structure of U_6Mn (Figure 4), and as the button is polycrystalline, preferred orientation was observed. Several scans of the same surface was taken, with each scan representing a rotation of the sample surface around the sample normal.

Peaks were matched and compared against a pattern of U_6Fe provided by [26]. Although UMn_2 is found in the microstructure (Figure 4), no appreciable amount was detected (UMn_2 pattern compared against ICSD pattern 104996). The XRD scans were also compared against patterns of αU (ICSD 24-0748), UO_2(ICSD 77700), and αMn (ICSD 21-0547), with no detectable impurities.

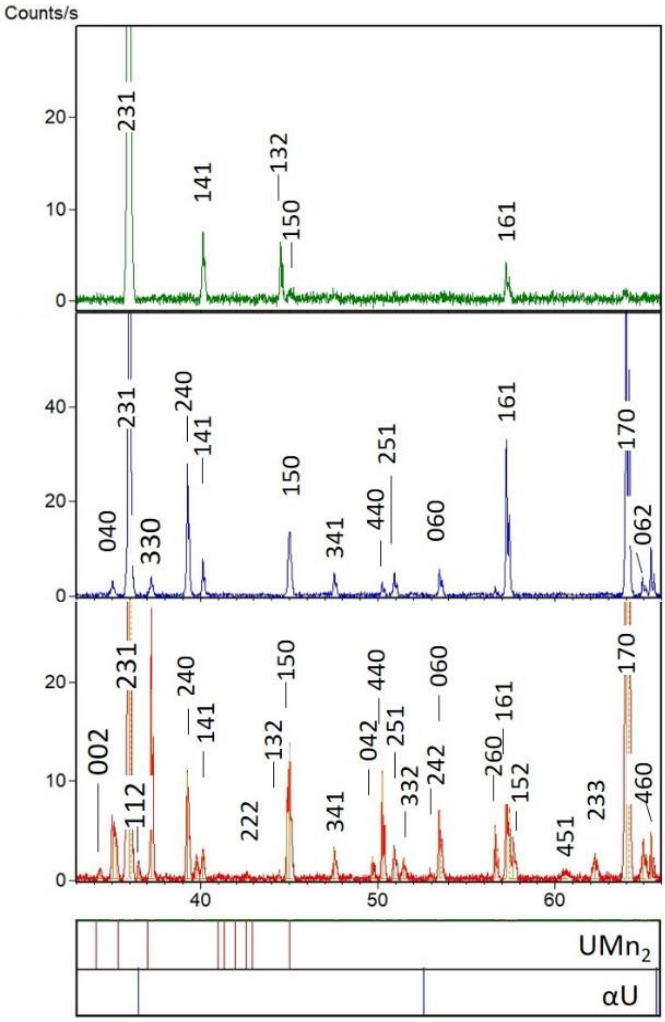

Figure 9) XRD analysis on sample 2, U-Mn5. Three different scans of a button, performed at different sample rotations, are presented

XRD analysis on powder samples are performed to analyze the effects of grinding, as DSC is performed on powder samples. Figure 10 shows a XRD pattern of UMn_2 taken from the button as is seen in Figure 6, and is compared against patterns for UMn_2 and UO_2. Due to grinding in ambient conditions (Table 2), these samples contained unavoidable surface oxides. An analysis of the XRD pattern shows that only UMn_2 and UO_2 two phases are present in sample 4, in amounts that are detectable by XRD.

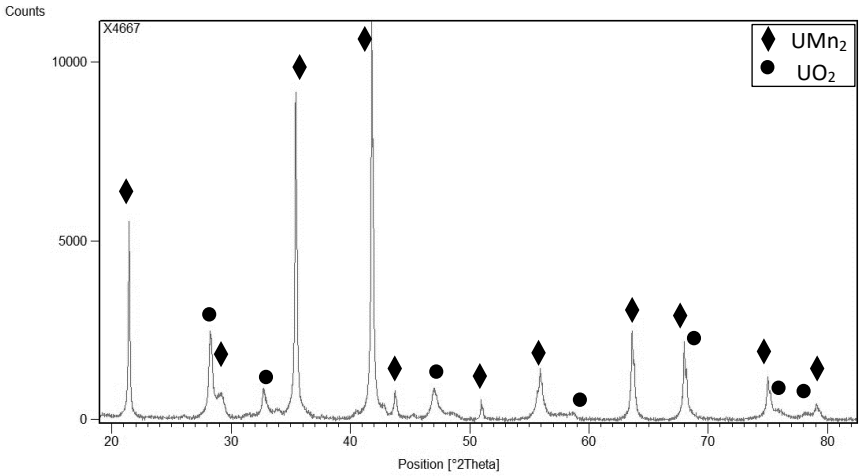

Figure 10) XRD diffractogram of Sample4, UMn_2. ICSD pattern 104996 matching UMn_2 is indicated with a diamond. ICSD pattern 77700 was used to match UO_2, indicated with a circle.

4.3 Transformation temperature and U-Mn phase diagram

TGA-DSC is used to evaluate transformation temperatures and enthalpies of the various U-Mn alloys. The DSC signals for solid-solid transformations were always sharp, allowing the determination of reliable transition temperatures. Transition temperatures were taken as the onset of an endothermic event. Furthermore, sub-cooling in the cooling curves, or delayed solidification, were evident in all alloys compositions, often up to 10-20°C lower.

A typical DSC thermogram and temperature profile is displayed in Figure 11 for the alloy composition U-Mn 55. As mentioned in the microstructure analysis (sec. 4.2), the U-Mn 55 consists of αMn + UMn_2 at room temperature. The pure Mn phase undergoes an allotropic transition to βMn at 698°C in the calculated phase diagram [22] while experimentally this transition was found to occur in pure Mn at 727°C [15] (Figure 3). Both phases melt simultaneously at 1035°C according to both. In the DSC performed here, the transition from αMn to βMn is observed by an endothermic peak at 731°C on the heating curve. Notably, its corresponding exothermic peak of the transition βMn to αMn is absent in the cooling profile. This is in agreement with both Wilhelm and Hensen reporting that the βMn phase is metastable and the retention of the β phase is due to the solid solution of UMn_2 [15]. A pure eutectic composition is evident by a singular endothermic

peak at 1051°C. Solidification upon cooling starts at 1055°C, however, the majority of the transformation occurred at 1042°C.

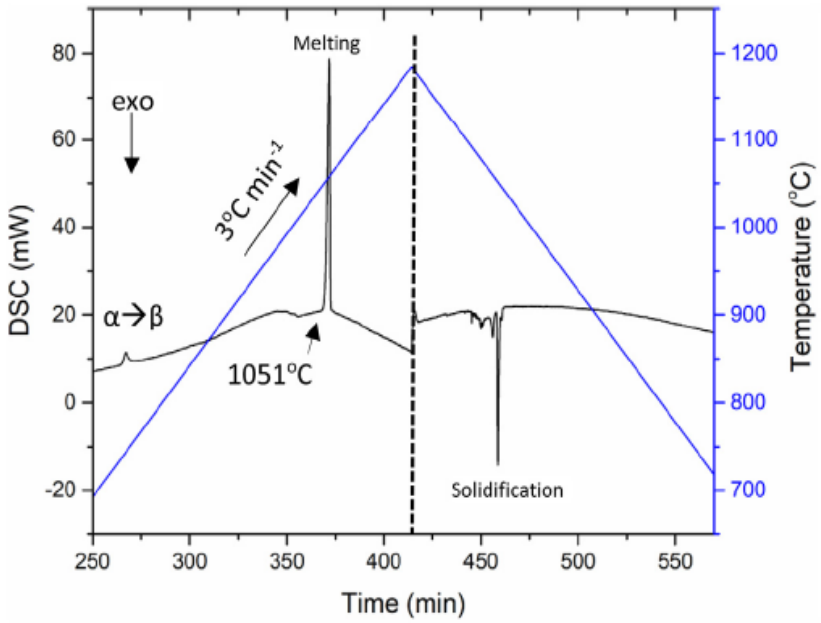

Figure 11) TGA-DSC profile of U-Mn 55. Heating temperature ramp is indicated in blue. DSC in mW/mg is represented in black. The transition of α to β Mn is evident in the ramping profile. The eutectic point is evident by a single transition peak occurring at 1051°C.

As is discussed in similar calorimetric studies of U and U alloys [16, 17], the discrepancies in the exact theoretical and experimental transition temperatures are not taken at face value in the following tables because the experimental values could be influenced by various experimental conditions, e.g., heating rate, purge gas flow rate, and instrument calibration. However, patterns and trends in transition temperatures can be discussed as a function of alloy composition. Furthermore, to measure the effects of heating rates on transition temperatures, two different heating rates were performed on a selected number of samples. The effects of heating rates on samples in the present study is discussed in section 4.5.

The transition temperatures for U-Mn5 at two different temperature heating rates and U-Mn16 are given in Table 4, in comparison with transitions of similar alloy compositions made by Wilhelm[15]. In the composition U-Mn5, the absence of a αU to βU transition around 650°C contributes an evidence that no pure uranium phase is present in the alloy at room temperature, and

that the alloys is at or above the composition of pure U_6Mn. Although a discussion on the effects of heating rate is outlined in more detail below (sec. 4.5). It is interesting to note that the transition of $UMn_6 \rightarrow \gamma U + liq$ and $\beta U \rightarrow \gamma U$ for the ramp rate $10^oC\ min^{-1}$ is in good agreement with literature (Table 4).In contrast, a singular transition was found for the same composition at the slower heating rate of $3^oC\ min^{-1}$ at 734°C. Because there is no transition that follows, it can be assumed that the alloy in the slower heating rate went directly to the γU phase, as it does with in the U-Fe system, and that the βU phase is unstable. Another possibility is on the sensitivity of minor compositional differences. As the alloy composition lies in between the eutectic point at 6wt% Mn and the pure intermetallic phase at 3.7 wt% Mn, even a compositional difference of 1%wt can affect the endothermal outcome of the system. However, the results given in Table 4 are the average of three experimental runs for a given thermal ramp, on powders from the same alloyed button. The alloy composition U-Mn16 shows two phase changes, namely $UMn_6 \rightarrow \gamma U + liq$ and a liquidus. Once again, the absence of a peak around 650°C (αU to βU) and 698°C (αMn to βMn) indicates an absence of pure precursor metals. The melting point of the U_6Mn phase in the U-Mn16 alloy containing 71.7% UMn_2 by volume (732°C) is relatively unaffected in comparison to an almost pure U_6Mn alloy U-Mn5 (734°C)

Table 4) On-heating transformation temperatures measured in the literature and the present study for U-Mn alloys.

Comp. Wt.% Mn	Source	αU → βU	βU → γU	$UMn_6 \rightarrow \gamma U + L$	liquidus
0	[15]	650	760	-	1132
4	[15]	626	749	728	866
5	This Study ($10^oC\ min^{-1}$)	-	745	733	880
5	This Study ($3^oC\ min^{-1}$)	-	-	734	885
				$UMn_6 + UMn_2 \rightarrow UMn_2 + L$	
16	This Study	-	-	732	1113
18	[15]	-	-	720	1133

Three samples are made for the hypo eutectic region and the eutectic point for alloys containing the phases UMn_2 and αMn, namely U-Mn32, U-Mn 35, and U-Mn55. The melting of αMn in a UMn_2 rich environment occurred at

1048°C and 1053°C for U-Mn32 and U-Mn35 respectively. The eutectic point itself was found in the composition U-Mn55, where 53% of the alloy by volume is attributed to UMn_2 and 47% as βMn melts simultaneously at 1051°C (Table 5).

Table 5) On-heating transformation temperatures measured in the present study for alloys U-Mn32, U-Mn35, and U-Mn55.

Comp. Wt.% Mn	Source	αMn + Mn_2U → Mn_2U + L	liquidus
32	This Study	1048	1110
35	[15]	1036	1104
35	This Study	1053	1101
Eutectic Composition		αMn + Mn_2U → L	
55	This Study	1051	
58	[15]	1036	

Finally, the Mn rich portion or the hyper eutectic region, is represented by the alloys U-Mn75, U-Mn92 (Table 6). All allotropic transitions of Mn are recorded in both samples and are in relatively good agreement with literature. For the first time, the transition of αMn to βMn was detected experimentally in alloys with as little Mn as U-Mn55 (Figure 11). In comparison, this transition was not reported by Wilhelm in samples with as much Mn as 95wt% Mn. The transition of βMn to γMn was also found in the alloy U-Mn75, while it was previously undetected in alloys with similar Mn content (Table 6). These results are in good agreement with the Mn rich portion of the calculated diagram provided by Liu (Figure 2)[22], and contrasts the earlier diagrams provided by Wilhelm and Hansen (Figure 1).

Table 6) On-heating transformation temperatures measured in the present study for alloys U-Mn75 and U-Mn92.

Comp. Wt.% Mn	Source	αMn → βMn	βMn→ γMn	γMn → δMn	βMn + Mn_2U → βMn+ liq	liquidus
75	This Study	731.6	1114	1138	1052.5	1120.3
79	[15]	-	-	1123	1035	-
92	This Study	735.7	1108	1144	1049	1133.1
95	[15]	-	1102	1153	-	1224
99.9	[15]	727	1100	1138	-	1245
100	This Study	727				1240
100	[27] (Rapoport)	726.9				1243.8
100	[27] (Braun)	730				1240.8
100	[27] (Nylor and Hultgren)	726.9				1243.8

4.4 Effects on heating rates and temperature variations

Different heating rate were applied to ensure that experimental conditions are appropriate to evaluate all thermal arrests. The heating rate of 10°C min^{-1} and of 3°C min^{-1} are chosen to represent slower approaches as already reported literature [10-12, 28]. A sample of U_6Mn, represented in U-Mn5, was examined in a DSC experiment at a ramp rate of 10°C min^{-1} up to 1185°C. Two endothermic transition occur with onset temperatures of 732°C and 745°C respectively (Figure 12, Left). In reference with the phase diagram (Figure 1), these thermal transitions coincide with the incongruent melting of U_6Mn to βU + L, and the allotropic transformation βU to γU which reportedly occur at 726 and 745°C. A shoulder of a smaller peak is detected

with an onset temperature of 765°C. A second trial run on a sample from the same U_6Mn button was performed with a ramp rate of 3°C min^{-1}. A single thermal event is found to occur at 734°C as confirmed by two more repetitions of the test. DSC on three other samples were performed at both ramp rates namely U-Mn16, U-35, and U-Mn55. A comparison of the

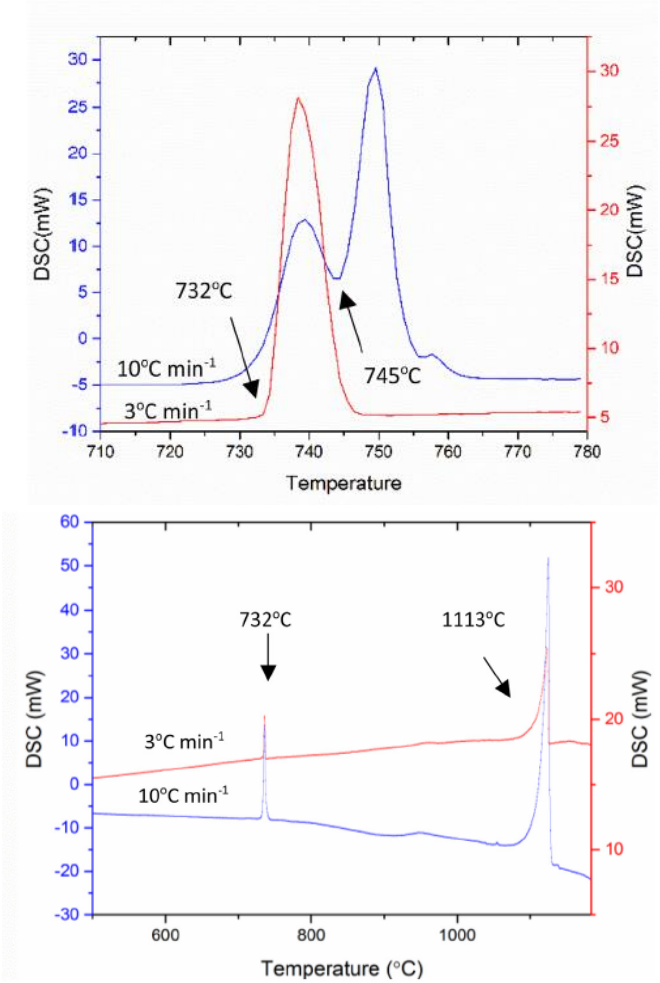

Figure 12) Isolated sections of thermograms. Left) Thermograms of U_6Mn in the temperature range 700-780°C. Heating rate of 3°C min^{-1} is indicated in red while the ramp rate 10°C min^{-1} is indicated in blue. Right) Thermograms of U-Mn16 in the range 550-1185°C with matching ramp rates.

thermograms can be found in (Figure 12, right) of the sample U-Mn16. In both experimental runs, the powder sample came from the same alloyed button. The incongruent melting of U_6Mn can be seen at 732°C and its

liquidus is reached at 1113°C. Onset temperatures of thermal events were identical within 1°C from both temperatures ramps, independent of heating rates. All other samples were characterized only at the slower ramp rate of 3°C min^{-1}.

The variation in temperatures across isotherms are presented to demonstrate the consistency of experimental conditions. The two eutectic isotherms can be derived. The isotherm for alloys comprised of U_6Mn and γUMn_2 can be found in samples in alloys U-Mn5 and U-Mn16. The isotherm was found to be located at 732°C, and can be seen in Figure 12. This isotherm is observed as the melting of UMn_2 in U-Mn5 and the melting of U_6Mn in the U-Mn16 sample. The second isotherm for alloys comprised of γUMn_2 and pure Mn is found with samples containing wt% Mn of 32 and above. Below a composition of 55%wt Mn, the isotherm is defined by the melting of pure Mn while above it is defined by the melting of UMn_2. It is found to be at 1051°C as defined by the eutectic composition found at U-Mn55 (Figure 13). The variation across this isotherm is 5°C, demonstrating internal consistency and experimental conditions that allow the sample to respond to thermal transition independent of heating rates.

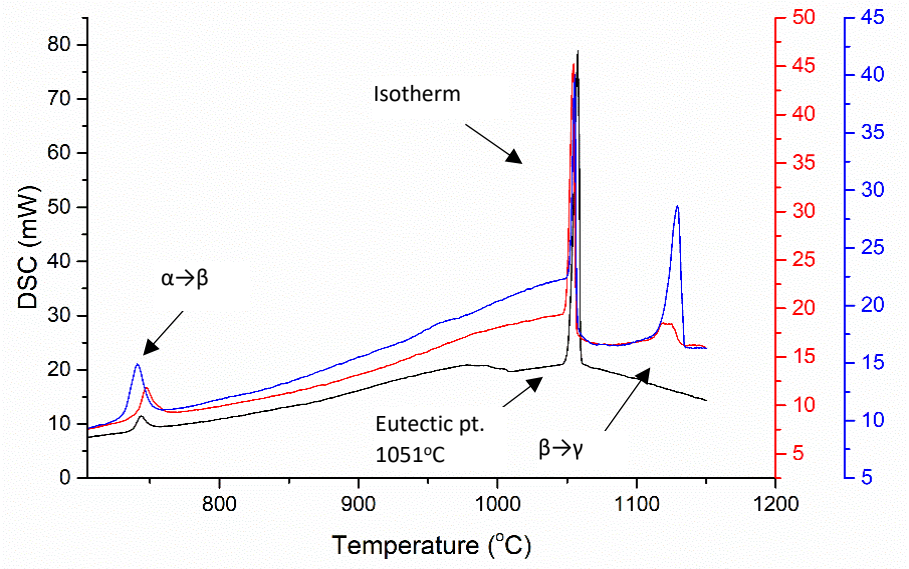

Figure 13) Eutectic Isotherm of Mn and UMn_2. U-Mn55 red, U-Mn75 in blue, and U-Mn92 black.

4.5 Enthalpies of transformation

As discussed in section 4.5, the intermetallic U_6Mn shows a difference in transition temperatures and number of transitions with different heating rates. Enthalpies of both are presented for comparison. According to Figure 1, an alloy consisting of 3.7 wt% Mn is pure U_6Mn at room temperature. The intermetallic undergoes two phase transition before reaching a liquidus, namely $U_6Mn \rightarrow \beta U + L$ and $\beta U + L \rightarrow \gamma U + L$. These transition enthalpies were found to be 8630 and 2380 J mol^{-1} respectively, when heating the sample at a rate of 10°C min^{-1}. The enthalpy for the liquidus was measured to have a value of 1310J mol^{-1}. In contrast, only a single endothermic event was measureable when the heating rate was reduced to 3°C min^{-1}. The energy of this singular transition was measured to be 71,000 J mol^{-1}.

Table 7) Transition Enthalpies of the intermetallic U_6Mn at different heating rates. The measured values are accurate to ±12%.

phase	Mass% Metal	$U_6M \rightarrow \beta U$ +liq (J mol^{-1})	$\beta U \rightarrow \gamma U$ +liq. (J mol^{-1})	$U_6M + \rightarrow \gamma U$ + liq (J mol^{-1})	Liquidus (J mol^{-1})	source
U_6Mn	5 at 3°C min^{-1}	-	-	71,000	-	Current
U_6Mn	5 at 10°C min^{-1}	8630	2380	-	1310	Current
U_6Mn	-			88,000		[29]
U_6Fe	5 at 3°C min^{-1}			17,000	3890	[10]

The second intermetallic in the U-Mn binary system is UMn_2, which melts congruently at approximately 1120°C. The enthalpy of fusion for this intermetallic was found to be 42,400 J mol^{-1} (Table 8). This value is within 1.5 kJ mol^{-1} of the value found for UFe_2, given by Chatain et al[30] but double the value reported by Arun Kumar Rai et al[10]. The enthalpy of the liquidus was found to decrease with compositions moving away from a pure UMn_2 phase. The alloy U-Mn16 passes the UMn_6 + UMn_2 eutectic isotherm with an enthalpy of 35,300 J mol^{-1} with a liquidus at 37,200 J mol^{-1}. In contrast, the alloy U-Mn35 passes the α-Mn + UMn_2 isotherm at 2420 J mol^{-1} with a liquidus of 29,900 J mol^{-1}.

Table 8) Enthalpies of the pure intermetallic phase UMn_2 and compositions surrounding.

Phase present	Mass% Metal	Mass% U	$UMn_6 + UMn_2 \rightarrow UMn_2 + L$ (J mol^{-1})	Liquidus (J mol^{-1})	Source
$UMn_2 + U_6Mn$	18	82	35,300	37,200	Current
$UFe_2 + U_6Fe$	20	80	11,100	9220	[10]
UMn_2	31,6	68.4		42,400	Current
UFe_2	32	68		43,700	[30]
UFe_2	32	68		20,900	[10]
			α-Mn + $UMn_2 \rightarrow UMn_2$+ L (J mol^{-1})		
$UMn_2 + \alpha Mn$	35	65	2420	35,100	Current
$UFe_2 + \alpha Fe$	35	65	2110	20,100	[10]
$UFe_2 + \alpha Fe$	45	55	16,600	3090	[10]

Mn rich alloys starting after the U-Mn55 eutectic point can have five physical transitions including three allotropic transformations of Mn, an eutectic isotherm, and a liquidus. The eutectic point U-Mn55, demonstrated to have one allotropic transition $\alpha \rightarrow \beta Mn$ with and enthalpy of 1580 J mol^{-1} and the eutectic point itself having an enthalpy of 53,700 J mol^{-1}. The enthalpy at the eutectic isotherm between $\beta Mn + Mn_2U$ decreases with increasing concentration of Mn (Table 9).

Table 9 Enthalpies of Mn rich alloys.

Mass% Metal	Mass% U	α-Mn -> βMn (Jmol^{-1})	βMn -> γMn (J mol^{-1})	γMn -> δMn (Jmol^{-1})	β-Mn + Mn_2U -> βMn+ liq (J mol^{-1})	Liquidus (J mol^{-1})	Source
58	42	1580	-	-	-	53,700	Current
75	25	1702	1743	199	52,300	11,100	Current
90	10	1892	1953	212	40,100	9210	Current
100	0	1970	2110	-	-	10,200	Current
100	0	2225	2120			11,000	[27] (Desai)

5 Discussion

The goal of the present study is to analyze the temperature and composition dependent phase evolution of the U-Mn binary system using differential scanning calorimetry, together with an analysis of the microstructure of these alloys. Although there is existing literature on the calculated enthalpies of transformation based on the CALPHAD method, this study represents the first full-scale experimental calorimetric study on these compounds known by the authors.

The microstructure was examined on the alloyed buttons. The development of the two intermetallic phases, U_6Mn and UMn_2, in these alloys has been observed as a function of Mn concentration. U_6Mn was found to grow in long two dimensional crystals with UMn_2 forming along grain boundaries. The UMn_2 phase grows along favorable planes with increasing Mn concentration and forms domains in a continuous U_6Mn matrix in U-Mn16. In contrast, UMn_2 develops in a Mn rich solution as grain boundary precipitation in U-Mn92. The network grows throughout the alloy in U-Mn75, until a complete eutectic composition is reached in U-Mn55. The microstructure of these alloys, as presented here, can aide future research on the mechanical and chemical properties of these compounds.

As TGA-DSC experiments are performed with powdered samples, an examination of the sample preparation is discussed first before the results on temperature transition and enthalpies are. As noted in Table 2, samples were crushed and oxide layers were observed on the powdered samples. There exists a wide body of literature assessing the effects of size and oxidation of metallic powders on DSC experiments (in particular for gold, silver, tin, indium, lead and aluminum) [31-34]. In general, the melting point and the heat of fusion decrease with decreasing particle size. Melting point depression is predicted by the so-called Gibbs-Thomson equation for spherical particles, which expresses a linear relationship between the melting point depression and the inverse of particle size. Additionally, it has been found that the oxide layer contributes to melting point depression through increased pressure on the core of the particle through differential thermal expansion between the metal core and oxide shell, and through the increased fraction of lattice defects or irregularities in the crystal structure [31]. Similarly, the depression of the heat of fusion is also predicted through the increased fraction of lattice defects or irregularities with decreasing particle size. However, these affects have only been observed on nanometer

sized particles. The latent heat of fusion and melting temperature for aluminum powders, for example, reach bulk value for particles that are at least 3 μm in size [31]. Although the amount of melting point and heat of fusion depressions are not studied here, the powders in these experiments were well in the micrometer range. A comparison against standards and are discussed independently below, to assess the effects on of the oxide layer on these values.

The transition temperatures observed here represent all alloys in the U-Mn system. In addition to the calibration of DSC against standards, the combined error accumulated from sample preparation, oxidation, and signal analysis on transition temperatures have been evaluated against the allotropic α → β transition and the melting temperature of pure Mn. In comparison against reported values[27] (Table 6) ,The measured phase transformation temperatures are accurate to ±4°C. The uncertainty on elemental composition will have no effect on isotherm temperatures, which span across many alloy compositions. However, melting temperatures are dependent on sample composition. The liquidus reported here is, in general, in agreement with Wilhelm[15].

Many of the transition temperatures in this study were found to be 5 to 15°C different than literature. This adds to the body of literature that describes transition temperature differences, in this range, found in uranium bearing systems using TGA-DSC [10, 17, 22]. The primary function of transition temperatures here is to serve as a delineation point between two physical states in an alloy and to attribute the values of enthalpy measured as a property of a given transition. That being noted, some transitions do closely agree with reported values as is the case with the transition of αMn to βMn. In pure Mn, it was found identically at 727°C and with only a few degrees difference in alloys U-Mn92 and U-Mn72. Additionally, the transition of βU to γU in U-Mn5 occurs exactly at 745°C when heated at a rate of 10°C min^{-1}. On the Mn rich side, the transition of γMn to δMn as found to be within 5°C of what is expected. This study is the first to detect allotropic transitions of αMn to βMn in as much Mn as U-Mn55, and βMn to γMn in as much manganese as U-Mn75. This represents the first known experimental confirmation of the Mn rich portion of the calculated diagram.

In contrast, the eutectic isotherm βMn + UMn_2 → L is 15°C higher than expected, regardless of heating rates. Similarly, a temperature difference of 25°C is found in literature for the homologous and well-studied transition of

Fe + UFe_2 → L [10]. The eutectic isotherm U_6Mn + UMn_2 → L is found 12°C higher than expected. Regardless of this temperature difference, transition temperatures are internally consistent. The variation in temperature on the eutectic point βMn + UMn_2 → L and its isotherm is less than 5°C. This bears testimony that the heating rate of 3°C min^{-1} is well suited for these experiments.

The effects of the heating rate has also been determined on the thermogram of U_6Mn. When examining the intermetallic at a heating rate of 10°C min^{-1}, two separate transitions are clearly visible, in agreement with previous studies and occurring at the reported temperature value of 745°C [15]. As a ramp rate of 10°C min^{-1} is a standard, it is likely to be what was used by Wilhelm and other diagrams. However, once the system is heated at a rate of 3°C min^{-1} a single transition in this temperature range is observed. As any point in a phase diagram represents an equilibrium state, the slower heating rate is taken to be more representative of that system at a given temperature indefinitely. In this view, the phase diagram should connect U_6Mn immediately to γMn + L, as it does so in the diagram of the U-Fe system[10]. The reason for this dependency could lie in the stability of the beta phase. Perhaps this allotrope is only meta-stable, and could be a contributing reason why its crystal structure is yet to be fully solved [35-37]. It should be noted that all other samples did not show a dependency on the temperature heating rate.

Enthalpies of many transitions in the U-Mn system are reported for the first time. When comparing the enthalpies of transition of pure Mn compared to those reported in literature[27], it is found that the sample preparation process may lead to an uncertainty of up to 12%. As the depression of the heat of fusion is most affected on a nanometer scale by lattice defects and irregularities, the authors believe that this uncertainty may be due to sample contact with the crucible.

The enthalpy of fusion for U_6Mn is higher than for U_6Fe. This reflects the fact that U_6Mn has the shortest bond length of the U_6Metal family [38], and consequently the highest bond energy. The enthalpy of fusion of UMn_2 was found to be within 1kJ of energy compared to UFe_2 by Chatain et al. The eutectic point in U-Mn55 was found to have an enthalpy of 53kJ mol^{-1} and decreases along this isotherm with increasing Mn content. The enthalpies of the allotropic transformation αMn → βMn → γMn → and δMn were found

to be in the range of hundreds of joules and very slightly across different alloys with pure Mn phases.

6 Conclusion

Alloys of U-Mn were prepared and analyzed for a calorimetric investigation of the U-Mn binary system. Microstructure analysis and growth of the two intermetallic phases were investigated with SEM and EDX as a function of its Mn concentration. The main findings of this study are the following:

i) Experimental observations confirm extensions of Mn allotropic transitions provided in calculated phase diagram.

ii) The eutectic transformation involving UMn_2 and βMn occurs at 1051°C at a composition of 55 wt% Mn. The Enthalpy of transformation is found to be at 53,700 J mol^{-1}.

iii) The enthalpies of melting for U_6Mn and UMn_2 were found to be 71,000 J mol^{-1} and 42,400 J Mol^{-1} respectively.

iv) The eutectic isotherm for U_6Mn and UMn_2 is found to occur at 732°C.

v) The transformation of U_6Mn to βU + L can be detected only at fasters heating rates. U_6Mn undergoes a single transition at 734°C at slower heating rates.

As a perspective, further thermal, chemical, and mechanical experiments must be performed to allow the use of U_6M fuels for medical-isotope production. This study represents a themo-chemical analysis of the as-prepared fuel. However, target production and irradiation changes the physical properties of the cladding and fuel. In particular, the cladding-fuel interaction can create an intermediate layer or evolve to block channels and pores in the fuel needed to dissolve the material in an industrial relevant timescale [3]. A more comprehensive investigation into full target behavior is required to assess the viability of this fuel as expected during the target life cycle.

References

1. *Non-HEU production Technologies for Molybdenum-99 and Technetium-99m.* IAEA Nuclear Energy Series, 2013(No.NF-T-5.4).
2. *Safety Evaulation Report related to the Evaluation of Low-Enriche Uranium Silicide-Aluminum Dispersion Fuel for Use in Non-Power Reactors.* NUREG-1313, 1988.
3. Snelgrove, J.L., et al., *Development and Processing of LEU Targets for Mo-99 Production -- Overview of the ANL Program.* RERTR, 1994.
4. Snelgrove, J.L., et al., *Development of very-high-density low-enriched-uranium fuels.* Nuclear Engineering and Design, 1997. 178: p. 119-126.
5. Van den Berghe, S., et al., *From High Enriched To Low Enriched Uranium Fuel In Research Reactors*. Vol. 73. 2011.
6. *Medical Isotope Production Without Highly Enriched Uranium.* National Academies Press (US): p. 220.
7. Meyer, M.K., et al., *Irradiation behavior of U6Mn–Al dispersion fuel elements.* Journal of Nuclear Materials, 2000. 278(2-3): p. 358-363.
8. G.L. Hofman, R.F.D., G.L. Copeland, *Irradiation behavior of low-enriched U6Fe-Al dispersion fuel elements.* Journal fo Nuclear Materials, 1987. 150: p. 238-243.
9. Ugajin, M., et al., *Irradiation behavior of high uranium-density alloys in the plate fuels.* Jounral of Nuclear Materials, 1998. 254: p. 78-83.
10. Arun Kumar Rai, S.R., M. Vijayalakshmi, *A calorimetric study of high temperature phase stability in Fe-U alloys.* Journal of Nuclear Materials, 2012. 432: p. 520-528.
11. H.G. Huang, H.B.K., P. Zhang, Y.M. Wang, P.G. Zhang, M. Wu, T.W. Liu, *Effect of minor alloying on the glass formation of U-based alloys.* Journal of Alloys and Compounds, 2016. 688: p. 599-604.
12. Blomquist, L.L.R.A., *Thermodynamics and phase equilibria of the iron-uranium system.* Journal of Nuclear Materials, 1991. 184: p. 47-52.
13. *Good Practices for Qualification of High Denstiy Low Enriched Uranium Research Reactor Fuels.* IAEA Nuclear Energy Series, 2009(No. NF-T-5.2).
14. Conturbia, G.R. and M. Durrazo, *Study of thermomechanical treatment for manufacturing UAlx/Al dispersion targets.* RRFM Abstract, 2017.

15. H.A. Wilhelm, O.N.C., *The Uranium-Manganese and Uranium-Copper Alloy Systems.* ASM, 1950. 42: p. 1311.
16. Rai, A.K., et al., *Effect of heating and cooling rate on the kinetics of allotropic phase changes in uranium: A differential scanning calorimetry study.* Journal of Nuclear Materials, 2009. 383(3): p. 215-225.
17. Ahn, S., S. Irukuvarghula, and S.M. McDeavitt, *Thermophysical investigation of the uranium-zirconium alloy system.* Journal of Alloys and Compounds, 2014. 611: p. 355-362.
18. M. Hansen, K.A., *Constitution of Binary Alloys*. 1958, New York, NY: McGraw-Hill.
19. Baenzinger, N.C., et al., *Compounds of uranium with the transition metals of the first long period.* Acta Crystallographica, 1950(3): p. 34-40.
20. Bowles, P.J., et al., *AERE-M/R-581.* Nuclear Sci. Abstra., 1951. 5: p. 2424.
21. Thaddeus B. Massalski, H.O., P.R. Subramanian, Linda Kaaprzak, *Binary alloy phase diagrams 2nd ed*. Vol. 3. 1990.
22. Liu, X.J., et al., *Thermodynamic modeling of the U-Mn and U-Nb systems.* Journal of Nuclear Materials, 2008. 380(1): p. 99-104.
23. B.C.Giessen, D.E.P., *Development and Initial Characterization of Amorphous Metals Rich in W and/or RE*, L.L. Laboratory, Editor. 1978: Boston, Massachusetts.
24. Lebedev, V.A., et al., *Thermodynamic Properties of U-Mn Alloys.* Russian Metallurgy, 1973. 2: p. 107-109.
25. F.C.Campbell, *Phase Diagrams-Understanding the Basics*. 2012: ASM International.
26. Kimball, C.W., et al., *Phonon anomalies and local atomic displacements in the exchange-enhanced superconductorU6Fe.* Physical Review B, 1985. 32(7): p. 4419-4425.
27. Thurnay, K., *Thermal Properties of Transition Metals.* Forschungszentrum Karlsruhe Technik und Umwelt, 1998(FZKA 6095): p. 36-42.
28. Ho Jin Ryu, Y.S.K., Gerard L. Hofman, Jong Man Park, Chang Kyu Kim, *Heats of formation (U,Mo)Al3 and U(Al,Si)3.* Journal fo Nuclear Materials, 2006. 358: p. 52-56.
29. Finlay, M.R., G.L. Hofman, and J.L. Snelgrove, *Irradiation behaviour of uranium silicide compounds.* Journal of Nuclear Materials, 2004. 325(2-3): p. 118-128.
30. Chatain, S., et al., *Thermodynamic Assessment of the Fe-U Binary System.* Phase Equalibria, 2002. 24: p. 122-131.

31. Sun, J. and S.L. Simon, *The melting behavior of aluminum nanoparticles.* Thermochimica Acta, 2007. 463(1-2): p. 32-40.
32. Joshi, N., et al., *Size effect on melting temperatures of alumina nanocrystals: Molecular dynamics simulations and thermodynamic modeling.* Computational Materials Science, 2018. 145: p. 140-153.
33. Unruh, K.M., T.E. Huber, and C.A. Huber, *Melting and freezing behavior of indium metal in porous glasses.* Physical Review B, 1993. 48(12): p. 9021-9027.
34. Singh, M., S.o. Lara, and S. Tlali, *Effects of size and shape on the specific heat, melting entropy and enthalpy of nanomaterials.* Journal of Taibah University for Science, 2017. 11(6): p. 922-929.
35. Tucker, C.W., *The Crystal Structure of the β Phase of Uranium.* Acta Crystallographica, 1950. 4(425).
36. Donohue, J., Einspahr, H., *The Structure of β-Uranium.* Acta Crystallographica, 1971. B27(1740).
37. Grenthe, I., Drozdzynski, J., Fujino, T., Buck, E., Albrecht-Schmitt, T.E., Wolf, S.F, *The Chemistry of the Actinide and Transactinide Elements, Chapter 5.* 2006. 1.
38. Engelhardt, J.J., *Lattice Parameters and Superconductivity of The Compounds U_6Mn, U_6Fe, U_6Co, and U_6Ni and Alloys Between Them.* Journal of Physics and Chemistry of Solids, 1974. 36: p. 123-126.

Chapter 6

Digestion of U_6Mn and UAlx fuel with oxidative accelerants

Summary

This chapter explores different methods to digest U_6Mn and UAlx fuels. In order for U_6Mn to be a viable candidate for isotope production, it must be able to undergo a digestion process to release the isotopes. Currently, none of the U_6Metal alloys have been digested and reported in the literature. Presented here for the first time is a successful transformation of U_6Mn to sodium diuranate.

The digestion of U_6Mn in standard ROMOL99 like conditions is performed to see if a direct conversion is possible. After 120 minutes of digesting U_6Mn in a 4M NaOH bath at 95°C, it was found that only partial oxidation occurred where UO_2 formed as the main product. It was discovered that additional reagents are required to help aid digestion. The oxidant potassium permanganate ($KMnO_4$) and sodium carbonate were chosen as promising agents to help digestion. A digestion of U_6Mn performed with $KMnO_4$ demonstrated that the oxidant was able to transform U_6Mn into UO_2 and $Na_2U_2O_7$. Cross sections of digested fuel particles proved that this reaction is a surface reaction which only penetrates approximately 10µm into the particle.

In order to fully digest the fuel particles, two methods are explored. The first method is the use of an "external force" or ultrasonication. It was found that ultrasonication can separate the digested surface shell from the undigested fuel core. Once the fuel is freed from its passivation layer, it can continue to digest to completion. The second method is an "internal" method, where the composition of the fuel was changed. Previously, it was found that UMn_2 preferentially oxidizes compared to U_6Mn. A digestion composition of U-Mn 7wt% produced a microstructure where U_6Mn formed discrete phases within an UMn_2 phase, and where the digestion front could penetrate through the UMn_2 phase, allowing for the fuel particle to be digested.

Presented here for the first time are different ways to digestion U_6Mn by combining an oxidant with methods of advancing the digestion front. The strategies developed to aid digestion here are found to also be applicable to other fuels such as UAlx. Using these strategies, U_6Mn has become a viable candidate to replace UAlx fuel in medical isotope production.

Table of Contents

1 Introduction 201

2 Results.....203

2.1 Experiment 1: Digestion of U_6Mn in ROMOL-99 conditions.....203

2.1.1 U_6Mn as-prepared and digested for five minutes 203

2.1.2 U_6Mn digested for 30 minutes and 120 minutes.....204

2.1.3 Experiment 1 conclusions 207

2.2 Experiment 2: digestion of U_6Mn with oxidants.....208

2.2.1 Digest U_6Mn + $KMnO_4$.....208

2.2.2 XRD of filter cake.....209

2.2.3 Images of Particle Cross-sections 210

2.2.4 Experiment 2 conclusions 212

2.3 Experiment 3: Digestion of UAlx + $KMnO_4$.....212

2.3.1 Filter cake comparison.....213

2.3.2 XRD comparative results.....214

2.3.3 SEM, EDX, and surface analysis of digested UAlx 215

2.3.4 Digestion of UAlx target with $KMnO_4$ 216

2.3.4.1 Type I Particles.....217

2.3.4.2 Type II particles.....219

2.3.5 Experiment 3 conclusions 220

2.4 Experiment 4: Digestion by leaching - sodium carbonate 221

2.4.1 XRD of digested fuel.....222

2.4.2 Experiment 4 conclusions 223

2.5 Experiment 5: Methods of advancing the digestion front.....224

2.5.1 External methods - core shell separation 224

2.5.2 Internal method – preferential digestion within an U_6Mn – UMn_2 eutectic 226

2.6 Chapter discussion.....230

2.7 Conclusions.....232

Table of Experiments

Identification	Sample	Solution	Temp (°C)	Time (min)
Experiment 1	U_6Mn	4M NaOH, 4M $NaNO_3$	95	120
Experiment 2	U_6Mn	4M NaOH, 4M $NaNO_3$ $KMnO_4$	95	120
Experiment 3	UAlx	4M NaOH, 4M $NaNO_3$ $KMnO_4$	95	120
Experiment 4	UAlx	4M NaOH, 4M $NaNO_3$ $NaCO_3$	95	60
Experiment 5-1	UAl_3 and U_6Mn	H_2O	95	120
Experiment 5-2	U_6Mn-UMn_2	4M NaOH, 4M $NaNO_3$	95	15

1 Introduction

The extraction of medical isotopes is based on converting fuel into an oxide, allowing isotopes to escape the fissile material and collected from the solution. Chapters 2 and 3 have revealed that in UAlx fuel, grain sizes and grain boundaries are important features to consider to design corrosion susceptible fuel particles. However, it seems difficult to digest fuel within the time frame and digestion conditions often stated in literature [1] and it is always advantageous to decrease the digestion time overall. If digestion times need to be decreased, then external parameters would need to be changed. This chapter is focused on the use of additional reagents to improve digestion times and process.

Additionally, the digestion of U_6Mn has not been explored, with or without the addition of extra reagents. As this crucial step for isotope recovery in U_6Mn is unknown, there are many things to consider in designing a digestion for a novel fuel. The only universal metric is that a yellow cake of sodium diuranate (in the form of $Na_2U_2O_7$) is the optimal end state of a digestion fuel, as it adsorbs the least amount molybdenum. However, it is unknown if U_6Mn would ever reach this oxidative state in a standard or modified caustic solution. It is also unknown if there are any intermediate products during the digestion or if there are any grain boundary effects such as those seen in UAl_3 in earlier chapters.

To study the digestion of a novel fuel and the use of additional oxidants, a few key questions must be answered:

1) How does U_6Mn perform in a digestion bath with a standard solution of NaOH and $NaNO_3$? Does it digest and how does it digest? How does it compare to the digestion of UAlx?

2) If the fuel does not digest well, is there an oxidant or accelerant that can be used?

3) How does UAlx fuel perform with the same oxidant or accelerant?

4) Are there methods to ensure that digestion goes to completion?

To answer the questions above and to organize the experimental results, the digestion of U_6Mn and UAl_3 with additional reagents is outlined in Figure 1.

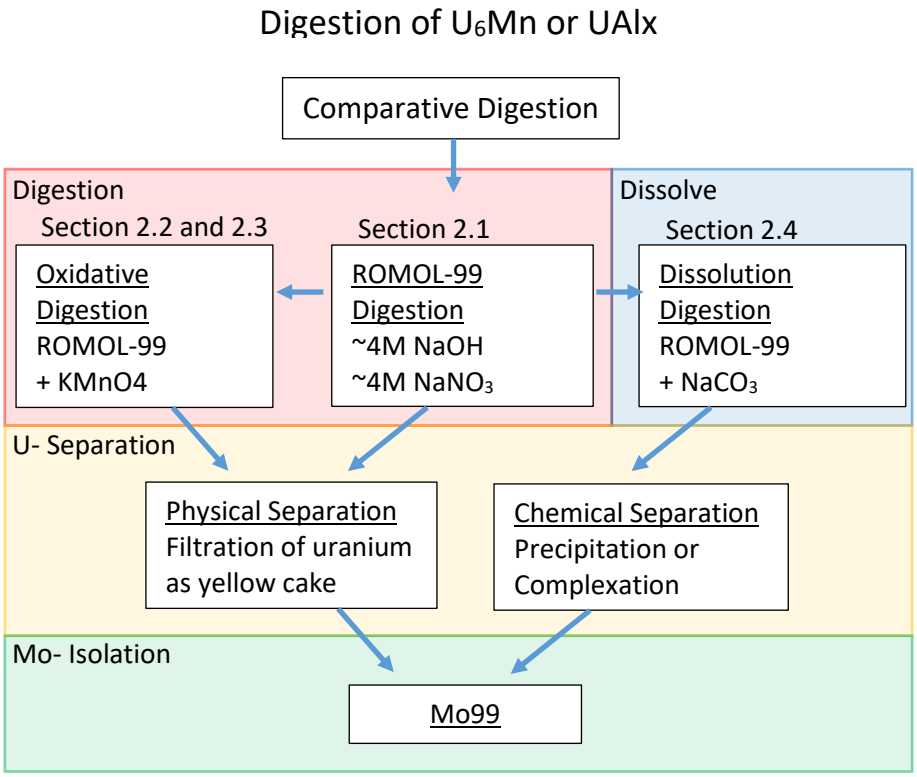

Figure 1) Schematic of digestion strategy for a new fuel. For a reference, digestion will start in standard ROMOL99 conditions. For oxidative digestion, $KMnO_4$ is studied. For dissolution of the fuel, $NaCO_3$ is studied. Different filtration methods would be necessary to separate the uranium from the isotopes

In experiment 1, the digestion of U_6Mn in standard ROMOL-99 conditions is studied (section 2.1) as a point of reference. In parallel, the digestion of U_6Mn with the oxidant $KMnO_4$ will be studied in experiment 2 (section 2.2) along with its use with UAl_3 in experiment 3 (section 2.3). Additionally, the use of sodium carbonate is studied in experiment 4 to see the effects of this leaching agent (section 2.4). This chapter ends with experiments on advancing the digestion front in experiment 5 (section 2.5), or methods to help ensure that a complete digestion is reached in all conditions.

2 Results

2.1 Experiment 1: Digestion of U_6Mn in ROMOL-99 conditions

This experiment is performed as a reference for all of the digestion experiments with U_6Mn. When examining if a new fuel could replace UAlx fuel for isotope production, the fuel's performance in standard conditions must be assessed. If it can be digested in ROMOL99 conditions (i.e. with NaOH and within 90 to 120 minutes) then a direct conversion can be made. If a digestion reaction does not occur or not to completion, then the solution must be changed in order to ensure that the fuel particles can convert to an oxide or a yellow cake. The results from this experiment can be directly compared to the digested UAl_3 and UAl_3-UAl_4 particles presented in chapters 2-4.

2.1.1 U_6Mn as-prepared and digested for five minutes

The U_6Mn fuel particles used in this study are from the same button as the ones made and analyzed in Chapter 5. U_6Mn was made in an Arc 200 cold crucible arc melting furnace under highly pure argon gas. Before melting, both metals (natural uranium and 99%Mn) were stripped of its surface oxide layer. The surface oxidation layer on the uranium was removed with 60 % by volume nitric acid and wiped with acetone while manganese oxide on the manganese chips were sanded with silicon carbide paper and rinsed in acetone. Once the precursors were loaded into the copper hearth, the furnace chamber was put under a vacuum of $4x\ 10^{-3}$ mbar, backfilled with argon, then vacuumed a second time to $2.3\ x10^{-4}$ mbar for one hour to ensure that as little oxygen is present in the chamber while arc melting.

The production of U_6Mn is almost always accompanied with UMn_2 along its grain boundaries (Figure 2A) in the form of a eutectic decomposition. This occurs for two reasons. One is the fact that U_6Mn does not precipitate directly from the liquid phase and needs an additional heat treatment for purification. Also, the final stoichiometric amount is difficult to predict. Difficulty in knowing how much Mn is in the final alloy is due to manganese loss by vaporization and is significant during production of U_6Mn in an arc-melter [2]. An over stoichiometric amount of manganese is added to the production process to ensure that as little pure uranium phase is formed in the final alloy but leading to some UMn_2.

Figure 2B shows the effects of putting a powder of U_6Mn, which came from the ingot in Figure 2A, in for 5 minutes of digestion. Sections of the particle surface is oxidized. This oxidation layer highly porous in comparison to the oxide layer of UAl_3 (chapter 2). The oxidation layer can penetrate deep into the particle but primarily along the grain boundary network of Mn_2. Networks of UMn_2 on the inside of the particle are not oxidized or corroded at this stage.

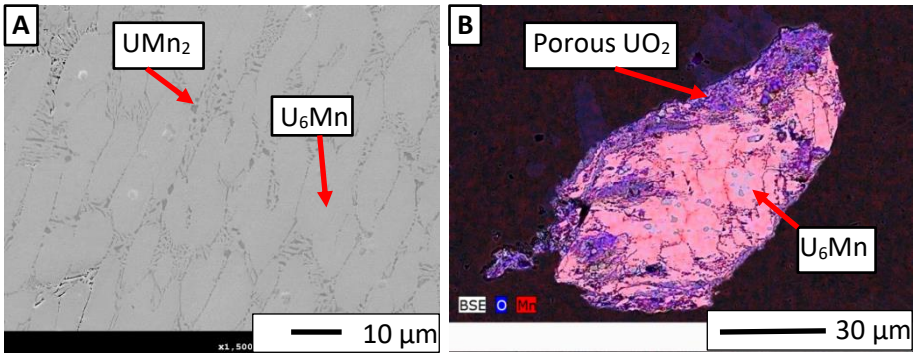

Figure 2) A. BSE image of U_6Mn as arc-melted and annealed. Alloy contains U_6Mn as grains, with UMn_2 at grain boundaries. B. A combined BSE-EDS map of an U_6Mn particle after 5 minutes of digestion.

2.1.2 U_6Mn digested for 30 minutes and 120 minutes

The digestion of U_6Mn alloy proceeds through the particle to form uranium dioxide for the rest of the digestion process. Figure 3A and B shows U_6Mn particles after 30 minute digestion time. Oxidation can be seen at the surface (Figure 3A) and even channel through the particle (Figure 3B).

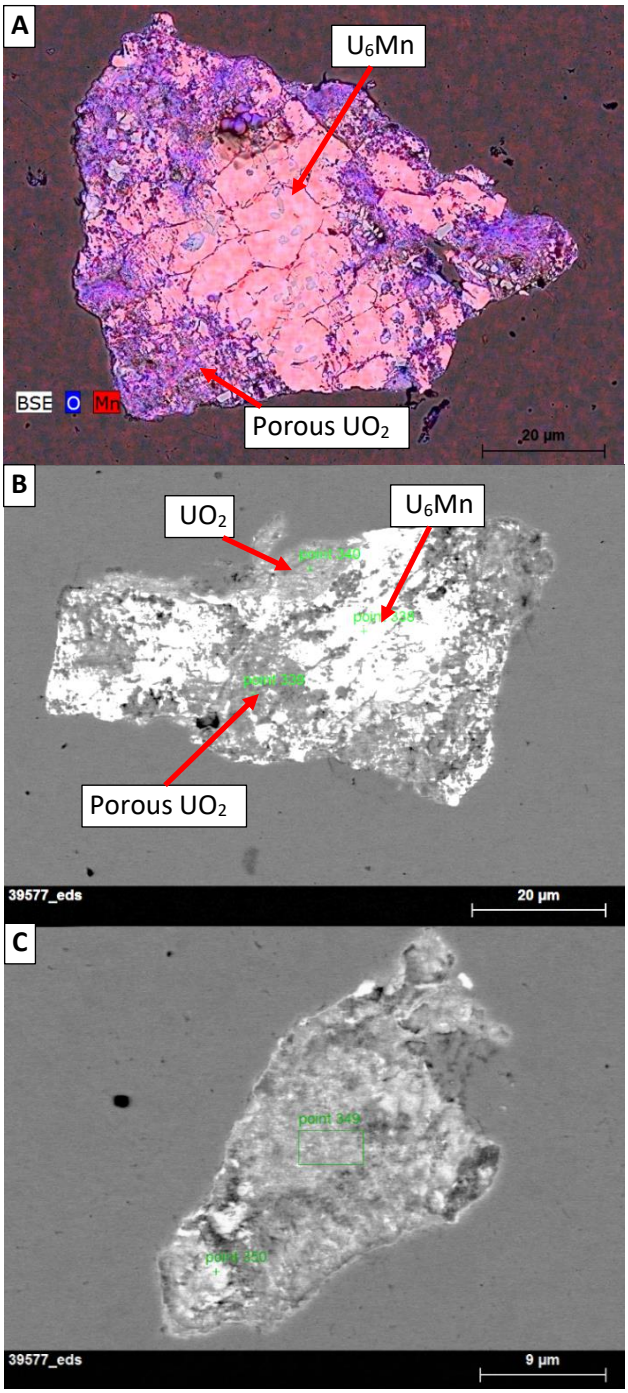

Figure 3) Digested U_6Mn particles after 30 minutes of digest. A. A composite image of a BSE-EDX elemental map with oxygen in blue, and manganese in Red. B-C. BSE images of a digested fuel particle.

Although it is not clear if the regions that are oxidized includes any particle that was original U_6Mn in origin, the regions of the particle surface and core that did not digest were pure U_6Mn regions. The digestion of U_6Mn progress past 30 minutes to develop the uranium oxide phase. After 120 minutes of digestion, the remaining particles were filtered through a Grade 5 Whitman cellulose filter (2.5µm cut-off limit). The digested particles were rinsed in additional water to eliminated sodium and nitrate salts and to prevent them from recrystallizing upon drying.

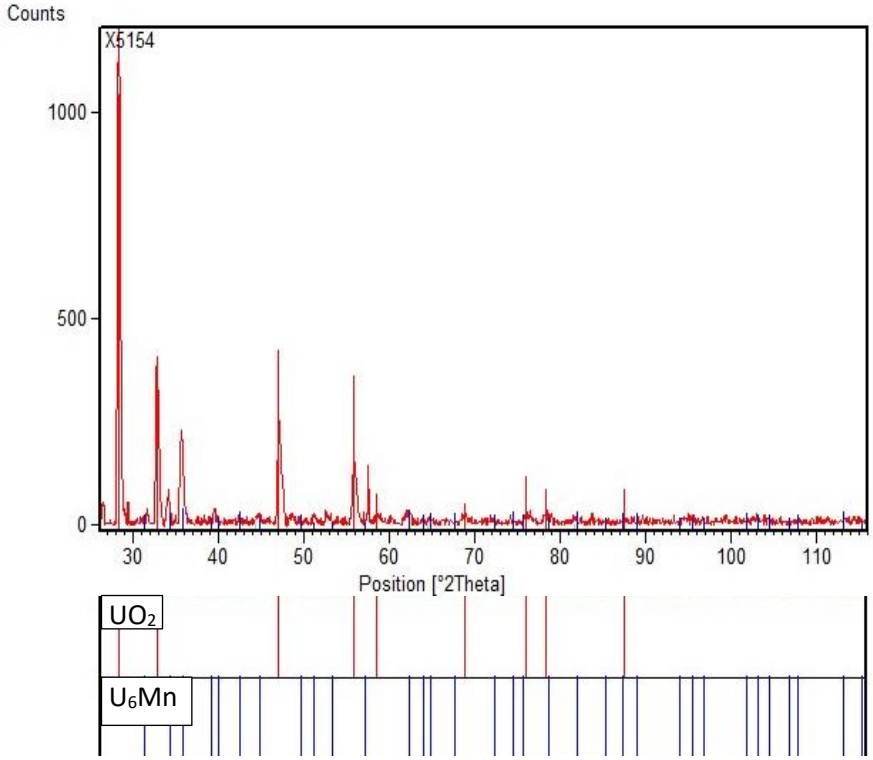

Figure 4) XRD diffractogram of digested U_6Mn after 120 minutes of digestion. Diffraction pattern for UO_2 indicated in red, and U_6Mn in blue.

Figure 3C shows a typical digested particle found after 120 minutes of digestion. In Figure 3C, a small particle can be seen that is predominantly uranium oxide. An EDX spot analysis demonstrated that this particle was 33 at% Uranium and 66 at% O. To identify the reaction products, powdered X-Ray Diffraction (XRD) was performed on digested fuel particles. The resulting diffractogram (Figure 4) indicated that UO_2 (Fm-3m, No. 225) was the only digestion product of U_6Mn and that no sodium diurinate has formed in levels that are detectable by XRD. Additionally, U_6Mn still remained even after 120 minutes of digestion time.

2.1.3 Experiment 1 conclusions

The high U-density compound U_6Mn was digested in ROMOL-like conditions for 2 hours to evaluate how this fuel performs is similar digestion conditions as UAlx fuels do. After 5 minutes of digestion (Figure 2) UMn_2 that is close to the particle surface has oxidized, leaving a porous UO_2 phase. Corrosion or oxidation follow along pathways of UMn_2 phase boundaries, until the phase has completely converted to UO_2. After 2 hours of digestion time, small particles (ferret diameter ≤40µm) have completely converted to UO_2. However, Larger particles (Figure 3D) was converted to UO_2, with large amounts of U_6Mn phases still remaining within the particle core.

The results from this experiment shows that U_6Mn is more resistant against corrosion or digestion than UMn_2 and UAlx. Although there was a conversion of the fuel to UO_2, no sodium diuranate in the form $Na_2U_2O_7$ was formed. Isotopes formed in this fuel after irradiation could be extracted, but not as efficiently as if it would turn into sodium diuranate. If U_6Mn were to be used for isotope production, a modified ROMOL99 solution would have to be adapted or a completely new approach would have to be envisioned.

The digestion of the U_6Mn produced here is similar to that of UAlx with discrete aluminum phases at the boundaries. Digestion favors the minor phases that develop along the boundaries, and the boundaries serve as a pathway for the digestion reagent to proceed through. The digestion shown here would apply to almost all the U_6Mn produced in literature using similar methods with similar microstructures [3-5]. The production of pure U_6Mn

without solute segregation has been reported once [6], and would likely be more difficult digest in the exact same conditions.

2.2 Experiment 2: digestion of U_6Mn with oxidants

The previous experiment demonstrated that the U_6Mn does not digest to completion in standard conditions. The UMn_2 phases had oxidized. However, parts of the particle that were U_6Mn were left undigested and none of the particle advanced to sodium diuranate. As is discussed in chapter 1, the use of $KMnO_4$ is a promising oxidant. In this experiment, $KMnO_4$ is added to the digestion mixture to see if an oxidant could help aide in digestion.

2.2.1 Digest U_6Mn + $KMnO_4$

In this experiment, two digestion were performed in parallel; one with $KMnO_4$, and one without. Both digestions were performed with 4M NaOH and 4M $NaNO_3$ and held at 90°C. 0.5g of annealed U_6Mn was used in each reaction vessel, each 200 mL of solution for one hour. Additionally to the shorted time, 0.71g of $KMnO_4$ (calculated via eq.5, Ch.1, sec. 4.3) was added to the second digestion vessel.

Several particles from the filter cakes were removed, cleaned and imaged with SEM and EDXS. An EDX Surface analysis of a digested particle without $KMnO_4$ (Figure 5A) showed that these particles were identical to those in Figure 3, where oxygen had developed on the surface. The same analysis on a surface particle with half of the digestion time and with $KMnO_4$ (Figure 5B) showed atomic percentages: Oxygen: 70±3%, Uranium: 16.5±2%, Sodium: 13±1%.

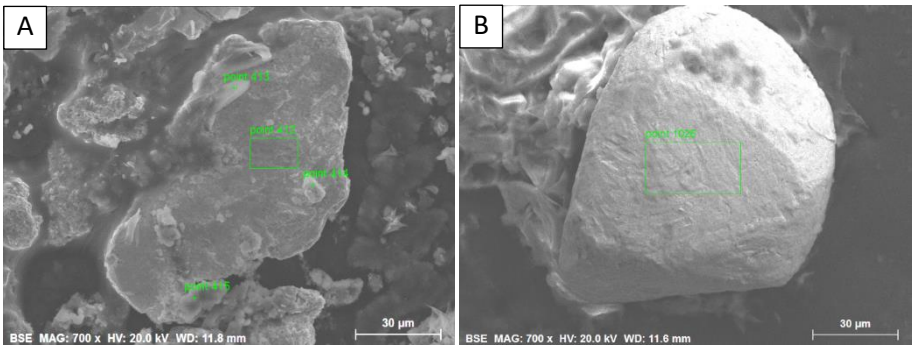

Figure 5) SE images of digested particles with and without $KMnO_4$. A) Digested particle without $KMnO_4$. B) Digested particle with $KMnO_4$.

2.2.2 XRD of filter cake

In the EDX spot analysis, the digested fuel particles with $KMnO_4$ showed that the fuel particles developed into a yellow cake with sodium, uranium, and oxygen in their composition. However, the structure of this yellow cake cannot be determined through EDXS. Additionally, SEM images are only taken of a few particles and is not an examination of the whole cake itself. To determine what compounds form in the yellow cake, X-ray diffraction was performed. All of the yellow cake was scrapped off and dried in air. A full scan of the cake was taken from 13 to 100 degrees in 2θ was taken, with a section up to 52 degrees presented in Figure 6. The XRD pattern is compared again $Na_2U_2O_7$ (ICSD pattern 00-026-0973), $NaNO_3$ (ICSD pattern 01-070-1518) and the pattern of U_6Mn is compared with a pattern of U_6Fe from [6] (whose crystal structure and lattice parameters are the same). The dominating pattern is sodium diuranate in the form of $Na_2U_2O_7$. This stoichiometry is in agreement with the surface EDX analysis performed in Figure 5B. For the

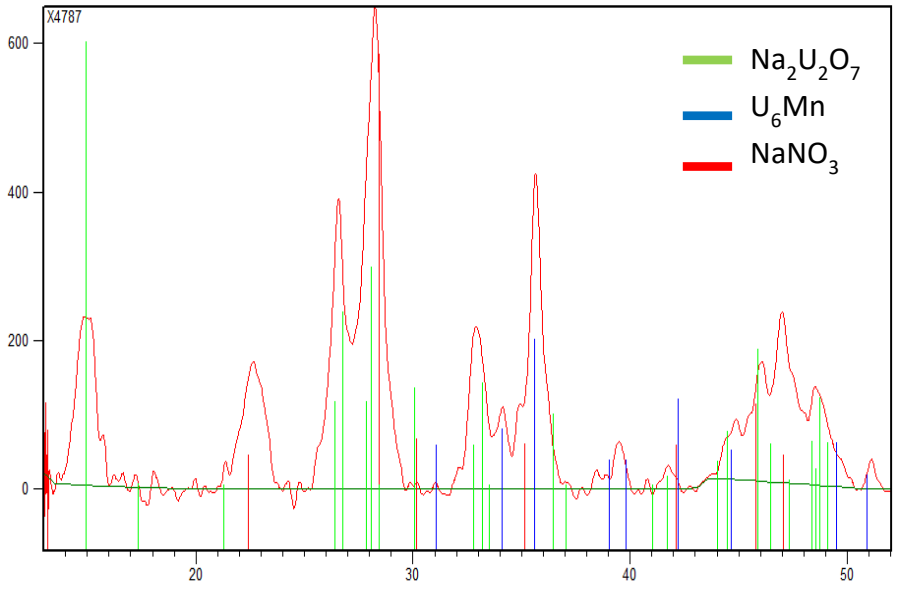

Figure 6) XRD of yellow cake from U6Mn digestion with $KMnO_4$. NADU is indicated in green, U_6Mn is indicated in blue, and $NaNO_3$ is indicated in red.

used reagents, nitrate is found in the XRD scan but NaOH is not. Finally, U_6Mn is found as another major product in the XRD pattern. U_6Mn was not found as a particle in any of the previous SEM image analysis of the particles. Therefore, it is unlikely that U_6Mn particles exist alongside NADU particles. Imaging of digested particle cross sections are needed to see how much of the fuel particles were digested and converted to NADU.

2.2.3 Images of Particle Cross-sections

The XRD scans showed that U_6Mn is still found in the filter cake, but no U_6Mn particles were found in SEM imaging. To investigate further into the nature of the digested particle, cross section of the particle were taken as explained in *sample preparation* section. A resulting image can be seen in Figure 7. On the left of Figure 7 a BSE image is presented of a singular multiphase particle containing cracks. As the contrast in a BSE image depends on the density of the material, the particle can be seen with three different densities. At the

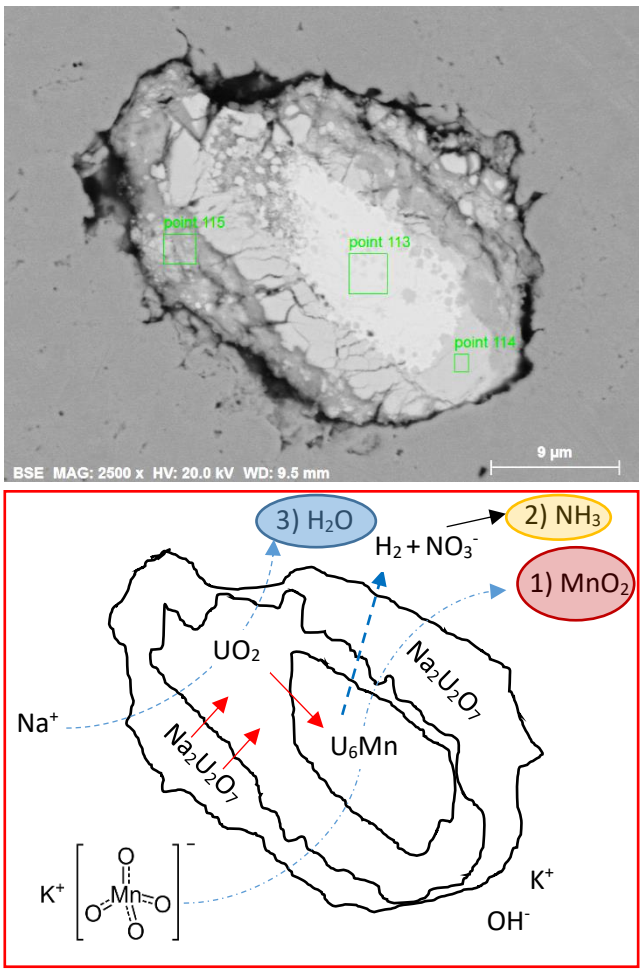

Figure 7) Digested U_6Mn particle. Left) BSE image of a cross-sectioned partially-digested particle. Right) schematic diagram of digestion. Pathway 1: Reduction of $KMnO_4$ to MnO_2 converting U_6Mn to UO_2. Pathway 2: conversion of U to UO_2 releasing hydrogen, reacting with nitrate to form ammonium. Pathway 3: UO_2 reaction with Na to produce $Na_2U_2O_7$ and H_2O. The reaction fronts, indicated with red arrows, show the progression of UO_2 and $Na_2U_2O_7$.

core of the particle, the initial fuel can be seen that has partially oxidized. EDX analysis of this area shows that the average atomic percentage of this area is: Uranium: 59±3%, Manganese: 21±1%, and Oxygen: 18±1%. The second lightest region, located immediately outside the core, is found to have the atomic percentages: Oxygen: 61.5±2%, Uranium: 36±3% with less than 1% manganese and sodium. This region is the intermediate UO_2 as described in equation 2 and 4. Finally the darkest part of the particle, at the particle edge has nearly the same atomic composition as Figure 5B: Oxygen: 66±2%, Uranium: 14±3%, sodium: 13±2%.

Additionally to intermediate phase UO_2, another possible intermediate phase has been found. Figure 8 shows another cross section of a digested particle. The BSE image (A) and EDX map (B) shows that there are three distinct densities in the digested particle as the core, UO_2 and $Na_2U_2O_7$, outline in the schematic (C). Additionally, between the U_6Mn core and UO_2, there is an UO_X intermediate. EDX analysis shows this section has the atomic

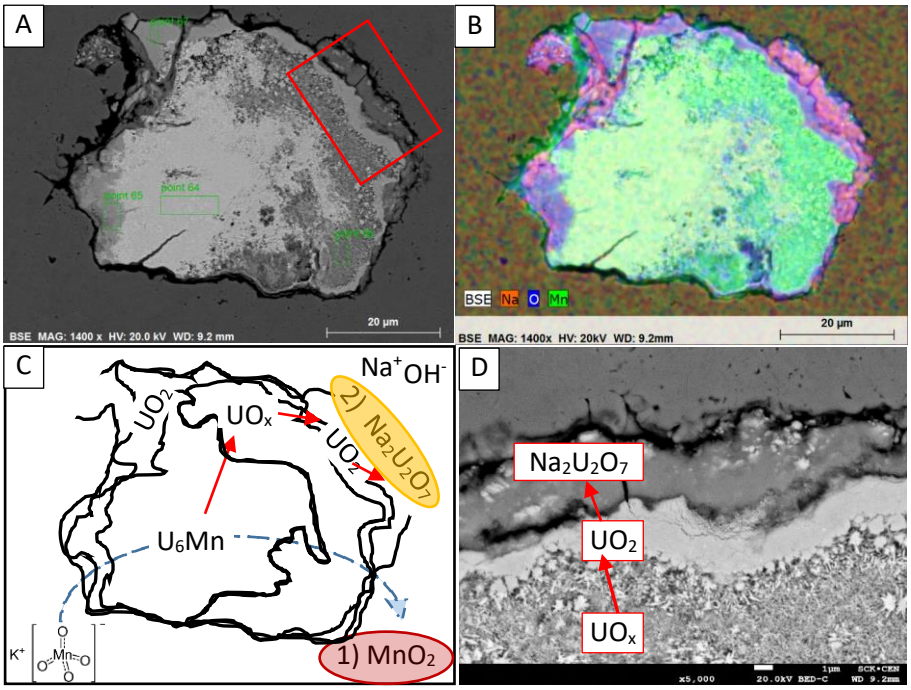

Figure 8) Cross-section of digested particle with $KMnO_4$. A) SEM-EDX spectrum imaging. A is a BSE image map of a partially-digested and polished particle. B) BSE-EDX map with manganese, oxygen, and sodium superimposed on a BSE image. C) schematic diagram of the redox reactions. Red arrows indicate the oxidation pathway of uranium, Blue arrows indicate the reduction of Mn and Na. D) Cropped BSE images of the reaction front, highlighted in image A.

composition: Oxygen: 55.7±2%, Uranium: 27.4±3, Manganese: 16.9±1%. In Figure 8 C, the red arrows show the oxidation of uranium leading to the final NADU product 2. The blue arrows indicate the reduction of $KMnO_4$, to MnO_2 via eq.4, and of Sodium via eq2.

2.2.4 Experiment 2 conclusions

In the field of isotope production, previous studies have talked about the theoretic use of U_6Metal alloys in isotope production [7-9]. However, a digestion has never been demonstrated in the literature. Presented here is the first demonstration of an U_6Metal converting into a yellow cake. The use of $KMnO_4$ successfully converted the surface U_6Mn to an oxide of UO_2 and finally a yellow cake of $Na_2U_2O_7$. The results show that the reaction is a surface oxidation that can penetrate only up to ~10μm of the particle surface. No intergranular oxidation is found in U_6Mn particles in contrast to UAl_3 particles. If the reaction is confined to the surface, than an optimization of particle size or the surface to volume ratio would be necessary.

In the digested particles, there are two types of oxides that have been identified. One type is an open porous UOx network (Figure 8D) while the other is a UO_2 network (Figure 7). The porous network would allow ions to pass through this area, facilitating digestion. Once the pores start to close, ions are prevent from reaching the fresh fuel, digestion of the core is arrested. In any case, it is clear that UO_2 is an intermediate of U_6Mn converting to a yellow cake. Also demonstrated here is an approximate chemical composition of the yellow cake. The end products of the reaction is $Na_2U_2O_7$. This compound is considered to be the optimal for isotope production as molybdenum does not adsorb to it [1].

Further research would have to be done in many areas. Discussed below in section 2.5 is how to advance the digestion front in order to allow the reaction to go to completion. Not covered in this chapter or thesis are, among other things; filtration of the yellow cake, purification of ^{99}Mo, effects of irradiation on the microstructure of U_6Mn, and the effects of irradiated on particles and its digestion.

2.3 Experiment 3: Digestion of UAlx + $KMnO_4$

The digestion of UAl_3 was thoroughly studied in chapters 2 and 3 in ROMOL conditions. In the digestions presented in those chapters, the fuel often did not digest to completion, or would require a longer digestion time than that which is commonly used. Here, we investigate how digestion of this fuel

could proceed with the oxidant $KMnO_4$ and if an oxidant can speed up the reaction time. Cross-sectional imaging of the digested particles is taken similar to those taken in chapter 2, to compare how an oxidant changes a metallic fuel to an oxide. To perform this experiment, a similar procedure was used with the addition of $KMnO_4$. 1.17g of UAl_3 was digested in 200ml of 4M NaOH and 4M $NaNO_3$. The reaction was held at 90°C for the duration of the experiment. The Digestion was stopped and filtered at 60 minutes of digestion.

2.3.1 Filter cake comparison

A comparison of fiter cakes of digested UAl_3 fuel without $KMnO_4$ and with $KMnO_4$ is presented in Figure 9A and B respectively. The digestion cake without $KMnO_4$ shows that most of the fuel is undigested after one hour. In comparison with the digestion of UAlx with $KMnO_4$, the sodium diuranate is more visible as yellow with no visible traces of undigested fuel. Additionally, spent $KMnO_4$ in the form of MnO_2 is visible as the color brown on the filter cake (Figure 9B) and through SEM imaging (Figure 14) presented below. Although these results shows progress in the digestion of the fuels, XRD and SEM analysis of the particles in these cakes need to be performed to analyzed how much of the particles were digested.

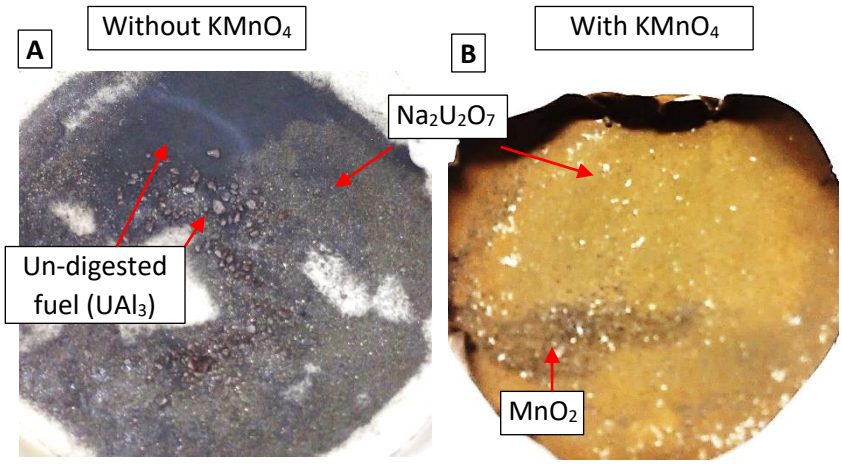

Figure 9) photo comparison of filter cake with and without $KMnO_4$. A) Digestion of UAl_3 without $KMnO_4$. Un-digested metal fuel is seen as black; B) Filtercake of digested UAl_3 with $KMnO_4$. $Na_2U_2O_7$ is seen as yellow, and MnO_2 is seen as brown.

2.3.2 XRD comparative results

A comparison of the XRD diffractograms from annealed UAl_3, Digestion of annealed UAl_3 for 1 hr at 90°C without $KMnO_4$ [10], and the digestion described above with $KMnO_4$ is shown in Figure 10. In diffractogram A, shows that the starting material for these digestions are almost pure and annealed UAl_3 with small amounts of UAl_2 present in the alloy. Diffractogram B shows the digestion of this fuel at an elevated temperature and without an accelerant. Although some of the fuel had started to oxidize, no detectable amount of NADU is visible in the diffractogram. Key differences in the diffractogram are a split in the highest intensity peak of UAl_3 at 29.5 degrees in 2θ, and additional peaks at 33.5, and around 38 degrees in 2θ. These additional peaks have been attributed to sodium nitrate that crystalized on fuel, and not to oxidation.

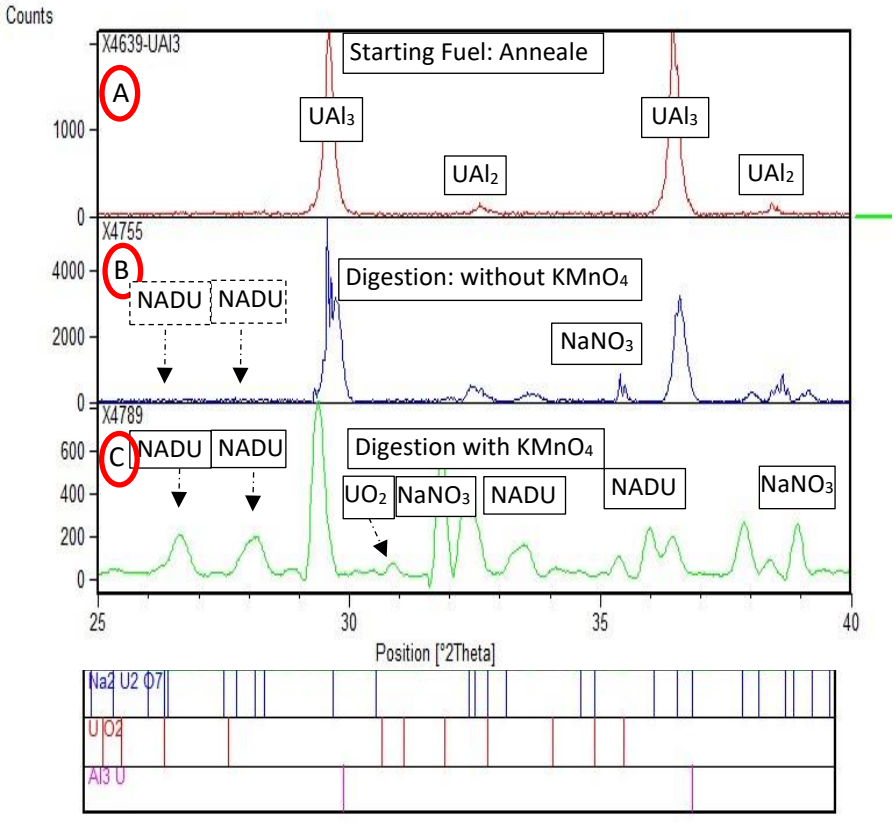

Figure 10) XRD scanes of 1) UAl_3 fuel that has been annealed, 2) digested fuel using ROMOL-99 at 90°C for one hour, 3) digested fuel using ROMOL-99 with $KMnO_4$.

Finally, diffractogram C shows digestion with an oxidant addition. After 40 minutes, $KMnO_4$ was added and allowed to digest for 20 minutes. Fuel particles were extracted from the reaction vessel and neutralized in water. In this diffractogram, sodium diuranate is shown to have developed in the cake. UAl_3 is still clearly a component of this yellow cake. Additional, the UAl_2 peaks remains visible, and is likely to remain in the fuel as it is known to be hard to digest.

2.3.3 SEM, EDX, and surface analysis of digested UAlx

Digested particles were taken from the filter cake and rinsed with pure water. After the particles were dried in ambient air and placed on carbon tape for SEM and EDX analysis. EDXS point analysis (inset of Figure 11) shows that the atomic composition of this particle is: Oxygen 68±3%, Uranium 16±2% and Sodium 15±3%. This is in agreement with the NADU stoichiometry of $Na_2U_2O_7$. To support this analysis, a closer investigation of the XRD diffractogram of the filter cake is presented in Figure 11, compared with the NADU pattern (ICSD 00-0260973) in green. Additionally, UAl_3 in blue (ICSD 00-007-0301) and UAl_2 in magenta (ICSD 00-018-0073) are found in the diffractogram.

A comparison of Figure 11, with and EDX analysis and an XRD scan, demonstrates the advantages and limitations of each technique. In EDX analysis, an approximate of the elemental analysis is given, although this technique is not strictly quantitative. The information volume, or the volume of material that is probed by this technique is around 1μm from the surface, and therefore only represents the surface layer. Similarly, the penetration depth of Cu K-alpha (wavelength 1.5406) of pure uranium is around 5 to 10μm and again only represents the surface. As UAl_3 and UAl_2 is found in the diffractogram (Figure 10 and Figure 11), it is likely that the NADU is only formed on the surface of the particle. To confirm this hypothesis, imaging of

the core is again necessary to determine how deep the digestion friend has penetrated the particle and in what way.

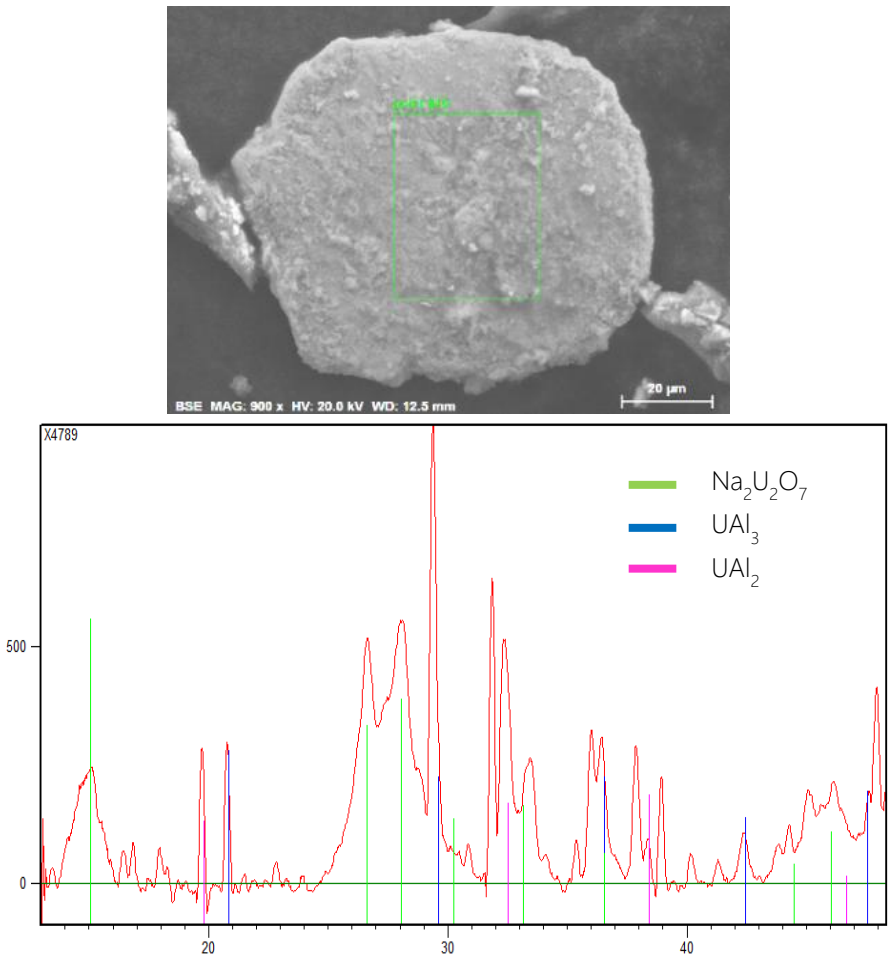

Figure 11) Analysis of diffractogram of digested UAl_3. Inset: BSE imaged of digested fuel particle with EDX scanned area in green.

2.3.4 Digestion of UAlx target with $KMnO_4$

This experiment was used to compare the difference between digesting powders individually, and digesting a target piece that has undergone a full target making process. The target digested here, is an LEU target that had all three of the UAlx intermetallics (UAl_2, UAl_3, and UAl_4) and cladded with Al6061. A digestion was performed to test the effect of $KMnO_4$ on the digestion of an UAlx target. A piece of target weighing 4.57g. The

concentrations of the reagents were kept at 4M NaOH and 4M $NaNO_3$. The target piece was placed into the digestion solution at room temperature and reached the reaction window in one hour with the reaction window lasting approximately 15 minutes. This reaction crest is the digestion of the aluminum cladding that surrounds the fuel. The oxidant was added after the primary digestion window had ended (cladding had dissolved), to avoid the consumption of $KMnO_4$ by H_2 gas, produced by the digestion of the cladding (product of eq. 6, Ch.1, sec 4.3). 4.53g of $KMnO_4$ was added, assuming the weight of the target was approximately all from UAl_3 (via eq. 5, Ch.1).

2.3.4.1 Type I Particles

There are two distinct classes of particles found on the filter cake which are designated as having originated from the fuel versus the oxidant. Type one particles are particles that are found to have a core and a shell to be of two different materials and are digested fuel particles. In this digestion, type one particles are found with a core of either UAl_2, UAl_3, or UAl_4, with a sodium diuranate shell. This can be seen in Figure 12, were an SE image (A), a BSE image (B) and EDX map (C) is presented for comparison. In the SE and BSE images, the core of the particle can be seen in the middle as two light spots surrounded by a shell had a thickness ranging approximately 4-8µm thick. An EDX point analysis done on the lower core spot indicated that this area was rich in aluminum, uranium, and oxygen, with only trace amounts of sodium. The shell immediately surrounding the core was found through an EDX area scan to be of the similar composition as sodium diuranate. Finally the outermost layer can be seen as a black region in images A and B, and as an oxygen rich region in C. A point analysis on this region found that it was unspent $KMnO_4$.

Several type one particles were found, each having the same shell type (NADU) with different cores of UAl_2, UAl_3, and UAl_4. A comparison of these particles can be seen in Figure 13. All four images show that the NADU layer forms roughly 3 to 10µm around the core, regardless of the core type and size. Comparing the same core for instance, images A and B have the same core of UAl_3. The core of A at its longest is above 20µm while the core of B is around 3µm. Both A and B have roughly the same NADU shell thickness. Both have cracks going through the NADU layer going perpendicular from the particle surface and ending at the core, possibly in response to imaging preparation. Additionally in image A, four light spots can be found in the core, which was determined to be rich in aluminum through EDX point analysis.

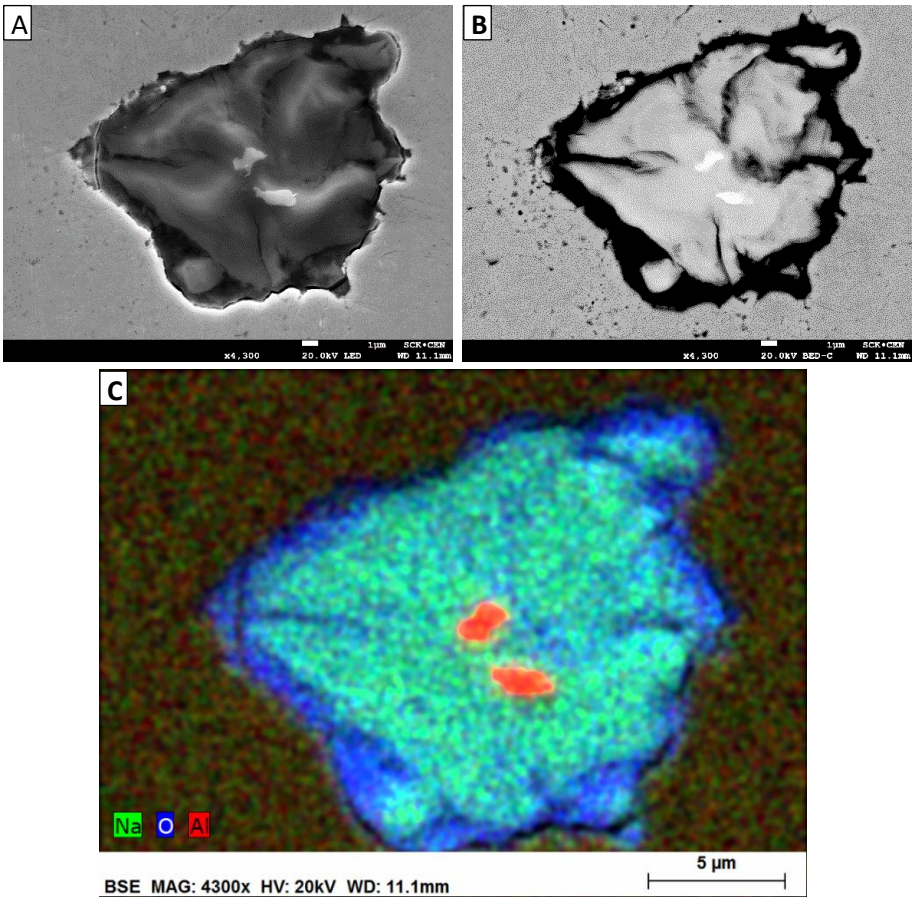

Figure 12) Type two particle from the yellow cake. A)SE image B)BSE image C)EDX map of a partially-digested UAl_3 particle. The core aluminum (red) is seen with a coating of sodium diuranate (sodium in green) the outer blue are is found to be spent $KMnO_4$.

The same shell thickness can be seen in Figure 13C (UAl_2 core) and D (UAl_4 core) with similar cracks through the NADU shell.

None of the particles imaged in this digested showed intergranular oxidation or oxidation at triple junctions. This is especially surprising for UAl_3 particles (Figure 13A and B). The digestion solution did still contain sodium hydroxide in the same concentrations as the experiments in chapters 2 and 3. The formation of the sodium hydroxide layer seems to prevent intergranular oxidation.

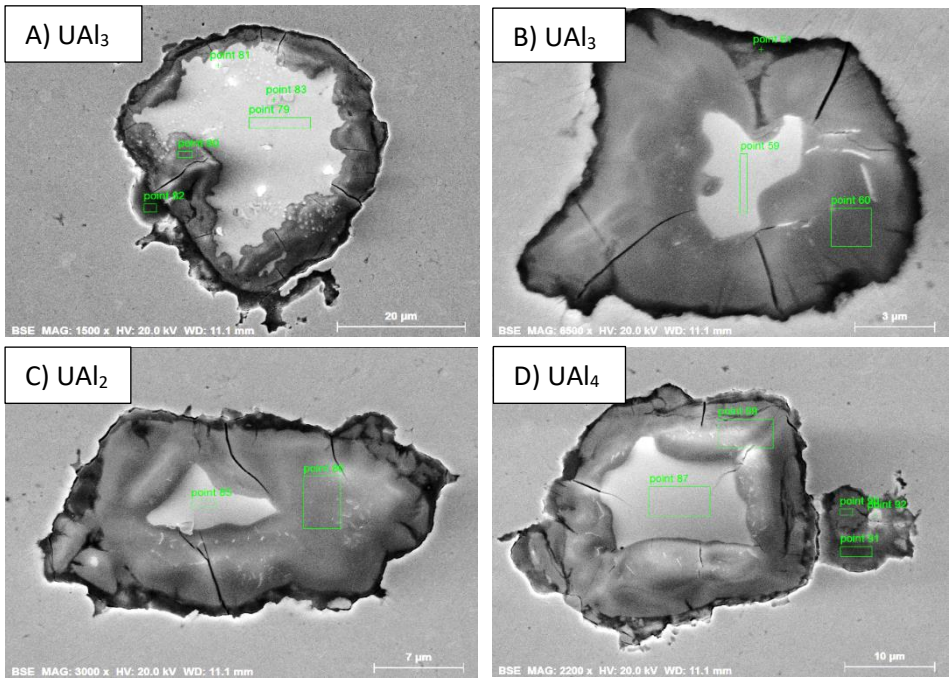

Figure 13) BSE images of partially digested UAl_3 particles. Comparison of core/shell type two particles. A and B) UAl_3 cores with NADU shell C) UAl_2 core with NADU shell and D) UAl_4 core with NADU shell.

2.3.4.2 Type II particles

A second type of particle can be found that is predominantly one phase. These particles can be identifies by being a spheroid or a section of a spheroid, and are often above 10µm in diameter (Figure 14). Through EDX point analysis, type three particles have the atomic percent composition of: Oxygen 65.3%, Manganese 24.7%, Magnesium of 3.6%, and minor amounts of sodium and aluminum. These particles are likely to be MnO_2 (through eq.4) with trapped impurities. The dark spots (indicated in red arrows) were found through EDX point analysis to have the following composition by

atomic percentage: Oxygen 34.4%, Magnesium 32.7%, Manganese 17.2%, Silicon 10.7%, and minor amounts of aluminum and sodium. This composition, whose crystal structure has yet to be identified through XRD, is likely to have originated through the cladding material or through the borosilicate glass reaction vessel. It appears to be inclusions within the manganese oxide particles. Both the cladding and the reaction vessel have minoring amounts of magnesium and silicone, and while the cladding is dissolved in the processes as expected, the glassware also shows signs of corrosion.

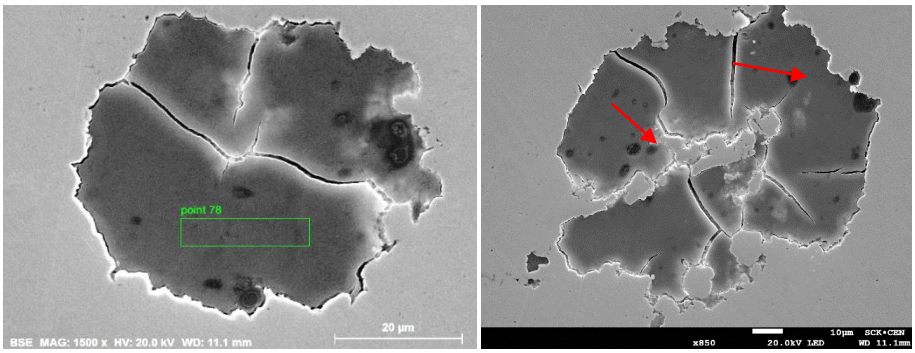

Figure 14) BSE image of a particle of MnO_2.Impurity Mg-Mn-Si inclusions within the fractured MnO_2 particle are indicated with red arrows.

2.3.5 Experiment 3 conclusions

This experiment shows the effects of using the accelerant $KMnO_4$ for the digestion of an LEU-UAlx target piece at 90°C. The results show that the conversion of U to a yellow cake occurs with the reduction of $KMnO_4$ to MnO_2 (Figure 14). MnO_2 is a solid product that stays on the filter and in the filter cake, as its size is well above the filter cutoff size. A downside to the accumulation of MnO_2 would be the increase of filtration time due to its presence on the filter. To ensure that $KMnO_4$ does not contaminate the downstream process, all of the accelerant should be reduced at this stage. After this reaction is complete, only the potassium ion K^+ from $KMnO_4$ would pass through the filter. This could be changed by using sodium permanganate ($NaMnO_4$), where the sodium ion would a redundant ion in solution, with the sodium coming from the caustic reagent.

It was observed that the formation of $Na_2U_2O_7$ forms as shell layer on the outside of core particles of UAl_2, UAl_3, and UAl_4. For the digestion performed

here, the thickness of the NADU layer on average ranges between 3 and 5µm. Further experiments would need to be performed to see if this is a critical thickness, before surface passivation limits the reaction. However, this is the same thickness found on U_6Mn fuel particles (Figure 7 and Figure 8). The results here also suggest that this would be a viable way include UAl_2 in the target, if digestion with $KMnO_4$ is used. Including UAl_2 into a production target could be an advantage because UAl_2 has a higher U-density (6.6 g cm^{-3}) than UAl_3(5.1 g cm^{-3}) and UAl_4(4.5 g cm^{-3}).

2.4 Experiment 4: Digestion by leaching - sodium carbonate

As mentioned in the introduction, the simultaneous dissolution of U and Mn has been studied for geochemical reasons with sodium carbonate. Sodium carbonate leaching has been known for some time in the ore processing of uranium [11]. The use of carbonates is derived from the highly stable uranyl(VI) tricarbonate ion, $UO_2(CO_3)_3^{4-}$ in aqueous solution at low hydroxide-ion concentrations. Uranium (VI) can be isolated from a carbonate solution, because the vast majority of other metal ions form insoluble compounds with carbonate and can be filtered using physical methods.

To perform carbonate leaching, oxidation is commonly used to help facilitate the dissolution of uranium oxide as following

Eq1) $2UO_2 + O_2 \rightarrow UO_3$

Eq2) $UO_3 + H_2O + 3CO_3^{2-} \rightarrow UO_2(CO_3)_3^{4-} + 2OH^-$

Eq3) $OH^- + HCO_3\text{-} \rightarrow CO_3^{2-} + H_2O$

Where eq3 demonstrations the formation of the uranyl(VI) tricarbonate ion from the addition of carbonate in solution. As shown in Eq.5, bicarbonate is used as a preventative measure to decrease the hydroxide concentration to keep the uranium in an aqueous phase as an ion. To precipitate the uranium ion out of solution, we can omit bicarbonate and increase the sodium concentration to yield sodium diuranate:

Eq4) $UO_2(CO_3)_3^{4-} + 2OH^- + 2Na+ \rightarrow Na_2U_2O_7 + 6CO_3^{-2} + 3H_2O$

Where eq4 demonstrates the displacement of the carbonate complex to form a solid yellow cake. Although this type of uranium chemistry has been applied to the extraction of uranium from ores, it has never been used demonstrated in the extraction of medical isotopes. To carry out an experiment that follows these steps, a digestion was performed with a

powder of UAl_3 at 95°C and with 4M NaOH for one hour. The amount of sodium carbonate was calculated from eq4 to ensure the formation of uranyl(VI) tricarbonate. Although less than 1M of NaOH is required for the formation of $Na_2U_2O_7$ via eq6, the concentration of sodium hydroxide is kept at 4M to be in agreement with all other experiments here.

2.4.1 XRD of digested fuel

The XRD diffractogram of the yellow cake is presented in Figure 15. The yellow cake was crushed in a crucible and scanned from 28 to 80 degrees in 2θ. The narrow peaks of the spectrum demonstrate that the yellow cake is highly crystalline and not amorphous, or more crystalline than the yellow cake made from potassium permanganate (FWHM of the highest intensity peak at 26.5 in 2θ is 0.173). The uniform shape of the peaks indicate it comes from one material with minimal impurities. One unassigned peak at 31.16 degrees in 2θ indicates at least one impurity that cannot be identified.

There are a few reported crystal structures of sodium diuranate in literature with the space group C2/m including monoclinic [12], hexagonal [13], and orthorhombic [11]. The pattern of the cake matches the yellow cake of $Na_2U_2O_7$ provided by Toussaint and Avogadro [13] (ICSD pattern 00-026-0973). The crystal system here is hexagonal with lengths a= b= 3.95Å, c= 17.92Å and angles α= β= 90° and γ= 120°. Finally, one important feature of this diffractogram of the filter cake is that no pattern for un-digested UAl_3 could be traced. This is a first indication that digestion went to completion.

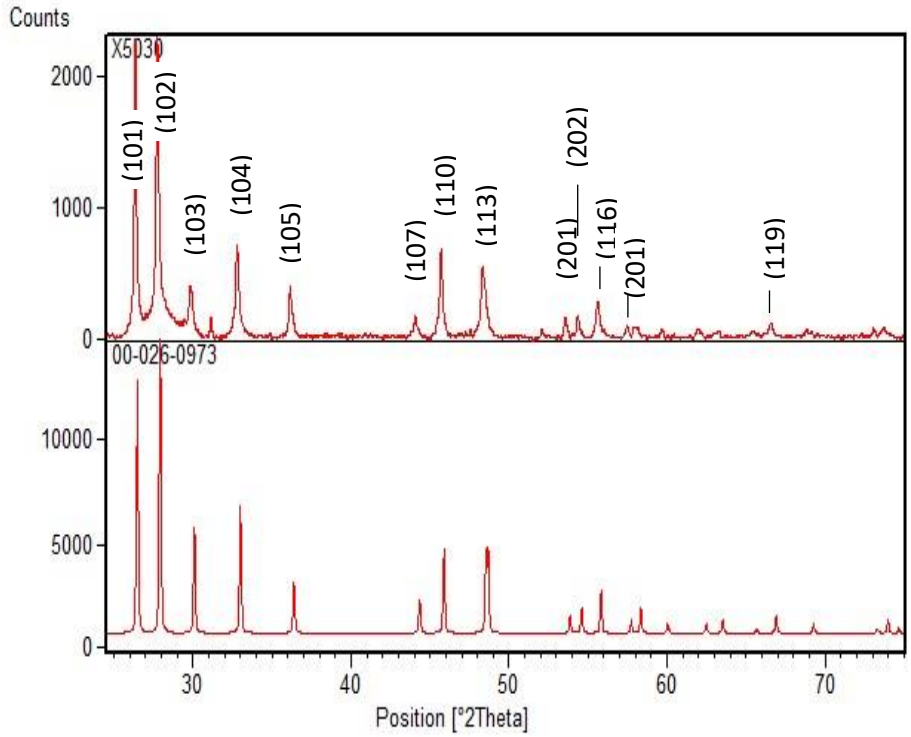

Figure 15) Diffractogram of yellow cake. Digestion of UAl_3 with sodium carbonate. ICSD pattern of $Na_2U_2O_7$ – 026-0973 and a simulation of that pattern is provided below

2.4.2 Experiment 4 conclusions

Presented here is the first time a digestion of a UAlx material using carbonate chemistry. The digestion of UAl_3 is in agreement with leaching methods of uranium from ore. Both processes transform uranium to a uranium oxide, then to an ionic solution containing uranyl(VI) tricarbonate. Unlike ore processing, bicarbonate was not added which allowed the sodium from the digestion solution to precipitation the uranium as a yellow cake. This within one hour of the digestion conditions. As the intermediate is an actual dissolution of the uranium into an ion, any trapped isotopes would certainly be able to escape the irradiated fuel and could be collected in the aqueous phase.

The main motivation behind carbonate leaching of uranium (compared to acidic leaching) is that it is relatively specific for uranium. However, a follow up research would include how or if carbonate complexes with molybdenum or iodine and if the two could can be successfully separated. It would also be necessary to see if molybdenum adsorbs to the yellow cake.

Absent from this study is the digestion of U_6Mn with sodium carbonate. The results presented in this experiment make it a promising candidate to digest U_6metals. A follow up study is encouraged to complete this analysis. The results presented here with UAl_3 can be used to compare any future study of carbonates and fuel digestion.

2.5 Experiment 5: Methods of advancing the digestion front

2.5.1 External methods - core shell separation

In the experiments in chapters 2-4 and experiments 1-3 in this chapter, particles were not digested to completion as demonstrated by the examination of particles in cross-section. This is unexpected as the digestions were performed for longer durations than is reported. A possible cause for this discrepancy is the ability to separate the core fuel from its UO_2/NADU shell during the digestion process. This may be done by increase of pressure in the reaction vessel [14] which could break the shell layer. This can also be done by vigorously mixing the solution by a stir, or naturally when the aluminum from a whole target digestion releases its exothermic energy upon digestion. Another alternative may be through temperature ramps, taking advantage of the mismatch between the thermal expansion coefficient of the different materials [1].

There are a few methods that can be used to externally apply a force to separate a core from its shell layer. Mechanical milling, micronization, magnetic stirring, magnetic separation, and ultrasonication are just a few examples of these techniques. In these examples, no additional reagents are added to the solution and no microstructural changes are made to the fuel, and therefore, no additional purification techniques would be needed.

In an experiment to use an external method, ultrasonication was used to demonstrate if sound energy could accomplish core-shell separation. Samples of filter cakes were taken from a digested UAlx target, digested U_6Mn powder, and undigested particles were taken and placed into separate vials (Figure 16A). The vials were placed in an ultrasonic bath, and were exposed to 40 kHz of sonication for 15 minutes. The results of this experiment can be seen in Figure 16C. Immediately after removing the vials from the ultrasonic bath, all the particles from the undigested fuel vial (Figure 16C, 1) sank to the bottom of the vial. For the vials that contained digested fuel (vials 2 and 3) some particles sank to the bottom of the vials, while other took a longer time sink. The digestion solution also turned an orange/red after sonication, compared to the solution before sonication and to the undigested particles.

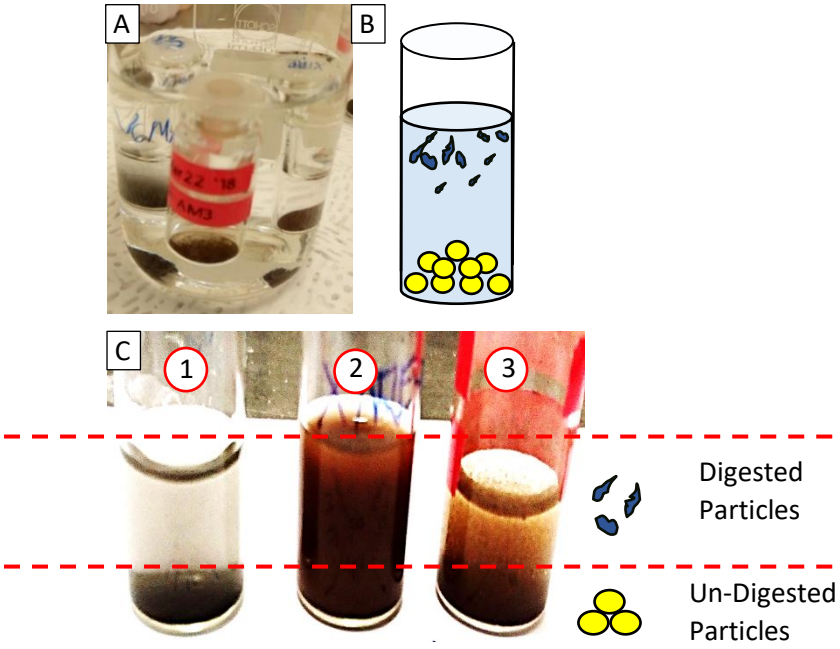

Figure 16) Core shell separation. A) Three samples of digested fuel particles before ultrasonication. Samples included a vile of U_6Mn, one of UAlx target, and one of undigested fuel B) Depiction of separated core and shell. C) Vessels of digested fuel after ultrasonication. 1) Undigested U_6Mn fuel 2) Digested UAlx target 3) Digested U_6Mn.

Particles from these vials were metallographically prepared to analyze the particles in cross-section. Figure 17 shows typical particles observed after ultrasonication. Figure 17A, a BSE image of a particle is seen with no shell layer surrounding the particle. EDX analysis of this particle showed that it has the following atomic composition: Uranium 82±3%, Mn 13±2%, with minor amounts of oxygen. Figure 17B shows a BSE image of a particle with different densities. EDX analysis over a large area indicated that this particle was predominantly uranium and oxygen in composition. Unlike the other images presented here (Figure 12 and Figure 13), these particles did not have any $KMnO_4$ surrounding the particle, and the particle edges come into direct contact with the silver matrix. This indicates that the $KMnO_4$ is not chemically attached to the particles. Instead, sodium diuranate may be electrostatically attraction to the negative molybdate ion $[MnO_4]^-$.

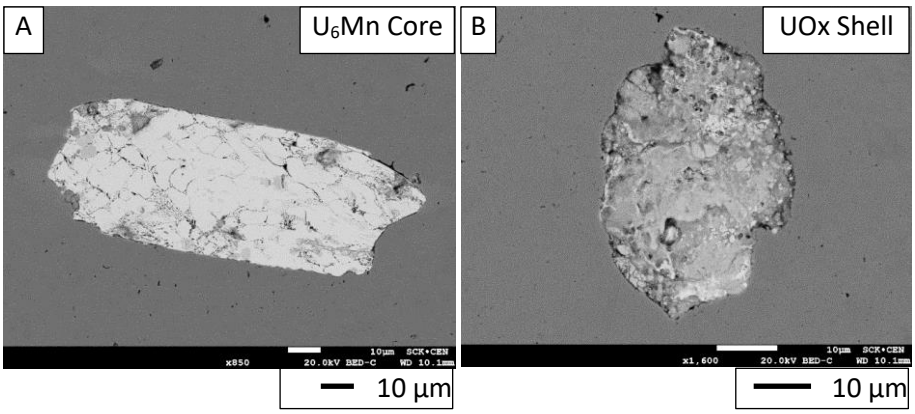

Figure 17) BSE images of particles that have been both digested and ultrasonicated for 15 minutes. A) A core particle of U_6Mn without a UO_2/NADU shell B) NADU without a core.

2.5.2 Internal method – preferential digestion within an U_6Mn – UMn_2 eutectic

Another method of advancing a digestion front is to change the microstructure or composition of an alloy. Examples of this have been explored in chapters 2 and 3, where grain boundary engineering was used to enhance the digestion of UAl_3. The advantage of an internal method would

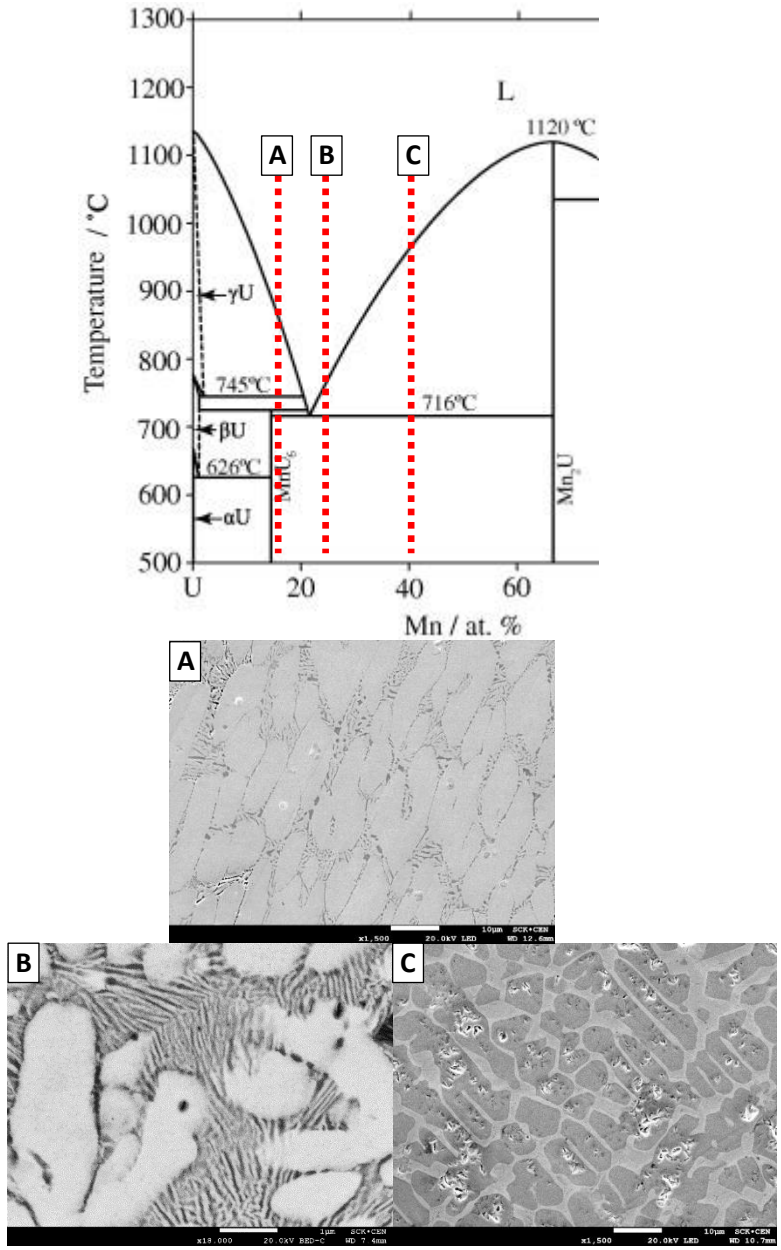

Figure 18) Eutectics of U_6Mn and UMn_2. A) BSE image of an alloy of uranium with 3.7%Mn by weight. B) BSE image of a 7%Mn by weight and C)SE image of a 20%Mn by weight. Light regions are U_6Mn while dark regions are UMn_2.

be to reduce the number of components that could fail (i.e. transducer or a gear) and could lead to a more consistent digestion product if the

microstructural modifications are even throughout the fuel. Another example of an internal method is preferential oxidation, or the selective etching of one phase over another in a bimetallic specimen. The main disadvantage of this method is that multiple phases could have multiple reaction products, which could increase the number of purification steps.

The selective oxidation of a U_6Mn-UMn_2 could be an alternative to advance the digestion front without external forces. Pure U_6Mn would be an ideal intermetallic to increase isotope production within a target with its uranium density of 17.1gU cm^{-3} close do pure uranium at 19.1 gU cm^{-3}. However, digesting U_6Mn is difficult in standard ROMOL99 conditions and time. As is clearly outlined in section 2.1, UMn_2 converts to UO_2 readily in ROMOL99 conditions. However, the UMn_2 phase has a lower U-density than U_6Mn and should be minimized. Ideally, the amount of UMn_2 phase should be above the "percolation threshold" or the amount necessary to make a continuous path through U_6Mn. This would ensure that the digestion solution could pass through the material and enough surface area would be exposed [15]. Figure 18 shows three alloys having both U_6Mn and UMn_2 phases with different concentrations of Mn by weight. Figure 18A is same alloy used in an is 5.6 Mn wt% [2]. This alloy was demonstrated to not have a sufficient UMn_2 pathway for an efficient digestion as there were many areas of U_6Mn that was not exposed to the caustic reagent. In contrast, the eutectic of Figure 18C (16.7 wt% Mn) has large islands of UMn_2 in a matrix of U_6Mn pathways, which decreases the U-density of the alloy all together. An intermediate eutectic of Figure 18B could allow for a digestion pathway to move through the alloy, while minimizing the amount of the lower density UMn_2 phase. '

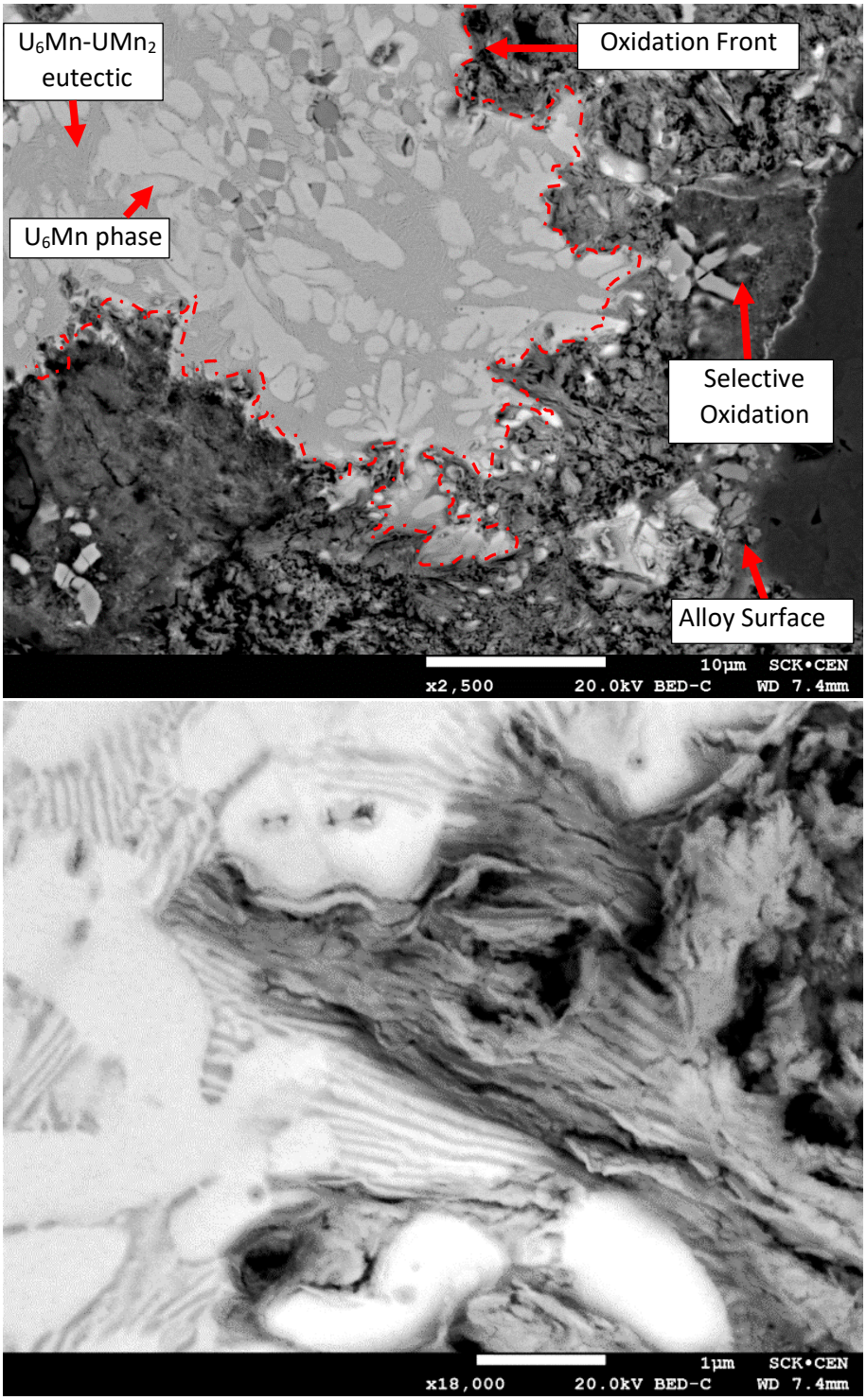

Figure 19) BSE images of digested U_6Mn-UMn_2 eutectic after 15 minutes demonstrating selective oxidation.

Figure 19 shows BSE image of a digested U_6Mn-UMn_2 eutectic (approx. 12.6 %wt Mn) after 15 minutes of digestion. The eutectic system has decomposed by the selective oxidation of the UMn_2 phase, by more than 10 µm past the particle surface. A close up of the digestion front in Figure 19 shows that the UMn_2 phase (darker phase) dissolves more favorably than the U_6Mn (lighter phase). Islands of U_6Mn can be found in the zone between the digestion front and within the alloy surface. The digestion front advances almost exclusively along UMn_2 pathways.

2.6 Chapter discussion

Although it is known that potassium permanganate can oxidize UAlx fuel [14], it was unknown how this reaction occurs. With the cross-sectional imaging presented here for the first time, it is clear that it is only a surface reaction that converts the fuel into a yellow cake, and not by intergranular oxidation or another means. In the past, the amount of digestion or yield was estimated through a gamma counting method to determine the difference of molybdenum in the filtrate compared to the molybdenum trapped in the yellow cake. The amount of ^{99}Mo activity would be determined by gamma counting at 11.1, 739.4, and 77.8 keV [14], and the difference between the activity in the filtrate, versus the total amount would indicate the yield and digestion. Although this technique accurately assesses how much total digestion occurred, this technique does not give insight into how the yellow cake formed and therefore an optimization of this process was primarily through brute force (higher temperature, higher pressure, more oxidants). With an understanding of the oxidation process through cross-sectional imaging, we have the opportunity to engineer solutions with controlled parameters.

Given the advantages of using an accelerant, there are three immediate drawbacks that can be identified and should be addressed. The first is the inherent increase in filtration time due to the accumulation of MnO_2. MnO_2 particles can be filtered with the uranium as they were found to be well above 3µm or a common cut-of diameter of a filter. It is an advantage that the reaction products can be filtered easily but the change in the filtration time should be studied to ensure that it does not become too slow or clog. A second change concerning the filter cake is the decrease in purity. Previously, filter cakes were nearly pure $Na_2U_2O_7$. If there is reprocessing and recycling of the filter cake, this would make it more difficult to do. A method to separate $Na_2U_2O_7$ and MnO_2 should also be studied. The third and important

concern is the effect of using $KMnO_4$ on any surface that it touches. As it is can react with uranium, it is also a strong oxidant to many metals and tubing and all surfaces that might come in contact must be checked. Before any waste is disposed of or processed, it should be ensured that any remaining $KMnO_4$ be reduced down to MnO_2. MnO_2 itself is known as a catalyst to breakdown peroxides [16], and any secondary reactions should be studied. Besides interactions with peroxides, MnO_2 could still be reduced to Mn^{2+} with hydrogen gas and other side products.

An advantage of using $KMnO_4$ combined with U_6Mn is that, MnO_2 is a redundant reaction product. It comes from the reduction of the accelerant, and the manganese in the fuel. Other oxidants such as peroxides, chromates, iron and copper (see chapter 1 figure 11) will have reaction products that are not a manganese derivative and the overall reaction will therefore have two or more impurities. Having a common reaction product would simplify the purification of the cake or the filtrate.

In this chapter, we have explored two methods of advancing the digestion reaction front: An external method of ultrasonication, and an internal method of selective oxidation or selective digestion. Perhaps a combination of two practices would work such as selective oxidation followed by ultrasonication. Although these methods have been proven to work, there could be drawbacks in using this technique. If it can break the NaDU layer, it is also very likely to change the particle size distribution of the NaDU particles. This could become a problem for filtration if the NaDU particle size shrink and become comparable to the filter pore size. A similar problem could happen with the particle sizes of MnO_2, which is also stopped by the filter. It is therefore necessary to find the minimum time needed to use ultrasonication to separate the shell from the core in order to minimize the change in particle sizes. Another shortcoming of ultrasonication is its scalability. Although it is easy to perform sonication on the gram scale with a small volume, the dissipation of energy in a large reaction vessel with several targets may be difficult. Finally, sonication devices are operated with transducers. Transducers can deteriorate with exposure to radiation and may need to be frequently replaced. Probe type sonication devices exist, such that the main transducer is further away from the probe, which would then be shielded from the fuel particles.

A final consideration is that the work that has been provided here has been restricted to cold tests, or tests of materials that have not been irradiated

and using natural uranium. Although the digestion of U_6Mn has been demonstrated, a more representative proof of concept needs to be performed. To bring this process to its next step towards industrial use, an irradiation of a plate followed by a digestion using these methods would be required. By combining a test like a gamma count as mentioned above to demonstration ^{99}Mo yield, with the cross sectional imaging of the yellow cake, could provide a stronger case for the transition of using UAlx targets to a more advanced target with U_6Mn.

2.7 Conclusions

The experiments in this chapter seeks to understand how U_6Mn digests in normal and modified conditions, and compare these digestions against the digestions UAlx fuel. It was found that U_6Mn does not digest well in a caustic digestion bath. However, presented here for the first time is the successful conversion of U_6Mn into sodium diuranate with the use of the oxidant potassium permanganate (experiment 2, sec.2.2). This breakthrough technology allows this alloy, and the whole family of U_6Metals, to be a serious consideration as a replacement fuel for the production of medical isotopes. It was found that the digestion reaction is limited to the surface of particles and therefore need a modification or an additional step to digestion to completion. The use of ultrasonication was found to break up the passivated surface and allowed the digestion to continue. Otherwise, it is important to have a mixed U_6Mn-UMn_2 particle where the digestion can selectively proceed through the UMn_2 phase. The work presented in experiments 2 and 5 lay the ground work for this process to be up-scaled and used in real targets.

An additional experiment (experiment 3 sec. 2.3) was performed to evaluate the use of $KMnO_4$ on a whole target piece containing UAl_2, UAl_3, UAL_4 and Al6061 cladding. Figure 13 shows that the development of $Na_2U_2O_7$ occurs at the same rate for all UAlx compounds, including UAl_2 which is difficult do digest [17, 18]. Although currently UAl_2 is not allowed in UAlx targets, digesting it with $KMnO_4$ would allow for the presence of this phase in a target.

In the digestion of UAlx fuel with $KMnO_4$, no intergranular oxidation was identified in the digestion fuel particles. This is particularly surprising in UAL_3 and for the fact that the concentration of sodium hydroxide was kept the same. In other words, the $KMnO_4$ digestion mechanism prevents the intergranular oxidation mechanism. The $Na_2U_2O_7$ layer passivates the surface

and does not allow for other reactions to occur. In the case of U_6Mn, this is not a problem as intergranular oxidation is not a mechanism of digestion. However, intergranular oxidation is very important in digesting large UAl_3 particles. If intergranular oxidation is halted, then the use of an oxidant would be disadvantageous. Surface digestion alone could never fully digest a large fuel particle and the total amount of digestion would decrease.

References

1. Muenze, R., et al., *The Fission-Based 99Mo Production Process ROMOL-99 and Its Application to PINSTECH Islamabad.* Science and Technology of Nuclear Installations, 2013. 2013: p. 1-9.
2. Cea, A.K., et al., *Microstructure and calorimetric analysis of the U Mn binary system.* Journal of Nuclear Materials, 2019. 514: p. 380-392.
3. H.A. Wilhelm, O.N.C., *The Uranium-Manganese and Uranium-Copper Alloy Systems.* ASM, 1950. 42: p. 1311.
4. Meyer, M.K., et al., *Irradiation behavior of U6Mn–Al dispersion fuel elements.* Journal of Nuclear Materials, 2000. 278(2-3): p. 358-363.
5. Ugajin, M., et al., *Irradiation behavior of high uranium-density alloys in the plate fuels.* Jounral of Nuclear Materials, 1998. 254: p. 78-83.
6. Kimball, C.W., et al., *Phonon anomalies and local atomic displacements in the exchange-enhanced superconductorU6Fe.* Physical Review B, 1985. 32(7): p. 4419-4425.
7. Ryu, H.J., et al., *Metallurgical considerations for the fabrication of low-enriched uranium dispersion targets with a high density for 99Mo production.* Journal of Radioanalytical and Nuclear Chemistry, 2014. 305(1): p. 31-39.
8. Cea, A.K., et al., *Microstructure and calorimetric analysis of the UMn binary system.* 2019. 514: p. 380-392.
9. Ryu, H.J., et al., *Development of High-Density U/Al Dispersion Plates for Mo-99 Production Using Atomized Uranium Powder.* Nuclear Engineering and Technology, 2013. 45(7): p. 979-986.
10. Cea, A., *Progress Report 3: Digestion studies of UAlx and U6Mn.* 2018: p. 29.
11. Grenthe, I., Drozdzynski, J., Fujino, T., Buck, E., Albrecht-Schmitt, T.E., Wolf, S.F, *The Chemistry of the Actinide and Transactinide Elements, Chapter 5.* 2006. 1.
12. Kovba, L.J.S.R., v. 14, no. 5, pp. 746-749, *Crystal structure of sodium diuranate.* 1972.
13. Toussaint, C. and A. Avogadro, *Uranate formation in alkali nitrate melts*. 1974, Commission of the European Communities, Ispra, Italy.
14. A. V. Gelis, et al., *ANL progress in developing an leu target and process for mo99.* RERTR 2003, 2003.

15. Štěpánek, F., *Effect of microstructure and pure component properties on the dissolution rate of a binary composite material.* Computational Materials Science, 2008. 44(1): p. 145-151.
16. Alyea, H.N., *MnO2 as a catalyst for H2O2 decomposition. Dem. 646.* Journal of Chemical Education, 1969. 46(7): p. A496.
17. Giovanni, R.C. and D. Michelangelo, *Study of Thermomechanical Treatment for Manufacturing UALx/Ual Dispersion Targets.* RRFM Meeting, 2017.
18. Cols, H.J., P. R. Cristini, and A.C. Manzini, *Mo-99 From Low-Enriched Uranium.* International Meeting on Reduced Enrichment for Research and Test Reactors, Las Vegas, Nevada, Outubro, 2000: p. 1-6.

Chapter 7

Conclusions and future outlook

1 Conclusion

The results presented in this thesis demonstrate advancements on two fronts of medical isotope production with the use of LEU. Chapters 2-4 develop a better understanding of the digestion of the currently used UAlx fuel and targets while chapters 5 and 6 demonstrate the possibility of using the uranium-manganese alloy system for next generation isotope production targets. A thorough analysis on the digestion of both fuel types relying on extensive cross sectional imaging is presented in order to compare both digestion types and allow future researches to make direct comparisons with other fuels.

The breakthrough in this thesis is the use of cross sectional imaging on digested fuel particles. Although cross sectional imaging of fuel particles is known in the nuclear industry for coatings of particles [1-6], microstructure and EBSD analysis [7, 8], and target analysis [3, 4, 9-11], it has never been used to study the digestion of fuel particles in open literature. There are likely two reasons for this. The first is the dangers involved in handling a digestion reaction and the second is the fact that it may not have been needed until now. Typical digestion solutions are on the extreme ends of the pH spectrum, are heated, highly exothermic, and involve materials that are both pyrophoric and gamma irradiation emitters. If researchers and industrial producers were able to achieve the digestion of targets without the need to look into the particles, then there may not have been the drive to do so.

However, the reliance on old analysis techniques should change to improve new digestion techniques and targets. A direct change from HEU to LEU UAlx based targets left the yield of the isotopes lower, and a drive for new designs and cost efficient digestions came into question. The first step in conversion was to increasing the total amount of uranium in a target by increasing the dimensions of the fuel area, which had been done successfully [12]. The next step was to change the fuel composition itself to an alloy with a higher U-density, which has been unsuccessful. Uranium-silicides has been heavily researched for its use in LEU based isotope production targets [13-15]. However, it is the digestion step that could not be solved to a greater extent to this day. In general, the lack of a deep understanding of the digestion step itself made it the weak step in isotope production and in predicting if a new target concept would become successful. Indeed, as target properties such as fuel swelling, thermal conductivity, mechanical properties [16, 17] are well studied, and as the isolation, separation, and biological chemistry of isotopes

are also well studied [18, 19], then the digestion of the targets is left as the largest uncertainty in the isotope production process and in designing new methods.

This thesis provided methodologies to understand and compare digestion processes. The study of digested fuel particles with cross sectional imaging and with samples taken at different stages of the digestion process directly helps optimize the digestion process as they are now and future processes. It can help to see *if* digestion goes to completion and *how* it goes to completion. These techniques can be used in current UAlx fuel targets and future targets. It is the beginning in understanding how U_6Metals digest in caustic solution and is a reference for the digestion of future high U-density alloys.

More specifically, the key findings of this thesis are:

Part I

- In chapter 2, we demonstrate that the digestion of UAl_3 is not a surface reaction, as it was previously presumed. Our results show that digestion proceeds in three distinct stages, namely; surface oxidation, oxidation of triple junction, and oxidation of grain boundaries. The fact that triple junctions are observed to be oxidized first is attributed to voids and intraparticle cracking present in the particles. Our results shift the focus of digestion from surface engineering to grain boundary engineering. The consequences of having an UAl_2 impurity is shown to prevent GB oxidation within its network, while aluminum phases at the grain boundaries enhance the digestion process by allowing TJ and GB to digest simultaneously. Finally in this chapter, we present a classification system of triple junctions that allow developers to strategically control the digestion properties of UAl_3. UAl_3 made of R0 and R1 TJs are shown to create oxidation resistant UAl_3 while R2 and R3 junctions are shown to promote digestion.

- In chapter 3, EBSD is used to further analyze how each boundary type in UAl_3 responds to a digestion bath. With this technique, we have proven that high angle grain boundaries are the most oxidation susceptible while Σ3 and Σ9 boundaries are oxidation resistant. Equally important is the discovery that grain sizes also play a role in digestion. Particles with small grain sizes are the most optimal for digestion. We have found that when the average grain size exceeds 40μm, particles become oxidation and digestion resistant.

Combining the performance of each individual grain boundary with the junction classification presented in chapter 2, gives the most complete model of the digestion of UAl_3 possible, with the current techniques available.

- In chapter 4, the digestion for of UAl_3-UAl_4 mixed particles is studied. We reveal three phases of digestion; surface oxidation, oxidation of the UAl_4 continuous phase, and finally the oxidation of the UAl_3 phase. We show that oxidation occurs with a "worming effect" rather than surface roughening, due to the difference in the oxidation rate of the two intermetallics. Our most important finding is on the importance of phase sizes and the fact that phases of UAl_3 larger than 10µm do not digest to completion within standard digestion conditions. phase size is currently not a target design criteria that is looked at in open literature. However, the findings in this chapter gives evidence that it should be a consideration for UAlx isotope production targets.

Part II

- In chapter 5, the microstructure, growth kinetics, and high temperature phase equilibria of the U-Mn binary system is presented. This study is performed for two reasons. Firstly, DSC is performed to fulfil qualification standards for isotope production targets. If a target fails, the energy of each transition state is now experimentally confirmed and can be used in failure analysis. Secondly, the detailed analysis of the microstructure of these alloys can be used to strategize a selective oxidation process found in chapter 6. In chapter 6, UMn_2 is found to be selectively leached from mixed U_6Mn-UMn_2 particles, a strategy that could be used to completely digest a particle. With the microstructural analysis in chapter 5, future developers can adjust the network of UMn_2 to a desired amount for optimal digestion. '

- In chapter 6, we demonstrate the digestion of U_6Mn with the use of $KMnO_4$. This is the first recorded instance where an U_6metal is converted to $Na_2U_2O_7$. This finding is a critical step in proving that U_6Mn can in fact be used for medical isotope production. The reaction product MnO_2, coming from both the fuel and the oxidant, is easily filtered off with the yellow cake, which keeps the reaction products out of the filtrate. With the potential to increase the amount of produced ^{99}Mo per target, and with a comparable amount of liquid waste, U_6Mn can now be economically competitive for isotope

production, and is now a leading candidate to replace the currently used UAlx LEU targets.

2 Perspectives and outlook

2.1 Comparison on the digestion of UAlx and U_6Mn

The current understanding of the digestion process is that it proceeds as surface reaction [20] with no consideration about microstructure or phases. In chapter 2, surface oxidation appears only as the beginning of the digestion process, and that triple junction and grain boundary oxidation occur as two distinct phases in mid to late digestion (Figure 1) for pure UAl_3 fuel particles. The fact that triple junctions oxidize first is attributed to voids and intraparticle cracked found throughout the particle. We also discovered that aluminum phases at grain boundaries aid the digestion process and that UAl_2 prevent intergranular oxidation. In chapter 3, the digestion of grain boundaries is further developed by analyzing which boundaries are more susceptible to oxidation though EBSD analysis. Finally in chapter 4, the importance of phase sizes within UAl_3-UAl_4 systems is shown as large UAl_3 phases or "islands" above 10µm do not fully digest. Altogether, this thesis introduces concepts of grain boundary engineering into the field of medical isotope production in order to understand the mechanisms of conversion and to understand what digestion really means.

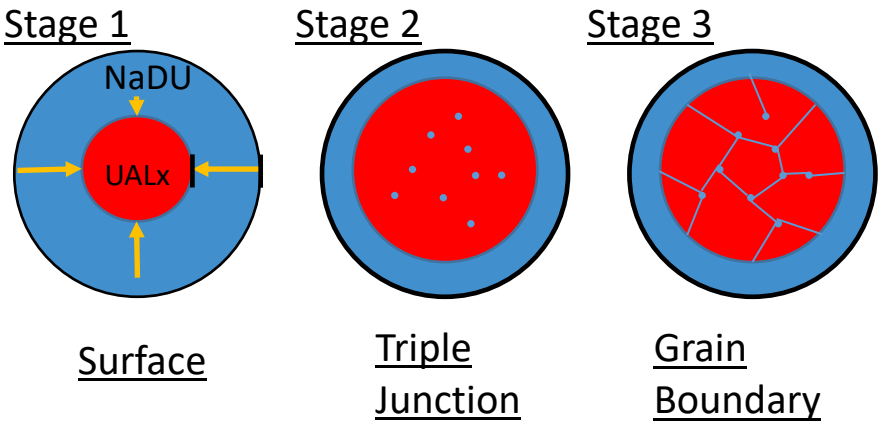

Figure 1) Stages of the digestion of pure and polycrystalline UAl_3.

GBE has classically been applied to cubic systems [21] and in particular fcc material. As UAl_3 is an fcc material (group no. 221 Pm-3m), it is no surprise

that it follows the intergranular oxidation behavior of other materials within similar crystallographic group. It could be speculated that, only cubic materials that follow intergranular oxidation should be considered for isotope production, if the particles are polycrystalline. However, UAl_2 is also a fcc material (group no. 227, Fd-3m) [17] and does not show signs of intergranular oxidation. The reason for its ability to resist digestion is unknown. This exception might give some insight into a more developed theory later on. However, the ability for a material to oxidize via intergranular oxidation, or some way to penetrate the fuel particles, should be a consideration for future materials in isotope production to ensure complete digestion.

The results presented in chapters 2-4 indicate that it is important to study the effects that different manufacturing steps have on the microstructure of the fuel. The production of a plate involves hot rolling, cold rolling, and a prolonged anneal [22, 23]. These steps are performed to make the plate into its final dimensions and to ensure its safety within a reactor. However, each one of these steps has the ability to change the grain size, reduce high energy grain boundaries, and oxidation resistant grain boundaries. Further research should be done to analyze these steps and their effect of the microstructure of the fuel.

The results in chapters 5 and 6 study the physical and digestion properties of U_6Mn and provides the first method to digest this material successfully. The family of U_6Metals has the highest know U-density and could be the fuel that allows for the highest amount of uranium in a target (Figure 2).The fuel loading in a target is allowed to go up to 50%, making the range of possible U-densities in a target to be between 4 and 9 gU cm^{-3}. The U-density of LEU dispersion targets utilizing UAlx fuel is in the range of 2.5-3gU cm^{-3}. Candidate alloys with a higher U-density than UAlx and that have been researched are: UO_2 (9.7 gU cm^{-3}) [15], U_3Si_2 (11.3 gU cm^{-3}), U_3Si (14.7 gU cm^{-3}) [13, 24] and U_6Mn (16.8 gU cm^{-3}). If U_6Mn can successfully replace UAlx, then it would be the maximum U-density that could exist in a LEU target. However, a method to digest U_6Mn was not known until now. The successful application of $KMnO_4$ to a caustic digestion bath converts the surface of U_6Mn to $Na_2U_2O_7$. Furthermore, ultrasonication or a selective oxidation of the material allows for digestion to proceed throughout the material. Combining these techniques allows for the digestion of U_6Mn to be complete and within a time scale suitable for industry.

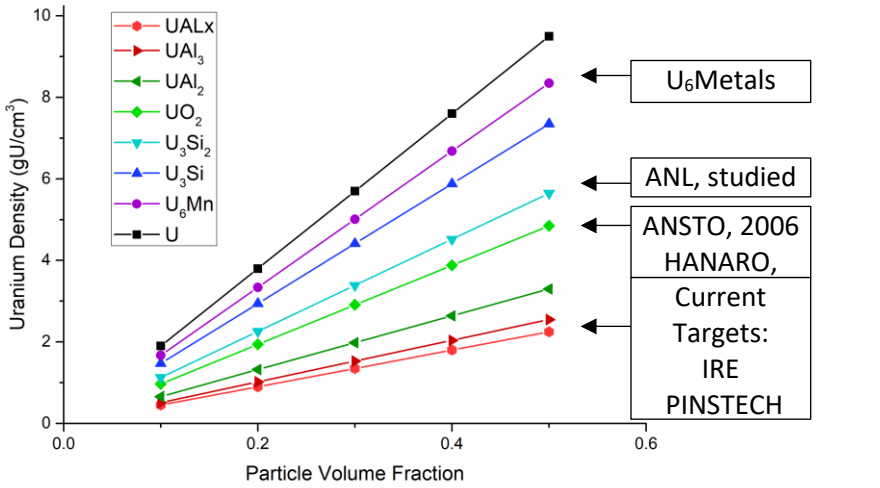

Figure 2) U-density of high density alloys of known alloys as a function of particle volume fraction.

There are many significant differences in the way that U_6Mn digests compared to uranium aluminides. Firstly, it was found that it cannot be digested in standard caustic digestion baths and that a catalyst or oxidant is needed. It was demonstrated in Chapter 6 that the use of potassium permanganate has the ability to convert the surface of U_6Mn particles to an oxide and sodium diuranate. This discovery alone implies the possibility of using U_6metals in isotope production. This discovery also highlights the problems that may occur when digestion cannot happen via intergranular oxidation. An additional step is needed to ensure the entire particle is digested and this additional step will likely cost time or add impurities. A crucial additional step is a way of advancing the digestion front, which was made possible by using ultrasonication to separate the core from its oxide shell, or digesting an U_6Mn-UMn_2 alloy, which selectively oxidizes the particle as UMn_2 oxidizes more readily.

A good strategy to ensure the digestion of fuel particles if intergranular oxidation is not possible, is to selectively oxidize or through selective leaching. Comparable cases can be made between the alloy systems of U_6Mn-UMn_2 and UAl_3-UAl_4. In the case of uranium-manganese alloys, there is a dissolution of the UMn_2 phase, creating cavities that allow the digestion solution to flow through the structure. In the case of uranium-aluminum

alloys, it is the selective oxidation of the UAl_4 phase that is able to penetrate deep into the particle. A similar effect is also the case for aluminum rich grain boundaries. In all these cases, there is a percolation network or a continuous path for the solution to travel though. In all cases, there must be an optimization of phase sizes and the connectivity of the continuous phase. If U_6Mn-UMn_2 alloys were to be used in future targets, these effects and parameters would have to be researched further to ensure total digestion. If a competing process would like to use another high U-density alloy that has difficulty in digesting, then creating a eutectic composition or a biphasic alloy with an oxidation susceptible second phase should be explored.

A promising aspect of using U_6Mn targets is in the reduction of waste. When using the combination of NaOH with $KMnO_4$, the volume of digestion solution does not need to increase. The solvent volume will still be determined by the solubility of sodium aluminate at 2.1M/L. If the U-density is roughly in U_6Mn is roughly 4 times the U-density in UAlx, this would also mean roughly 4 times as less waste for the same amount of molybdenum produced, assuming no further processing of the yellow cake is necessary. A drawback in LEU targets in general is the presence of higher concentrations of alpha emitters [12]. Irradiated LEU targets will contain higher amounts of neptunium-239 and plutonium-239 than the equivalent HEU targets[11]. It is estimated that LEU targets produces about 25 times more plutonium-239 than in an equivalent HEU target. However, HEU targets contain higher concentrations of uranium 234 which is also an alpha emitter. Both uranium and plutonium isotopes can be effectively removed during target processing [25] .

2.2 Bringing U_6Mn technology from lab scale to industry

This thesis only demonstrated the possibility for U_6Mn to undergo a digestion process which theoretically will release isotope from the fuel and into solution. There are many steps that need to be done in order to prove and evaluate the use of U_6Mn for isotope production on a large scale. These steps can be separated into three general topics: 1) nuclear design and neutronic calculations; 2) post irradiation examination (PIE), digestion of irradiated plates, and qualification of targets; 3) upscaling experiments.

For nuclear design [26] and neutronic calculations [27], a parametric study needs to be performed to nominate parameters for evaluation, define the

[11] LEU targets contain more U-238 than HEU targets, U-238 turns into Np-239 through neutron capture, which decays with a half-life of 2.3 days to Pu-239

parameter range, specify the design constraints and analyze the results of each parameter variation. More specifically, a parametric study for the target design, optimization of dimensions of the meat, cladding specifications, location of the target in a reactor and other parameters related to the irradiation of the target. In designing target parameters, the optimization of yield ratio ($Ci^{99}Mo/gU$) and surface heat flux should be compared for different target irradiation locations, target thickness, and target geometry. Neutronic calculations would need to be made to predict the expected ^{99}Mo activity in a target identified in the parametric studies. In early stages of target qualification, mini-plates are used instead of full sized targets as an initial validation, but the parameters of the mini-plate and a full sized target need to be checked.

The next steps to be taken after neutronic calculations is the irradiation of mini-plates and experiments relating to irradiated targets. Irradiated target would be examine on how they performed in a PIE analysis. As the irradiation of mini-plates containing U_6Mn has already been performed [28-30], many aspects their irradiation performance is already known. However, it is important to see if there is any interaction layers that develop and how these interactions affect the digestion process.

Although it is often thought that the chemistry of irradiated and un-irradiated plates do not change due to the low burn-up they experience [12], it cannot be taken for granted. In the case of U_3Si_2, irradiated silicide digested slower than un-irradiated due to the bonding of the silicide particles during irradiation [14, 15]. A thermodynamic assessment of a U-Mn-Al ternary system would help evaluate the effects of an interaction layer. With irradiated targets, the yield of ^{99}Mo from this digestion process can be calculated, as it could not be with the cold samples digested in this thesis.

If all of the aforementioned studies result in a positive assessment, then an upscaling of the process would need to be examined. Digestion of isotope production targets normally occurs in batches of three or more [31] and would need to be performed in a digestion vessel that could handle this amount of material. The digestion of U_6Mn targets could be done at existing process facilities using the same hot cells and digestion vessels that are used to digest UAlx targets. The filtration time, the thickness of the yellow cake, and the purification of the isotopes could also be studied at these facilities.

2.3 Expanding grain boundary engineering

This thesis explores many concepts and techniques to digestion isotope production targets. Three reoccurring ideas in this thesis are:

1) Incorporating GBE into isotope production targets

2) Expanding GBE to include favorable corrosion in the form of digestion

3) Controlling the microstructure of materials to control the digestion rate

The use of grain boundary characteristics into isotope production targets is currently only a topic in the characterization of targets, pre- and post-irradiation. Previously, efforts in advancing the digestion reaction was focused on adding oxidants or accelerants [13, 20, 32] or in decreasing particle sizes. Presented here is evidence that small grain sizes and random high angle grain boundaries accelerate the digestion process. Further research into this can be found in nanostructured alloys and sever plastic deformation (SPD) [33, 34]. The concept of "large plastic strains" that are characterized by a high value of accumulated strain ($e \geq 0.5$) are realized at low temperatures (≤0.4 melting point) and is an emerging technique in nanogranular or ultrafine-grained (UFG) material. There have been a few basic rules proposed for the formation of UFG structures with primarily high-angle grain boundaries through SPD processing [35]. These rule are adapted and are variables to consider in producing digestion susceptible UAlx particles:

1) SPD processing at low-temperatures (temperatures less than 0.4 T_m) is referred to as an important requirement. Only in this temperature regime is it possible to achieve dislocation densities of 10^{14} m^{-2} or higher. Higher processing temperatures result in a lower accumulated dislocation densities and increase in grain size, as presented in chapter 2 for uranium aluminides.

2) The degree of strain during processing should exceed 6-8. Although considerable refinement in microstructure is obtained at strain of 1-2, the formation of UFG with a majority of high-angle grain boundaries requires further straining.

3) High hydrostatic pressure, usually > 1GPa, are important for efficient SPD processing.

Techniques for bulk production of nanocrystalline materials are emerging [33], but bringing these techniques to isotope industry will require further

research. A caution in pursuing nanocrystallinity in the digestion of fuel is to first identify if a nanocrystalline structure would actually favor digestion or corrosion, as the relationship between nanocrystallinity and digestion/corrosion varies significantly from one material to the next. A fine grained structure could lead to enhanced passivation causing oxidation resistance [36], or enhanced catalytic or kinetic activity promoting oxidation susceptibility [37]. In the case of UAL_3, where surface passivation does not stop intergranular oxidation (Ch. 2 and 3), then nanocrystalline techniques are likely to succeed in making the material oxidation susceptible. In the case of U_6Mn which is restricted to surface oxidation and passivation (Ch. 6), then it is likely to make it more digestion resistant.

Finally, the use of low-enriched uranium based medical isotope production has only recently been a major production path for medical isotopes. It is my hope that this thesis will provide new design concepts that can improve existing targets and pave the way for next generation targets. By improving our understanding of these targets and their digestion, I hope to contribute to nuclear non-proliferation, to the increase of medical isotope production, and to the stability of the supply chain.

References

1. Van den Berghe, S., A. Leenaers, and C. Detavernier, *SELENIUM fuel: Surface engineering of U (Mo) particles to optimise fuel performance*, in *RRFM 2010 transactions*. 2010.
2. Leenaers, A., S. Van den Berghe, and C. Detavernier, *Surface engineering of low enriched uranium–molybdenum.* Journal of Nuclear Materials, 2013. 440(1-3): p. 220-228.
3. Leenaers, A., *Surface-engineered low-enriched Uranium-Molybdenum fuel for research reactors.* University of Ghent-SCK• CEN, 2014(ISBN 9789076971223).
4. Ryu, H.-J., et al., *The effect of Si-rich layer coating on U-Mo vs. Al interdiffusion.* Nuclear Engineering and Technology, 2011. 43(2): p. 159-166.
5. Kim, Y.S., et al., *In-pile test results of U-silicide or U-nitride coated U-7Mo particle dispersion fuel in Al.* Journal of Nuclear Materials, 2014. 454(1-3): p. 238-246.
6. Jungwirth, R., et al., *Heavy ion irradiation of UMo/Al samples PVD coated with Si and ZrN layers.* Journal of Nuclear Materials, 2013. 434(1-3): p. 296-302.
7. Iltis, X., et al., *Microstructure of as atomized and annealed U-Mo7 particles: A SEM/EBSD study of grain growth.* Journal of Nuclear Materials, 2017. 495: p. 249-266.
8. Jadernas, D., et al., *Microstructural characterization of as-fabricated and irradiated U-Mo fuel using SEM/EBSD.* Journal of Nuclear Materials, 2018. 509: p. 1-8.
9. Leenaers, A., et al., *Effect of fission rate on the microstructure of coated UMo dispersion fuel.* Journal of Nuclear Materials, 2017. 494: p. 10-19.
10. Ye, B., et al., *A modelling study of the inter-diffusion layer formation in U-Mo/Al dispersion fuel plates at high power.* Journal of Nuclear Materials, 2018. 499: p. 191-203.
11. Leenaers, A., et al., *Post-irradiation examination of uranium–7 wt% molybdenum atomized dispersion fuel.* Journal of Nuclear Materials, 2004. 335(1): p. 39-47.
12. *Medical Isotope Production Without Highly Enriched Uranium.* National Academies Press (US): p. 220.
13. Buchholz, B.A. and G.F. Vandegrift, *Processing of LEU targets for 99Mo Production -- Dissolution of U3Si2 Targets by Alkaline Hydrogen Peroxide.* (INIS-XA-C--2005). International Atomic Energy Agency (IAEA), 2004.

14. Sameh, A. *Production of fission Mo-99 from LEU uranium silicide target materials*. in *Invited Papers on Symposium on Isotope and Radiation Applications*. 2000. ROC.
15. *Non-HEU production Technologies for Molybdenum-99 and Technetium-99m.* IAEA Nuclear Energy Series, 2013(No.NF-T-5.4).
16. Olander, D.R., *Fundamental aspects of nuclear reactor fuel elements: solutions to problems*. 1976, California Univ., Berkeley (USA). Dept. of Nuclear Engineering.
17. *Gmelin Handbook of Inorganic Chemistry U Supplement Volume B2 Alloys.* 1989: p. 333.
18. Vértes, A., et al., *Handbook of Nuclear Chemistry: Vol. 1: Basics of Nuclear Science; Vol. 2: Elements and Isotopes: Formation, Transformation, Distribution; Vol. 3: Chemical Applications of Nuclear Reactions and Radiation; Vol. 4: Radiochemistry and Radiopharmaceutical Chemistry in Life Sciences; Vol. 5: Instrumentation, Separation Techniques, Environmental Issues; Vol. 6: Nuclear Energy Production and Safety Issues*. 2010: Springer Science & Business Media.
19. Grenthe, I., Drozdzynski, J., Fujino, T., Buck, E., Albrecht-Schmitt, T.E., Wolf, S.F, *The Chemistry of the Actinide and Transactinide Elements, Chapter 5.* 2006. 1.
20. Wymer, R., R.J.I. Blanco, and E. Chemistry, *Uranium-aluminum alloy dissolution.* 1957. 49(1): p. 59-61.
21. Tan, L., et al., *Microstructure tailoring for property improvements by grain boundary engineering.* 2008. 374(1-2): p. 270-280.
22. Ali, K.L., et al., *Development of low enriched uranium target plates by thermo-mechanical processing of UAl2–Al matrix for production of 99Mo in Pakistan.* Nuclear Engineering and Design, 2013. 255: p. 77-85.
23. Saliba-Silva, A., et al., *Research reactor fuel fabrication to produce radioisotopes.* 2011.
24. Dittrich, S., *History and Actual State of Non-HEU Fission-Based Mo-99 Production with Low-Performance Research Reactors.* Science and Technology of Nuclear Installations, 2013. 2013: p. 1-9.
25. Vandegrift, G.F., *Facts and myths concerning 99 Mo production with HEU and LEU targets*. 2005.
26. Cho, D.-K., M.-H. Kim, and D.-S.J.J.o.t.K.N.S. Sohn, *Nuclear Design Methodology of Fission Moly Target.* 1999. 31(4): p. 365-374.
27. Lee, B.C. and H. Kim, *Neutronic analysis for the fission MO production using LEU target at HANARO*. 2002.
28. Meyer, M.K., et al., *Irradiation behavior of U6Mn–Al dispersion fuel elements.* Journal of Nuclear Materials, 2000. 278(2-3): p. 358-363.

29. G.L. Hofman, R.F.D., G.L. Copeland, *Irradiation behavior of low-enriched U6Fe-Al dispersion fuel elements.* Journal fo Nuclear Materials, 1987. 150: p. 238-243.
30. Ugajin, M., et al., *Irradiation behavior of high uranium-density alloys in the plate fuels.* Jounral of Nuclear Materials, 1998. 254: p. 78-83.
31. Muenze, R., et al., *The Fission-Based 99Mo Production Process ROMOL-99 and Its Application to PINSTECH Islamabad.* Science and Technology of Nuclear Installations, 2013. 2013: p. 1-9.
32. Gelis, A.V., et al., *ANL progress on the Cooperation with CNEA for the MO99 Production.* RERTR 2004, 26 International meeting on Redduced Enrichment for Research and Test Reactors, Jan 2004.
33. Valiev, R., *Producing bulk nanostructured metals and alloys by severe plastic deformation (SPD)*, in *Nanostructured Metals and Alloys*. 2011, Elsevier. p. 3-39.
34. Pineau, A., A. Amine Benzerga, and T. Pardoen, *Failure of metals III: Fracture and fatigue of nanostructured metallic materials.* Acta Materialia, 2016. 107: p. 508-544.
35. Valiev, R.J.I.j.o.m.r., *Nanostructuring of metallic materials by SPD processing for advanced properties.* 2009. 100(6): p. 757-761.
36. Ambat, R., N.N. Aung, and W.J.C.s. Zhou, *Evaluation of microstructural effects on corrosion behaviour of AZ91D magnesium alloy.* 2000. 42(8): p. 1433-1455.
37. Jung, H. and A.J.E.A. Alfantazi, *An electrochemical impedance spectroscopy and polarization study of nanocrystalline Co and Co–P alloy in 0.1 M H2SO4 solution.* 2006. 51(8-9): p. 1806-1814.

Appendix I
Digestion of pure UAl_2

UAL_2 is found to not digest in the conditions that were studied in this thesis. Experiments were performed between 4 and 8M NaOH, at 95°C and for the duration of 3 hours. Figure 1 shows a UAL_2 particle that was in a digestion bath of 4M NaOH at 95°C for 3 hours. The sample was prepared in the method described in chapter 2 sec. 2.3. It can be seen that even surface oxidation is not present. A small amount of UO_2 developed, but no TJ or GB are digested.

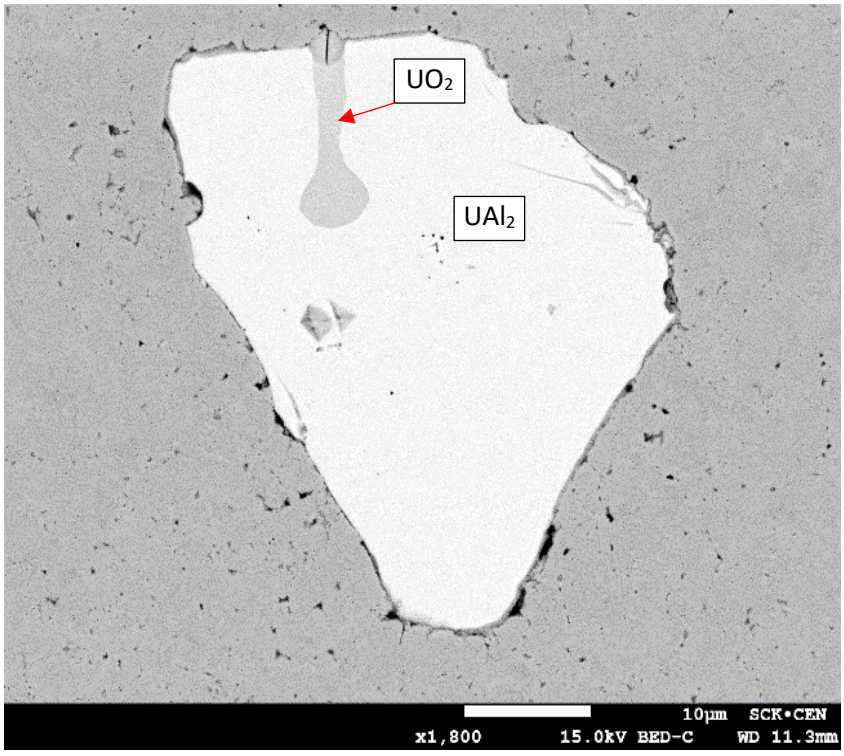

Figure 1) Digestion of a UAl_2 particle in 4M NaOH, at 95°C for 3 hours.

Appendix II
Digestion of pure UAL_4

Pure UAl_4 is found to digest in caustic media. Figure 2 demonstrated a UAl4 particle digested in 4M NaOH at 95°C for one hour. Surface digestion occurred with an approximate thickness of 10µm. Oxidation is found inside the surface, and was determined through EDX analysis to be $Na_2U_2O_7$. As the amount of digested pure UAL_4 was limited, the type of oxidation remains unclear. Figure 2 B shows that the fuel particle contains voids. The oxidation that is shown is likely to have originated in voids, as the centers of the digested zones are also voids. A follow up digested is recommended to clarify if UAl_4 undergoes intergranular oxidation or only surface oxidation and oxidation of voids.

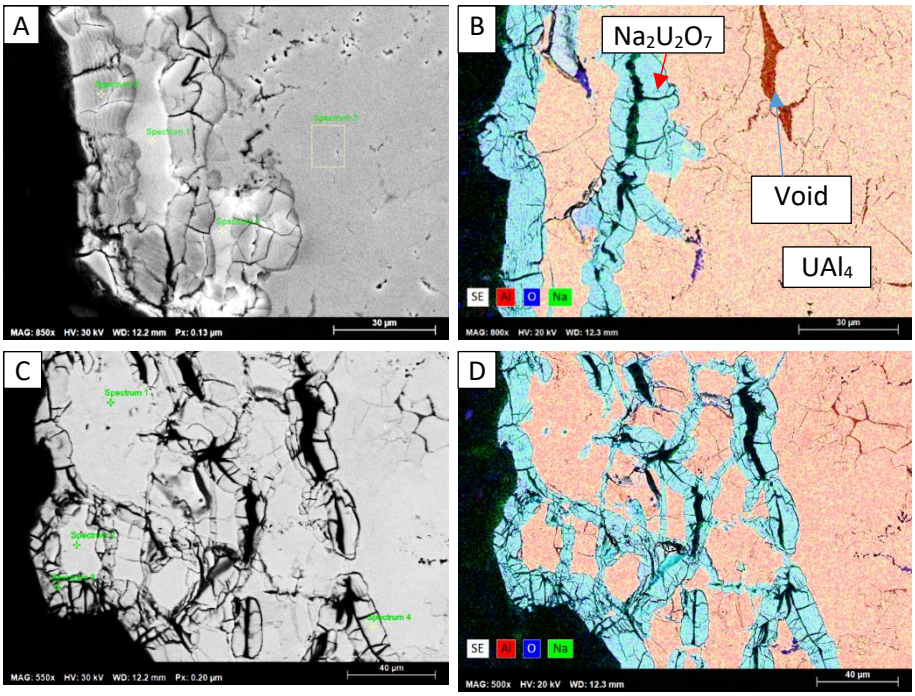

Figure 2) Digestion of UAl_4 particle. 4M NaOH at 95°C for 1 hour. A and C) BSE image of digested UAl_4 particle. B and D) SE-EDXS elemental map, sodium in green, oxygen in blue, aluminum in red.

Appendix III
Grain size evolution

Chapters 2 and 3 of demonstrate the importance of grain sizes in digesting UAl_3. Additionally, digestion of as-fabricated fuel particles often did not go to completion. This is a likely consequence of its grain size. Figure 3 demonstrates the differences in grain sizes of samples in this thesis. Figure 3 blue and green, are the grain size distribution of UAl_3 buttons that were prepared in an arc-melter and annealed for 3 days (see sec. 2.1). The red and black lines are the grain size distribution of different UAlx fuel targets. The average grain size by area fraction in target 1 is 2µm. In order to complete digest particles, grain sizes should be below 10µm.

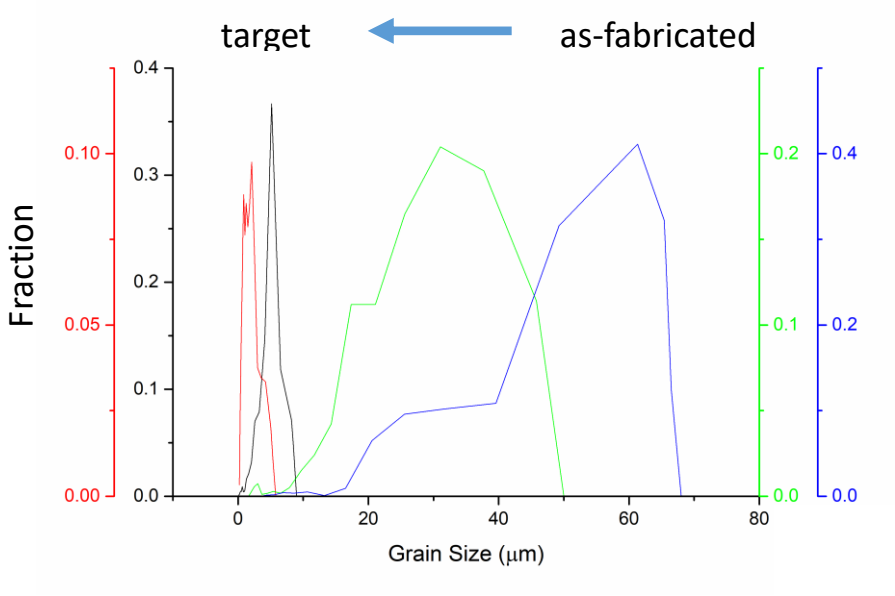

Figure 3) Comparison of grain sizes in as-fabricated fuel and in targets. blue- UAl_3 annealed.; green- UAl_3 annealed; black - HEU target 1; red- HEU target 2.

Appendix IV
Digestion of UAl_3 inside a target

The digestion of pure UAl_3 particles in a target has been demonstrated to digest with the same mechanisms that the as-fabricated fuel used in chapters 2 and 3. Figure 4 shows the digestion of a UAl_3 fuel particle in a target after 30 minutes of digestion at 60^{o}C. The fuel particle shows both TJ and intergranular oxidation. Figure 4B is and IPF and Figure 4 is a unique grain map. Both maps demonstrate that not all grain boundaries are oxidized. The inset of Figure 4A shows a Σ9 boundary that is not digested. More particles need to be analyzed to have a statistically relevant analysis. However, the examples that were found follow the digestion stages that have been outlined in this thesis. A completion of this analysis is recommended.

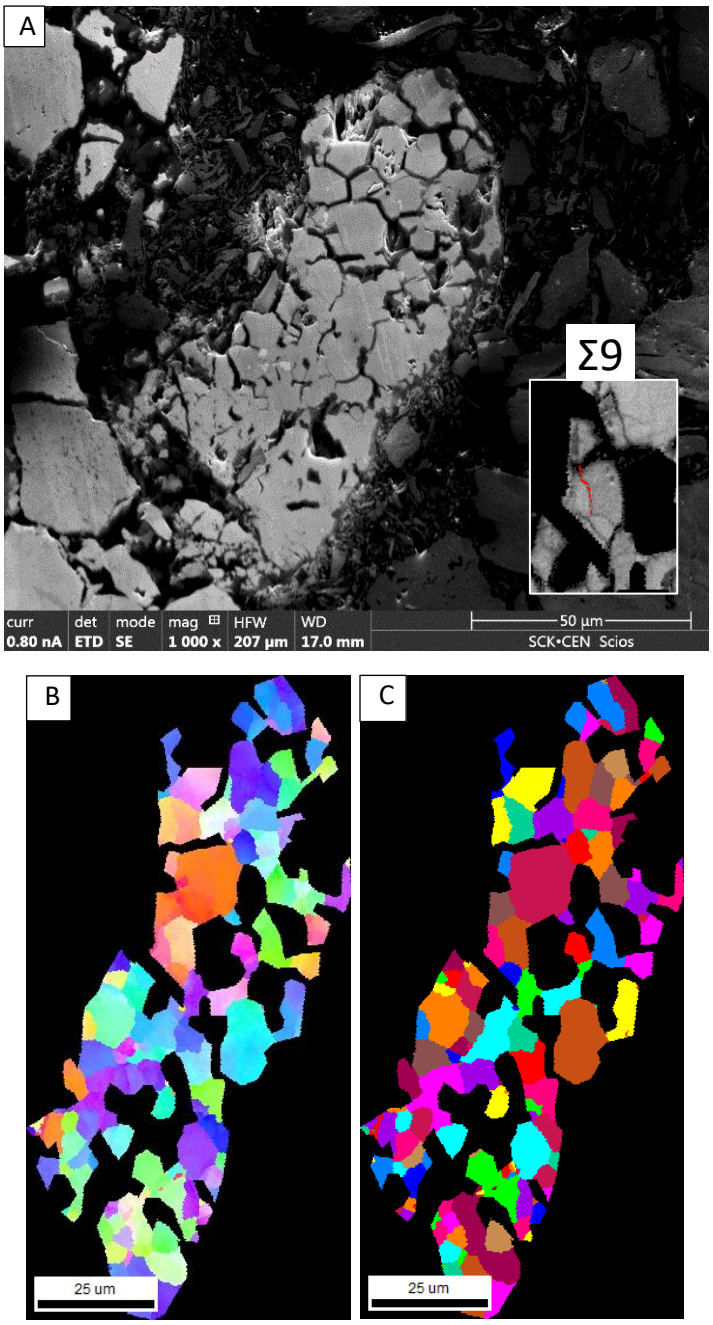

Figure 4) Digested UAl_3 in an HEU target. Digest occurred for 30min. at 60°C in 4M NaOH. A) SEM image; B) IPF; C) Unique grain